On Tropospheric Rivers

by

Yuanlong Hu

B.S. in Meteorology, Beijing University (1985)
M.S. in Atmospheric Physics, Chinese Academy of Meteorological Sciences (1988)

Submitted to the Department of Earth, Atmospheric, and Planetary Sciences
in partial fulfillment of the requirements for the degree of

Doctor of Philosophy

at the

MASSACHUSETTS INSTITUTE OF TECHNOLOGY

May 2002

Author .....
Department of Earth, Atmospheric, and Planetary Sciences
May 2002

Certified by .....
Reginald E. Newell
Professor of Meteorology
Thesis Supervisor

Accepted by .....
Ronald G. Prinn
Head of the Dept. of Earth, Atmospheric, and Planetary Sciences

On Tropospheric Rivers

by

Yuanlong Hu

Submitted to the Department of Earth, Atmospheric and Planetary Sciences
on May 3, 2002 in partial fulfillment of the
requirements for the degree of
Doctor of Philosophy in Meteorology

ABSTRACT

In this thesis, we investigate atmospheric water vapor transport through a distinct synoptic phenomenon, namely, the Tropospheric River (TR), which is a local filamentary structure on a daily map of vertically integrated moisture flux.

Firstly, an automated procedure for identifying and tracking these rivers (named TRICKS, i.e., the Tropospheric River Identifying and traCKing Scheme) is described and its performance is evaluated. This procedure enables the maxima of moisture flux (so-called TR cores) to be detected and accurately located. The relationships among the adjacent TR cores are then evaluated to construct the axes of rivers. A river is tracked from birth to termination and its life cycle properties are recorded, thus allowing various statistics of TR distributions and movements to be estimated. All these stages of the scheme are performed without intervention once a number of governing constants have been decided upon.

We then apply the scheme to the vertically integrated moisture flux calculated from 43 years of 6-hourly NCEP/NCAR reanalyses and present a climatology of mean TR behavior. On average, there are 4 - 5 rivers per analysis in the Northern Hemisphere and 5 in the Southern Hemisphere. Northern Hemisphere TRs form and intensify near the eastern seaboards of Asia and North America. They move eastward and poleward during their lives before weakening in the two principal graveyards: over the Gulf of Alaska and the region to the southeast of Greenland. In comparison, Southern Hemisphere TRs are more evenly distributed and tend to form in a band extending from the southeast coast of South America into the Atlantic, across the Indian Ocean, and throughout much of middle latitudes of the Pacific sector. The corresponding genesis regions are also found to be adjacent to (or slightly equatorward to) the maximum SST gradients in these regions. It appears that both TR genesis and termination maxima tend to be displaced near the upstream equatorward flanks of cyclogenesis and lysis maxima. We suggest that the TR formation and termination could be a leading predictor for the occurrence and decaying of extratropical cyclones. TR axis length appears to be longer during the warmer season and in the Southern Hemisphere. The distance traveled by TR systems shows a broad distribution and a sizeable fraction (~25%) of systems travel in excess of 3000 km. One unique feature is

that although TRs occur very actively over the Indian ocean sector with highly densed tracks, large translational speeds, and intensities, they contribute little to meridional water vapor transport, while the reverse situation can be found in the South Pacific where southward transport is sometimes comparable to those over or off the east coast of South America. The rivers seem to account for a substantial fraction of the total meridional moisture transport in both middle and subtropical regions.

Finally, we complete the TR climatology with an analysis of the variability and trends exhibited by many aspects of rivers during the 43-year period. The annual average number of TRs per analysis has undergone an overall increase during the last couple of decades and is more significant in the Southern Hemisphere. The greatest increases occur in the 50°–30°S and 50°–70°N belts. We suggest that warming and cooling trends in surface air temperature are accompanied, respectively, by increases and decreases in TR frequencies (particularly in the Southern Hemisphere). We also examined the extent to which changes in TR frequency and strength might be related to the variations in broader atmospheric system such as the ENSO phenomenon.

The results of the mean and variability of TR behavior have added to our knowledge of atmospheric water vapor transport and represent a data set which may be used to aid in the understanding of the complex mechanisms governing the atmospheric circulation.

Thesis Supervisor: Dr. Reginald E. Newell
Title: Professor of Meteorology

Acknowledgments

Writing this thesis has incurred many debts. I owe a special debt to Professor Reginald E. Newell, supervisor of this thesis, for his insights, encouragement, support, and guidance throughout my studies at MIT. I greatly benefited from his knowledge of climate changes, atmospheric chemistry, meteorological data, etc. Without his enthusiasm, inspiration, and support, this work could not have been done. I extend my sincere thanks to my other thesis committee members, Drs. Alan Plumb, Kerry A. Emanuel, and Elfatih A. B. Eltahir, for their constructive criticism and helpful suggestions during the final course of this work, and their close and perceptive reading of the thesis manuscript.

I have benefited from scientific communications with Drs. Ian Simmonds and Ross J. Murray of the University of Melbourne in Australia, Mark R. Sinclair of Embry-Riddle Aeronautical University in Arizona, and Isabel F. Trigo of the University of East Anglia in UK. All of them kindly provided the original codes of their cyclone finding and tracking schemes that were very helpful in developing the numerical scheme in the thesis.

I also have enjoyed both the academic and social interactions with many people at MIT. I would like to thank all of my friends presently or formerly at EAPS and CE. In particular, Dr. Zhongxiang Wu, Dr. Jingfeng Wang, Dr. Xinyu Zheng, Dr. Jeremy S. Pal, Dr. Jeff Scott, Mr. Jiyong Wang and his wife Haiyan Zhang, Chris Winkler, and Bruce Kuo.

I am grateful to Dr. John Y. N. Cho for proofreading the thesis manuscript and many inspiring conversations on various topics, Will Heres for computer supports, and Dorothy Frank and Mary Elliff for valuable administrative assistance.

The most important people in this whole endeavor have been my parents, Zhimin Hu and Aiqing Ye. They encouraged me to pursue my true interests and would have been supportive of any path I chose. I can't express how grateful I am to my parents whose unbounded love has continuously flowed across the Pacific. Appreciation is extended also to my parents-in-law, Zhongshun Gao and Mei Chen, and my sister-in-law, Prof. Haiyan Gao. I owe a great deal to my mentors and dearest friends, Liang Fei and Xingzhang Tang at the Shanghai Meteorological Bureau, who encouraged me to challenge the new world and always be there when I need advice.

Finally, I wish to express my deepest affection to my wife, Yang Gao, for her love, joy,

patience, and understanding. Our love story was among one of the beautiful romantic stories that occurred on the campus. Without her sacrifice, endurance, and unconditional support during my late years at MIT, my study at MIT would not have been so smooth and colorful. It is to her that this work is dedicated.

Contents

List of Figures

List of Tables

Chapter 1

Introduction

1.1 General Remarks

Water vapor is critically important to life on Earth. The global and continental scale transport of water vapor has important implications for climate variability and hydrology owing to the following factors: (1) enormous amounts of energy are consumed or released upon phase changes of water vapor; (2) the distribution of atmospheric water vapor may significantly alter the efficiency with which the Earth system converts the incident solar radiation to energy that is available for driving dynamic atmospheric circulation; (3) water vapor is the principal greenhouse gas responsible for re-radiating the longwave flux emitted by the heated Earth's surface; and (4) water vapor is a limiting factor in the functioning of the biosphere, which exerts significant control over various hydrologic and atmospheric processes. Furthermore, these factors are linked and have influential feedbacks on each other. A detailed depiction of the atmospheric hydrological cycle may have significant relevance to a variety of atmospheric chemistry investigations. Reliable water vapor distributions are necessary for the accurate estimation of atmospheric oxidizing power and concentrations

of various chemical species. With its great mobility and brief atmospheric residence time, water vapor is a central component of the global hydrological cycle. It is also of considerable interest to determine how the atmospheric branch of the hydrological cycle might respond if the planet were to warm from the rise in greenhouse gases. Lorenz (1991) even speculated "that the pressure systems of an earlier generation, which by 1970 were more often called circulation systems, might some day be called water systems...".

Constructing a quantitative picture of water's cycling through its major reservoirs on our planet is a complex, challenging puzzle involving scientists of many disciplines. At present, we have only a rough, qualitative understanding of the earth's large-scale hydrological cycle (National Research Council 1991, 1999). Its temporal and spatial variability has been systematically explored only in relatively restricted regions or time periods, and a completely consistent atmospheric branch of the hydrological cycle within the context of the water budget balance has not been established. Understanding the mechanisms of climate change requires accurate estimates of the hydrological cycle and its linkages on both regional and global scales. The importance of constructing this quantitative understanding is underscored by the high priority the World Meteorological Organization has given to the Global Energy and Water Experiment (Chahine 1992; National Research Council 1999), which is coordinating numerous water cycle research projects worldwide.

Reasons for the scant quantitative knowledge of our atmospheric hydrological cycle stem mainly from the lack of observations, especially over the oceans, and their spatio-temporal variability. Rainfall and clouds often occur on quite small time and space scales, so that a single point of precipitation observation may not be representative of more than an area with dimensions of a few kilometers across or for more than a small fraction of a day. The study of the atmospheric hydrological cycle has experienced a remarkable

renewal of interest in recent years due to the emergence of new observation and assimilation techniques and new diagnostic approaches. There has been a significant number of papers that have examined the behavior of atmospheric moisture and its transport. In the next section, I attempt to give an overview of atmospheric water vapor transport studies. Though not exhaustive and comprehensive, it will serve as a guideline of how we derive our thesis motivation.

1.2 A Review of Previous Studies

Water vapor is transported in the atmosphere by molecular and turbulent diffusion, convection, and advection. The vertical flux of evaporation from the oceans and the land surface into the atmospheric boundary layer is accomplished by diffusion, and the vapor is vertically mixed by diffusion and convection. On the temporal and spatial scales of lateral transport, advection is the dominant mechanism. On these scales, water vapor can be treated as a scalar admixture advected by the horizontal wind. Water vapor transport has been a prominent subject of research in meteorology for more than several decades. The list of contributions from observational works alone is immense. Early estimates of atmospheric water vapor fluxes based on rawinsonde measurements helped to highlight both the importance of the low-level winds for determining the moisture transport, and the inadequacy of the rawinsonde network for obtaining accurate estimates of water vapor flux convergence (e.g., Benton and Estoque 1954; Rasmusson 1967, 1968; Rosen et al. 1979; Peixoto et al. 1981; Salstein et al. 1983; Savijarvi 1988). The latter is a key quantity that, if sufficiently accurate, offers the opportunity to estimate a number of other difficult-

to-observe hydrological parameters. For example, Rasmusson (1968) showed how evaporation can be estimated over North America as a residual of the atmospheric water budget provided estimates of precipitation are available. Furthermore, surface-subsurface water storage changes can be estimated if the streamflow is known. While promising, that study pointed to deficiencies in the atmospheric station data that limits the application to regions with a high density station network and requires spatial averaging over a sufficiently large area. This so-called atmospheric water balance method (or budget method), which was presented firstly by Starr and Peixoto (1958), has been used substantially since then.

Although the rawinsonde network over major continents has changed little since these early studies, there is now a vast amount of new operational data and information available. Several campaigns have been conducted or are ongoing with the major objective of documenting the time/space variability of the hydrologic cycle in the atmosphere, at the land surface, and in the upper oceans (International GEWEX project office, 1994). This includes the GEWEX (stands for the Global Energy and Water Cycle Experiment) Water Vapor Project (GVaP) and related NASA Water Vapor Projects (NVAP, Randel et al., 1996), Global Precipitation Climatology Project (GPCP, Huffman et al., 1997), International Satellite Cloud Climatology Project (ISCCP, Rossow et al., 1991), and Global Runoff Data Center (GRDC, Koblenz, 1994), etc.

As mentioned before, large radiosonde data gaps over the oceans, and even over some land areas (e.g., Africa), limits our ability to define the global water vapor distribution. The newer data sources, such as those from infrared and microwave satellite sensors, can greatly enhance the global coverage on a daily basis. Examples of presently available large-scale water vapor data sets include satellite microwave retrievals from the Special Sensor Microwave Imager (SSM/I) data of Defense Meteorological Satellite Program

(DMSP) over ocean (Jackson and Stephens 1995), Television and Infrared Operational Satellite (TIROS) Operation Vertical Sounder (TOVS) infrared retrievals over land and ocean (Rossow et al., 1991; Wittmeyer and Vonder Haar, 1994), upper-tropospheric relative humidity from geostationary satellite (Schmetz et al., 1995), and a number of data sets using special radiosonde measurements for research purposes on limited time and space scales.

An attractive method for integrating the total information content of the data from a heterogeneous mix of observations is the four-dimensional data assimilation (4DDA) process which is part of the forecast/analysis routine. Operational weather forecast centers such as the NCEP (the National Centers for Environmental Prediction, i.e., the NMC, the National Meteorological Center prior to October 1995) and ECMWF generate consistent global data despite model biases. The most promising data sets introduced recently are the reanalysis products created by these two operational centers, and the same reanalysis project is also carried out in the NASA Data Assimilation Office (DAO).

While 4DDA should in principle provide a description of the water vapor flux field that is superior to that obtained from objective analysis of rawinsonde observations alone, such expectation has not yet been convincingly realized for the vapor flux fields over the continents. Before 1980 the operational analyses did not permit a realistic evaluation of the moisture transport. Early work by Rosen and Salstein (1980) using hemispheric gridded analyses showed that the NMC analyses did not contain a mean meridional circulation and water vapor values were too high. In recent years new estimates of the moisture fluxes have been obtained by using the budget method applied to model or assimilation data. Matsuyama (1992) compared the atmospheric flux convergence of water vapor to river discharge in the Amazon Basin. He concluded that the seasonal change pattern of precipi-

tation shows good correspondence to that of water vapor flux convergence except that the latter needs to be multiplied by a factor of 1.37 in order to match its annual value to the annual river runoff. Roads et al. (1994) conducted a comprehensive study of the United States hydrological cycle employing observations and the NCEP operational analyses. While the results were generally encouraging, significant discrepancies existed between surface water estimates from residual atmospheric moisture flux calculations and measurements of pan evaporation. Trenberth and Guillemot (1995) investigated the applicability of the analyses from NCEP and ECMWF to atmospheric moisture budget studies, but made no final conclusions, stating that "there is no acknowledged source of truth" for water vapor characteristics. Schmitz and Mullen (1996) utilized the ECMWF analysis data to study water vapor transport into the Sonoran Desert during the monsoon period. They pointed out that when only the mandatory level analyses are used, the ECMWF analyses do not possess sufficient resolution to yield accurate estimates of highly differentiated quantities such as the divergence of the vertically integrated flux of water vapor even at a T106 resolution. Higgins et al. (1996) studied the moisture budget of the NCEP/NCAR and the NASA/DAO reanalysis data sets. They found that both reanalyses overestimate the climatological mean precipitation rates by nearly a factor of 2 over the southeastern United States, and that there are substantial differences in the mean moisture divergence fields. In another study employing the same two data sets, Mo and Higgins (1996) found that the large-scale moisture transport is in general agreement in the two reanalyses despite regional differences, and that the discrepancies of moisture transport in the tropics are largely due to the divergent wind. Large and significant biases of moisture fields in the tropics from NCEP analyses were also confirmed by Trenberth and Guillemot (1998). Brahmananda et al. (1998) studied the moisture budget of the Walker circulation and showed that the large differences in rainfall between the two contrasting years (El Niño

and La Niña) in the western Pacific are accounted by the differences in the moisture flux convergence. Cohen et al. (2000) evaluated the zonal-mean meridional transport of water vapor across the globe using the 50 year NCEP/NCAR reanalysis and found that the values of transport tend to be notably larger than in climatologies derived from radiosonde-only-based analyses, and that the interannual variability in the transport is marked by a strengthening of water vapor transports over much of the winter hemisphere during ENSO warm events. Hu et al. (2001) studied the moisture circulations during the NASA Pacific Exploratory Mission in the Tropical Pacific phase B (PEMT-B) using also the NCEP/ NCAR data and suggested that there is a close relationship between the moisture circulations in the tropics and the atmospheric oxidizing power.

The effects of variability of atmospheric water vapor and its transport on weather systems and regional climate cannot be researched further without numerical experiments. Because of the high variability of water vapor in nature, such modeling efforts are still occasional in spite of the urgent needs in understanding the structure and dynamics of atmospheric water vapor and its transport, as well as the information needed for development and validation of improved coupled model subcomponents. Water vapor processes, including horizontal and vertical moisture transport, and formation of clouds and precipitation, are among the least satisfactory aspects of the current climate models and numerical prediction models (National Research Council 1991). Gaffen and Barnett (1992) compared interannual variations of specific humidity from radiosonde observations with simulations from the University of Hamburg version of the ECMWF GCM and found general agreement. More GCM simulation results on moisture flux have been compared with the 4DDA analyses and the observations including satellite data (Roads et al. 1992; Boyle 1993; Soden and Bretherton 1994; Bony et al. 1995). Chen et al. (1996) conducted a ten-year climate simulation using the NASA Goddard Laboratory for Atmospheres GCM as

part of their participation in the Atmospheric Model Intercomparison Project (AMIP). They showed that the hydrological mechanism maintaining the annual variation of the global precipitable water is coexistent with that of the observational study. Lau et al. (1996) evaluated the hydrologic processes from 29 GCMs from the AMIP project and found that while the majority of the models have a reasonable global water budget, about a quarter of the models show significant errors in the total global water balance, and a systematic underestimate of the frequency of occurrence of light precipitation events is present in almost all the AMIP models. Gaffen et al. (1997) accessed the water vapor simulations from 28 GCMs in AMIP and concluded that the models tend to underestimate the decadal mean precipitable water by approximately 5% over North America and globally as compared with radiosonde observations, and over the Pacific basin as compared with satellite SSM/I observations. These models appear to overestimate the poleward flux of moisture, which probably contributes to the general overestimate of atmospheric poleward energy flux. High-resolution limited area models (LAMs) were also used to study the water vapor transport over the continental scale or smaller to better address the problems encountered by the GCMs. One such effort is discussed by Giorgi et al. (1993, and references therein). They showed that it is possible to produce reasonable simulations of the regional hydrologic cycle by using the NCAR/PSU (Pennsylvania State University) limited area model (MM4) with boundary conditions taken from ECMWF analyses. Berbery et al. (1996) studied the North American continental-scale hydrology using the NMC Eta model (Eta is referred to the vertical coordinate using a step-like mountain representation as a generalization of the well-known sigma vertical coordinate, see Mesinger 1984). They found that the diurnal cycle of the water vapor fluxes and their seasonal changes obtained from the model forecasts are in good agreement with observations. Preliminary results from the Project to Intercompare Regional Climate Simulations (PIRCS, an LAM version of AMIP

with 12 regional climate models involved, Gutowski et al. 1998; Takle et al. 1999) showed that most models produced accumulated precipitation during the 1993 summer flood over the upper Mississippi River basin within about 10% of observed amounts (Arritt et al. 2000).

For all the GCM/LAM related studies, it has been increasingly recognized that further progress in atmospheric modeling is critically dependent on improving the simulation of water vapor processes. Yet the inaccuracy of water vapor observations, analysis error, and the vertical discretization of water vapor (which varies by several orders of magnitude) into model layers are the three major difficulties. One promising approach that is worth mentioning is the effort directed by both theoretical and empirical evidence that the analysis and simulation of joint transport of mass, potential temperature, and water vapor is better resolved in isentropic coordinates than in either isobaric or sigma coordinates. Johnson et al. (1993) and the subsequent research (Zapotocny et al. 1993; Zhu 1997) emphasized that the dry-adiabatic nature of the long-range transport of water when modeled in isentropic coordinates precludes dilution and ventilation prior to condensation and thus results in more accurate simulations. They suggested that isentropic modeling of the hydrologic cycle will more accurately resolve precipitation processes that stem from long-range water vapor transport.

While most studies of atmospheric water vapor transport mentioned above adopted an Eulerian approach, the Lagrangian approach, which follows the moisture transport through particular synoptic events, has seen a revival recently. Anderson and Oliver (1970) described "cloud surges" or "tropical intrusions" as seen in pictures from geostationary satellites. These surges were later termed "moisture bursts" since the associated high or middle cloud bands transport moisture polewards and eastwards from the tropics

(McGuirk et al. 1987; Kuhnel 1989). Harrold (1973) described a well-defined flow which he labelled the 'conveyor-belt' typically a few hundred kilometers wide and a few kilometers deep, which flows parallel to and immediately ahead of the surface cold front. This relatively narrow airflow is the most significant single feature in the production of precipitation and conveys large quantities of heat, moisture, and westerly momentum poleward and upward as well. Browning (1990) and Bluestein (1993) gave a more detailed review of this phenomenon, particularly the warm conveyor belt (WCB). Newell et al. (1996, 1999) showed evidence for the layering structure of atmospheric water vapor from several field missions conducted over the Pacific and Atlantic oceans. Thin layers of atmospheric water vapor were also found by Iselin and Gutowski (1997) in over half of the soundings they examined from the Storm-scale Operational and Research Meteorology-Fronts Experiment System Test (STORM-FEST). The examination was extended recently by Gutowski et al. (2001) to include a follow-on project STORM-WAVE (Weather Assimilation and Verification Experiment). They discovered that although the contribution of these thin moisture layers to water transport climatology is small, episodes occur fairly frequently where these layers contribute 20% or more of the horizontal transport.

Several new theories and algorithms have been developed recently in revealing the features of atmospheric water vapor transport and its relation to the general circulation. Of the most interesting one is a series of studies carried out by an MIT group (Newell et al. 1992; Newell and Zhu 1994; Zhu and Newell 1994, 1998). Computations of daily global tropospheric water vapor fluxes show the presence of filamentary structures which were called "Tropospheric Rivers" (TR in abbreviation for Tropospheric River throughout the thesis), so termed because some of these filaments may carry as much water as the Amazon River (Newell et al. 1992). A more detailed review on the current status of TR research will be given in the second section of the following chapter. Here we mention two

recent independent studies related to the TRs. Smirnov and Moore (1999) gave an example of TR observational validation. They presented a structure consisting of a chain of moisture pulses coming into the Mackenzie Basin from the Pacific Ocean carried either by low pressure centers or by the external parts of cyclonic eddies passing outside the basin. The changes of the TR axis with season and the relation between the TR and storm tracks in that area were also discussed briefly. Another interesting study was conducted by Joseph and Moustaoui (2000) who investigated the Lagrangian transport of particles and its role in the redistribution of moisture and rainfall in a monsoonlike flow using a simple, dynamically consistent model of the heat-induced tropical circulation. The results indicated that the transport, for finite times, is filamentary in structure and these moist filaments become thinner and the rainfall becomes more chaotic and scattered in the upper troposphere than in the lower troposphere in the vicinity of the dominant cyclone in the Northern Hemisphere.

1.3 Thesis Motivation and Outline

Regardless of the numerous efforts made in the past decades to explore the atmospheric branch of the global hydrological cycle, the mean behavior and variability of the atmospheric water vapor transport are still not fully analyzed and understood. As mentioned in the previous section, the Lagrangian approach to moisture transport study has clear physical relevance, yet the method has only sporadically been explored. No systematic climatology has been established based on this approach because such efforts were largely impeded by the nature of atmospheric water vapor transport (namely, the great mobility

and brief atmospheric residence time), the availability of data and its quality, and especially, a void of suitable objective techniques based on a Lagrangian approach. In attempting to advance our knowledge on the TR concept invented by the MIT group (Newell et al. 1992; Newell and Zhu 1994; and Zhu and Newell 1994, 1998) with a global setting in mind, an automatic scheme to detect and track the TRs has been developed in this thesis, and the related climatologies have been compiled making use of the most recent long-term reanalysis products and other available new data sets.

Specific questions we will address in the thesis include: (a) Is an automatic scheme for detecting and tracking the major moisture transport bands using the gridded data applicable? (b) What are the mean behaviors of major atmospheric water vapor transport in terms of TR? (c) How do these transports vary temporally and spatially? and (d) What are the implications on numerical and operational weather forecasts?

The thesis can be outlined as follows: Chapter 2 contains more background material concerning the tropospheric rivers. Various data sets utilized in the thesis and the computational method for vertically integrated moisture flux are also described in that chapter. An automatic scheme for detecting and tracking TRs has been developed and described in Chapter 3. We then pay special attention to the application of the scheme and the choices of the detecting and tracking parameters. In Chapter 4, we present the first climatology for the mean behavior of tropospheric water vapor transport in terms of TRs from the 43-year NCEP/NCAR global reanalyses spanning the period 1958-2000. We seek to establish where and when the rivers occur, the difference between the TR genesis and termination rates, the characteristics of TR translational speeds, the strength of the moisture transport, the TR track duration and length, and many other frequency and regressed quantities. The analysis of the variability and trends exhibited by many aspects of tropospheric rivers is

conducted in Chapter 5, which serves mainly to be complementary to the mean climatology discussed in Chapter 4. The extent to which changes in TR frequency and strength might be related to the variations in broader atmospheric system such as ENSO phenomenon is also examined. Finally in Chapter 6, we summarize our main results and sketch some future research plans.

Chapter 2

Review of Tropospheric Rivers (TRs) and Data Description

2.1 Introduction

One of the most remarkable features of atmospheric water vapor transport in both hemispheres is the presence of intense, mobile filaments discussed in a series papers recently (Newell et al. 1992; Newell and Zhu 1994; Zhu and Newell 1994, 1998). These filaments are linked with daily weather over a significant fraction of the globe and, particularly, on the coastal regions of continents. These filaments are associated with considerable fluxes of moisture along with heat energy that is associated with the phase changes of water vapor, and hence they play an important role in the maintenance of the global energy and hydrological cycles. The study of these systems is an important component of understanding the workings of weather and climate.

In this chapter, a review of the tropospheric river studies conducted so far is presented in section 2.2. Following a brief description of the data sets utilized throughout the thesis

in section 2.3, section 2.4 introduces the method used to calculate the related water vapor transport fields.

2.2 Gross Observational Features of Tropospheric Rivers (TRs)

In seeking an explanation of the puzzling findings during the NASA Measurement of Air Pollution by Satellites (MAPS) program (Reichle et al., 1990) on high values of carbon monxide that was well removed from potential sources and in regions where neither vertical transport in the free troposphere from the boundary layer nor horizontal transport by the prevailing wind provided a straightforward interpretation, Newell et al. (1992) examined daily values of water vapor flux in the troposphere to see if there was any relationship with the carbon monoxide transport problem. A significant meteorological phenomenon emerged when observing the daily global tropospheric water vapor fluxes. Figure 2.1 shows two examples of calculated water vapor flux for October 12 and 13, 1991 (adapted from Figure 1 in Newell et al. 1992, re-calculated using NCEP/NCAR data). It is evident that the water vapor flux is concentrated into filaments in which the along-stream dimension is often many times the across-stream dimension. The filaments were termed "Tropospheric Rivers" (TRs) by the authors because of their appearance and the water flux they carry (some could contain as much water flux as the Amazon River which is near 1.65×10^8 kg sec^{-1}). These TRs are present at all times and move and develop in a coherent manner. They found that there are typically four or five rivers leading from the tropics into middle latitudes of both hemispheres on the daily water vapor flux maps and the same filamentary structure was also visible on the Total Ozone Mapping Spectrometer (TOMS)

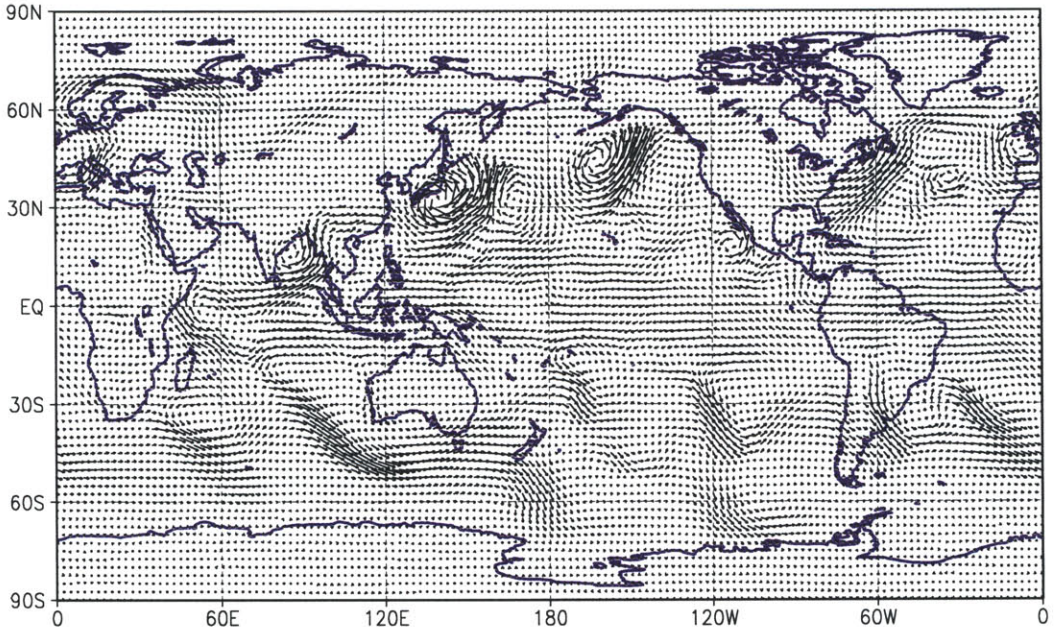

(a) October 12, 1991 $\overrightarrow{1000}$

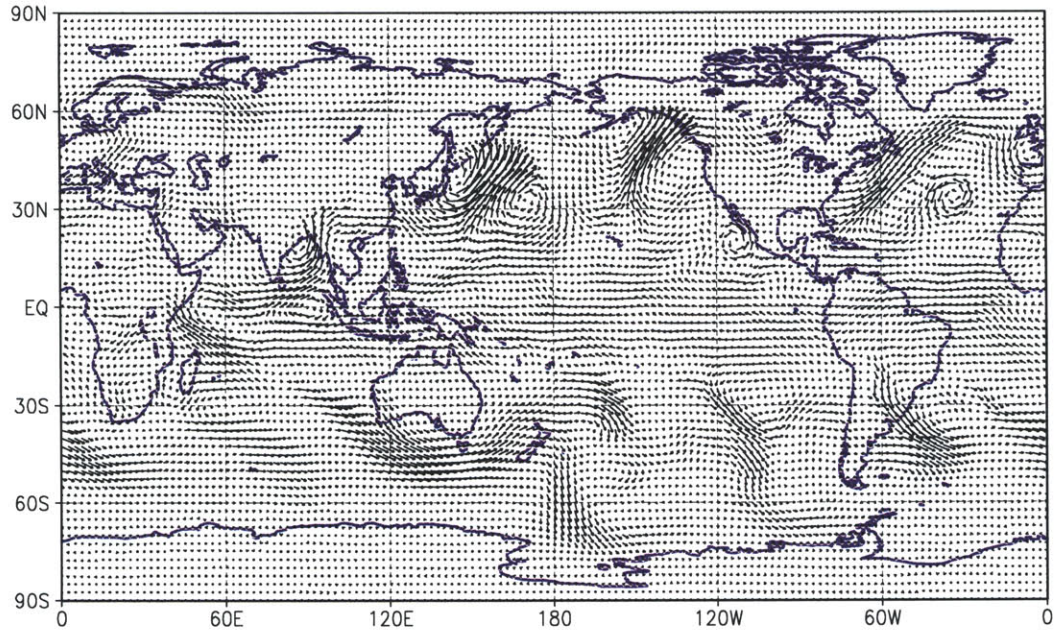

(b) October 13, 1991 $\overrightarrow{1000}$

Figure 2.1: Vertically integrated water vapor flux vectors for (a) October 12, 1991 and (b) October 13, 1991. Unit: kg $m^{-1}sec^{-1}$ (adapted from Figure 1 in Newell et al. 1992, re-calculated using NCEP/NCAR data).

channel centered at 360 and 380 nanometers where ozone absorption is very small, reflecting that the solar radiation originates from the cloud that often accompanies the rivers. They estimated subjectively from the analysis charts that these rivers may persist for about 10 days or more while being translated generally eastwards at speeds of about 6 m sec^{-1}, which corresponds to the mean zonal wind at 850 hPa.

The morphology of TRs has been examined based on twice daily gridded data from ECMWF (Newell and Zhu, 1994). A harmonic analysis of the vertically integrated water vapor flux fields calculated from 1-yr data was performed to localize the areas with highly variable moisture transport. Three frequency domains were examined with corresponding periods shorter than 3 days, 3-6 days and longer than 6 days. The high frequency maps (periods less than 3 days) turned out to show the highest amplitudes among the three domains, indicating that river residence time in a region was shorter than that of the cyclonic systems into which some of them were drawn. However, low-frequency harmonics (with periods longer than 4 days) are harder to detect as a result of changes in the position of the river axis. Examples of the resulting high frequency filtered flux vector maps for January and July are given in Figure 2.2 (Figure 1 in Newell and Zhu, 1994). In January, large oscillation amplitudes corresponding to intense rivers are found in the North Atlantic, North Pacific, South Atlantic, South Indian Ocean and South Pacific; except that in the southwest Pacific, large maxima are in the middle latitudes. In July, similar large amplitude features can be found except that South-East Asia is now also an important area which is related to the presence of typhoons and other monsoon storms. The paper also presented an interesting application of the river concept to the ice core data over Greenland. It was suggested that rivers which terminate in regions where precipitation

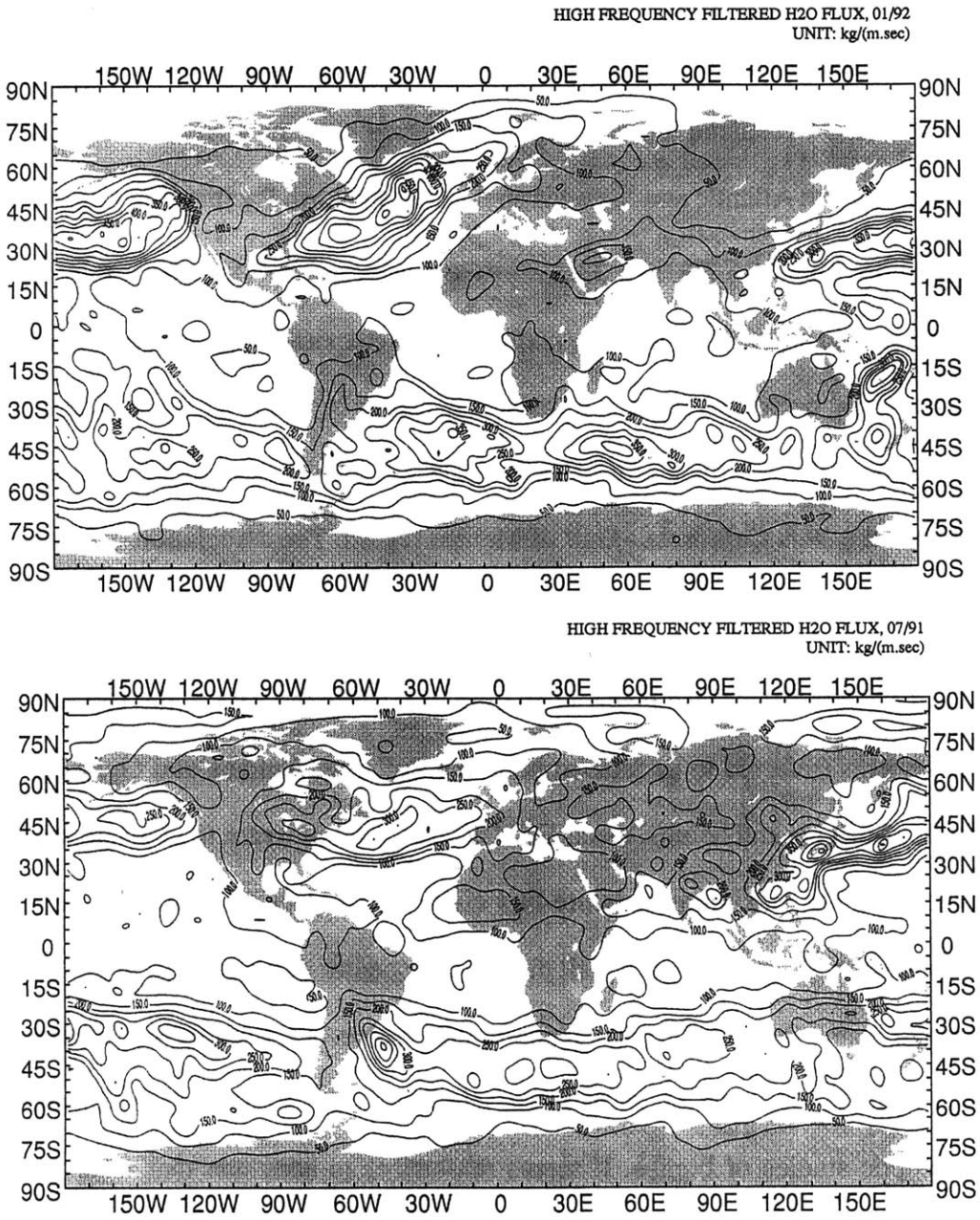

Figure 2.2: Amplitude of high frequency filtered water vapor flux components from harmonic analysis. Unit: kg m^{-1} sec^{-1}. Upper: January 1992. Lower: July 1991. (Figure 1 in Newell and Zhu, 1994).

accumulates to form ice cores may originate from different sources at different times. If the $\delta^{18}O$ in the source region of the rivers is markedly different, then there may be changes in $\delta^{18}O$ in the ice cores which do not reflect local climate changes but rather changes in the trajectories of the rivers. This was illustrated with an example of water vapor flux convergence over the Greenland ice-core region from two separate rivers, one originating in the southwest North Atlantic and the other in the central North Pacific. The salinities in the two regions are about 36.7‰ and 33.3‰ respectively and $\delta^{18}O$ at the water surface is strongly related to salinity as both are controlled by evaporative processes. The implication that on some occasions there is a transfer of vapor between the ocean basins can be traced in Figure 2.2 when the North Atlantic and North Pacific large amplitude regions are joined across the Baja California - Gulf of Mexico region. The association between rivers, frontal boundaries and storm tracks is also discussed.

Zhu and Newell (1994) also made an attempt in relating the TRs to the fast developing cyclonic systems (referred to as "atmospheric bombs" after Sanders and Gyakum, 1980). Case studies of rivers and bombs, using ECMWF sea level pressure to characterize the latter, showed that the maximum moisture-flux convergence occurring near the head of the filament was often the position at which the cyclonic center was found 12 hours later. Furthermore the water vapor flux convergence in that region, when converted to latent heat, gave equivalent heating rates of 25-30 K/day which are close to those found in some individual synoptic studies of bombs. It seems reasonable to conclude that when a river is entrained into a cyclone in favorable circumstances, it can contribute to development by latent heat liberation, enhanced vertical motion, and vortex stretching. The idea of rivers and their association with cyclones is not new. For example, in a period when routine analyses of moisture on isentropic charts were made, Starr (1942) pointed out that "moisture

emanating from the Gulf of Mexico may flow northward usually in the form of a rather narrow tongue situated above a surface cold front so that the forward position of the moist outbreak is found in the vicinity of a cyclonic disturbance at the ground." The idea of using the TR concept to forecast "atmospheric bombs" is a brilliant one, but this possible practical application relies first on the identification of the rivers (specifically the leading edges of TRs), which may suffer from a clear objective definition and require tedious subjective analysis for an individual forecaster. These are probably the reasons why there has been no such attempt in this regard since the idea was proposed. Another question raised in the same paper was how to quantitatively estimate the origins of the river flows. One way of considering this was to combine the low level divergent wind field with the evaporation rates from the surface.

A new algorithm that divides the water vapor fluxes into filamentary structures known as TRs and broad flux fields was proposed by Zhu and Newell (1998). The results show that the TRs may carry essentially the total meridional transport observed in the extratropical atmosphere, but may occupy only about 10% of the total longitudinal length at a given latitude. It was shown that the transient fluxes in traditional Starr-type studies do not catch the filamentary structures completely and may therefore underestimate the fraction of transport assigned to moving systems, as well as lacking the geographical concentration. The mean flow and eddy fluxes evaluated by the new algorithm are considered to be more physically realistic.

Of all the TR studies mentioned above, one of the remaining tasks, and perhaps the most difficult one impeding the practical use of the concept, is how to identify and track the filamentary structures on a day-to-day (or even hour-to-hour) basis while forecasting.

2.3 The NCEP/NCAR Reanalysis Data

The National Centers for Environmental Prediction (NCEP) and National Center for Atmospheric Research (NCAR) have cooperated in a reanalysis project to produce a retro-active record of more than 50 years of global analyses of atmospheric fields in support of the needs of the research and climate monitoring communities (Kalnay et al. 1996; Kistler et al. 2001). This effort involved the recovery of land surface, ship, rawinsonde, pibal, air-craft, satellite, and other data. These data were then quality controlled and assimilated with a data assimilation system kept unchanged over the reanalysis period (The model used for the NCEP reanalysis is a medium-range forecast T62 model, which is identical to the one used for operational analyses of early 1994 except for the horizontal resolution. There are 28 sigma levels in the vertical with seven levels below 850 hPa. The analysis scheme is a three-dimensional variational scheme cast in spectral space denoted spectral statistical interpolation). This treatment eliminated perceived climatic jumps associated with changes in the operational data assimilation system, although the reanalysis is still affected by changes in the observing systems. There may be three distinct periods during which the observing system underwent certain significant changes, namely, the "early" period from the 1940s to the International Geophysical Year in 1957 (when the first upper-air observations were established); the "modern rawinsonde network" from 1958 to 1978; and the "modern satellite" era from 1979 to the present (Kistler et al., 2001). During the earliest decade (1948-57), there were fewer upper-air data observations and they were made 3 hours later than the current main synoptic times (e.g., 0300 UTC), and primarily in the Northern Hemisphere, so that the reanalysis is less reliable than for the later years. For this reason, we exclude the pre-1957 era and use only the 6-hourly reanalyses spanning from 1958 to 2000. The introduction of satellite data in 1979 resulted in a significant

change in the climatology, especially above 200 hPa and south of 50°S, suggesting that the climatology based on the years 1979 - present day is most reliable.

It is difficult to observe atmospheric water vapor well for climate studies, which may temper expectations for the insight the reanalysis can provide into the hydrologic cycle. Part of this difficulty is due to measurement limitations inherent in even the most accurate, routinely used instruments, rawinsondes (Pratt 1985; Elliott and Gaffen 1991; Wade 1994; Elliott 1995). Standard humidity sensors carried by radiosondes are prone to error, plus changes in these sensors can introduce biased discontinuities into the record. Satellites may provide data covering the whole globe, but the data suffer from poor vertical resolution in the lower troposphere, where virtually all vapor transport takes place (Randel et al. 1996). Also, atmospheric water vapor exhibits substantial variability on relatively small horizontal and vertical scales (Houze and Hobbs 1982; Iselin and Gutowski 1997), thus impeding the ability of typical observation networks to capture water vapor's three-dimensional distribution. The analysis scheme itself could introduce errors into analyzed water vapor. For example, the underlying forecast model may tend to evolve its hydrologic cycle toward a model, rather than real-world climatology (Donner and Rasch 1989; Slonaker and van Woert 1999). These factors raise doubts about the quality of water vapor transport computed from reanalyses. Indeed, Trenberth and Guillemot (1995, 1998) have suggested that even a state-of-the-art reanalysis may be deficient in this regard. For example, over a data-rich region like the central United States, estimates of the mean moisture-flux convergence from this product differ significantly from that needed to balance independent, more reliable streamflow data (Gutowski et al. 1997). Large-scale meridional transports of water vapor calculated by Mo and Higgins (1996) for an overlapping period between the NCEP/NCAR and the NASA/DAO reanalyses showed significant differences particularly in the tropics in association with differences in the strength and location of winds in the lower

levels of the mean Hadley cell. Nevertheless, Gutowski et al. (1997) demonstrated that the temporal variability of the mean moisture-flux convergence is more realistic, and Mo and Higgins concluded that the NCEP/NCAR moisture-flux products are "able to depict inter-annual variability related to the ENSO cycle quite well." Though one should always be cognizant of the problems that may be associated with the NCEP/NCAR reanalyses, these analysis products can still be regarded as one of the most complete, physically consistent meteorological data sets. The more than four-decade period covered by these analyses makes them particularly useful for our task.

NCEP optimal interpolation sea surface temperature (OI SST) data are utilized in our study. The OI SST analysis technique described by Reynolds and Smith (1994) was developed for operational purposes at NCEP. It follows the analysis methods of Reynolds (1988) and Reynolds and Marsico (1993), which combine in situ and satellite-derived SST data using Poisson's equation to produce 'blended' products, with an analysis of the sea ice edge as one boundary at -1.8°C. The in situ SST data used consist of quality-controlled ship and buoy observations available over the Global Telecommunication System (GTS). Satellite data are obtained from the Advanced Very High Resolution Radiometer (AVHRR) on National Oceanic and Atmospheric Administration (NOAA) polar orbiting satellites. The SST retrievals are produced operationally by NOAA's Environmental Satellite, Data and Information Service (NESDIS) and are available for the period of January 1982 through August 2000 on a 1° latitude and longitude grid.

2.4 Calculation of the Water Vapor Transport Fields

The atmospheric specific humidity and the zonal and meridional components of the wind are variable in both space and time, *i.e.*, the four-dimensional domain of these variables is defined by latitude, longitude, pressure, and time in a geophysical coordinate system. Following Peixoto (1973) and Peixoto and Oort (1983), the dimensionality of the domain is reduced to two by defining a vertically integrated, time-averaged vapor flux vector.

At a given point in space and time, a vector field of the advective transport of water vapor by the horizontal wind is defined as follows:

$$q\mathbf{V} = (qu)\mathbf{i} + (qv)\mathbf{j} \tag{2.1}$$

in which q is the specific humidity, $\mathbf{V}$ is the horizontal wind vector, u and v are the zonal and meridional wind components respectively, and $\mathbf{i}$ and $\mathbf{j}$ are the unit vectors in the zonal and meridional directions, respectively. As a product of terms, $q\mathbf{V}$ increases with either velocity or specific humidity; for example, slow-moving moist air may transport water vapor at the same rate as less moist but fast-moving air.

For a vertical atmospheric column with a unit base, the vertically integrated water vapor transport fields are obtained by taking the mass-weighted vertical integral of Eq. (2.1), namely,

- the vertically integrated zonal water vapor flux per unit latitude

$$Q_\lambda = g^{-1}\int_{300hPa}^{p_{sfc}} qudp \tag{2.2}$$

- the vertically integrated meridional water vapor flux per unit longitude

$$Q_{\varphi} = g^{-1}\int_{300hPa}^{p_{sfc}} qvdp \tag{2.3}$$

where g is the gravitational acceleration and p_{sfc} is the surface pressure. The 6-hourly wind and humidity at eight standard pressure levels (1000, 925, 850, 700, 600, 500, 400, and 300 hPa) with the horizontal resolution of 2.5° × 2.5° longitude/latitude, along with the surface pressure p_{sfc} with the same temporal and horizontal resolution, were used to form Q_{λ} and Q_{φ}. As vertically integrated quantities, Q_{λ} and Q_{φ} express the magnitude and direction of the net transport of water vapor through the depth of the integration above a point of the Earth's surface; a small value of either component does not necessarily imply negligible transport at all levels in the atmosphere. Equations (2.2) and (2.3) may be averaged over a time period to compute the corresponding mean values Q_{λ} and Q_{φ}. It is also of interest to calculate the water vapor transports for the upper troposphere. This can be examined by using equations similar to (2.2) and (2.3) with the integration limits from 700 hPa to 300 hPa.

Chapter 3

A Numerical Scheme for Identifying and Tracking Tropospheric Rivers from Gridded Data

3.1 Introduction

So far many meteorologists have plotted the tracks of migratory cyclones or anticyclones in order to understand the behavior of these systems (Petterssen, 1956; Zishka and Smith, 1980; Sinclair, 1997; Trigo et al., 1999; Simmonds and Murray, 2000a, b). Some were trying to follow the troughs, ridges, and fronts associated with them (Bell and Bosart, 1989; Lefevre and Nielsen-Gammon, 1995). Since water vapor is one of the most important elements that can directly affect the development, movement, and distribution of these synoptic phenomena, it is natural to think of a method that can be applied to identify and track the water vapor and its transport, especially those major transport belts — the Tropospheric Rivers (TRs), as described by Newell et al. (1992). It would be more meaningful to compile a TR climatology with the object of describing and explaining TRs' impacts on synoptic systems, global hydrologic cycle, and climate. So far no such attempts has been

made and there is no TR climatology and associated statistics. We believe that this compilation of TR climatology could be an important contribution to climate study as well as to in situ weather forecasting.

The exercise of recording moisture-flux maxima, identifying the TRs, and following them from day to day has proven to be a very tedious and time consuming operation. Moreover, where operational charts were used, inconsistencies may have arisen even from the beginning in locating the moisture-flux maxima by different analysts. These inconsistencies would be carried through all of the subsequent TR identifying and the tracking stages (which needs the association of successive daily positions of TRs) later on.

To overcome these drawbacks, an objective and fully automated scheme is desired. The Tropospheric River Identifying and traCKing Scheme (abbreviated as TRICKS) has been developed to perform the work using gridded data that is available either in analyses, reanalyses, or forecasting forms.

In this chapter, we will first give a detailed description of the scheme in section 3.2, then the performance of the finding and tracking program will be evaluated and the choice of some governing parameters will be discussed in section 3.3. It will be followed by a summary of the chapter in section 3.4.

3.2 Scheme Description

Any objective scheme for identifying maxima or minima in a meteorological field needs to have a sound physical basis, be robust in application, and yield realistic results. The TRICKS is based on the Melbourne University numerical cyclone detecting and tracking algorithm (Murray and Simmonds, 1991; Simmonds and Murray, 1999; and Simmonds et al., 1999), which has been acclaimed as one of the most sophisticated and reliable automatic schemes (Simmonds and Keay, 2000a, b). Their scheme has been used to reveal many aspects of synoptic behavior when applied to the observational analyses (e.g. Jones and Simmonds 1993, 1994; Godfred-Dpenning and Simmonds 1996), as well as to the outputs of numerical modeling (e.g. Simmonds and Wu 1993; Murray and Simmonds 1995; Simmonds and Law 1995).

It is important to bear in mind that there are a number of assumptions which have to be made in devising such a scheme and that these may have to be re-thought when the scheme is applied to different atmospheric properties with different temporal and spacial resolutions, global or regional grids, maxima or minima, vector or scalar, at mean sea level or at upper levels, etc. Since the Melbourne University scheme was tailored to work with Southern Hemisphere (SH) mid-latitude cyclones (i.e. the input field is the mean sea level pressure in the SH), modifications must be made in order to accommodate the changes that are peculiar to our problem and data set. In TRICKS, we expanded its capability to identify and track the Tropospheric River. In fact, our scheme can be adapted to detect and track any atmospheric properties that have maxima/minima aligned to a line (for instance, a trough/ridge at 500 hPa) at any given vertical level (or integrated column quantities) on either global or regional grids.

The rationale to consider a TR as a quasi one-dimensional feature is due to the observational facts that TR is filamentary in nature (i.e., its along-stream dimension is often many times the across-stream dimension), and the moisture fluxes associated with a TR are mostly aligned to the along-stream dimension. In addition, the resolution of the data used to compute the moisture flux may not be sufficient enough to resolve the width of a river.

The flowchart of the TRICKS is sketched in Figure 3.1.

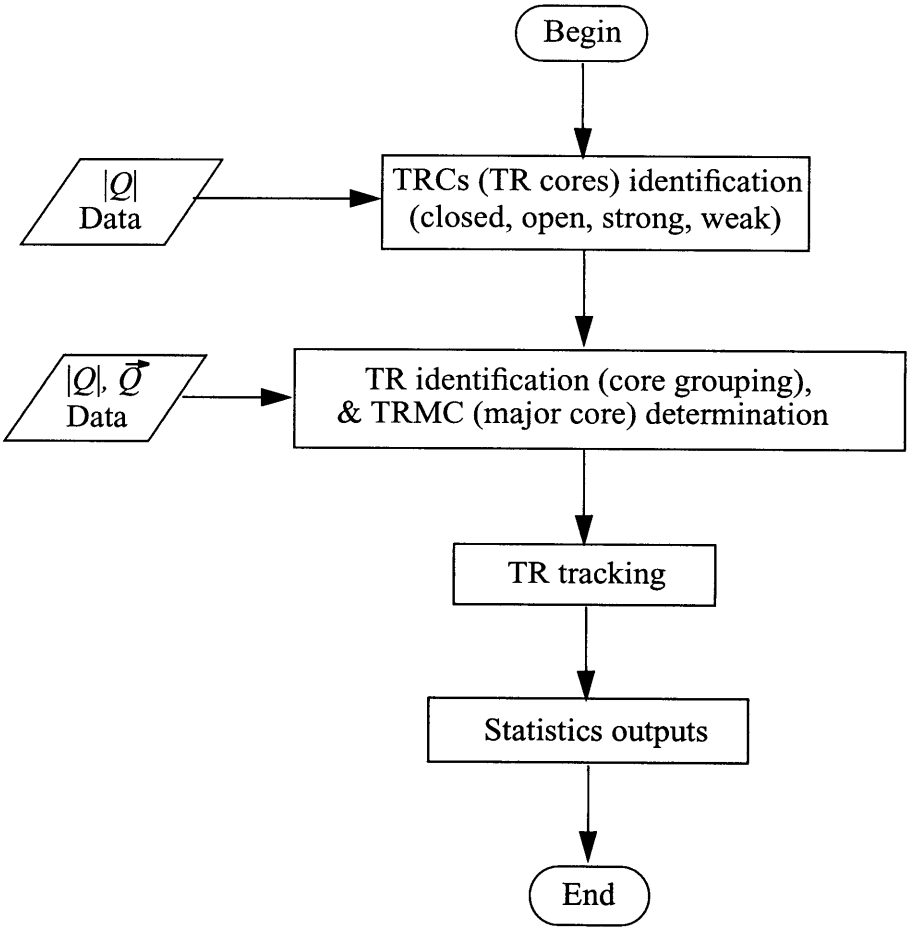

Figure 3.1: Flowchart of the Tropospheric River Identifying and traCKing Scheme (TRICKS).

There are four major stages involved in the scheme. Firstly, a procedure is developed which enables the maxima of the moisture-flux magnitude field (so-called TR cores) to be detected and accurately located. Each core will be assigned a status according to its shape and strength. Secondly, the relationships among the adjacent cores are accessed to construct the axes of rivers (this is essentially a pattern-recognition process). In the third stage, a TR tracking procedure is designed to follow a river from its birth to termination. Finally, a statistical routine is also included which allows various statistics of TR behavior to be compiled from the recorded TR property information. The following subsections will give a more detailed description of the flowchart.

3.2.1 Tropospheric River Cores (TRCs) Identification

a. Fitting the Water Vapor Transport Field

TRCs are objectively identified as maxima in the scalar water vapor transport field, namely, the q field (where $q = |Q| = \sqrt{Q_\lambda^2 + Q_\varphi^2}$, see the definitions in Chapter 2 section 2.4).

In order to locate the maxima of q more accurately, it was considered desirable to have q specified on a conformal or near-conformal projection. For computational convenience and because it has a map factor which can be taken to be locally constant, the polar stereographic (PS) grid is used in both finding and tracking programs. The latitude-longitude q field was transformed by bicubic spline interpolation to a PS array centered on either the North or South pole. To avoid loss of information upon regridding, the resolution of the PS

array should be at least as fine as that of the latitude-longitude data over most of the grids. For the q field calculated with $2.5^\circ \times 2.5^\circ$ latitude-longitude resolution, an 81×81 PS grid was found suitable. At the resolution of the grid, which is characteristically of the order of 300 km, the grid spacing is comparable with the radius of many of the smaller high q regions identified on operational charts.

After the grid transformation, a two-dimensional polynomial representation was used to model the q surface between grid-points analytically; this was found to be most efficiently achieved by fitting a bicubic spline function to the entire array. The q values between the grid points $q(x_i+\delta x, y_j+\delta y)$ were interpolated by applying a Taylor's expansion to q and its 15 derivatives using the following equation:

$$q(x_i + \delta x, y_j + \delta y) = \frac{1}{m!n!} \sum_{m=0}^{3} \sum_{n=0}^{3} q_{x^m y^n}(x_i, y_j) \delta x^m \delta y^n \tag{3.1}$$

where

$$q_{x^m y^n} = \frac{\partial q^{m+n}}{\partial x^m \partial y^n} \tag{3.2}$$

b. Detecting the Positions of TRCs

A common method employed for finding maxima or minima from gridded data involves a comparison of values at neighboring points. For instance, a high (low) center is deemed to exist at a grid-point at which the value is greater (less) than that at any of a small number of grid-points (4 or 8) surrounding it. This method has been employed in studies by Lambert (1988), Bell and Bosart (1989), Trigo et al. (1999), etc. It is also a widely used technique in graphics utilities for plotting highs and lows on contour maps. The maximization

(minimization) may be taken over a larger number of grid-points to prevent clutter in this type of application.

There are three major deficiencies related to the above technique. One is that a simple comparison of grid-point values takes no account of the likely variation between grid-points. The second one is the possibility of failing to identify some of the systems when the grid spacing is of the same order as their expected dimensions. The third one is that when the grid distance is not small compared to the expected system displacement between analysis times, the approximation of system positions by grid-points tends to result in a jerky checkerboard type of motion that complicates the tracking procedure and almost rules out useful calculations of system translational speed. The problems referred to may be alleviated by approximating the field surface through smoothly varying functions. An obvious way of using them would be to interpolate the data onto a finer grid and then carry out the comparison of values on the new grids. This has been done by Grotjahn (1990) and others to construct small grids for matching features in analyses and forecast fields.

While still only an approximation to the unknown form of the surface between grid-points, it is nevertheless believed that a higher order fit, such as the one described in the previous subsection, is a better approximation than the essentially linear representation. It has frequently been found possible for the bicubic fit to compose a small high or low in the absence of a nearby maximum or minimum grid-point value (i.e., Sinclair 1997). The method employed here allows systems to occupy a continuous range of positions between grid-points. For this purpose a two-step refining process was introduced in the detecting procedure.

The q array is firstly scanned for the sites of 'possible' maxima by comparing the values at neighboring grid-points. To allow for the possibility that a shallow raised region may not be detected by a local maximization of grid-point values, a less restrictive scanning procedure has been implemented. This procedure seeks grid-points at which the Laplacian of the q,

$$\nabla^2 q(x_i, y_j) = q_{xx} + q_{yy} \tag{3.3}$$

shall be smaller than at any of the eight surrounding points and smaller than a prescribed negative value. The scanning technique resembles the method used by Le Treut and Kanay (1990).

Once these 'possible' q maxima at grid-points are found, the finding program searches for a local maximum q_{max} (usually not at a grid-point) from each of these points. This is approached in an iterative way illustrated in Figure 3.2 and sketched by the following:

(i) An ellipsoid is defined by using the (interpolated) first and second space derivatives of the q at the point, whose orientation θ of the axes is given by

$$\tan 2\theta = 2\frac{q_{xy}}{q_{xx} - q_{yy}} \tag{3.4}$$

and the second derivatives in the axial directions by

$$q_{uu} = \frac{q_{xx} + q_{yy}}{2} - \sqrt{\left(\frac{q_{xx} - q_{yy}}{2}\right)^2 + q_{xy}^2} \tag{3.5}$$

$$q_{vv} = \frac{q_{xx} + q_{yy}}{2} + \sqrt{\left(\frac{q_{xx} - q_{yy}}{2}\right)^2 + q_{xy}^2} \tag{3.6}$$

where u and v are coordinates taken from the center of the putative ellipsoid along the major and minor axes, respectively.

(ii) The center of the ellipsoid becomes the next point in the iteration and a new ellipsoid is defined. The iterative technique is a two-dimensional extension of the Newton-Taphson algorithm, which can be applied independently to the u and v coordinates,

$$u^{(n+1)} = u^{(n)} - \frac{q_u(u^{(n)})}{q_{uu}(u^{(n)})} \tag{3.7}$$

$$v^{(n+1)} = v^{(n)} - \frac{q_v(v^{(n)})}{q_{vv}(v^{(n)})} \tag{3.8}$$

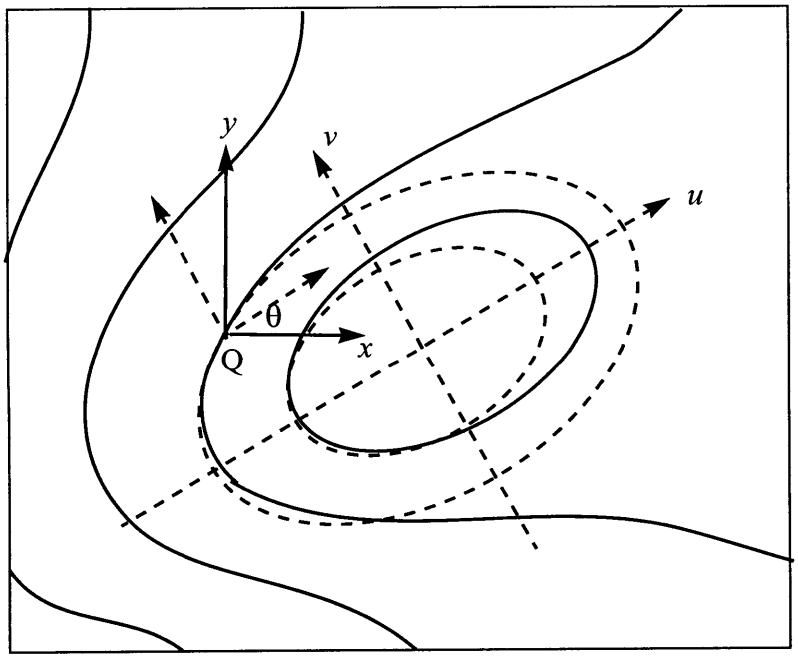

Figure 3.2: An example of a q pattern (solid lines) and the contours and axes (u and v) of the ellipsoid of best fit (broken lines) defined by the derivatives at the point Q.

Provided that a true maximum (i.e., a point at which the second derivative $q_{uu} < 0$ and $q_u = q_v = 0$) can be found within a specified radius of search, convergence to within 0.001 grid units of the maximum normally occurs within three or four iterations. The numbers and positions of centers identified by the finding program have been in good agreement with those inferred from the contoured numerical analyses and will be evaluated in section 3.3.

c. Status of a TRC

According to its shape and strength, a TRC can be assigned to a status of either in the category of *closed* and *open*, or in the category of *strong* and *weak*, or a combination of the two (i.e., *strong closed*, *strong open*, *weak closed*, and *weak open*).

It is convenient to refer to TRCs as *closed* or *open* according to whether they possess regions of closed contours or not. An open TRC could be as much important as the closed one when identifying a TR. This is owing to the fact that TR is filamentary in nature and TRCs found within a river may have less degree of symmetry.

The center of a closed TRC can be unequivocally identified with its point of maximum value q_{max} using the method detailed in the previous subsection and is normally found within one grid space of the $\nabla^2 q$ minimum, depending on the degree of symmetry of the TRC. However, there is no such point exists in the case of an open TRC. A suitable way to identify it would be to detect the inflexion point in the q surface near a $\nabla^2 q$ minimum. This point of inflexion, i.e., the point of minimum q gradient which is nearly always associated with a raised field, could be taken to indicate the most likely location of a closed system *below* the limit of resolution imposed by the grid.

The procedure to find an open TRC can be illustrated by a hypothetical cross-section of q shown in Figure 3.3.

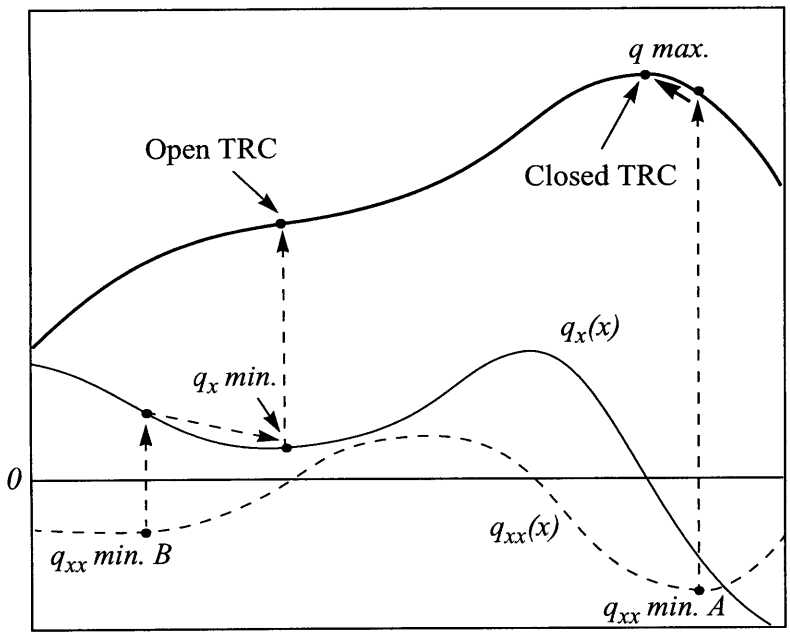

Figure 3.3: A hypothetical cross-section of q and its derivatives showing how two minima of q_{xx} (or $\nabla^2 q$ in two dimensions) A and B may be used as starting points in the search for both closed and open TRCs.

Firstly, the TRC detecting procedure scans through the array for grid-points at which $\nabla^2 q$ is minimized and each such position is taken as the starting point (e.g., the point A in the figure) in the search for a q maximum. As mentioned before, if a closed TR exists, it will normally lie fairly close to its associated $\nabla^2 q$ minimum, but will not be coincident with it unless the TRC is exactly symmetrical. To show the principle of this, $\nabla^2 q$ is represented as a continuous function in the figure; in practice it is sufficient to minimize it from grid-point values. Secondly, if a closed TRC cannot be found within a suitable radius of $\nabla^2 q$ minimum (e.g., the point B in the figure), then the program will seek an open TRC by

attempting to minimize the magnitude of the q gradient starting from the same grid-point. The position of minimum q gradient will be taken as the center of an open TRC.

Since the Laplacian $\nabla^2 q$ is not constant but normally increases rapidly away from the TRC center, an average value of the $\nabla^2 q$ over a specified radius from the center can be taken as a measure of the strength of the system. It also has the effect of smoothing the normally somewhat noisy $\nabla^2 q$ field. This averaging procedure is done over every few degrees of azimuth around a complete circle with a certain radial grid increment within a specified radius around the TRC center. A radial grid spacing of 0.5° latitude, an azimuthal increment of 20°, and an average radius of 2° latitude around the center were found to give good discrimination on TRC strength. The average is used not only to exclude insignificant systems but to discriminate between two status of TRCs, i.e., the *strong* and *weak* TRCs. These classes are used in TR identification when connecting a group of TRCs according to certain rules (see next section 3.2.2). The *strong* class is also used in the tracking, which at successive times preferentially matches the status of TRCs. The employment of these 'strength criteria' succeeded in disqualifying most of the closed TRCs in regions of slack q gradients while retaining open TRCs marked by a significant distortion of otherwise closely spaced contours.

It was found that not all the features identified have significance for large-scale moisture transports. To try to eliminate these features, a multipass smoother has been applied to the analyses prior to the TRC detecting procedure. This consisted of performing corrections of $\Delta q = (r^2/4n)\nabla^2 q$ to the q field, where r is the diffusive radius (2° latitude), and the number of passes (n) is set to 4. The effect of this is similar to the Cressman smoother applied by Sinclair (1997).

3.2.2 TR and Tropospheric River Major Core (TRMC) Determination

In the next stage of the scheme, the relations among the nearby TRCs will be assessed to determine whether they belong to the same TR. Among TRCs within a particular TR, one will be designated as the Tropospheric River Major Core (TRMC) having general properties of its associated TR.

The procedure and rules for TR identification and TRMC determination at a specific analysis time are as follows:

(1) The two components of moisture fluxes Q_λ and Q_ϕ at the corresponding analysis time are interpolated bicubically from grid points onto each TRC center. Thus the moisture flux of each TRC is known.

(2) TRCs within certain range and transport directions are grouped according to a distance screening and then a directional screening. This is achieved by assigning two TRCs to different groups when the distance between them is greater than 3000 km, or the difference of moisture-flux directions is larger than 90 degrees. These criteria for TRC grouping are established based on observations of daily moisture-flux maps and are usually less restrictive. Although a lack of coherence or continuity in terms of TRCs' positions and moisture transport directions can still be found within a resulting group, this procedure serves largely to identify the gross TR-related features (i.e., the TRC groups) and to reduce the number of TRCs within each group that will be further evaluated during the later processing.

(3) The status of TRCs (i.e., *strong closed*, *strong open*, *weak closed*, and *weak open*) within a group are examined and the weak groups are filtered with the notion that a

river must contain at least one strong TRC (either closed or open).

(4) A group which contains only one TRC is filtered since a river must contain at least two TRCs so that a geometric length can be obtained. Each TRC can only be counted once, or not at all (the possibility of TR merging and splitting that requires multiple counts of a TRC will not be considered in this thesis owing to its complexity).

(5) Up to this stage, only groups that contain multiple TRCs with at least one strong TRC are retained. Within such a group, a more discerning consistency check for the adjacent TRCs is stipulated. A position sorting is applied firstly to align the TRCs to a possible TR axis. This is attained by sorting the longitudes of TRCs. Then every three adjacent TRCs were subjected to a directional scan to prune out TRCs with anomalous transport directions (where the angle between its moisture-flux vector and the possible TR axis is greater than 45 degrees), and the remaining TRCs are connected to form the TR axis. An illustration of such screening is given in Figure 3.4. After the position sorting, the default possible TR axis would be simply connecting the TRCs 1 to 2 and 2 to 3. The directional consistency checking will screen through each θ_{abc} (defined in Figure 3.4) to rule out the TR axis when $\theta_{abc} > \theta_c = 45°$. For example, if ($\theta_{112} > \theta_c$ or $\theta_{212} > \theta_c$), then points 1 and 2 will not be joined; further if, ($\theta_{223} > \theta_c$ or $\theta_{323} > \theta_c$) but ($\theta_{113} \leq \theta_c$ and $\theta_{313} \leq \theta_c$), then TRCs 1 and 3 will form the TR axis and TRC 2 will be discarded. In case two axes from the same TRC both satisfy the directional criterion (i.e., a TRC has been counted twice, which is a violation of rule 4 set previously), the one which has the average transport direction closer to the TR orientation will be retained (for example, if ($\theta_{113} \leq \theta_c$ and $\theta_{313} \leq \theta_c$) and ($\theta_{223} \leq \theta_c$ and $\theta_{323} \leq \theta_c$), but ($\theta_{223} + \theta_{323}$) < ($\theta_{113} + \theta_{313}$), then TRC 1 will be screened out and points 2 and 3 will

be connected). The same rules are applicable when the group contains only two TRCs.

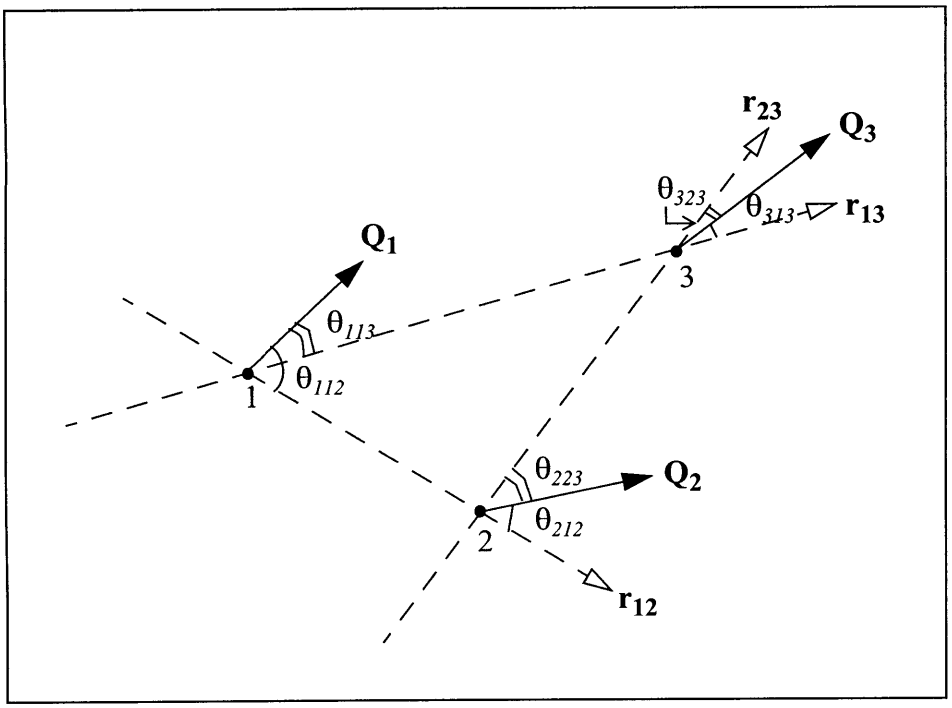

Figure 3.4: Directional consistency checking for three hypothetical TRCs (labeled 1, 2, and 3) that may form the TR axis. $\mathbf{Q_1}$, $\mathbf{Q_2}$, and $\mathbf{Q_3}$ are moisture vectors interpolated onto the positions of each TRC; $\mathbf{r_{12}}$, $\mathbf{r_{23}}$, and $\mathbf{r_{13}}$ are the possible TR axis vectors (formed by connecting each pair of TRCs); θ_{abc} denotes the acute angle between the **Q** and **r** vectors, where subscript *a* indicates the location of the **Q** vector (i.e., TRC label), and subscripts *bc* indicates the **r** vector onto which the **Q** is projected.

(6) Several scans from step (3) through (5) may be necessary if there are inconsistencies raised from applying different rules. Each resulting group will then be defined as a TR.

(7) The Tropospheric River Major Core (TRMC) is obtained by choosing the strongest TRC (i.e., the minimum averaged $\nabla^2 q$) within each TR.

Once a TR is defined, various TR properties such as the TR counts, each TR's length, the averaged moisture transports of each TR, the tally of the TRCs within each TR, etc. can then be easily computed.

3.2.3 TR Tracking

The tracking procedure is based on the projection of TRMC positions from one analysis time to the next and the comparisons of the projected positions with those of the TRMC analysis at the new time. A key assumption here is that TR moves following its TRMC. Although this appears to degrade the TR from a quasi one-dimensional structure to a 'point' analogue, it is believed that the strength of a TRMC (i.e., the strongest TRC) could be the least variable quantity within a TR, thus its position is a good representative for TR movement.

The construction of TR trajectories could be achieved by searching for a center within a selected radius of each TRMC position recorded at the previous analysis time. The difficulty with this method is that in a 6-hour period TRMCs often travel distances which are of the same order as their separations, so one is not always sure where each TRMC has traveled during this period. To make the appropriate decisions a three-step procedure was devised in which (1) a subsequent position is predicted for each TRMC, (2) a probability of an association between the projected TRMC and each TRMC present at the new time is calculated, and (3) a matching is made which maximizes the calculated probabilities of association between the projected and new positions, allowing the tracks to be extended by one analysis period.

a. TRMC Displacement Projection

The projected displacement of a TRMC depends on one or two velocity predictors: a velocity based on the persistent movement of a TRMC during the previous analysis interval: $\mathbf{u}_{pm}$, and a velocity based on climatological movement of a TRMC at its latitude (or latitude and longitude): $\mathbf{u}_{cl}$. If more than one be used, the prediction velocity $\mathbf{u}_{est}$ is a weighted combination of the two, *i.e.*,

$$\mathbf{u}_{est} = w_{pm}\mathbf{u}_{pm} + (1 - w_{pm})\mathbf{u}_{cl} \tag{3.9}$$

where w_{pm} is a weighting factor and its value will be discussed later in this subsection. Figure 3.5 shows an illustration of this displacement projection.

The rationale behind equation (3.9) is that the influence of inertia is greatest at short time intervals, but decreases relative to climatology with increasing time. Because the TR climatological velocities $\mathbf{u}_{cl}$ are not known *a priori*, it is necessary to generate them by doing several passes of the tracking and analysis, using progressively refined velocities. An economic way of processing this is to calculate the zonally averaged output velocity statistics first, then the results are fed back into the tracking program and statistics were recalculated. This was repeated a few times until stable values were obtained.

In addition, a value of moisture-flux q at the new TRMC position can also be estimated based on a weighted combination of persistence and its previous tendency,

$$q_{est}(t + \delta t) = q(t) + w_{qm}[q(t) - q(t - \delta t)] \tag{3.10}$$

The weighting factor w_{qm} quantifies the 'memory' of past motion and q tendency incorporated in the prediction. Similar estimates for zonal- and meridional- moisture fluxes are

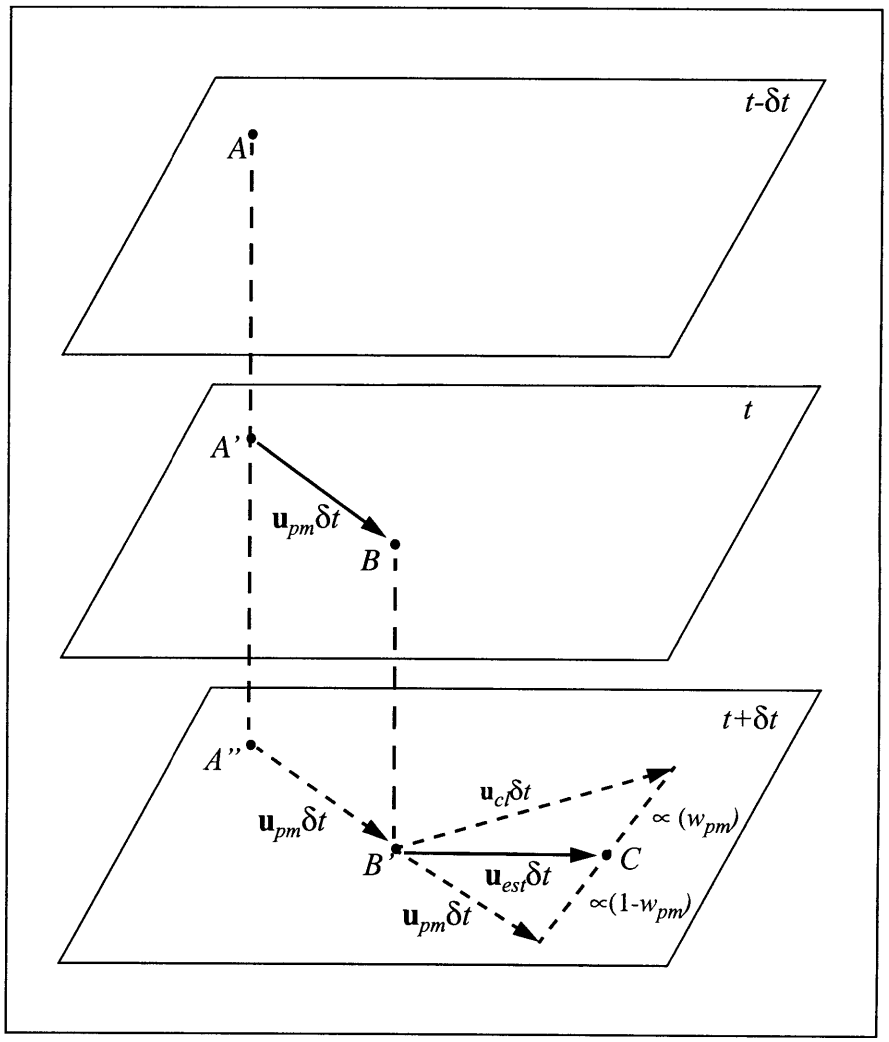

Figure 3.5: A TRMC located at point *A* at time *t*-δ*t* moves to point *B* at time *t*, and is projected to point *C* at time *t*+δ*t*. The new TRMC position *C* is predicted based on weightings w_{pm} of the previous displacement, $\mathbf{u}_{pm}\delta t$, and (1-w_{pm}) of the displacement based on climatological mean TRMC velocities, $\mathbf{u}_{cl}\delta t$.

also made at the projected position. For short time intervals a choice of w_{pm} and w_{qm} close to or equal to unity would be expected, and for long intervals one would select values closer to zero. On the basis of trials of the scheme, described later, weighting factors, w_{pm}

= 0.80 and w_{qm} = 0.80, were found suitable for use with the data; these values imply a relatively high memory of past motion and q tendency.

b. Probability Calculation

The tracking scheme relies on having suitable TRMC positions and accurate predictions of TRMC displacement in order that the positions projected to the new analysis time lie close to actual TRMC positions at that time. Because these expectations are not always attained, it is necessary to establish criteria to decide how the projected and actual TRMCs are to be associated, and which are deemed to have been born or to have died.

Probabilities of associations between predicted positions and actual positions at the new analysis time are calculated between all pairs of TRMCs that fall within a critical or pass radius of each other. Distances can either be calculated on the sphere or on a PS projection. The pass radius is a maximum equal to r_c for strong closed depressions that are at least two intervals in age. Each pair of predicted (m) and new (n) positions separated by a distance $r_{mn}<r_c$ is assigned a probability based upon a decreasing function of their separation and central value differences. This is done by including a component of q differential, δq, in the 'radius',

$$r'_{mn} = \sqrt{r_{mn}^2 + (k_{ad} \times \delta q_{mn})^2} \tag{3.11}$$

where k_{ad} is an adjustable constant. The problem is then to find the combination of mutually exclusive associations for which the product of the probabilities is a maximum.

The probability function is given by

$$P = (P_{max})_{mn} - R^2/[r_b + (1. - r_b)R^2] \tag{3.12}$$

where $R = r'_{mn}/r_c$, and r_b is the parameter that determines the shape of the function (i.e., $r_b = 1$ gives an inverted parabolic shape, $r_b > 1$ gives a Cressman function shape, and $r_b < 1$ yields a bell-shaped curve). P is set to zero should the above expression result in a negative value. The value of P_{max} is equal to $P_{stat} \times P_{age}$ which was adjusted to favor certain TRMC associations depending on their status and ages. P_{max} is a maximum when the two TRMCs are coincident ($R = 0$) and zero when they are displaced at or greater than r_c ($R \geq 1$). In the common case of an old (defined as more than one analysis time interval) and strong closed system, in which $P_{stat} = P_{age} = 1$, the function decreases with distance r_{mn}, becoming zero at radius r_c. When the TRMC at either the earlier or the later time is open, P_{stat} is given a value of less than unity, and, when the TRMC at the earlier time is newly found, $P_{age} < 1$. This type of penalty scheme helps the identity of the stronger and more established systems to be maintained. The rules for P_{max} can be summarized as:

$$P_{max} = P_{stat} \times P_{age};$$

$$P_{stat} = \begin{cases} 1; & \text{for a strong closed TRMC} \\ P_{open}; & \text{for a strong open TRMC} \end{cases}$$

$$P_{age} = \begin{cases} 1; & \text{for a TRMC more than one time interval old} \\ P_{new}; & \text{for a newly formed TRMC} \end{cases}$$

Values of $k_{ad} = 0.35$, $r_c = 12$ (° latitude), $r_b = 0.5$, $P_{open} = 0.75$, and $P_{new} = 0.75$ have been used with our data. In practice, the most probable combination of associations is found by maximizing the sum of the probabilities. This maximization is achieved by sorting the pre-

dicted-new TRMC associations into groups and determining the ensemble of matched pairs in each group with the highest overall probability.

An example of TRMC position grouping is illustrated in Figure 3.6. The associations are arranged into groups such that each old and new TRMC only occurs within the critical radius. The matching calculation finds the possible combinations of associations such that any one TRMC shall occur in only one association within the combination. The combination with the greatest probability gives the matching for the group. Histories of the consecutive positions and central values of each current system are thereby extended by one analysis interval, while those which are not paired up in this process are deemed either to have been born or to have demised.

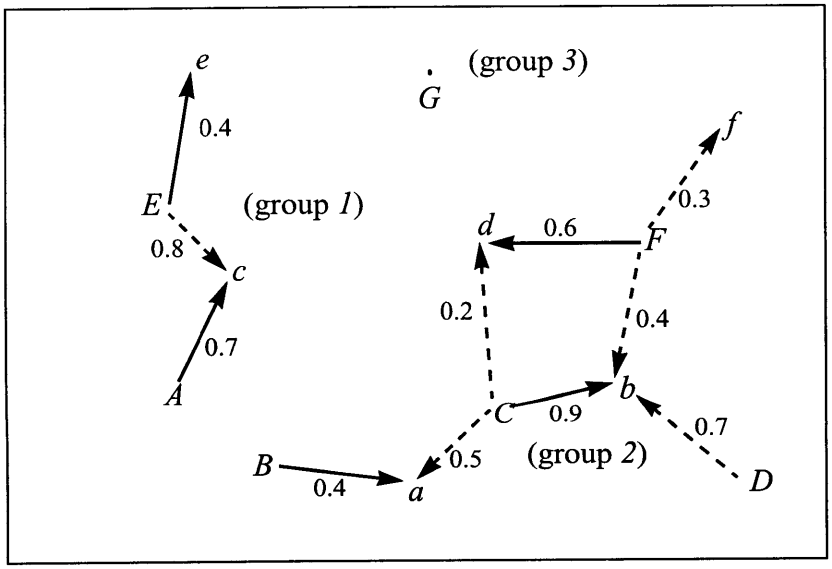

Figure 3.6: Grouping of predicted (capitals) and new (small letters) TRMC positions. Values of P_{mn} are given for possible matchings (arrows) of predicted and new positions. In each group the combination of associations with the greatest ΣP_{mn} is selected. The final associations are indicated by the arrows with solid lines (see explanation in the text).

In Figure 3.6, there are two predicted (indicated by capital letters *A* and *E*) and two new (small letters *c* and *e*) TRMC positions in group *1*. Within group *1* there are two possible matches, i.e., (i) *A-c*, *E-e* with $\sum P_{mn}$= 0.7 + 0.4 = 1.1; and (ii) *E-c* with $\sum P_{mn}$ = 0.8. The former set has the highest probability in the group and is therefore selected. A case with more predicted and new positions involved is presented for group *2* in the figure. The resulting matches for group *2* are (*B-a*, *C-b*, *F-d*) with $\sum P_{mn}$ = 1.9. After deciding these matchings we see that TRMCs *D* and *G* are defunct (no new TRMCs can be associated with) and *f* is new (no predicted TRMC can be traced back).

Provisions for division and merging of TR tracks have not been included into the algorithm yet.

3.2.4 Statistics Output

a. Statistical Variables

The last stage of TRICKS is to calculate various statistics for obtaining the average values of a number of quantities from the accumulated information of TR locations, tracks, and the associated moisture transport. The statistical program calculates both global (grid point) and zonal averages of various statistical quantities. The statistical variables fall into two groups, frequencies and regressions. Frequency quantities include TR densities, TR track fluxes, and the rates of TR genesis and termination. These quantities are proportional to the number (and lifespan) of participating systems and may decrease to zero in areas where there are no TRs. Regressed quantities include TR velocity, measures of TR strength (i.e., moisture fluxes), and the Lagrangian tendencies of these quantities. These

properties are not proportional to TR numbers and become undefined where there are no TRs.

The lifespan of a TR is the interval between the first and last analysis time recorded in the track history (TR genesis and termination). A minimum lifespan of at least four analysis intervals (i.e., 24 hours) is imposed in order to exclude ephemeral systems from the averaging and to enable the calculation of time derivatives (velocity and tendency).

In calculating TR frequencies, it is usual to normalize the resulting totals for averaging period and grid size. For instance, frequencies of TR genesis and termination are obtained from counts made at the first and last analyzed TRMC position of each track, respectively, and are normalized for time and area. They refer to the number of new TRs appearing or old systems disappearing per unit area per unit time.

TR density is the average number of TRs per unit area found in a particular region and is calculated by summing contributions from all sampled TRMC positions (recorded or interpolated along the tracks), and may be considered a measure of the proportion of the time that a point will be under TR influence.

TR track flux is used to denote the average number of TRs passing within unit distance of any point per unit time. It is usually preferable to calculate the flux as a vector quantity whose eastward and northward components represent the net number of eastward (northward) crossings per unit length of meridian (or parallel) per unit time.

Table 3.1 lists some of the statistical variables along with their units.

Table 3.1: List of statistical quantities

Quantity	Unit
TR density	#TR (°latitude)$^{-2}$
TR genesis	#TR (°latitude)$^{-2}$
TR termination	#TR (°latitude)$^{-2}$
Average TR track flux	#TR (°latitude)$^{-1}$ day^{-1}
E-W TR track flux	#TR (°latitude)$^{-1}$ day^{-1}
N-S TR track flux	#TR (°latitude)$^{-1}$ day^{-1}
Average TR moving velocity	m s^{-1}
E-W TR moving velocity	m s^{-1}
N-S TR moving velocity	m s^{-1}
Average TR moisture flux	(kg m^{-1} s^{-1})
E-W TR moisture flux	(kg m^{-1} s^{-1})
N-S TR moisture flux	(kg m^{-1} s^{-1})
Average TR intensity $\nabla^2 q$	(kg m^{-1} s^{-1})(°latitude)$^{-2}$

b. Methods of Computation

Because a TR may travel over more than one grid square in an analysis interval, each TR track is subdivided by interpolating it to a number of interpolated positions equally spaced in time. This is done by fitting a cubic spline to the tracked positions in each coordinate direction and interpolating to obtain the coordinates of the subdivided track. Spline fitting is also applied to the q-related quantities; it permits easy calculation of the time derivatives of the fitted quantities, i.e., velocity components and rates of change of TR moisture flux and intensity.

For the zonal average analysis, TRs and their properties for each sampled (i.e. recorded or interpolated) time are accumulated in latitude zones of specified extent and then normalized for time and area as appropriate. For the grid point statistics, TR counts and its properties are not assigned to grid cells, but rather are spread over nearby grid points using a Cressman-like function, i.e., the average values of system properties were obtained by contributing a weighted fraction of the value, p_k, of the quantity, p, at each sampled position, k, to the total for each grid-point (i, j) within the radius $r_{ijk} < r_{s1}$. The weighting factors were of the form,

$$w_{ijk} = \frac{r_{s1}^2 - r_{ijk}^2}{r_{s1}^2 + r_{ijk}^2(r_{s1}^2/r_{s2}^2 - 1)} \tag{3.13}$$

where r_{ijk} is the distance between the grid point (i, j) and the sampled position k, r_{s1} is the pass radius at which w_{ijk} becomes zero, and r_{s2} is a parameter which controls the shape of the function. The sum of the weighted values of the appropriate quantity p_{ij} for each grid point, taken over the entire run, was divided by the sum of the weights for the grid point, i.e.,

$$\bar{p}_{ij} = \frac{\sum_k p_k w_{ijk}}{\sum_k w_{ijk}} \tag{3.14}$$

Values of r_{s1} and r_{s2} are handled differently for frequency and regressed quantities (usually with a smaller pass radius for frequencies) to ensure continuity of the analysis in poorly represented locations and give an accurate but not too noisy plot. For frequency quantities, each TR is given a weighting of unity, i.e., the sum of all the statistical function values distributed to the points within the pass radius are normalized to this value. In practice, values

of r_{s1} = 5° and 10° latitude were selected for frequency quantities (except for TR genesis/ termination where r_{s1} = 7° latitude) and regressed quantities, and r_{s2} was set to 2.5° latitude for all quantities. For q-related quantities within a particular TR, the same average method is used except grid-point (i, j) now is the location of TRMC and r_{s1} is chosen as the 1.25 times the distance between the TRMC and the outmost TRC.

TR movement is calculated as its TRMC's average speed and its eastward/northward components. The q-related quantities for a particular TR include the average TR moisture flux with its zonal and meridional components and the average TR intensity (i.e., the magnitude of TR moisture flux), all are calculated by averaging the corresponding variables from the TRCs within the TR using the method described above. This procedure avoids the point measures (for instance, using only the quantities related to the TRMCs) that often fail to represent the true strength of a TR system.

Both the time interpolation and the analysis make use of the slow and smooth variation of the map scale on the PS projection. A 1.5-hour interval is chosen for the time interpolation and a constant map scale is assumed within the Cressman radius. Observations show that TRs are less likely to cross the Equator and even less likely to travel large distances from one hemisphere into the other. However, some precautions are needed when the track data are global. To guard against distortions of the projected tracks which might affect the spline fitting, tracks which stray more than 40 degrees into the opposite hemisphere are disregarded.

3.3 Operation of the Scheme

The scheme was first tested with 6-hourly vertically integrated moisture flux calculated from NCEP/NCAR reanalyses for the year 1993. The decisions of the detecting and tracking program are guided by a number of governing parameters. By adjusting the parameters separately and comparing the plotted TRCs, TRMCs, TR axes, and tracks with those arrived at subjectively from the successive daily charts, such as Figure 2.1, a usable (but not necessarily optimum) set of parameters was derived. The performance of TRICKS during the identifying and tracking stages are examined in the following subsections.

3.3.1 Performance of the TR Identifying Stage

On average, 44.6 TRCs and 10.7 tropospheric rivers were found globally by the scheme at each analysis time for the month of January, 1993 (see Table 3.2). The largest category of TR status is the strong closed one, representing nearly 55% of the total TRC number.

The parameter choices for TRC status classification were based on observations which can be determined from the techniques applied with the manual procedures and a detailed comparison of each analysis time. As mentioned before, the mean Laplacian $\nabla^2 q$ is taken as a measure of the strength of a TRC in the algorithm. TRCs with strength less than -50 kg/m/s/(° lat)^2 are classified as strong systems, while those with strength between -30 and -50 kg/m/s/(° lat)^2 are deemed as weak ones. The strength criteria were chosen to not only filter out the insignificant systems but also retain a certain ratio between strong and weak categories.

Table 3.2: Average number of TR cores (TRCs) with different status and TRs per analysis for January 1993.

	Total TRCs	Strong closed TRCs	Weak closed TRCs	Strong open TRCs	Weak open TRCs	TRs
NH	18.9	10.0	3.9	3.8	1.2	4.4
SH	25.7	14.2	5.1	4.5	1.9	6.3
Global	44.6	24.2	9.0	8.3	3.1	10.7

Figure 3.7 shows an example of the points at which TRICKS identifies TRCs for the 0000 UTC January 1, 1993. Solid symbols (circles or squares) indicate closed TRCs and hollow symbols open ones (where 'closed' and 'open' TRCs are as defined in section 3.2.1c). In addition, circles denote the TRCs classified as strong and squares those as weak.

In general, the agreement in locality is quite good. All strong closed TRCs found in the digital data fall close to high centers marked in the manual analysis (figure not shown), as well as many of the weak and open TRCs. However, by its nature, the automatic algorithm identifies more TRCs than the manual analysis and most of these additional TRCs are of the weak or open variety. There are several advantages in retaining these categories of TRCs at the TRC detecting stage and pruning them out during the TR axis definition and tracking stages. Firstly, most of these additional TRCs that are otherwise totally absent in a manual analysis are often located near the heads or tails of the enlongated moisture-flux features, as seen from Figure 3.7. Therefore, a more realistic TR structure can be defined with the help of these TRCs. Secondly, some of the weak TRCs will turn out to be the

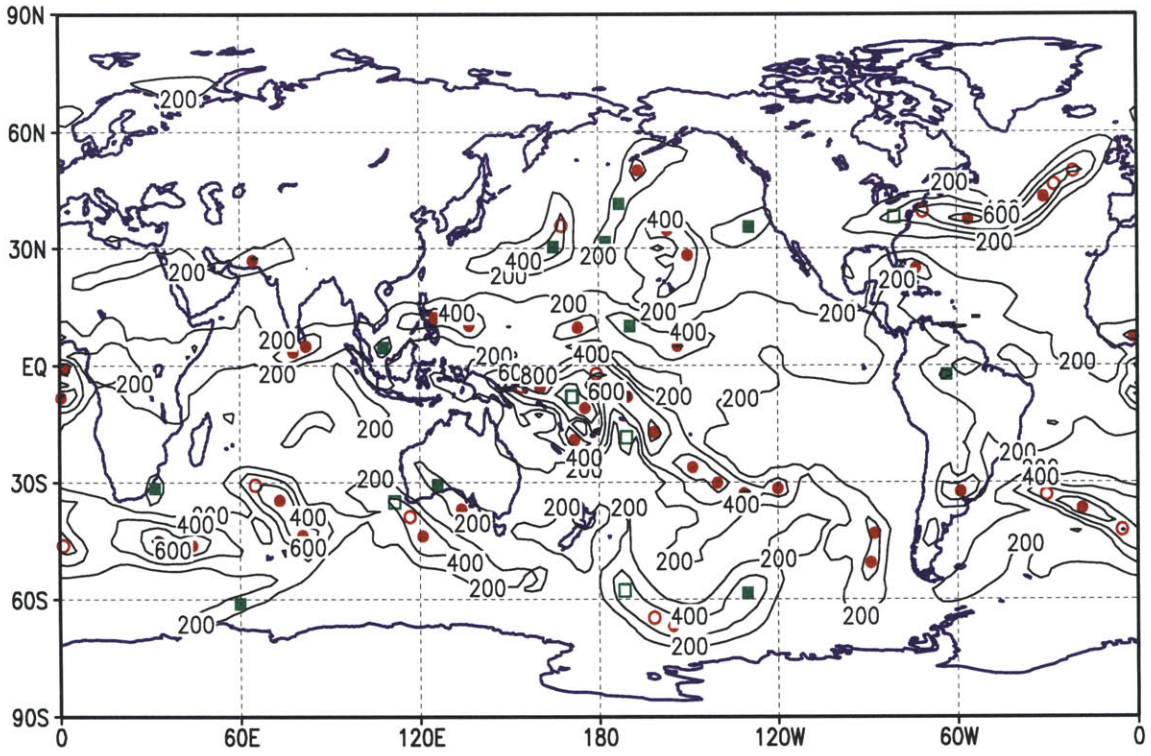

Figure 3.7: Magnitude of water vapor flux field q (unit: kg m^{-1} s^{-1}) and TRCs for the 0000 UTC January 1, 1993. The contour interval for q is 200 kg m^{-1} s^{-1}. The points at which the TRICKS algorithm identifies a closed (solid symbol) or open (hollow symbol) TRC. Circles (in red) denote strong TRCs and squares (in green) weak ones.

precursors of cores which later become strong, or to be the last remnants of strong cores. By recording them, one is able to have a more complete record of TR development than would be the case if they were recorded only after they had attained considerable intensity or symmetry.

A total of 17 TRs was found at 0000 UTC January 1, 1993 with 6 rivers in the Northern Hemisphere and 11 in the Southern Hemisphere. Although the numbers of total TRCs and TRs identified at this analysis time are not representative for that particular month (see

Table 3.2), it is believed that larger quantities in each category are more relevant in revealing different aspects of the detecting procedure.

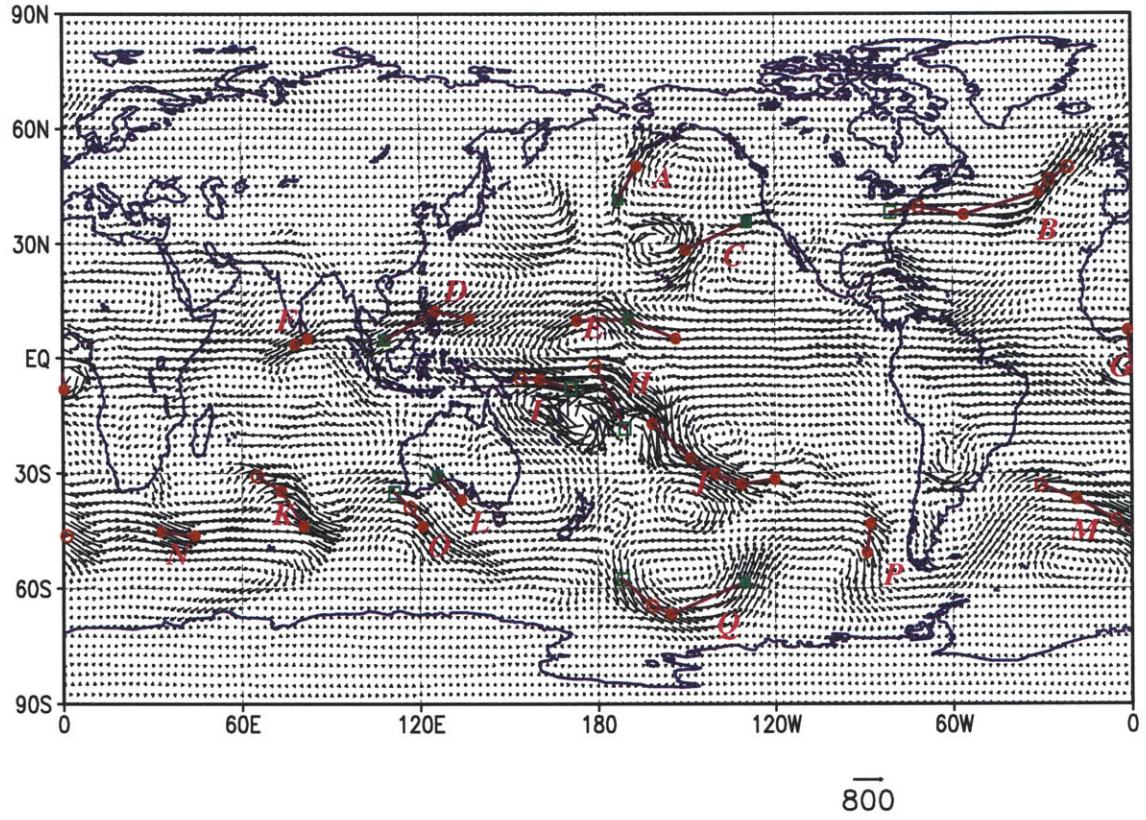

Figure 3.8: Tropospheric rivers found by the TRICKS (indicated by the purple lines connecting the TRCs) at 0000 UTC January 1, 1993 along with vertically integrated water vapor flux vectors (Unit: kg m^{-1} sec^{-1}). TRCs associated with each river are also plotted and the status symbols are the same as in Figure 3.7. TRs are alphabetically labeled from north to south according to the latitudes of TRMCs.

The TR axes were plotted in Figure 3.8 along with the moisture-flux vectors and the status of connected TRCs. The Tropospheric Rivers identified by our definition tend to follow the moisture-flux filaments fairly closely. They exhibit significant similarity compared with those judged subjectively. However, TRs identified visually (manual method) may be absent or different from those detected by automatic method due to a set of more stringent

rules being applied to the latter (for instance, one may define a swirling TR in the middle of the northern Pacific near 160°W and 30°N, while the direction criteria set by the numerical method can only associate the southeast part of the water vapor flux with nearby TRCs that transport moisture towards the North America, i.e., TR ***C*** in Figure 3.8). Conversely, it is also possible that a TR detected objectively may not be apparent to an experienced analyst (a plausible example is the TR ***L*** detected from ~ (125°E, 30°S) to ~ (135°E, 37°S) over the Great Australian Bight).

That open and weak TRCs do assist the TR definition is demonstrated in many TRs including ***A***, ***B***, ***C***, ***D***, ***E***, ***H***, ***I***, ***K***, ***L***, ***M***, ***O*** and ***Q***. There are two strong open TRCs forming the head of TR ***B*** and two open TRCs (one strong and one weak) forming its tail. In one situation, TR ***E*** has a weak closed TRC in the middle with strong closed TRCs at each end. This may be an indication of two merging (or splitting) TRs with a weak linkage in between, though there is no such discrimination design in the scheme. There are strong moisture fluxes corresponding to the vapor associated by the Southern Pacific Convergence Zone (SPCZ) over the Southern Pacific. The discontinuity of this moisture transport belt as indicated by the three individual TRs (i.e., TRs ***H***, ***I***, and ***J***) may be due to the ineffectiveness of the scheme in a situation when the directions of moisture fluxes change swiftly in a relatively short range (i.e., near the dateline of the SPCZ in this example), and a lack of a merging and dividing consideration as well. The failure of forming a coherent TR where the moisture fluxes become retrograde in latitudes owing to large directional changes, such as in the cases of the swirling TR in the middle of the northern Pacific and the discontinuity of the TRs associated with the SPCZ, remains a challenge for our objective algorithm. Nevertheless, it is believed that the major features of the tropospheric rivers can be realistically captured by the scheme.

3.3.2 Performance of the TR Tracking Stage

All tracks of TRs identified by the TRICKS for year 1993 are presented in Figure 3.9. To reduce the clutter, only tracks that have lifetimes longer than 24 hours are plotted.

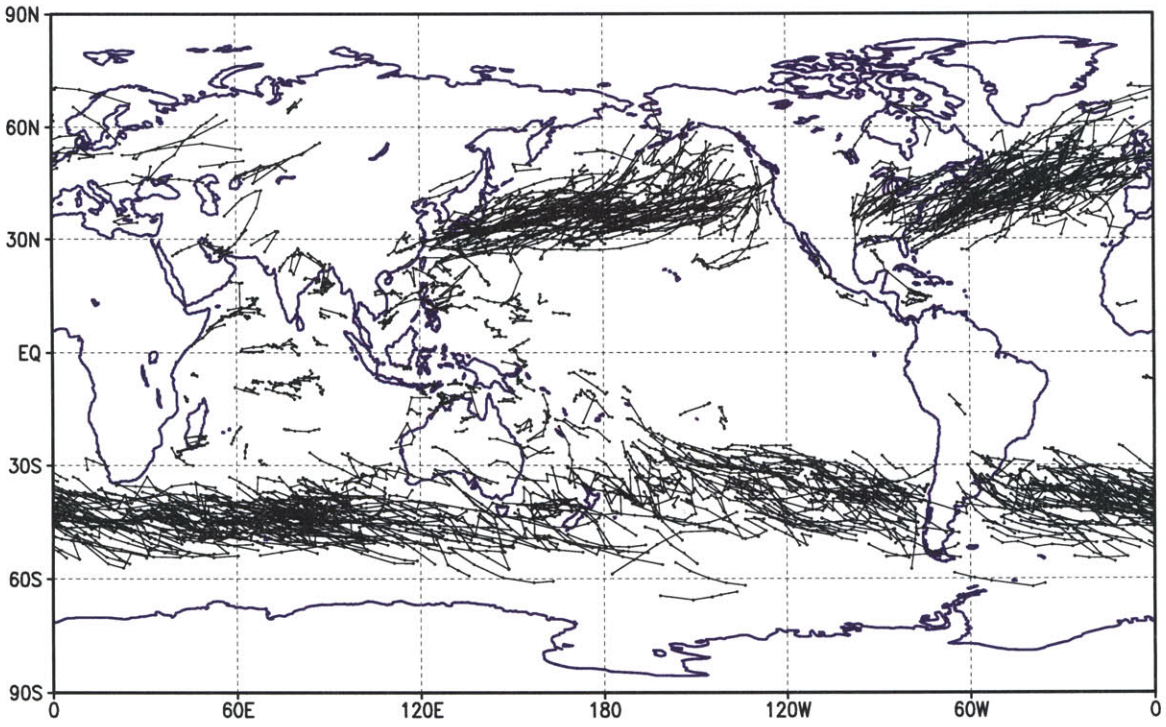

Figure 3.9: TR tracks for year 1993. Curves connect the positions of TRs surviving 24 hours or more. Dots mark the positions with 6-hour intervals.

There are a total of 811 paths during the whole year. A general impression is that the TRs occur frequently in the mid latitudes in both hemispheres and also have longer lifetimes there. The patterns of TR tracks appear to be in agreement with those of the storm tracks, which is an expected feature since water vapor transport processes are closely

related to these migrating systems. More details of track statistics will be discussed in the next two chapters.

Since the construction of TR tracks is based on the projection of TRMC positions from one analysis time to the next and the comparisons of the projected positions with those of TRMCs detected at the new time, as mentioned before, the problems that may be encountered in tracking are partly a consequence of using data spaced at 6-hour intervals, during which the TRMCs may travel distances comparable with their separations. The 6-hourly positions for each track (dot marks) are also indicated in Figure 3.9 and are seen to progress in a fairly regular and consistent manner. This helped to justify not only the use of fractional grid-point positions for locating TRCs, but also the three-step tracking procedure devised in section 3.2.3 that eliminates many of the uncertainties due to the time discontinuity. However, the rules which must be imposed upon the radii of search make it difficult for the scheme to anticipate sudden changes of movement which real TRs may undergo. Nevertheless, examples of such sudden changes in speed and direction may be discernible in a small number of tracks in Figure 3.9. We believe that the statistical basis of the tracking program is consistent with the performance of its intended task within the desired constraints on searching radii and other parameters. Sensitivities of the control constants to the scheme are examined. A final set of these control constants defined before have been used with our data (i.e., $k_{ad} = 0.35$, $r_c = 12$ (° latitude), $r_b = 0.5$, $P_{open} = 0.75$, and $P_{new} = 0.75$). Though atmospheric water vapor and its transport may have large variability in time scales less than a day, the method of using the TRMC as a TR's footprint appears validated from Figure 3.9.

A more detailed example of a TR progressing over the northern Pacific that occurred at 0000 UTC January 6 and ended at 0600 UTC January 7 is exhibited in Figure 3.10. Open

TRCs were interspersed among the closed TRCs to form the axis of the same TR at each analysis time with 6-hour intervals, and the strongest TRC chosen as the TRMC at each time step was tracked by the scheme to render a coherent TR track. The river changed its axial direction from a near SW-NE one to a N-S (indicated by the purple lines) as the whole system translated from the SW towards the NE (the TR track). This picture gives one example of a more concise depiction of the relationship between a TR axis and its track that is often observed on a daily water vapor flux map, and more quantitative information can be extracted from such practice.

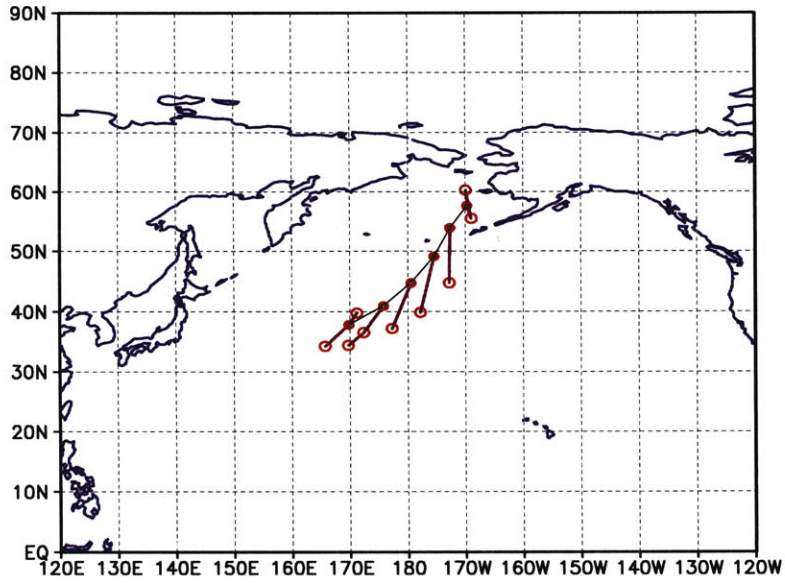

Figure 3.10: A TR progression history over the northern Pacific. The TR was tracked (solid black line) from its birth at 0000 UTC January 6 through its termination at 0600 UTC January 7, 1993, with TR axes (purple lines) and the status of TRCs indicated (status symbols are the same as in Figure 3.7).

While in the majority of cases the tracking program made the "correct" decision, there was always a small number of apparent discrepancies which could not be eliminated whatever adjustments were made to the controlling constants. Whether this was more a prob-

lem of data quality or rather a consequence of the complexity of atmospheric processes, which are simplified and truncated in a computer analysis, is not clear. In any event, the scheme appeared to be tracking in the desired manner most of the time.

3.4 Summary and Discussion of the Chapter

In this chapter, the Tropospheric River Identifying and TraCKing Scheme abbreviated as TRICKS was described and evaluated. Owing to the inherent limitations of manual techniques, the statistics for the water vapor transport from a Lagrangian view is nonexistent. The scheme developed herein is believed to have substantially achieved the aim of providing an efficient and much needed tool for the study of atmospheric water vapor transport and its climatology. It embodies several computational designs that are new to this context and circumvents much of the labor that has hindered this work in the past. Although Newell and Zhu (1994) and Zhu and Newell (1998) calculated the TR statistics from an Eulerian standpoint, no documentation has yet been reported on the frequencies of TR genesis and termination, and very little or no attention has been paid to the TR velocity, strength, and lifespans. These remarks underline the need to conduct an objective analysis of TR behavior to help us fill these gaps in our knowledge.

The accuracy of the outputs at different stages has been evaluated for the period of 1993 and specific analysis times within. The TRC detecting, TR identifying, and tracking routines performed satisfactorily, but a number of difficulties were experienced under certain circumstances. Some of these difficulties encountered were peculiar to the data, the time interval between analyses, and grid resolution used. For example, one problem asso-

ciated with weak and open TRCs is the accuracy and reliability of location since the search is in the field of the Laplacian of q, which is a higher order quantity and therefore more noisy even with averaging. The interesting thing is that even such weak cores do seem to progress in a credible way and maintain their identities most of the time, a fact that justifies their inclusion in the record. Therefore, the incorporation of open TRCs and the exclusion of insignificant TRCs using the strength criteria were found to result in a much more credible set of TR definitions and tracks.

Though not discussed in the chapter, it was seen that alterations in the detecting and tracking parameters brought about moderate changes in TR frequency and regressed statistical quantities. For instance, a widening of the radius of search (r_c) or a milder discrimination against open TRCs (greater P_{open}) favors the continuity of tracks, thereby increasing TR densities since fewer ephemeral systems are rejected.

From the preliminary results of this chapter, we are confident in applying the scheme to study the climatological behavior (both mean and variability) of the TRs from a long series of data, which are the contents of the next two chapters.

Chapter 4

Mean Tropospheric River Behavior

4.1 Introduction

The gross observational features of TRs described in chapters 2 and 3 show that these systems occur in preferred geographical areas and vary in intensity, frequency, and distribution during the year. Since TRs are such an important component of weather, climate, and climate variability over the globe that play a central role in the maintenance of global climate and are responsible for a large portion of the poleward transport of heat and moisture, there is an urgent need in determining their spatial and temporal distribution and relating these to the observed general circulation. Despite the significance of this need, little work has been undertaken in the past to document their behavior in an integrated and comprehensive manner. This has been partly because of the tremendous investment of time and effort required to identify and track TRs manually from a series of daily weather maps or satellite images, as well as the lack of high quality data sets. The most relevant contributions have come from an MIT group (Newell et al. 1992; Newell and Zhu 1994; Zhu and Newell 1994, 1998) that utilized data sets limited to a short period less than a few

sporadic months or years. None established any automatic objective methods to identify and track Tropospheric Rivers (TRs) from sequential analyses for a climatologicaly representative period. Therefore there has been no climatology and associated statistics on TRs and their tracks so far.

In this chapter we present a climatology of mean TR behavior for the globe which has been constructed paying explicit regard to the points raised above. The data set that we use are the NCEP/NCAR 6-hourly reanalyses spanning a 43-year period from 1958 to 2000. The availability of these analyses was a major impetus to undertake the current task. We will address TR variability for the same period of the analyses in the following chapter. The TRICKS scheme described in the previous chapter enables us to assemble what is the very first and probably the most reliable climatology of TRs. The seasonal mean climatological behavior of TRs will be described in the next section. Section 4.3 presents the zonal averages of various statistics. Section 4.4 will focus on the water vapor transported by the rivers. This will be followed by a summary of results in section 4.5.

4.2 TR Seasonal Mean Climatology

4.2.1 General Counts

The statistics which follow have been compiled for all systems having a lifespan of at least 24 hours (i.e., lasting five or more 6-hourly positions) unless otherwise specified. Some gross statistics of the counts of TRCs and TRs in both hemispheres are presented in Table 4.1. There are in excess of 10 TRs per analysis identified for the Globe. From limited data

resources, Newell et al. (1992) found subjectively that there are typically 4 - 5 rivers in the Northern Hemisphere (NH) and 5 rivers in the Southern Hemisphere (SH). These numbers are quite close to those identified by our scheme, i.e., 5.0 per analysis in NH and 5.3 in SH on average. The TR numbers display seasonality with the maxima (~ 6.3) being found in summer time in both hemispheres, and minima (~ 4.1) in spring in the NH and (~ 4.6) in southern winter in the SH. TRs occurring in winter and spring in both hemispheres appear to be closer in counts that are fewer (~ 40.9% in the NH and ~ 28.0% in the SH) than those in the other half of the year. The numbers of TRCs that help to identify TRs are also listed in Table 4.1. They have the same seasonality as TR numbers and the largest number was found in JJA in NH (~ 28.9). Of the 44.2 TRCs detected per analysis for the Globe, 54.3% were strong closed; 21.0% were strong open; 16.7% were weak closed; and 7.9% were weak open.

Table 4.1: Average numbers of TRs and TRCs (in parentheses) per analysis

	DJF	MAM	JJA	SON	ANNUAL
NH	4.2 (17.5)	4.1 (17.8)	6.3 (28.9)	5.4 (23.2)	5.0 (21.9)
SH	6.3 (26.4)	5.6 (23.9)	4.6 (19.3)	4.7 (19.8)	5.3 (22.4)
Globe	10.4 (43.9)	9.8 (41.7)	10.9 (48.3)	10.1 (42.9)	10.3 (44.2)

The total numbers of TRs counted in each season when broken up by latitude belts 20° apart are listed in Table 4.2 and are also plotted in Figure 4.1. In all seasons the greatest number of TRs is found in the mid-latitude band 30° – 50°S in the SH, and the second

Table 4.2: Counts of TRs found in a particular season and latitudinal band (20° apart) during the 43-year NCEP/NCAR reanalysis period.

	DJF	MAM	JJA	SON
90°N - 70°N	1	0	36	6
70°N-50°N	243	268	794	646
50°N-30°N	2699	2733	2639	2785
30°N-10°N	590	556	1250	893
10°N-10°S	560	274	278	400
10°S-30°S	888	723	660	511
30°S-50°S	3749	3791	3579	3427
50°S-70°S	400	514	147	197
70°S-90°S	0	0	0	1

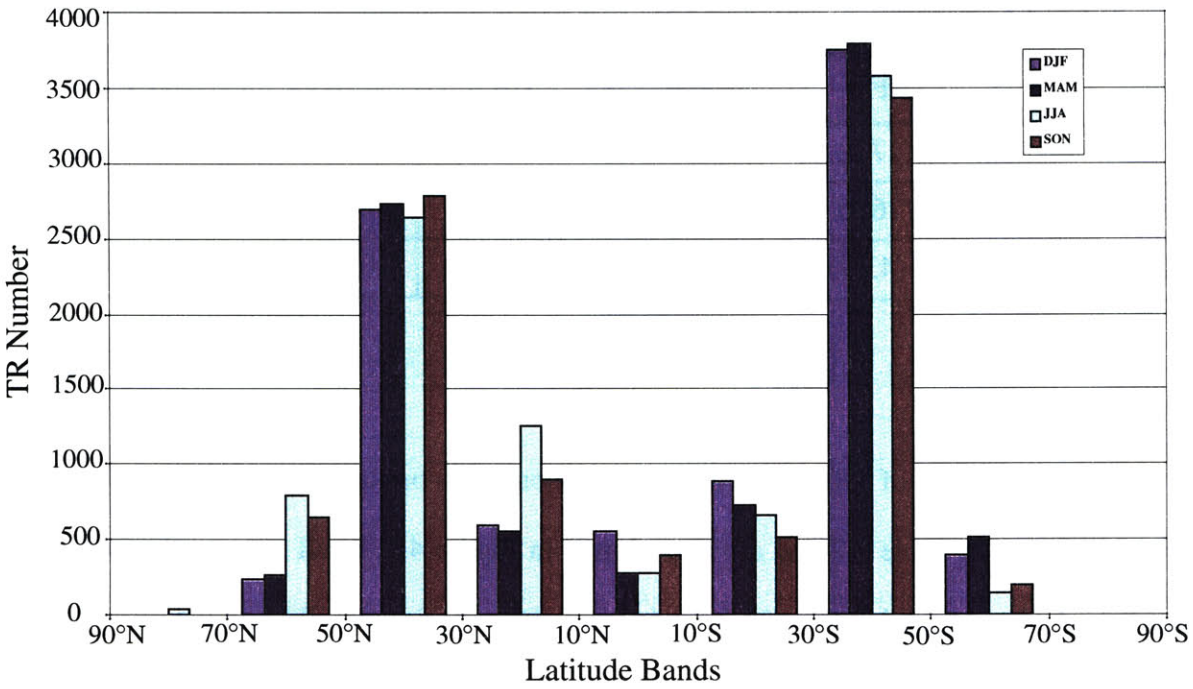

Figure 4.1: Total TR counts in different seasons and within different latitude bands 20° apart during the 43 year NCEP/NCAR reanalysis period.

maximum is observed in the belt 30° – 50°N in the NH which is ~ 25% less than the former. The vast majority of TRs are found in these two belts which account for ~ 70% of the total, reflecting predominantly river activities (i.e., water vapor transport processes) there. Only ~ 9% TRs occur in the high latitude bands (to the north of 50°N and the south of 50°S), and the rest (~ 21%) reside in the tropical belts (30°S – 30°N). The seasonality is stronger in the high latitude bands immediately to the north or south of the bands with the maximum frequency, as well as in the tropical bands.

4.2.2 TR Density, Track Flux, and Translational Speed

The density of systems is defined as the mean number per analysis found in a 10^3 (°latitude)^2 area. Figure 4.2 presents the TR spatial density (i.e., the distribution of TR occurrence) in the four seasons.

A survey of TR numbers in the previous section has shown that TRs are largely distributed in midlatitudes. The distribution of mid-latitude weather systems is known to be determined by a number of factors, including the distribution of land masses, sea surface temperature gradients, and the location and orientation of baroclinic zones. These conditions are rather different in the two hemispheres, and hence it is not surprising that the distribution of TR density contrast significantly.

In the Northern Hemisphere, there are two principal regions of TR activity for all seasons in middle to high latitudes best developed over the two ocean basins and least so in the regions of the continents and tropics. The high density band in the North Pacific shows a more zonal orientation in the winter and spring than that in the summer and autumn. The

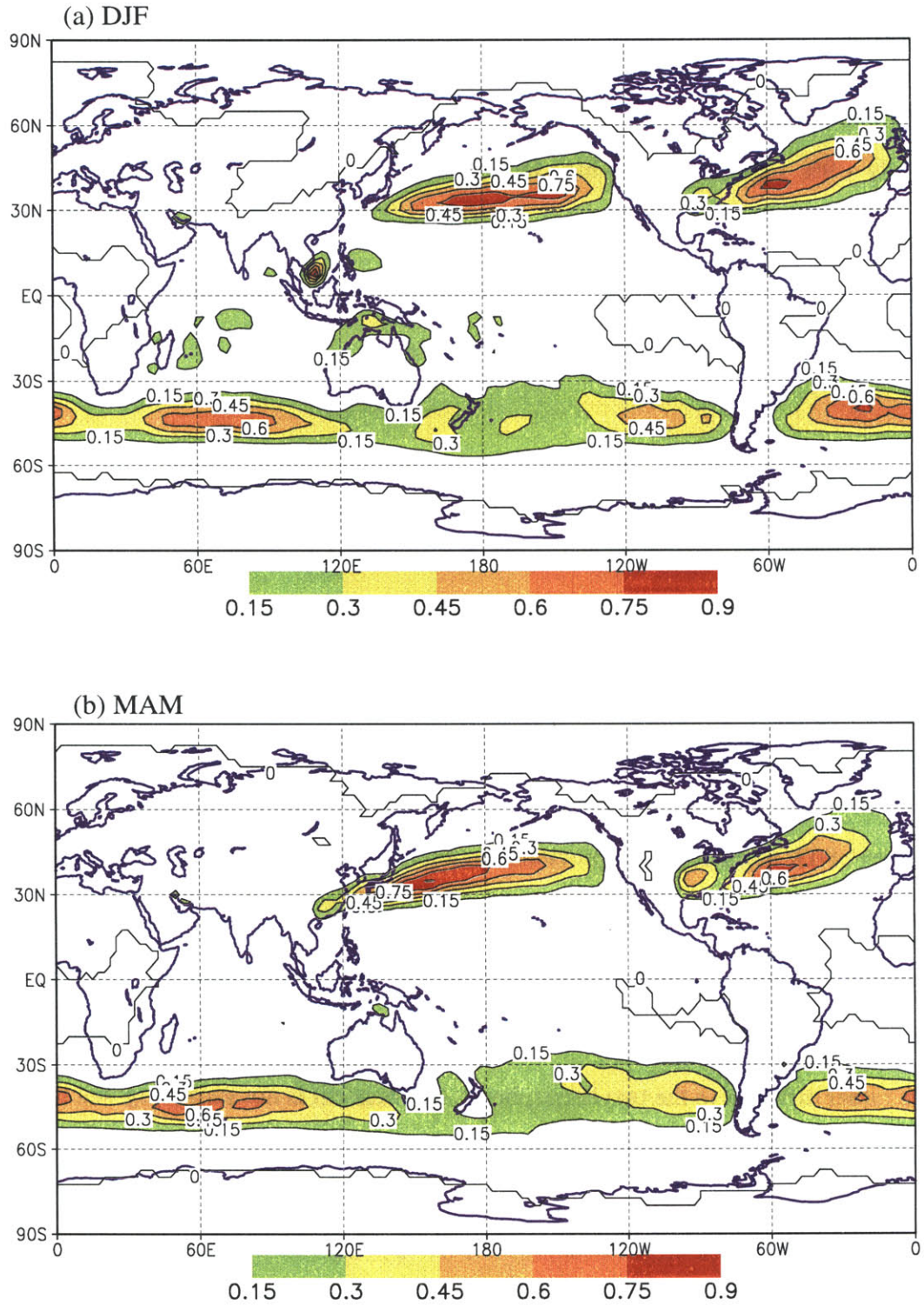

Figure 4.2: TR density for (a) DJF, (b) MAM, (c) JJA, and (d) SON. Unit: 10^{-3} TRs (°latitude)$^{-2}$. The contour interval is 0.15×10^{-3} TRs (°latitude)$^{-2}$. Values greater than 0.15×10^{-3} are color shaded.

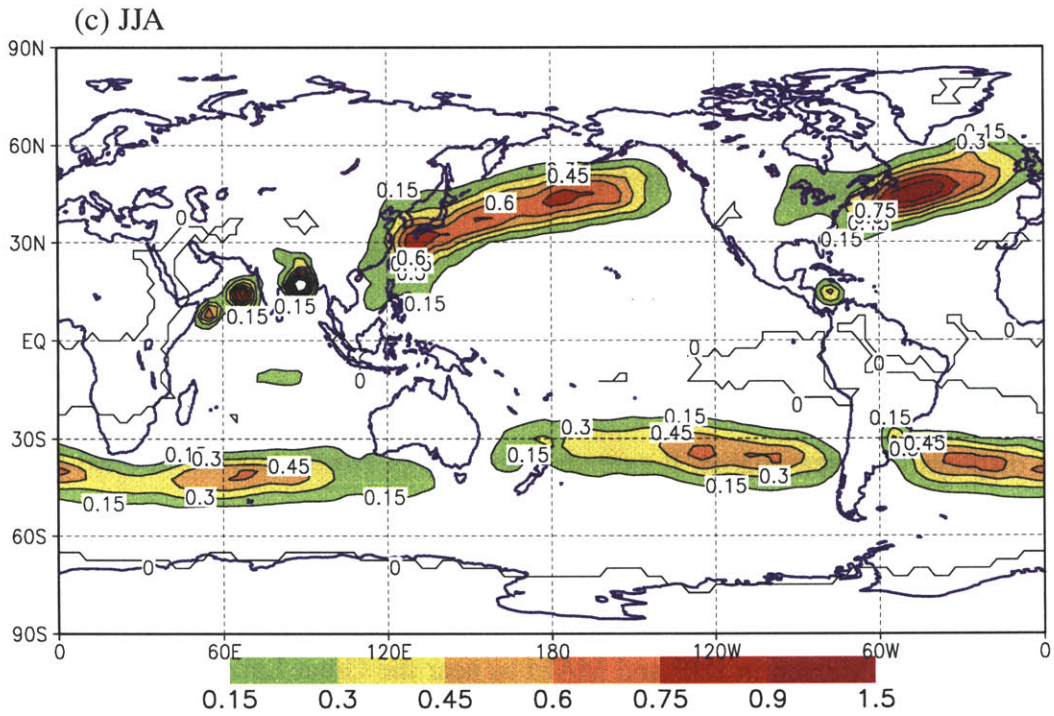

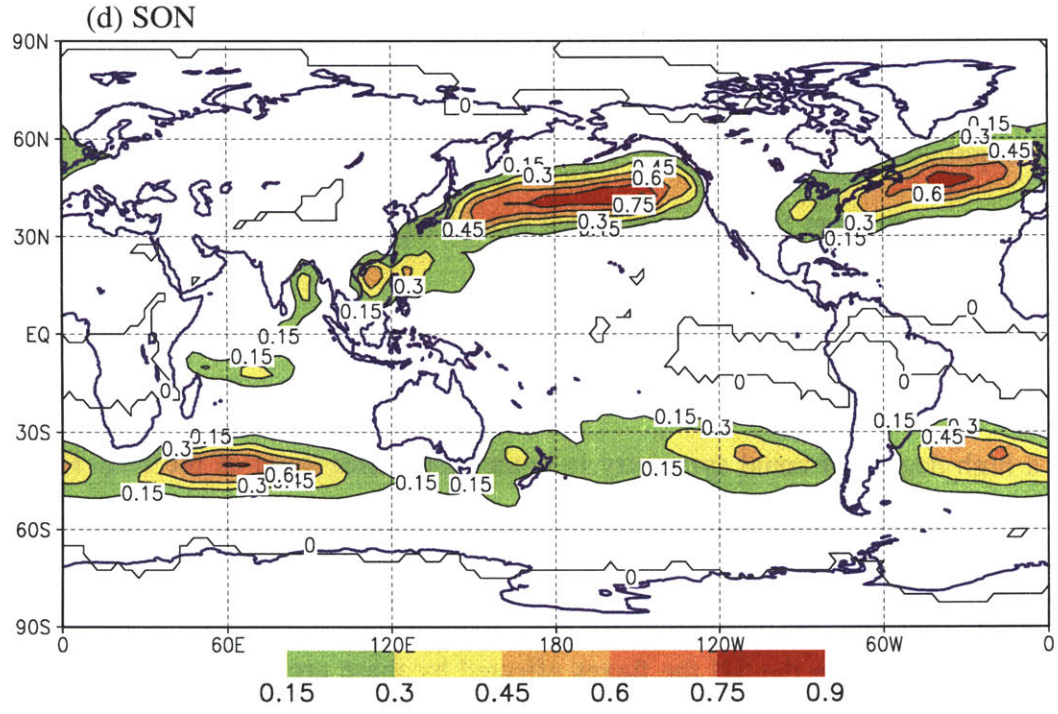

Figure 4.2: (*Continued*)

latter has a WSW- ENE orientation and extends further at both southwest (from near Japan in DJF to the South China Sea in SON) and northeast ends (from near the west coast of North America in DJF and MAM to the Gulf of Alaska in JJA and SON). The center of highest density that exceeds 0.75×10^{-3} TRs (°latitude)$^{-2}$ seems to migrate along the axis of maxima with its position situated in between the western sector of the North Pacific in spring and the eastern sector in autumn. In the Atlantic, there appears to be an enhancement of TR activity during the summertime, while the overall orientation of the density maxima displays little seasonality. It extends from east of North America toward Ireland and the Norwegian Sea. However, large seasonal TR activity is observed over eastern North America where high level of TR activity migrates north- and northeast-ward from north of the Gulf of Mexico in DJF and MAM to near the Great Lakes in JJA and SON. This is linked apparently with moisture transport activity from the Gulf of Mexico. The center of density maxima has nearly the same magnitude as that in the Pacific and moves along the axis when the season changes. Other localized maxima are seen next to the east of the Philippines, southern Indochina Peninsula, and Persian Gulf in DJF; the Bay of Bengal, southern Arabian Sea, and Caribbean Sea in JJA; near the South China Sea and the Bay of Bengal in SON.

In the Southern Hemisphere, like many other climate variables, TR density maxima exhibit a high degree of zonal symmetry in comparison with those of the NH. The NH winter climatology exhibits large-amplitude standing waves (induced by continentality and topography) and these are responsible for a significant poleward moisture and energy transport. By contrast, in the SH the fluxes effected by these are small (van Loon 1979; Peixoto and Oort 1992), which serves to underline the importance of transient disturbances in the maintenance of climate in that hemisphere. TR density maximizes between

30° and 50°S in the Atlantic and Indian Ocean sectors, and between 25° and 50°S in the Pacific. Some local maxima are scattered over the west-central Indian Ocean near 15°S for all the seasons except austral autumn (MAM), and next to the northern Australian coast in DJF. The region just off the coast of Argentina is host to densities in excess of 0.75×10^{-3} TRs (°latitude)$^{-2}$ in DJF, as well as near 40°S, 60°-70°E in SON. An area of high densities over the southeast Pacific that is weaker than those in the other two ocean basins experiences a rapid seasonal change migrating southward and northward in its position from SON to DJF and from DJF to MAM, with its southernmost position in DJF.

Figure 4.3 through 4.6 exhibit statistics for TR track fluxes and magnitudes for different seasons. TR track flux represents the average number of TRs passing within unit distance of any point per unit time. Although TRs follow a great variety of paths as shown for example in Figure 3.9 for the year 1993, there are preferred tracks.

In the NH, the areas of maximum fluxes can be found over the North Pacific and North Atlantic Oceans. In the North Pacific there is a fairly general eastward and then northeastward movement of systems from the east of the Asian coast, central North Pacific, into the Gulf of Alaska for all seasons except JJA. During summer, the track fluxes have a more northward component leading into the Bering Sea and Alaska, indicating a poleward displacement of TR frequency during the warmer months. Not surprisingly, therefore, the pattern is consistent with that of TR density. The magnitudes of track fluxes show that there is a marked tendency for this region to experience a maximum concentration of TR tracks in winter when the values exceed 10^{-2} TRs (°latitude)$^{-1}$ day^{-1} (Figure 4.3b). The same seasonality can also be found for the North Atlantic counterpart, which may not be so clear on the TR density charts (Figure 4.2). The North Atlantic flux maxima generally

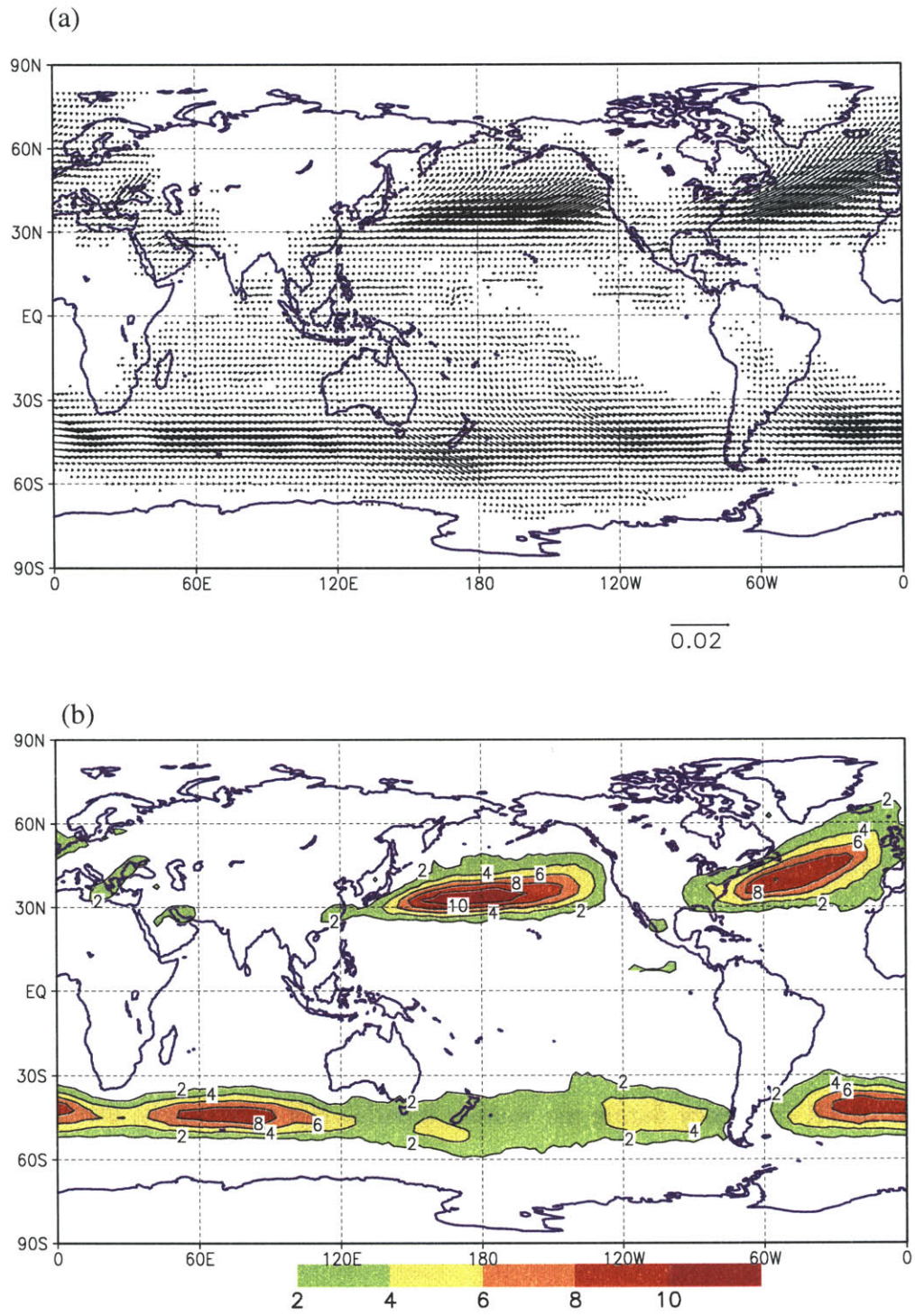

Figure 4.3: TR statistics for the NH winter (DJF), for the years 1958 - 2000. (a) TR track flux vectors. The vector at the bottom represents 0.02 TRs (° latitude)$^{-1}$ day^{-1}. (b) Contoured form of (a) in units of 10^{-3} TRs (°latitude)$^{-1}$ day^{-1}, drawn every 2×10^{-3} TRs (°latitude)$^{-1}$ day^{-1} with values greater than 2×10^{-3} color shaded.

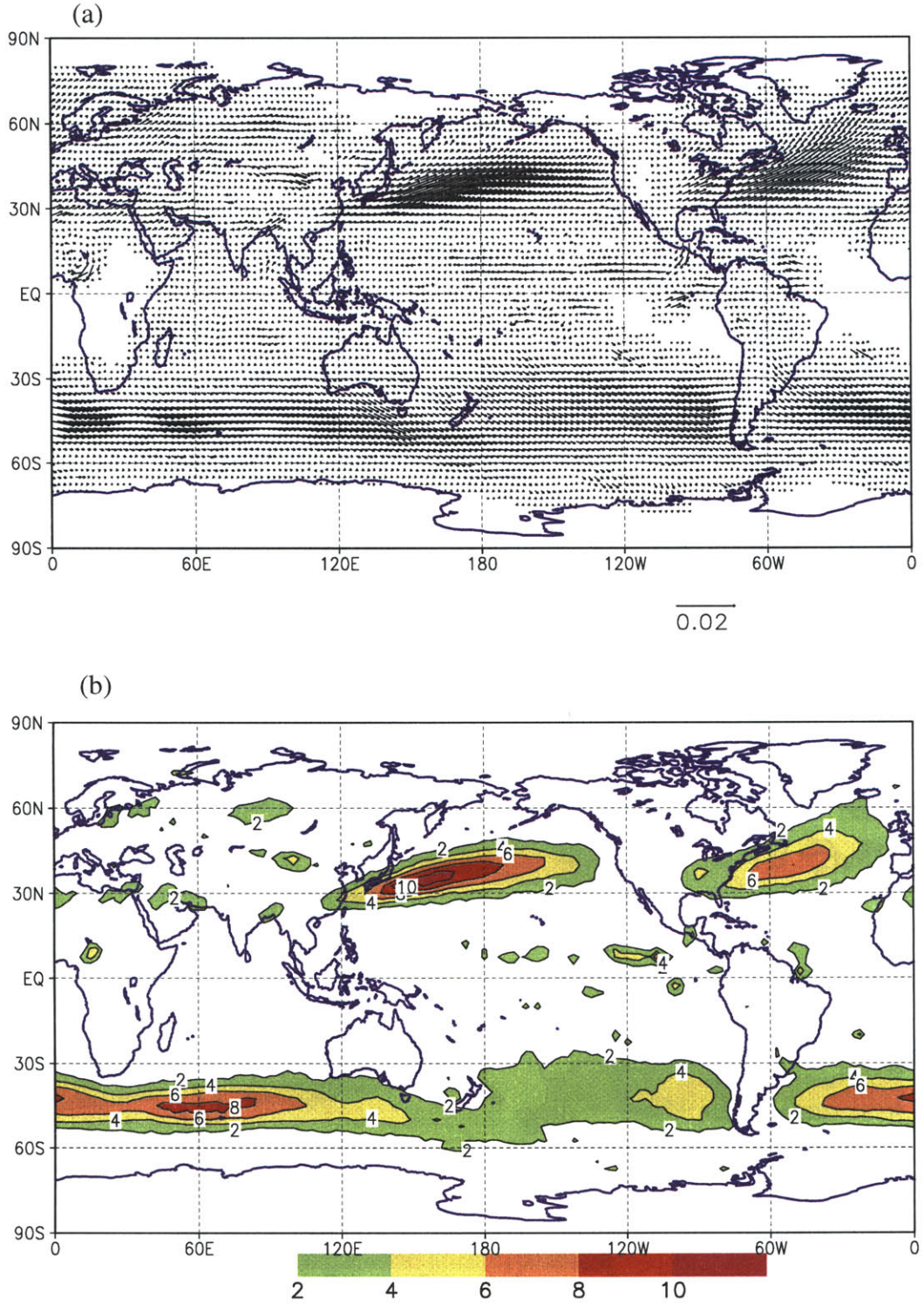

Figure 4.4: Same as Figure 4.3 except for NH spring (MAM).

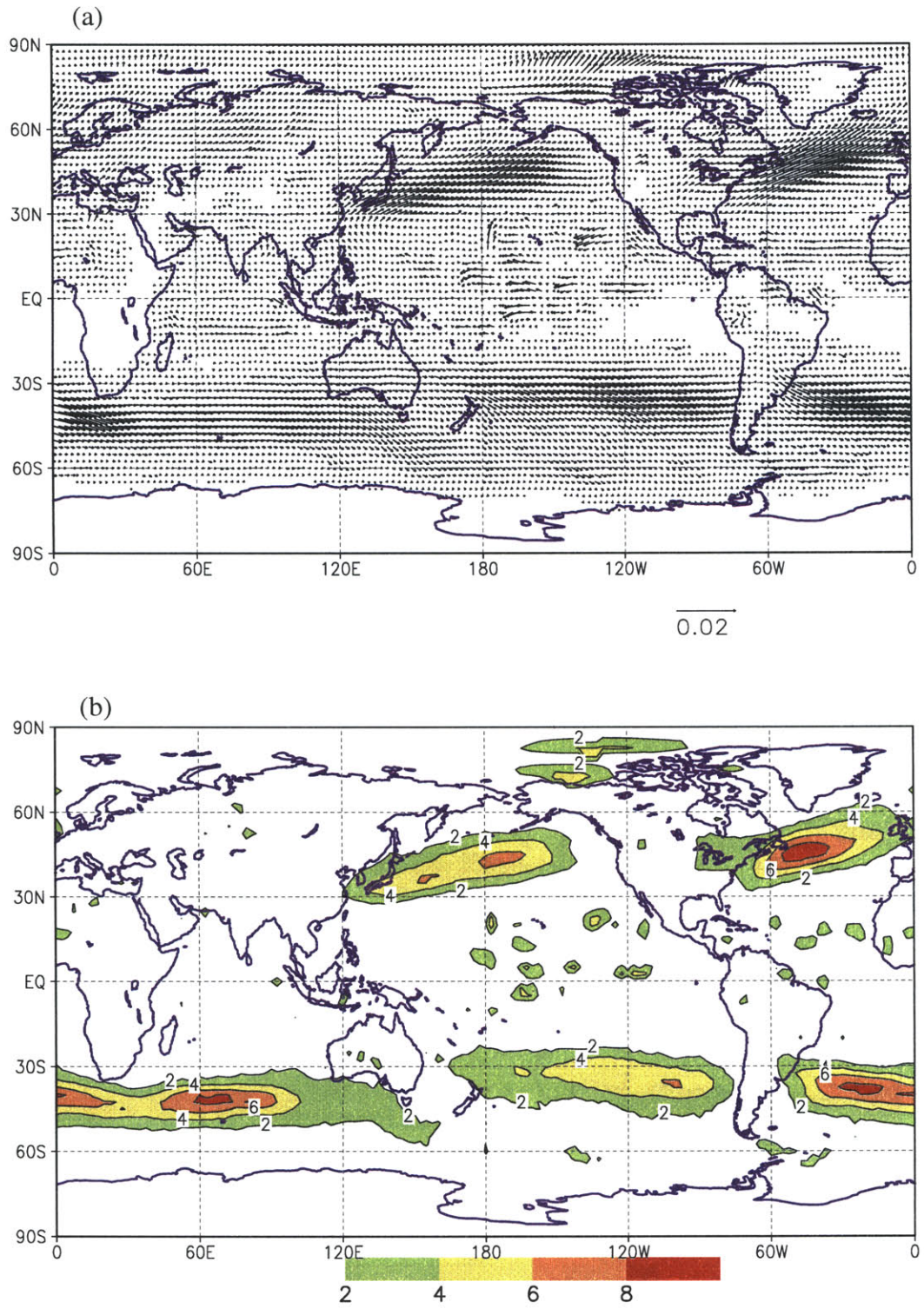

Figure 4.5: Same as Figure 4.3 except for NH summer (JJA).

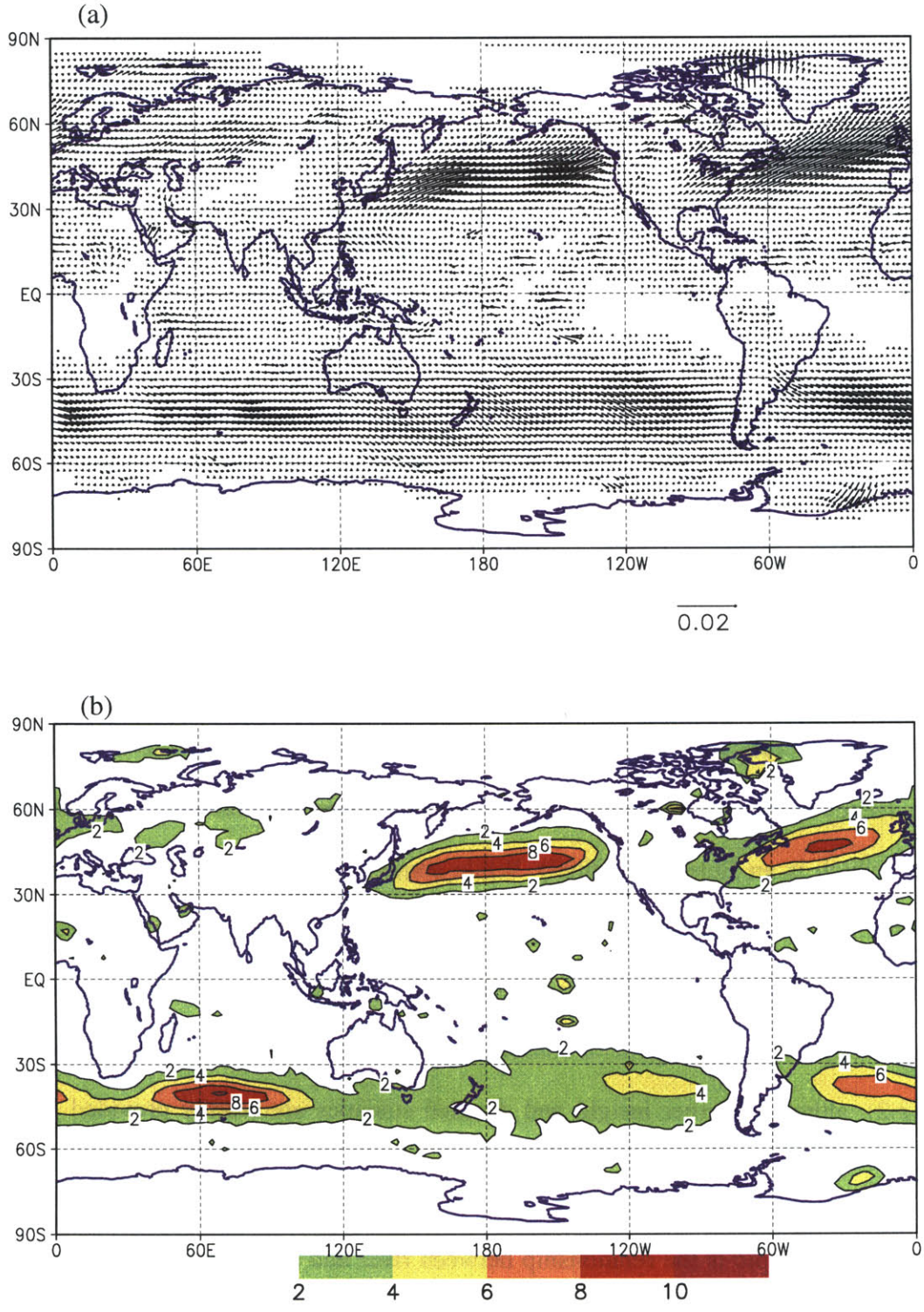

Figure 4.6: Same as Figure 4.3 except for NH autumn (SON)

follow a ENE to NE direction and penetrate well into the Arctic Ocean for all seasons. Again the southwest end of the magnitudes of dominant fluxes is located closer to the North American continent with a pronounced northward shift into the Great Lakes region during summer and autumn that is similar to the patterns of TR density.

In the SH, there is a fairly general east to east-southeast movement of TRs throughout mid-latitudes, with maximum concentrations in the three south oceanic basins. In comparison to the NH, the patterns of movement of TRs in the SH appear to have less longitudinal structure. A noteworthy regional feature of the track flux is the strong channelling of TR paths emanating from South America into the South Atlantic for all seasons.

The similarity between the patterns of TR density and those of TR track flux suggests that the TRs are migratory in character, although it should be stressed that the alignment of frequency ridges is not necessarily the same as the average direction of movement of TRs. Newell and Zhu (1994) obtained a morphology of TRs by examining the amplitude of high frequency filtered vapor flux components from a one-year record using harmonic analysis (which is an Eulerian method). While some disagreement exists between their results and ours on the extent and locality, it is encouraging to see that our patterns of TR frequency and track flux, derived from a totally different method (which is based on a Lagrangian approach), are in general consensus with their high frequency maps (shown in Figure 2.2), although further insight and detailed statistics are readily provided by our scheme.

An interesting topic is the relationship between river and cyclone activity since it has been recognized for a long time that many covariance quantities such as the moisture, transient eddy temperature, and vertical and horizontal momentum fluxes exhibit a strong "storm track" signature (Wallace et al. 1988; Trenberth 1991). There have been many

studies of the synoptic climatology of storms, fronts, cyclone and anticyclone tracks, and "storm tracks" (Petterssen 1956; Whittaker and Horn 1984; Wallace et al. 1988; Gyakum et al. 1989; Trenberth 1991; Jones and Simmonds 1994; Sinclair 1997). The latter term is often defined by the regions of maximum variance of geopotential height in the middle and upper troposphere arising from disturbances with periods less than about a week. The classical compilation of cyclone frequency and primary tracks followed by extratropical cyclones within the NH is that by Whittaker and Horn (1984) for the four mid-season months. Their cyclone frequency maps (Figure 2a through 5a in their paper) have the primary storm tracks extending from the east coasts of Asia and North America across the Pacific and Atlantic oceans respectively, in essentially the same positions as the TR high densities and track fluxes. There is also a fairly consistent poleward displacement during the warmer months for the two different synoptic phenomena. However, Gyakum et al. (1989) found the highest cyclone frequencies between 50° and 65°N during the cold seasons that lie just to the north of strong TR activities. In the SH, storm track activity is remarkably persistent throughout the year in both location and intensity as noted by Trenberth (1991). He found that storm tracks remain near 50°S year around and is strongest in the southern Indian Ocean and weakest in the South Pacific. The former could be linked to the TR coming out of Africa, or further upstream, to the strong TR activity out of South America as mentioned earlier. James and Anderson (1984) have shown that the trade wind easterlies, deflected by the Andes into the prevailing northwesterly winds over central South America, may constitute a source of moisture which could be entrained in the mid-latitude westerly flow. The high TR track fluxes there suggest that TRs may encourage the growth of baroclinic waves over the South Atlantic, with downstream effects on high frequency transient activity over the southern Indian Ocean. A similar but less persistent mechanism was postulated over the central Pacific Ocean. In summary, it is clear that TRs

are fundamentally associated with or acting as energy pipelines to cyclone activity in higher latitudes.

Figures 4.7 through 4.10 display the velocity vectors (computed as the weighted average of the velocity of all TRs passing near a data grid point) and vector magnitude isopleths for the four seasons. In general TRs travel in an easterly direction with a weak poleward meridional component that increases with latitudes in both hemispheres. It is of interest that the orientation of the migration vectors is similar to those of the track fluxes, but the patterns of their magnitudes are different. In the North Pacific during DJF (Figure 4.7), large velocities (over 18 m s^{-1}) were recorded from east of Japan eastward to near 170°W between 30° and 45°N, and to the north of 60°N near the Bering Strait. It appears that TRs decelerate when translating eastward after crossing the dateline and northward near 45°N, but may accelerate when moving further poleward after crossing 60°N, if they can still be identified then. On the other hand, TRs move across the North Atlantic at relatively smaller and more uniform speeds (~ 15 m s^{-1}). Some may accelerate over the eastern Europe or to the north of 70°N between Greenland and Scandinavia, though such events are rare since no significant system density occurred there (see Figure 4.2a). The seasonality of the average TR velocity displays a degree of complexity. In general the mid-latitudes show greatest migration velocities during the winter with an increase of typically 3 to 6 m s^{-1} over the North Atlantic and 3 to 9 m s^{-1} (from east to west) over the North Pacific when compared to summer.

In the SH, the average TR migration velocity shows zonality with velocities increasing poleward with latitudes. While the movement of TRs is dominated by a strong zonal signature, conspicuous areas of large mean velocities (over 18 m s^{-1}) are observed in the western South Atlantic, Indian Ocean, and in high latitudes over the South Pacific during

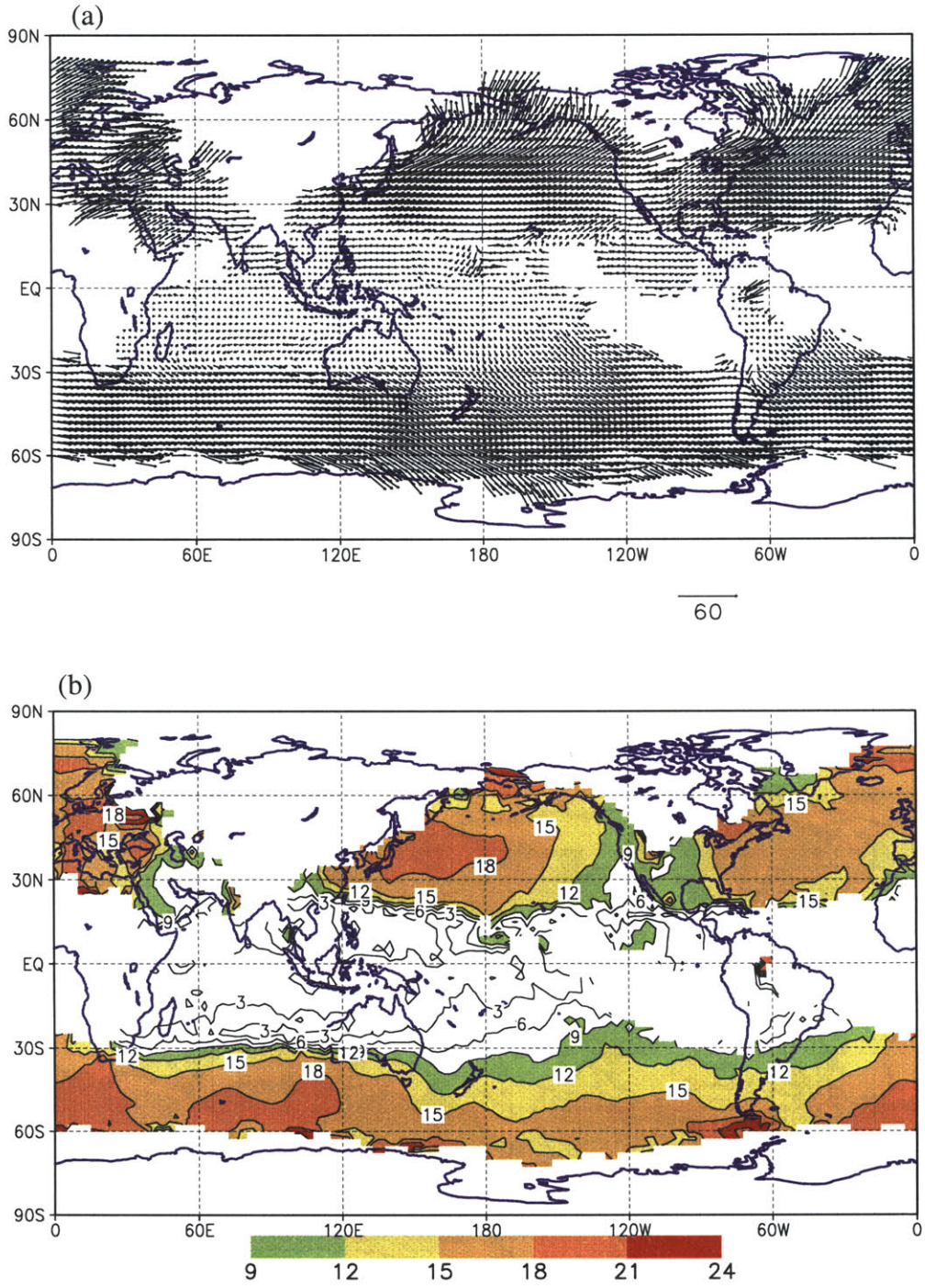

Figure 4.7: TR statistics for NH winter (DJF), for the years 1958 - 2000. (a) Average TR translation vectors. The vector at the bottom represents 60 m s^{-1}. (b) Magnitude of the TR moving speed (unit: m s^{-1}) drawn every 3 m s^{-1} with values greater than 9 m s^{-1} color shaded.

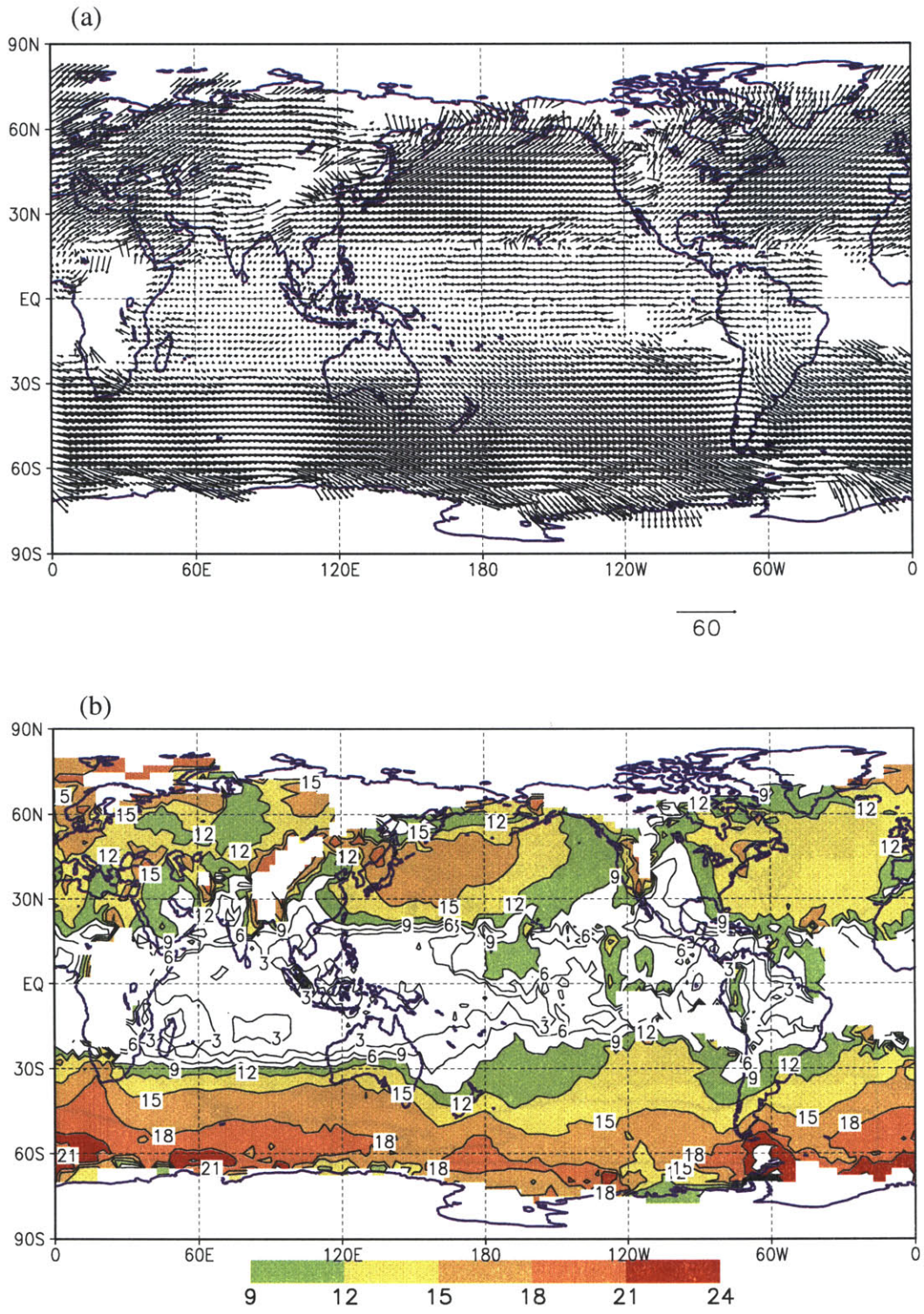

Figure 4.8: Same as Figure 4.7 except for NH spring (MAM).

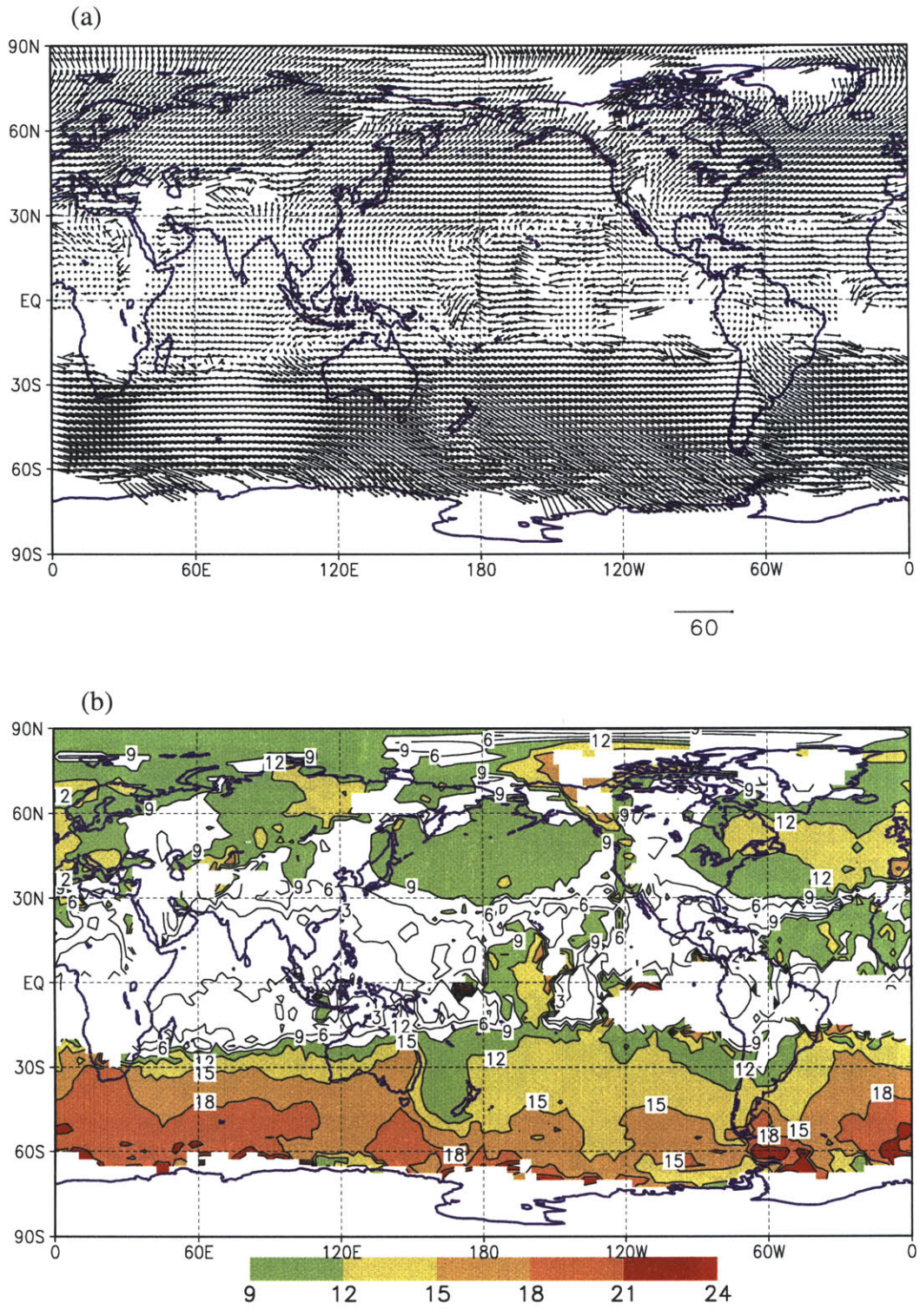

Figure 4.9: Same as Figure 4.7 except for NH summer (JJA).

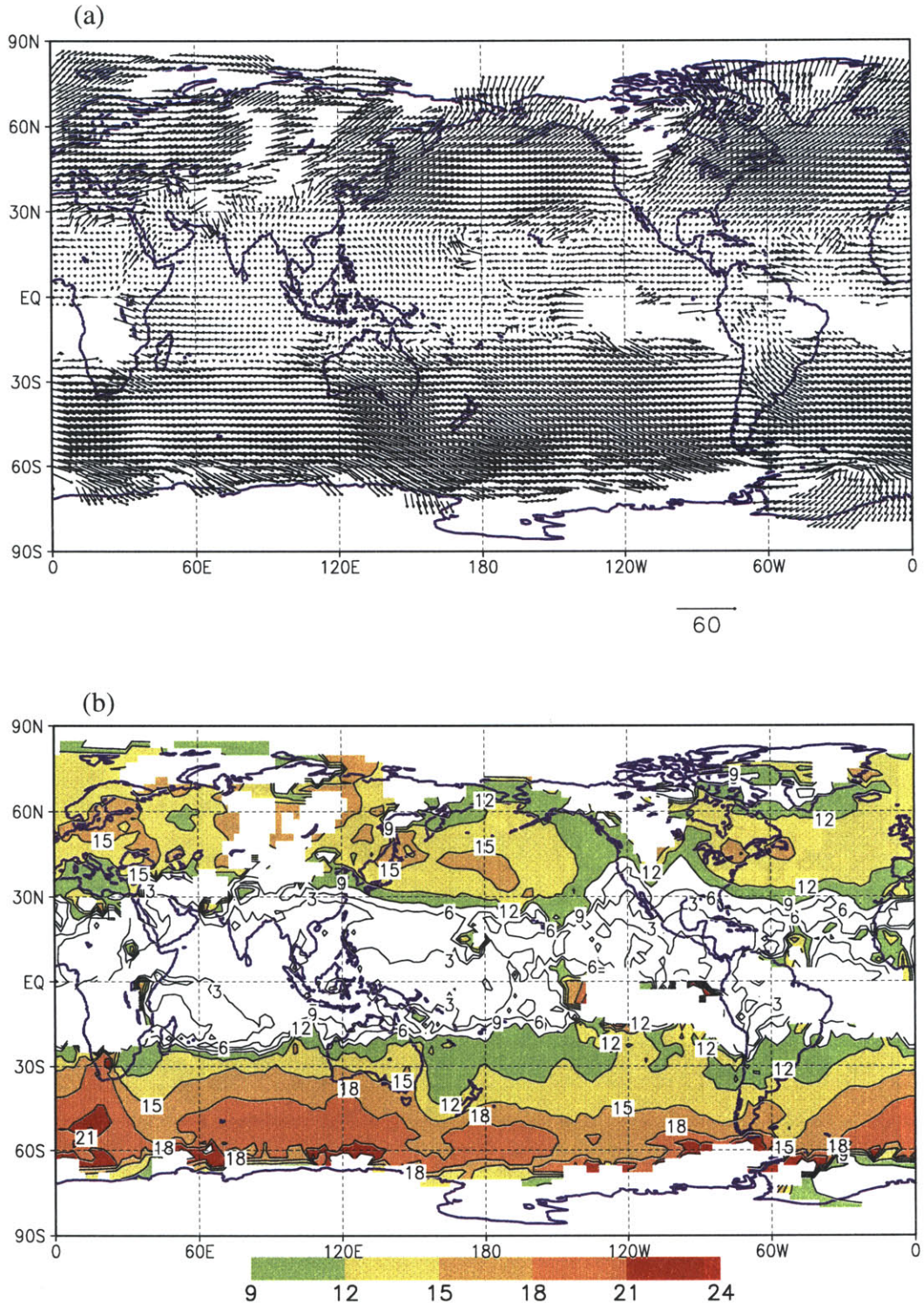

Figure 4.10: Same as Figure 4.7 except for NH autumn (SON).

all seasons. In midlatitudes over the South Pacific, the smaller velocities (compared to those in the other two ocean basins) combined with relatively small system densities and track fluxes indicate a slow migration of TRs over there, which is consistent with the results of Leighton (1992, 1994) who found generally enhanced levels of anticyclone immobility throughout the South Pacific indicating the frequent nature of blocking episodes in the region. In the southern Indian and South Atlantic Oceans, there is little evidence for blocking activity, the mean TR velocity isopleths and the previously displayed track flux suggesting generally progressive motion. The seasonality is less pronounced for the SH, though a slight latitudinal shift of maximum mean velocity zones is discernible.

It should be pointed out that the general TR translation velocity of ~ 6 m s^{-1} obtained manually by Newell et al. (1992) appears to be largely underestimated. Larger analysis time intervals, small sampling, different methodology and data set in that study may have resulted in this difference.

4.2.3 TR Genesis and Termination

The seasonal distribution of the area normalized temporal frequency of TR genesis is displayed in Figure 4.11.

In the NH, favored genesis areas include the warm waters over the Kuroshio Current and Gulf Stream for all seasons. TR occurs mostly over oceanic regions but some may develop over land such as over the southeast Asia during MAM and JJA, as well as over the eastern North America. Other formation regions with values in excess of 0.4×10^{-3}

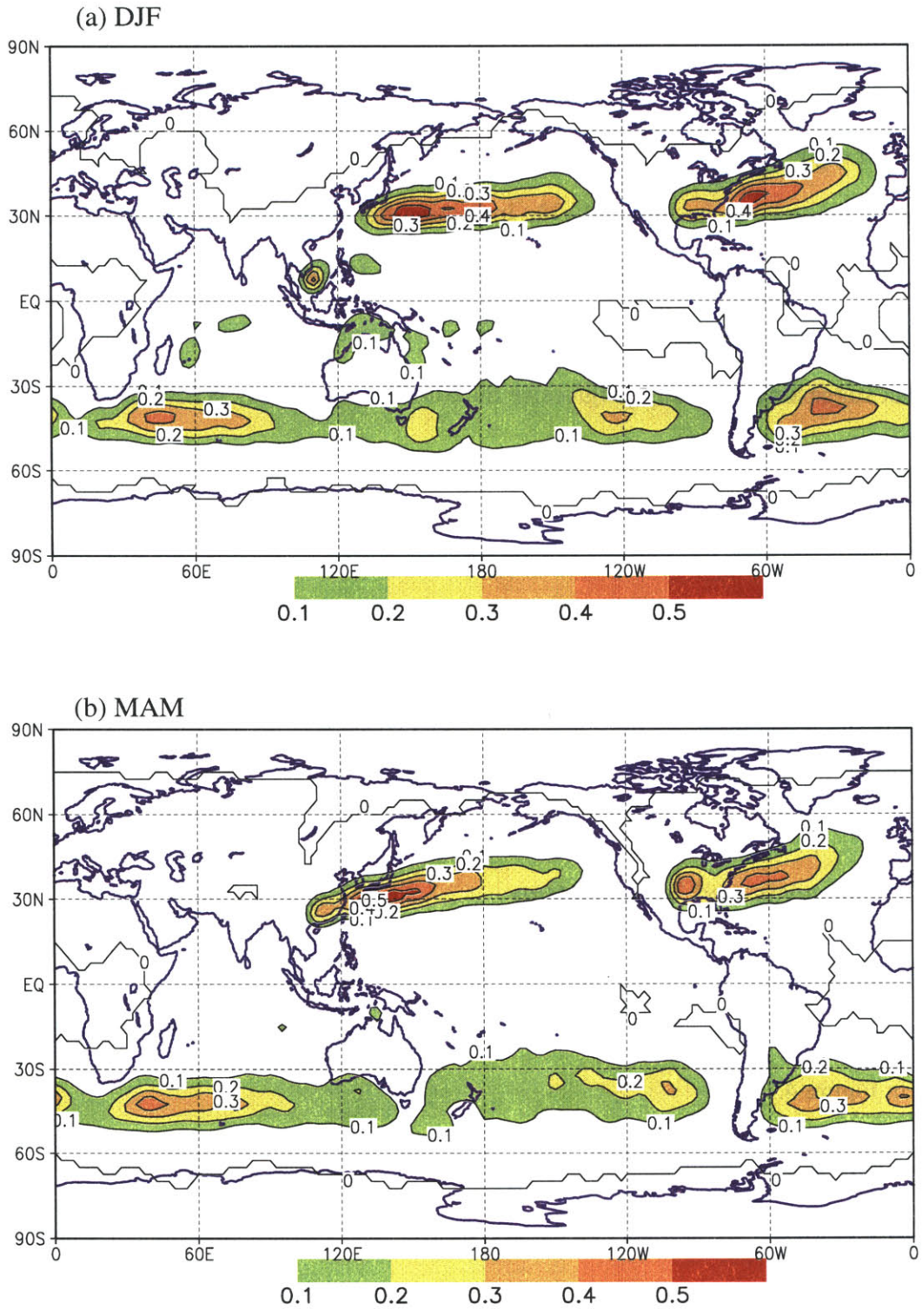

Figure 4.11: TR genesis density in (a) DJF, (b) MAM, (c) JJA, and (d) SON. The unit is 10^{-3} TRs (°latitude)$^{-2}$ day^{-1}. The contour interval is 0.1×10^{-3} TRs (°latitude)$^{-2}$ day^{-1}. Values greater than 0.1×10^{-3} are color shaded.

(c) JJA

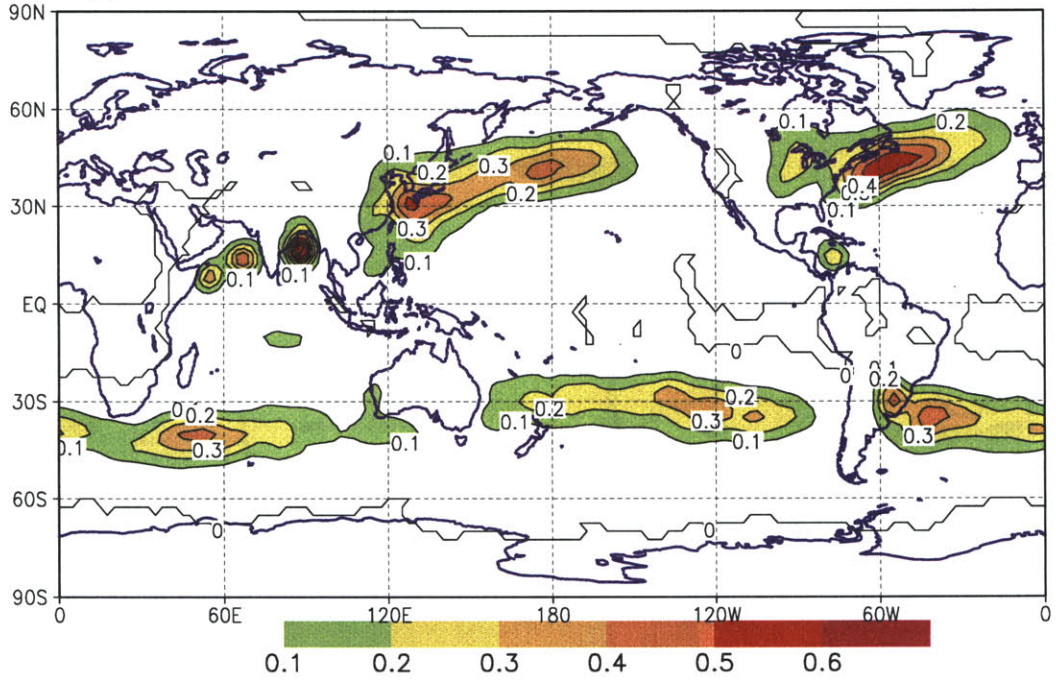

(d) SON

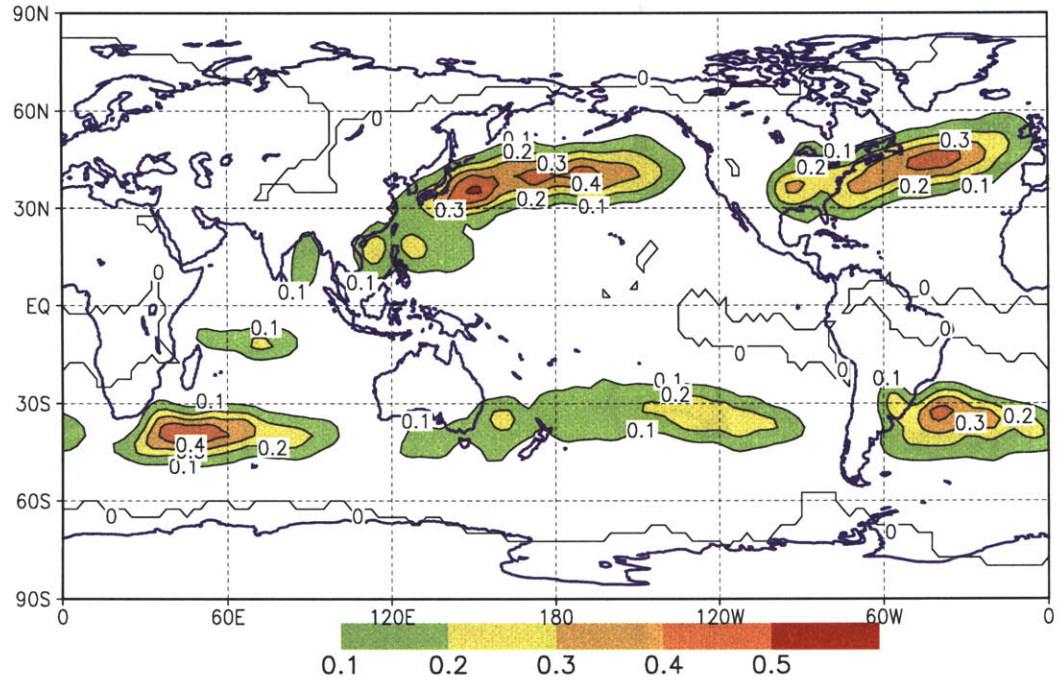

Figure 4.11: (*Continued*)

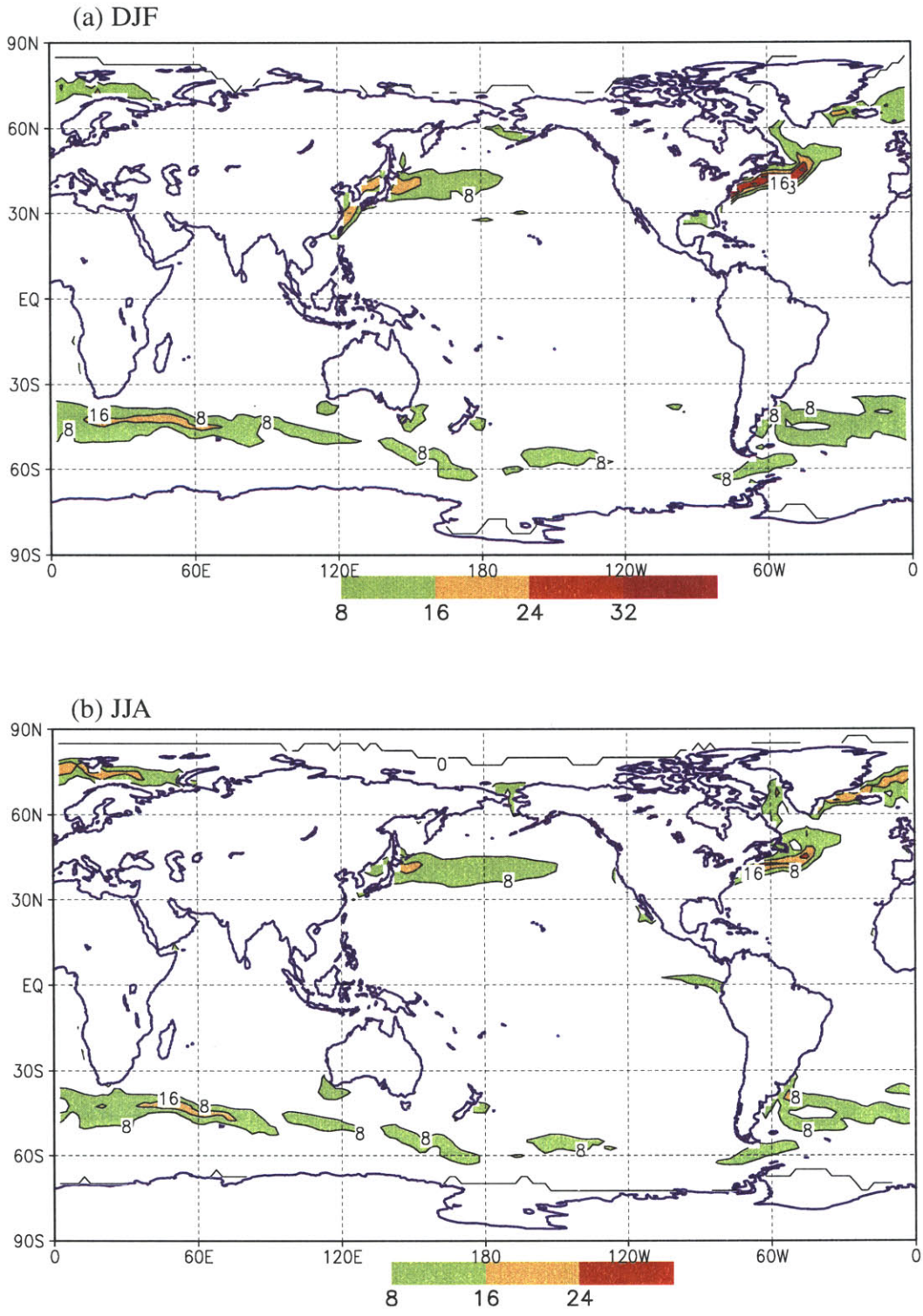

Figure 4.12: NECP OI SST gradient maxima for (a) DJF and (b) JJA. The unit is °C (1000 km)$^{-1}$. The contour interval is 8°C (1000 km)$^{-1}$. Values exceeding 8°C (1000 km)$^{-1}$ color shaded.

TRs (°latitude)$^{-2}$ day^{-1} are found to the north of the Gulf of Mexico for all seasons (highest during northern spring), the Bay of Bengal and the Arabian Sea in JJA, southern Indochina peninsula in DJF, and near the dateline in JJA and SON. It appears that the two elongated maximum TR genetic zones in the two oceanic sectors lie on the equatorward flank of the mean SST gradient maxima near the eastern seaboards of Asia and North America during winter (Figure 4.12a) and spring (figure not shown but similar to 4.12a), and nearly collocated with the latter during summer (Figure 4.12b) and autumn (figure not shown but similar to 4.12b). SST gradients are calculated from the NCEP Optimal Interpolation SST data set (see data descriptions in Chapter 2 section 2.3) for the period of January 1982 through August 2000. This result is consistent with the cyclogenesis pattern of Whittaker and Horn (1984) and Roebber (1984) who have noted that the regions of strong SST gradients are conducive in a climatological sense to the development of maritime cyclones.

In the SH, TR genesis is most prevalent in a band extending from the southeast coast of South America into the Atlantic, across the Indian Ocean (maximized near the southern African extreme), and throughout much of the middle latitudes of the Pacific sector (with maxima near 120°W). The corresponding genesis regions are also found to be adjacent to (or slightly equatorward of) the maximum SST gradients in these regions.

The distribution of TR termination shown in Figure 4.13, when taken in conjunction with the corresponding TR genesis maps (Figure 4.11), indicates that a significant proportion of the TRs born over lower latitudes of western oceanic sectors are mobile and move eastward/poleward before dissipating over the higher latitudes of eastern oceanic basins (more obvious in the North Pacific than in the North Atlantic). There is little TR termination activity over the warm Kuroshio Current region except in summer and autumn when tropical cyclones which bring abundant water vapor from the tropics and dump it along

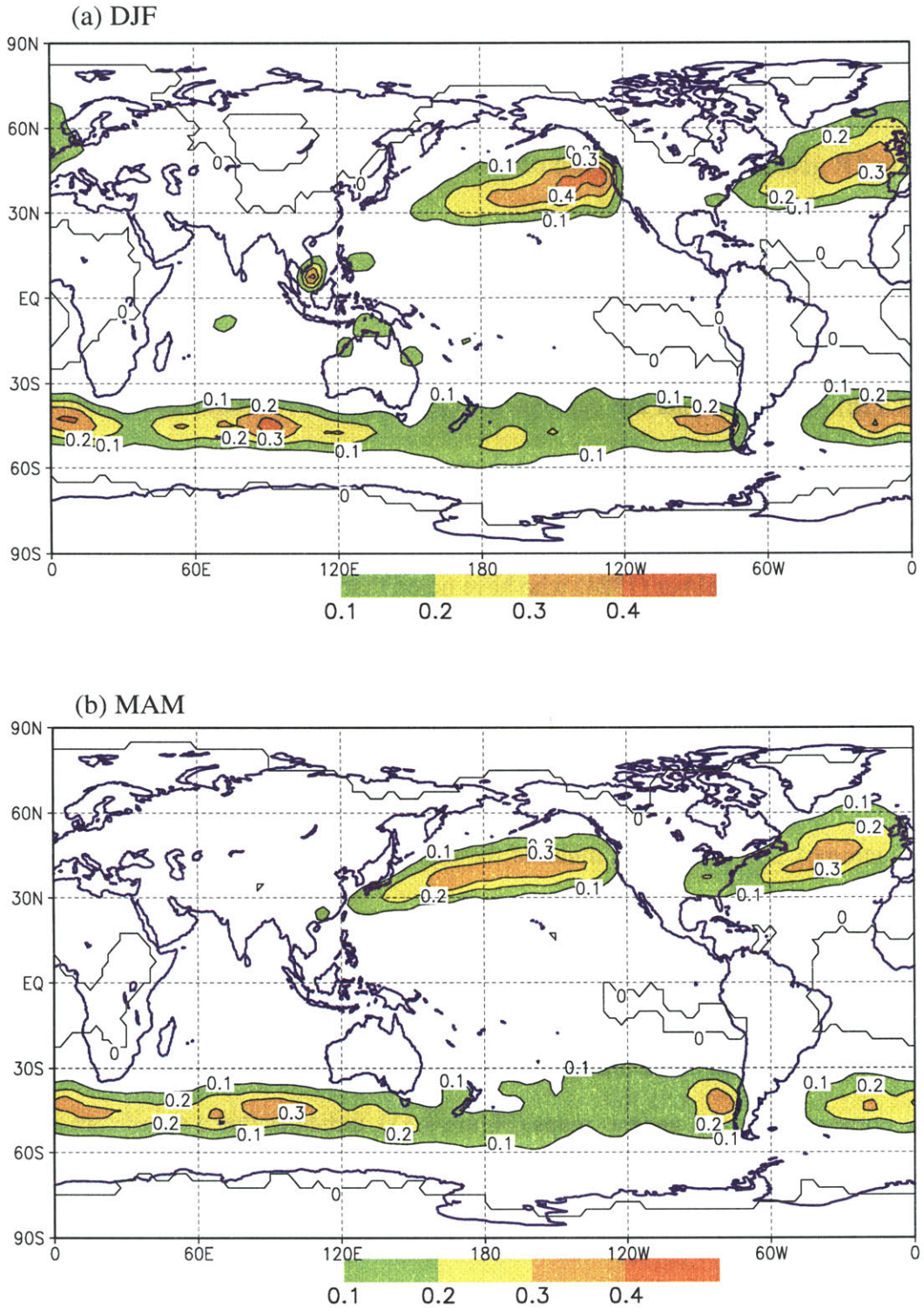

Figure 4.13: TR termination density in (a) DJF, (b) MAM, (c) JJA, and (d) SON. The unit is 10^{-3} TRs (°latitude)$^{-2}$ day^{-1}. The contour interval is 0.1×10^{-3} TRs (°latitude)$^{-2}$ day^{-1}. Values greater than 0.1×10^{-3} are color shaded.

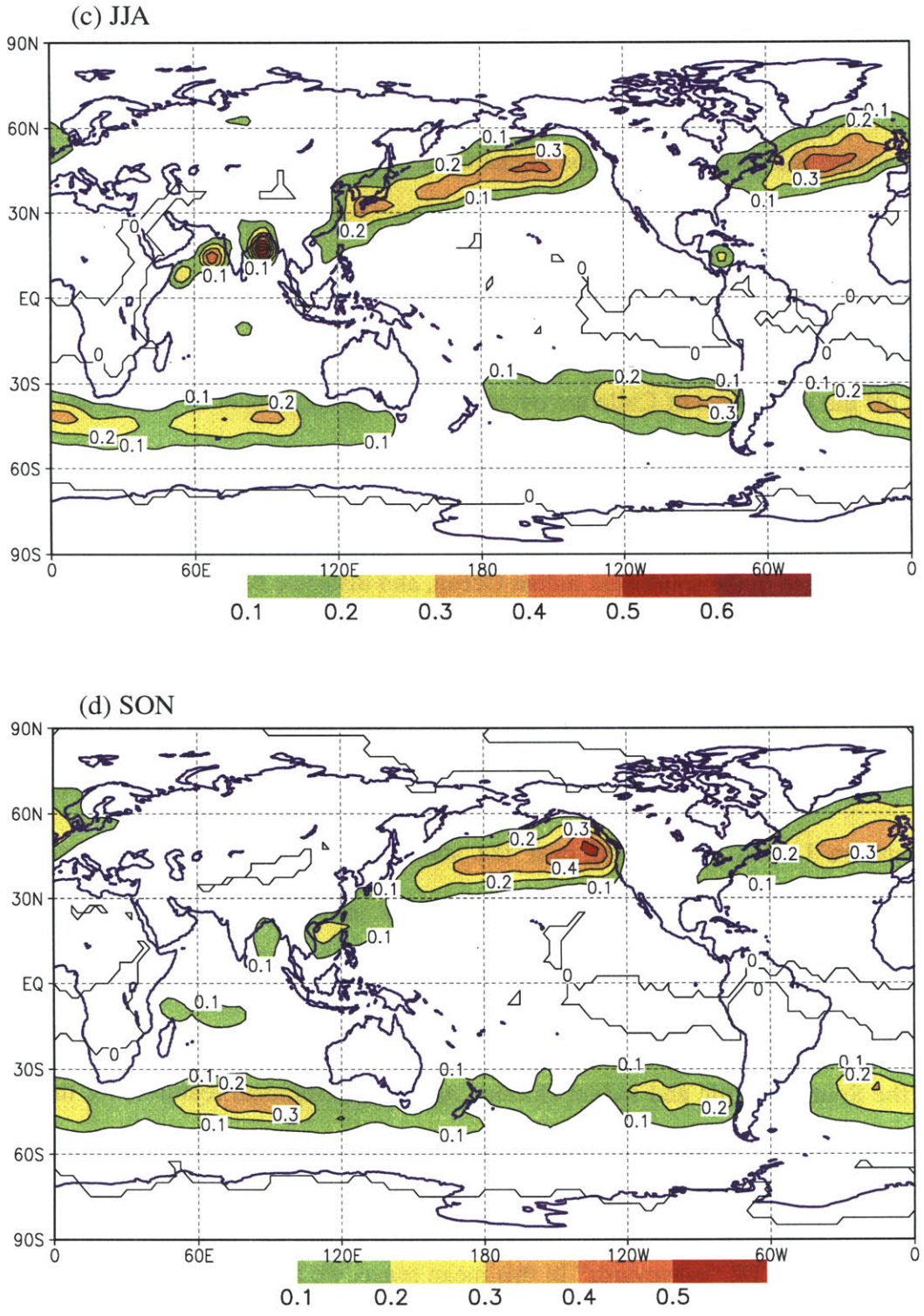

Figure 4.13: (*Continued*)

their courses die to the south and east of Japan. The Bay of Bengal and the Arabian Sea are also favored regions for TRs to end their tracks during northern summer (Figure 4.13c), and these are also areas of highest genesis (Figure 4.11c), suggesting that water vapor transport is a local phenomenon in character there that is related to the South Asian monsoon during this particular season. Similarly, the local maxima over northern Australia and the southern Indochina Peninsula during DJF bears the same signature. The weak dissipation activity off the east coast of Argentina and the large number of TRs terminating just off the west coast of Chile are evidence of a blocking effect by the Andes and of different TR origins over the Pacific and Atlantic in the SH. On the other hand, TRs originating over South America or in the Atlantic may travel through the southern Africa or to its south, reinforce in the southwest Indian Ocean, and dissipate further downstream.

The difference between the genesis and termination rates shown in Figure 4.14 exhibits a revealing picture of the relationship between the two statistics. The excess of genesis over termination near the eastern seaboards of Asia, North America, and South America, over southern United States, and over the southwest Indian Ocean is evident with enhanced levels during all other seasons but DJF. TR termination exceeds generation in the Gulf of Alaska that is also enhanced during the same seasons. Such regions can also be found over the northeast Atlantic, off the west coast of Chile, and over the southeast sectors of the South Atlantic and Indian Oceans. Aside from regional features, for the most part genesis exceeds termination south (north) of about 45°N (45°S) in the NH (SH), while the converse is true north (south) of this latitude. We stress, however, that while the higher latitudes are TR "graveyards" in this mean sense, we have seen that there are non-negligible levels of TR genesis in these regions.

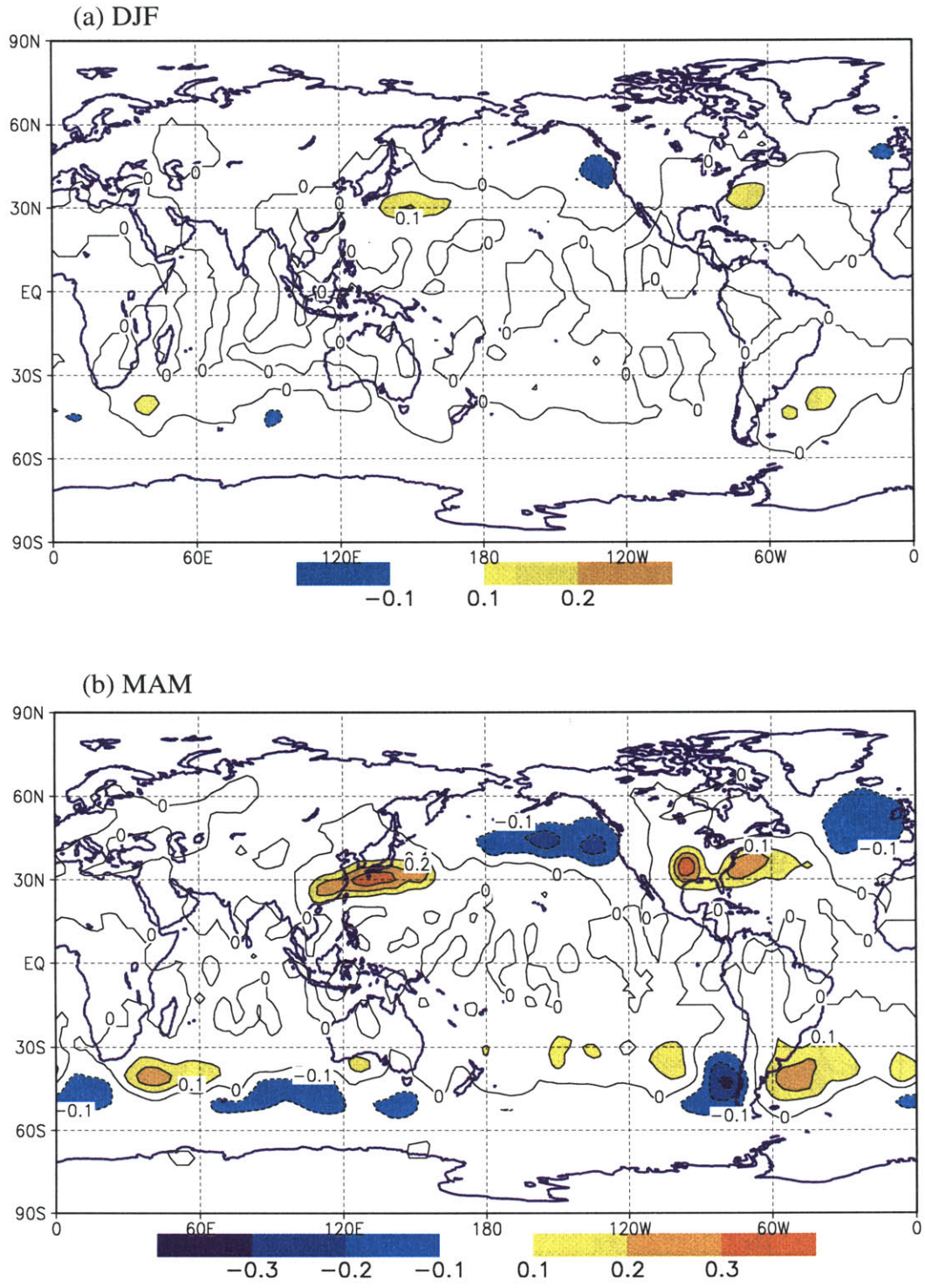

Figure 4.14: Difference between TR genesis and termination densities in (a) DJF, (b) MAM, (c) JJA, and (d) SON. The unit is 10^{-3} TRs (°latitude)$^{-2}$ day^{-1}. The contour interval is 0.1×10^{-3} TRs (°latitude)$^{-2}$ day^{-1}. Values greater than 0.1×10^{-3} or less than - 0.1×10^{-3} are color shaded.

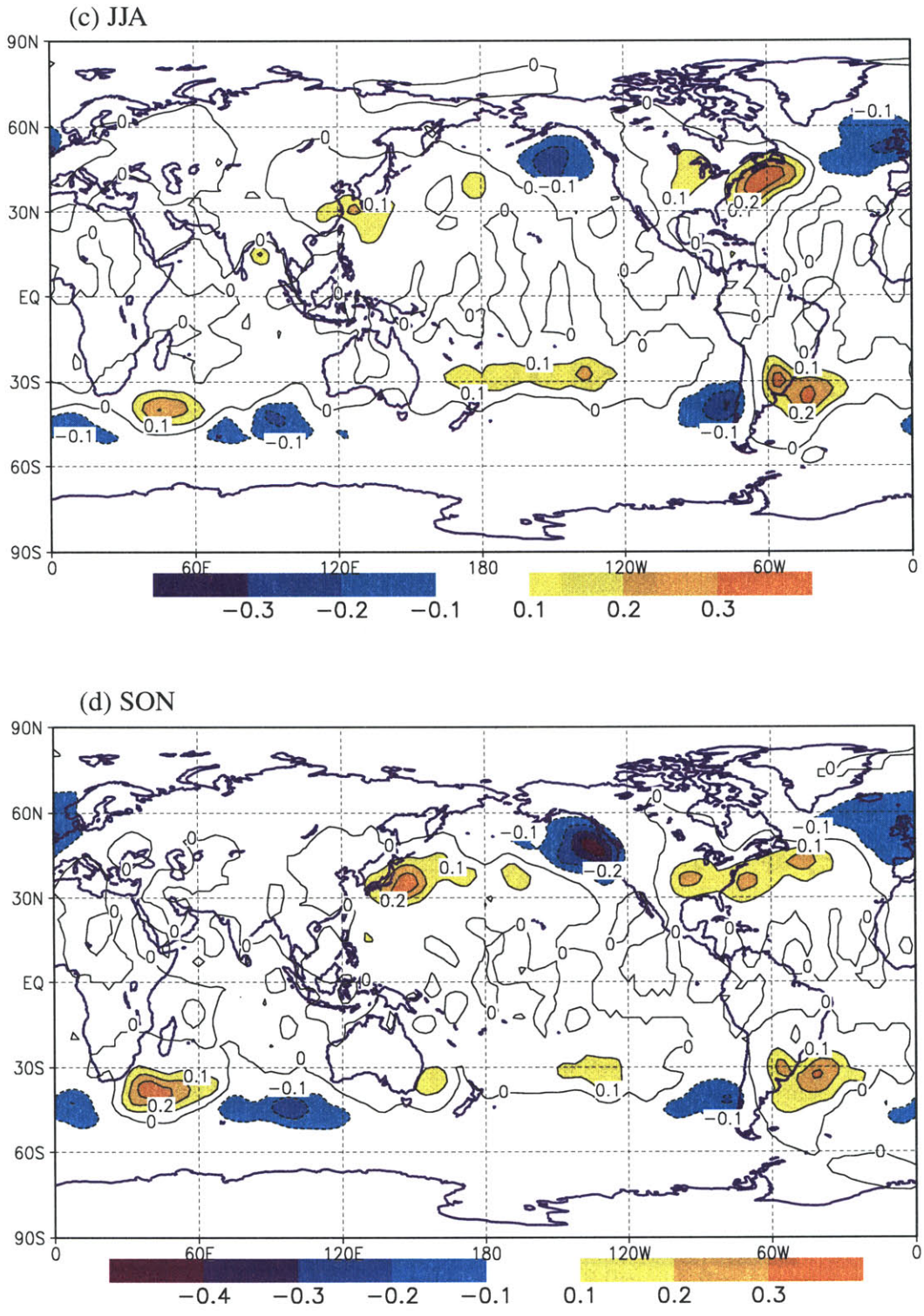

Figure 4.14: (*Continued*)

It is of interest to compare the patterns of TR genesis and termination to those of cyclogenesis and cyclolysis compiled by other studies (e.g., Sinclair 1997, Simmonds and Keay 2000). These cyclogenesis and cyclolysis compilations are only available for the winter and summer seasons. In general, both TR genesis and termination maxima tend to be near the upstream equatorward flank of those of cyclogenesis and lysis except for cyclogenesis maxima occurring in the lee of major mountain ranges and over land due to the thermal effect. We suggest that TR formation and termination could be a leading predictor for the occurrence and decay of extratropical cyclones. For example, if a TR associated with a cyclone terminates over the southeast Indian Ocean near 50°S in austral winter and spring, the cyclone can not sustain itself poleward of 60°S (where cyclolysis is overwhelmingly found), a region largely covered with sea ice. Further case studies are needed in this regard.

4.2.4 TR Axis Length, Lifespan, and Track Length

TR axis length is calculated by adding up the segments of distance between neighboring TRCs within a TR. In general, a real TR's head and tail should be further apart than those endpoint-TRCs obtained by our method. In other words, the TR axis lengths computed here are always underestimated. Establishing a relationship between TR axis length and its intensity has not been attempted largely because we have no quantitative clues for the attenuation of water vapor fluxes near the head and tail and the situation could be even more complicated during the lifespan of a TR and over different geographic locations (the same can be said to the width of a TR). Although caution must be exercised in interpreting the results, the quantity is more or less a reflection of TR strength since the moisture fluxes

associated with a TR are mostly aligned to the along-stream dimension. Table 4.3 gives the mean axis lengths of TR per analysis for various seasons and in different hemispheres.

Perhaps one general observation can be made safely: River axis lengths appear to be longer during the warmer season (JJA in the NH and DJF in the SH) and longer in the SH. The longest TR length is found in the NH summer time (2653.9 km). On average, the axis length of a TR is approximately 2284.0 km globally and annually.

Table 4.3: Mean TR axis lengths per analysis (km)

	DJF	MAM	JJA	SON	ANNUAL
NH	2179.2	2143.9	2653.9	2144.4	2280.4
SH	2429.2	2351.2	2284.9	2248.4	2328.4
Globe	2293.6	2228.4	2448.9	2165.0	2284.0

Another feature of TRs that is important for understanding their role in weather and climate is their lifespan. TRs are intimately tied up with the index cycle, which dictates their natural timescale (a discussion on the relationship between TRs and the ENSO index will be presented in Chapter 5 that deals with the variability of TR behavior). However, the variation of the Coriolis parameter, the location of the continents, the location of warm sea surface and SST gradients, and the location of baroclinic zones means that these timescales would be expected to vary accordingly.

Mean TR track durations (i.e., TR lifespans) of the 36,238 TRs that have been tracked for at least 24 hours during the 43-year period are listed for different seasons and hemi-

spheres in Table 4.4. The data are also stratified into latitude bands with 20° apart (a TR track is allocated to the latitude band in which it was located halfway through its life).

Table 4.4: Mean duration (in days) of TRs that have been tracked for at least 24 hours. A TR track is allocated to the latitude band in which it was located halfway through its life. The numbers in the parentheses are the standard deviations.

	DJF	MAM	JJA	SON
N.H.	2.00 (1.18)	2.07 (1.24)	1.93 (1.11)	2.12 (1.33)
S.H.	2.02 (1.22)	2.04 (1.20)	1.99 (1.12)	2.02 (1.16)
Globe	2.02 (1.20)	2.05 (1.22)	1.96 (1.12)	2.08 (1.26)
90°N - 70°N	1.09 (0.12)	1.41 (0.40)	1.62 (0.74)	1.44 (0.46)
70°N-50°N	1.58 (0.74)	1.55 (0.68)	1.71 (0.81)	1.70 (0.84)
50°N-30°N	2.06 (1.12)	2.22 (1.28)	2.03 (1.18)	2.19 (1.29)
30°N-10°N	2.07 (1.42)	1.98 (1.25)	1.99 (1.22)	2.27 (1.56)
10°N-10°S	2.00 (1.31)	1.94 (1.39)	1.78 (0.99)	2.03 (1.36)
10°S-30°S	2.21 (1.52)	2.14 (1.42)	2.16 (1.36)	2.18 (1.42)
30°S-50°S	1.98 (1.07)	2.06 (1.15)	2.01 (1.07)	2.03 (1.08)
50°S-70°S	1.64 (0.74)	1.66 (0.76)	1.46 (0.69)	1.52 (0.63)
70°S-90°S	0.0 (0)	0.0 (0)	0.0 (0)	1.00 (1)

The first three rows in Table 4.4 show for the four seasons the mean duration of all the TRs in the NH, SH, and Globe, respectively. The body of the table shows a breakdown of the durations into nine latitude bands, each 20° wide. This meridional distribution information is also plotted in Figure 4.15 as well. There is evidence that the lifespan of TRs does depend on latitude. It is seen that the TRs that are in the 10° – 50° latitude bands in both hemispheres have longer lifespans (~ 0.5 day) than those in the others with modest

seasonal variations but larger standard deviations (see Table 4.4). On a global average, TR duration displays a modest seasonality varying from 1.96 days in summer to 2.08 days in autumn.

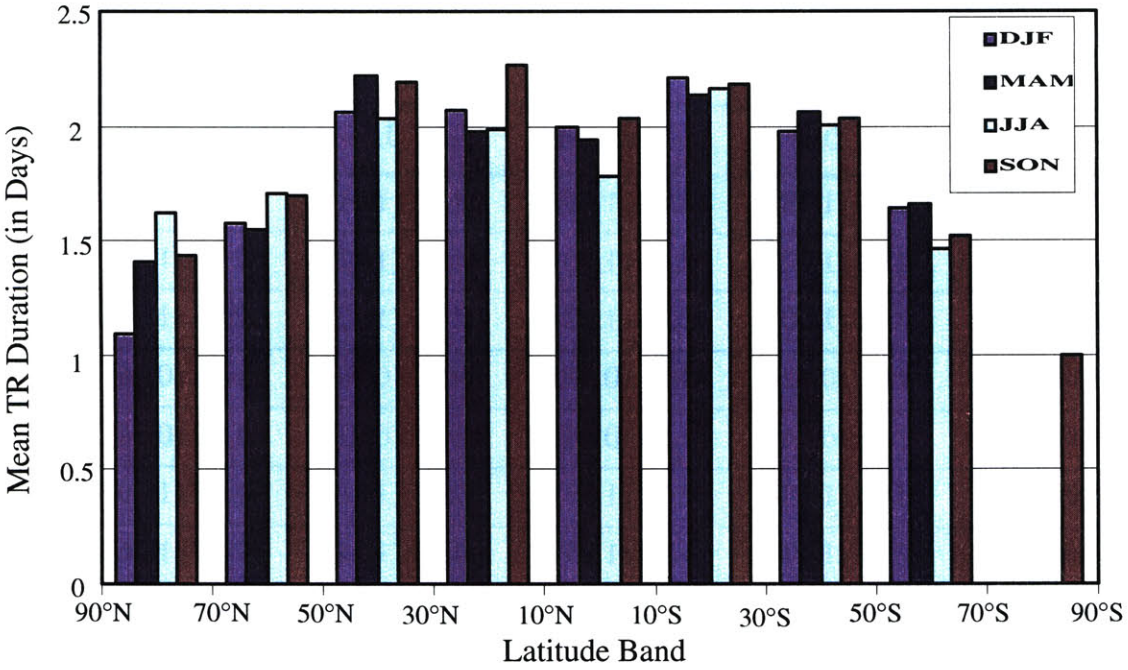

Figure 4.15: Zonal distribution (in latitude bands 20° apart) of mean durations (in days) of TRs with lifetime longer than 24 hours. A TR is allocated to the latitude band in which it was located halfway through its life.

When compared to the meridional distribution of TR counts shown in Figure 4.1, the longevity of TRs appears to be much less affected by the geographic locality.

Figure 4.16 shows a histogram of the distribution of all TR lifespans that have a lifetime of at least 24 hours for all seasons in the NH, SH, and Globe, respectively. For all three geographical averages, the distribution is strongly skewed and almost monotonically decreases with increased track duration (with over 65% of the TRs registered in less than 2

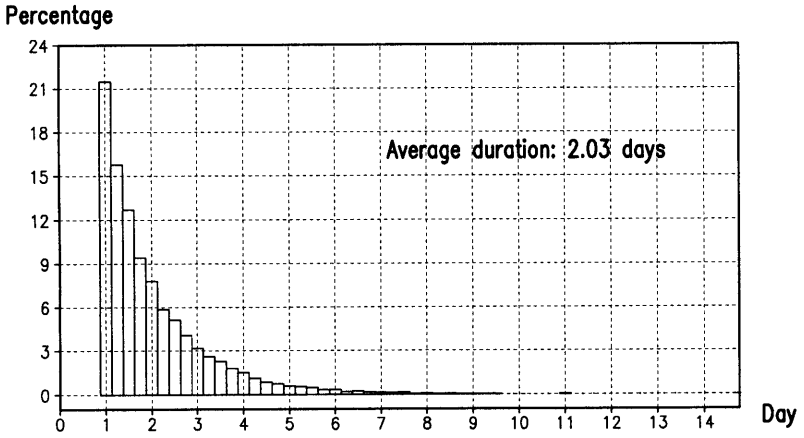

(a) Northern Hemisphere

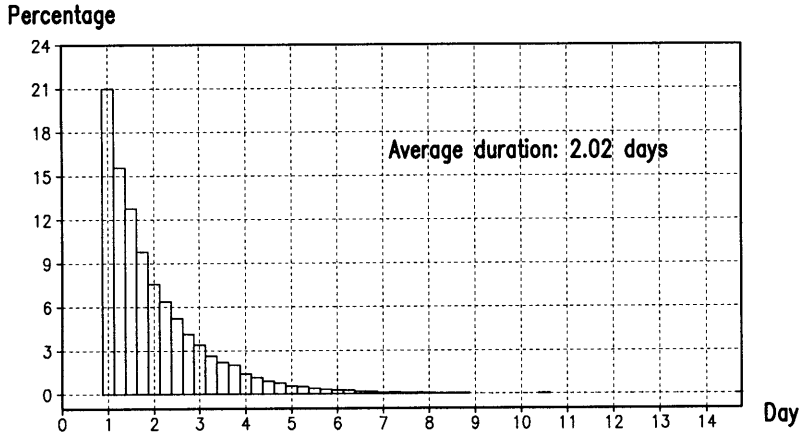

(b) Southern Hemisphere

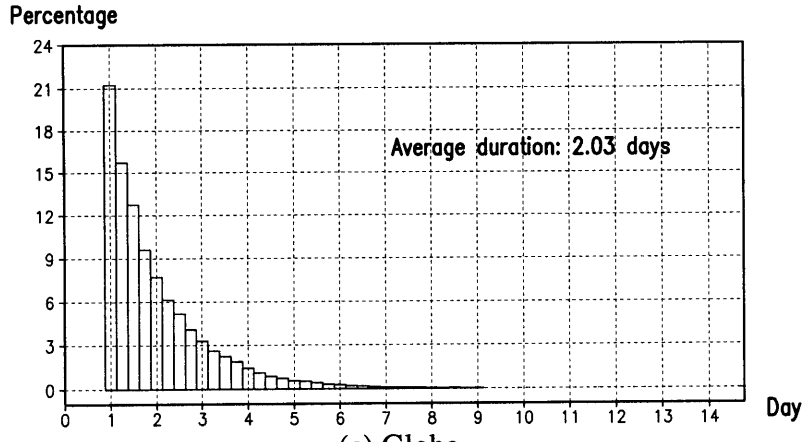

(c) Globe

Figure 4.16: Frequency distribution of TR duration with a lifetime of at least 24 h (binned in 6 hour intervals). (a) Northern Hemisphere, (b) Southern Hemisphere, and (c) Globe.

day periods and a much smaller number surviving one week or longer). This general structure is also reflected in the four separate seasons, as well as when the data are binned into latitude bands. The longest TR duration was ~ 14.50 days. The strong skewness towards short lifespan is consistent with the results from harmonic analysis by Newell and Zhu (1994) who found that the high frequency components (periods less than 3 days) are the dominant modes of rivers.

The average TR duration is a little over 2 days in either hemisphere. At first glance, this number seems being largely underestimated when compared to that from subjective observations (~ 10 days as estimated by Newell et al. 1992). One should alert that there is always a propensity to overestimate a TR's lifespan using manual analysis (depending how a TR is subjectively defined). On the other hand, a tendency of underestimation is also obvious in our scheme since the TR genesis (termination) point is defined as the first (last) TRMC which, according to its definition, must attain certain strength. The large standard deviations showed in Table 4.4 suggest that there could be an exaggeration of the difference for the lifespans obtained from the two methods. Nevertheless, the TR duration derived here seems to be reasonable when contrasted to that of a typical cyclone, which is about 3 days according to Simmond and Keay (2000a). The relationship of the time frames between TRs and cyclones is an interesting topic which needs more case studies. For example, Zhu and Newell (1994) made such an effort and have shown an example of a case where the low pressure center moved over to the leading edge of a river 12 hours earlier.

Another TR property that deserves attention is the distance it travels during its lifetime, i.e., TR track length (computed by connecting the 6-hourly tracking positions between the TR genesis and termination points). Figure 4.17 shows the frequency distribution of TR

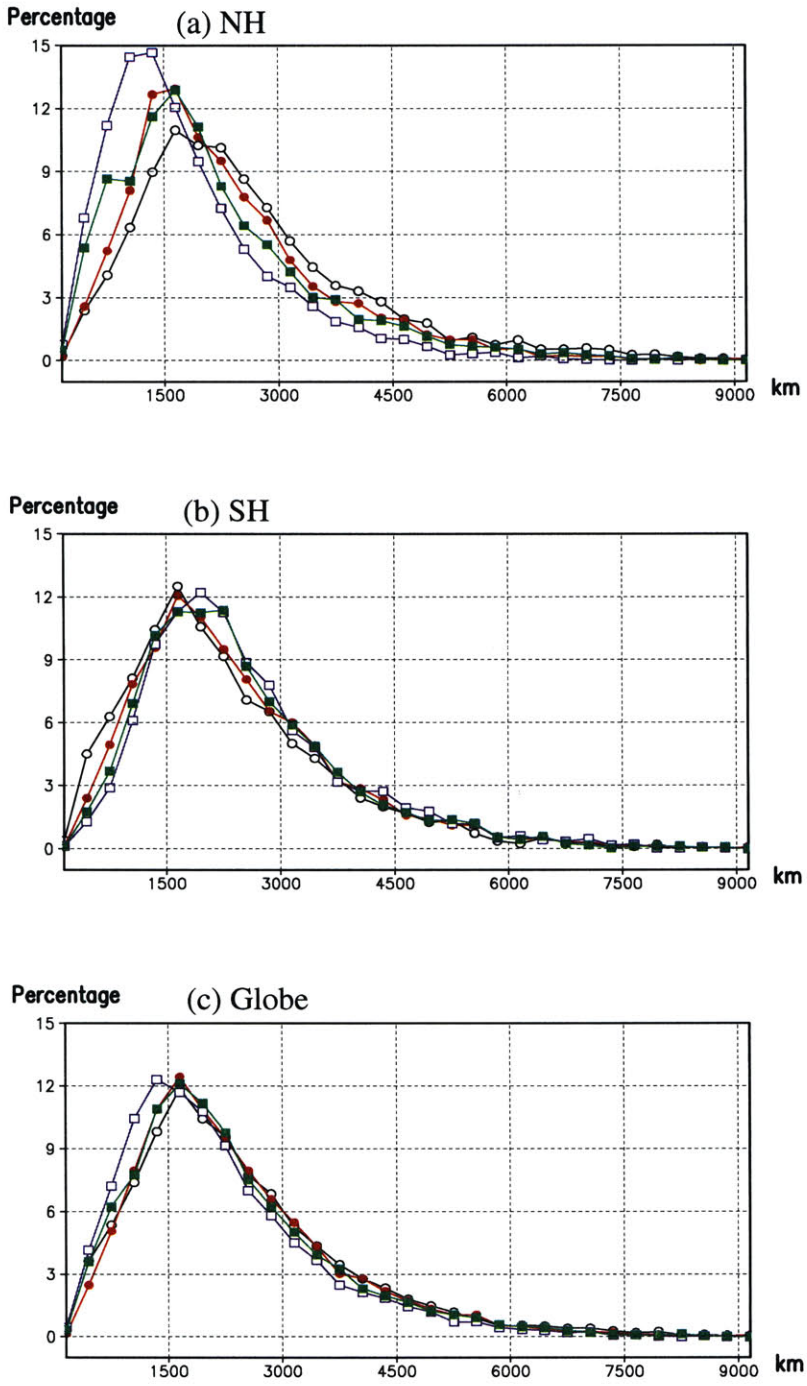

Figure 4.17: Frequency distribution of TR track length (binned every 300 km) for (a) NH, (b) SH, and (c) Globe. Legends: DJF (black open circle), MAM (red solid circle), JJA (blue open square), and SON (green solid square).

track length binned in every 300 km for all seasons and in the NH, SH, and Globe, respectively. Table 4.5 gives the mean length of a TR track and its number. On average, about 10% of all TRs travel less than 900 km and approximately 65% travel between 900 and 3000 km. The plots exhibit a steady decay in frequency at the longer translation distances, but a significant proportion of the systems travel in excess of 3000 km (~25%). Significant seasonality can be found for both the track length and its number in the NH. Although TR track number reaches its peak during the warmer seasons, large portions of TR track lengths are strongly biased towards shorter translation distances compared to those during the colder seasons. The shortest mean track length occurs in summer (1822.9 km), while the longest is found in winter (2623.5 km). The same signature is retained in the SH though less pronounced.

Table 4.5: Mean TR track lengths (km) and numbers (in parentheses)

	DJF	MAM	JJA	SON	ANNUAL
NH	2623.5 (3694)	2334.6 (3615)	1822.9 (4755)	2174.9 (4455)	2239.0 (16519)
SH	2304.4 (5193)	2455.3 (5019)	2557.9 (4382)	2491.4 (4190)	2452.3 (18784)
Globe	2436.9 (8887)	2404.7 (8634)	2175.4 (9137)	2328.2 (8645)	2336.3 (35303)

An interesting TR behavior emerges when taken into consideration of the TR axis length discussed earlier: warmer seasons host a larger number of TRs and TR tracks, with shorter translation distances (not necessarily shorter lives) but longer TR axis lengths. It suggests that a slow moving TR may enhance the chance for establishing a more coherent filamentary structure.

4.3 Meridional Profiles

In this section we explore the zonal averages of a variety of TR statistics. The description of the distribution and behavior of TRs by zonal averages is of considerable diagnostic value. In addition such averaging may highlight features which may not be clearly evident in the geographical figures.

4.3.1 TR Density

The zonally averaged TR densities are shown in Figure 4.18. One observes a sharply

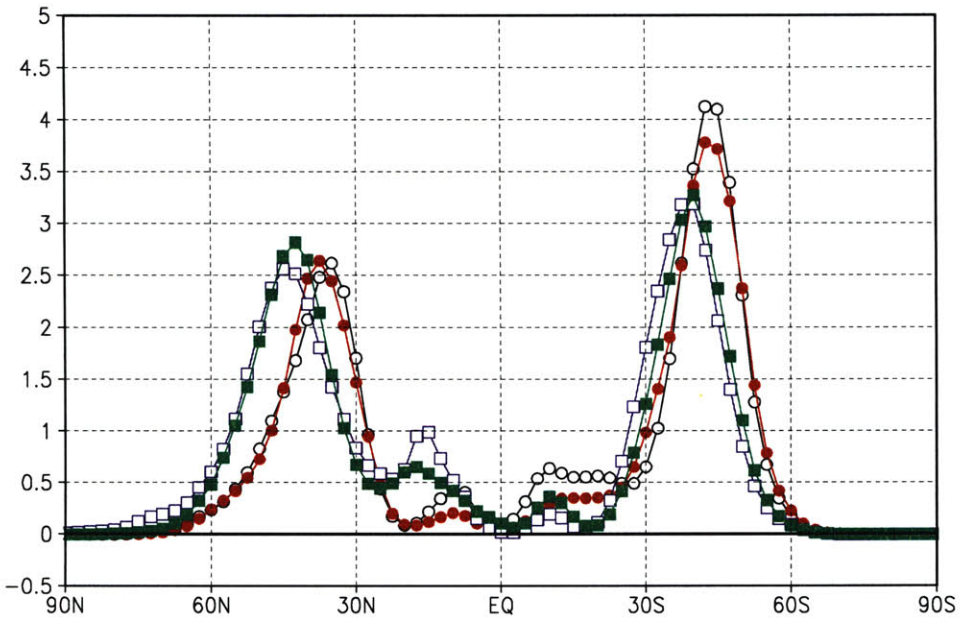

Figure 4.18: Zonally averaged TR densities for DJF (black open circle), MAM (red solid circle), JJA (blue open square), and SON (green solid square). Unit in 10^{-4} TRs (°latitude)$^{-2}$.

peaked maximum of TR activity near 41°S and a somewhat broader and lower peak near 40°N through the year. A subsidiary maximum near 15°N that only occurs in JJA and less pronounced in SON may be attributable to the Asian summer monsoon. System numbers are very low with virtually almost no system encountered north of 80°N and south of 70°S. Overall, there is little seasonal variation in the amplitude of the midlatitude maximum (its value varying by less than 10% in the NH and 21% in the SH), and the distribution for DJF appears displaced to its southernmost position and that for JJA to its northernmost by a few degrees with larger seasonality found in the NH.

4.3.2 TR Translational Speed

The latitudinal variation of the TR movement components are shown in Figure 4.19. The peak eastward velocity in the SH occurs near 60°S to the south of the system density maxima. The eastward movement of TR in the NH is more complicated since it appears that there are two maxima, one broad peak in the 25°–55°N zone and a sharp one near 73°N. The speeds of eastward movement fall away rapidly at higher latitudes in both hemispheres. The results may be compared with the meridional profiles of the vertical- and zonal-mean values of the zonal wind component shown by Peixoto and Oort (their Figure 7.20a, 1992). Though the amplitudes are similar, the peak of the mean zonal wind in the SH tends to be biased equatorward and there is no corresponding secondary high latitude maximum in the NH exhibited in Figure 4.19a.

It is of interest to note that the meridional translational speed increases almost monotonously from near zero at the equator to ~ 11 m s^{-1} at high latitudes before falling away

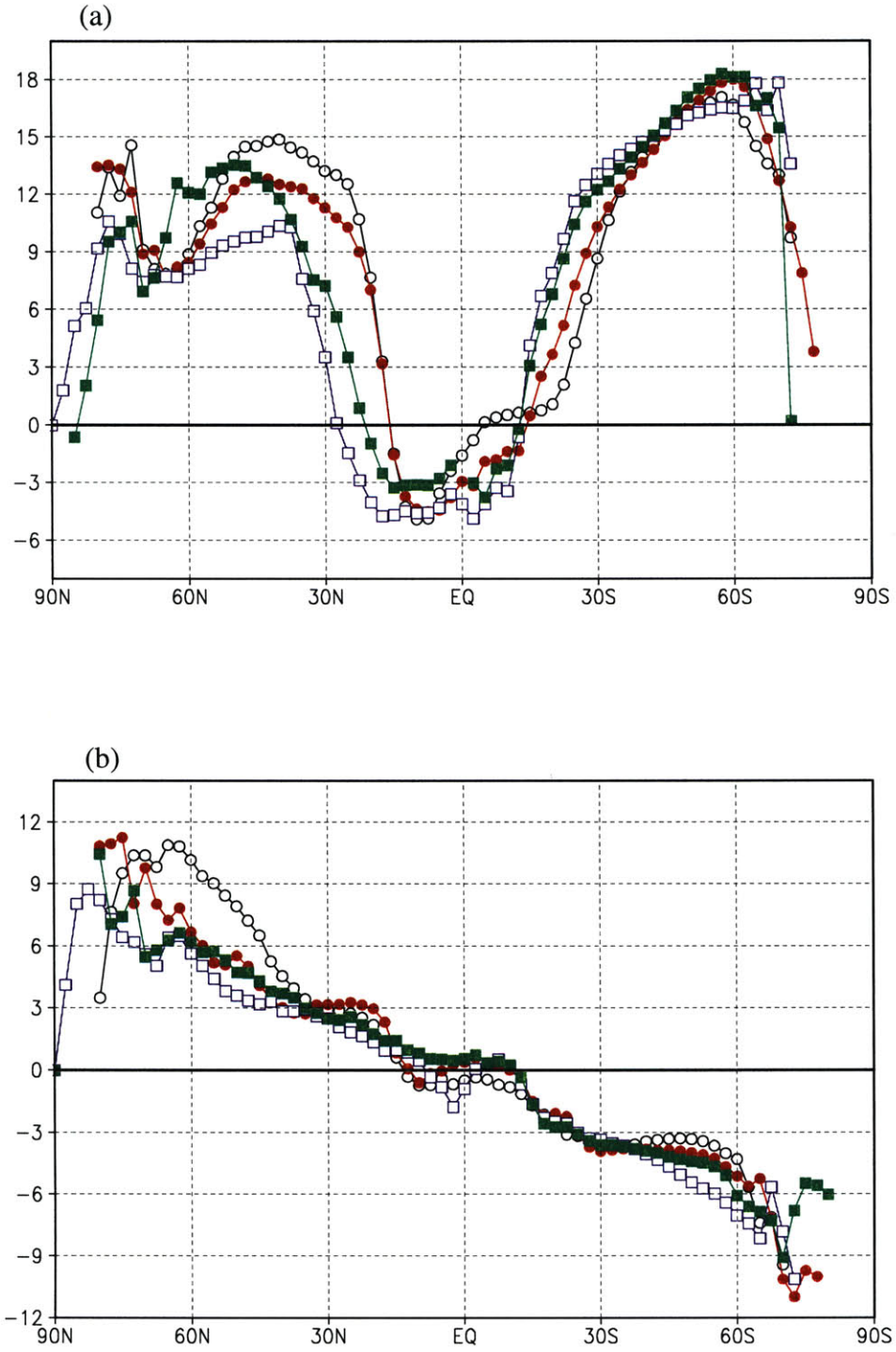

Figure 4.19: Zonally averaged TR translational speed with (a) E-W and (b) N-S components, respectively. Unit in m s^{-1}. Legends: DJF (black open circle), MAM (red solid circle), JJA (blue open square), and SON (green solid square).

near the circumpolar regions (Figure 4.19b). When compared to the same component of cyclone translational velocity obtained by Murray and Simmonds (1991) which is only available for the SH, the opposite trend can be observed, i.e., average southward movement of cyclones was higher in mid-latitudes (25°–50°S) and diminished towards high latitudes. The peculiarities of TR movement and the dynamical reasons for them warrant further investigation. For example, can any relationship be established between the movement of TRs and that of cyclone systems into which some of the rivers were drawn?

4.3.3 TR Genesis and Termination

The meridional distributions of TR genesis and termination shown in Figure 4.20 are similar to each other and also to that of TR density (Figure 4.18). As noted before, the distribution of TR termination is biased poleward to that of genesis (more so in the NH), with formation being predominant near 37.5°N (38.75°S) and dissipation near 42.5°N (43.13°S) in the NH (SH) annually. In the subtropical region of the NH, the subsidiary genesis and termination maxima during summer and in covariation in other seasons are closely related to the summer Asian monsoon (see also in Figure 4.11c), indicating the locality of TR activities by character there. The same can be said of the covariance of the genesis and termination curves in the subtropical area of the SH which may be related to the Northern Australian monsoon (see also in Figure 4.11a), though less pronounced and out of phase compared to those related the Asian monsoon.

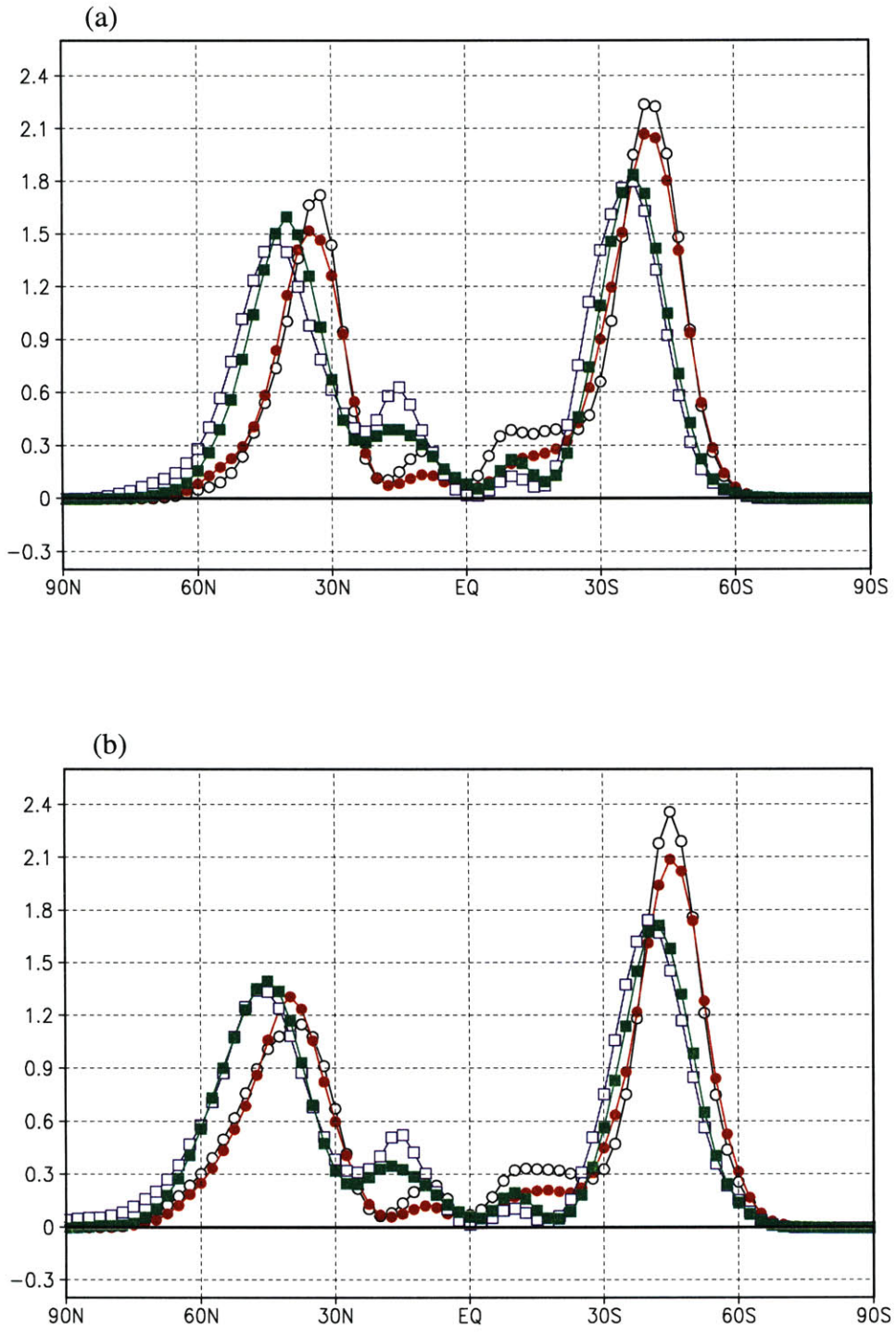

Figure 4.20: Zonally Averaged TR (a) genesis and (b) termination. Unit in 10^{-4} TRs (°latitude)$^{-2}$ day^{-1}. Legends: DJF (black open circle), MAM (red solid circle), JJA (blue open square), and SON (green solid square).

4.4 TR Moisture Fluxes

4.4.1 TR Strength and Meridional Transport

We discussed earlier in Chapter 3 the use of averaged magnitude of TR moisture flux over the associated TRCs within a TR as a measure of its strength, and the resulting value was assigned to the location of its TRMC. Therefore, the mean water vapor transport accomplished by an individual tropospheric river is equal to its mean flux multiplied by the river width. Since the scheme hasn't included an algorithm to estimate the individual width of a river yet (this is largely owing to the poor resolution of the input data to resolve the across-stream river structure), a work-around TR width estimation scheme is designed based on the method proposed by Zhu and Newell (1998). Zhu and Newell developed a procedure by sorting the water vapor fluxes at each grid point along a given latitude into two groups: those exceeding a certain limit related to the mean value at a given latitude, i.e., the river fluxes; and the rest, so-called the broad fluxes. The river fluxes in their study are defined as those with magnitudes greater than certain criterion, i.e.:

$$Q \geq Q_{mean} + 0.3(Q_{max} - Q_{mean}) \tag{4.1}$$

where Q_{mean} denotes the zonal mean along a given latitude of the magnitude of the flux; Q_{max} is the maximum flux along that latitude. The value of 0.3 was selected because it gave the best preservation of the river structure. Therefore, the zonal extent occupied by all rivers along a latitude can be estimated when the river fluxes found in our objective scheme met the criterion set by equation (4.1). When divided by the TR number at that lat-

itude, an individual TR's zonal scale can be derived (we assumed here that the zonal scales of TRs at a particular latitude are the same, an assumption that is clearly opposed to the observations but could be more or less justified by the narrowness and small standard deviations shown by the widths of the subsequent movements of TRs on the moisture flux charts). This zonal scale is usually greater than the width of a river since rivers do not lie meridionally in general. As illustrated in Figure 4.21, river width $W = L\sin\theta$, where L is the river zonal scale. Thus, mean TR moisture flux across the location of TRMC would be equal to $\mathbf{Q}W = \mathbf{Q}L\sin\theta$ with its zonal and meridional components of $Q_\lambda^r L\sin\theta\cos\theta$ and $Q_\varphi^r L\sin^2\theta$, respectively (superscript r denotes river). Note the difference between the unit of the river flux calculated here (kg s^{-1}) and that of flux $\mathbf{Q}$ (kg m^{-1} s^{-1}).

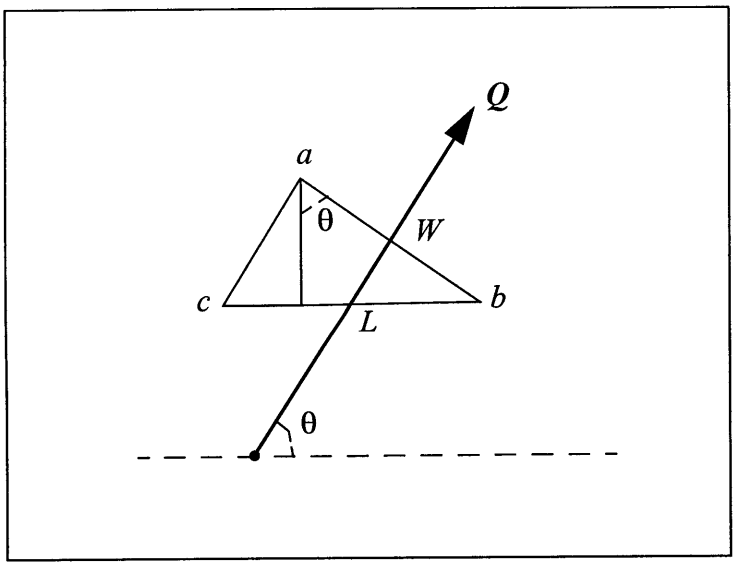

Figure 4.21: A hypothetical mean TR moisture flux vector with direction θ, its width W ($W = ab$), and its zonal scale L ($L = cb$).

At any instantaneous moment, unlike other frequency and regressed statistical quantities, after the influence of this averaged TR moisture flux at each TRMC was spread over nearby grid points using a Cressman-like function described in section 3.2.4b, the resulting moisture vectors at nearby grid-points were subjected to a correction constrained by the total water vapor transported by the river, i.e., the sum of the production of zonal (meridional) gird-point river vectors $Q^g_{\lambda i}$ ($Q^g_{\varphi i}$) multiplied by their corresponding longitudinal (latitudinal) grid distances $d_{\lambda i}$ ($d_{\varphi i}$), should be equal to the total zonal (meridional) TR moisture transport:

$$\sum_i Q^g_{\lambda i} d_{\lambda i} = Q^r_\lambda L \sin\theta \cos\theta \tag{4.2a}$$

$$\sum_i Q^g_{\varphi i} d_{\varphi i} = Q^r_\varphi L \sin^2\theta \tag{4.2b}$$

Where superscript g represents the values at grid-points and i denotes the grid-point involved.

When defined this way, the seasonal mean TR moisture flux vectors and their magnitudes are shown in Figures 4.22 through 4.25. The most intense TRs in the NH are seen to lie over the western portion of the two oceanic basins with maxima somewhat poleward of the regions of maximum density (see Figure 4.2) during all seasons. Figures 4.24 and 4.25 show that the systems are also significant in the region of the Asian summer monsoon, with the most intense found along the east coast of China to the south and east of Japan collocated with the TR density maxima. This is a well known fact that there is a large amount of water vapor transport over these areas during this season. The transport maps show large changes in the water vapor flux vectors every day, and the persistent monsoon

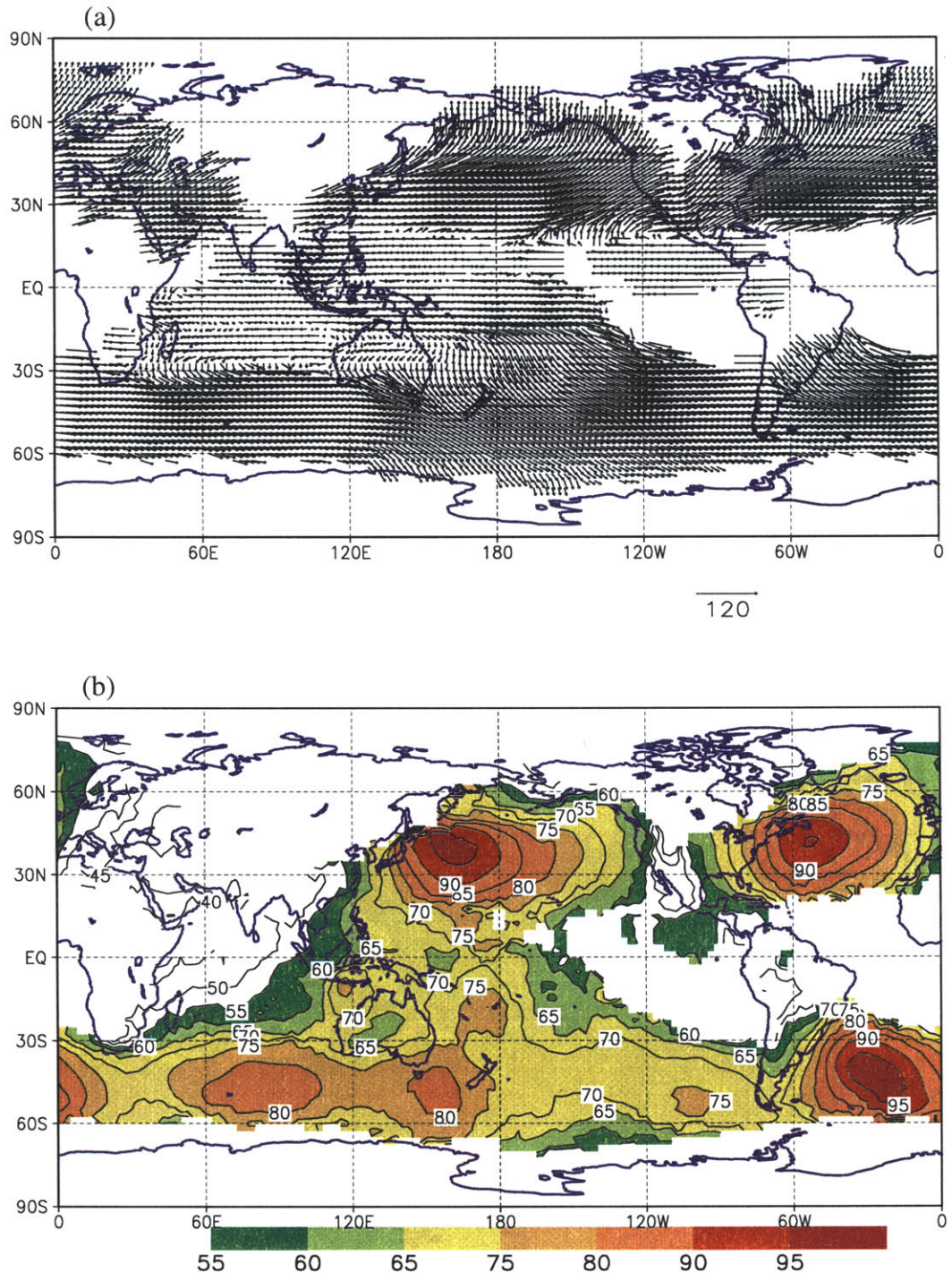

Figure 4.22: Mean TR moisture flux vectors and magnitudes for NH winter (DJF). (a) Mean TR moisture flux vectors. The vector at the bottom represents 120 (kg m^{-1} s^{-1}). (b) Magnitudes of the TR moisture fluxes. The unit is (kg m^{-1} s^{-1}). The contour interval is 5 (kg m^{-1} s^{-1}) with values greater than 55 (kg m^{-1} s^{-1}) color shaded.

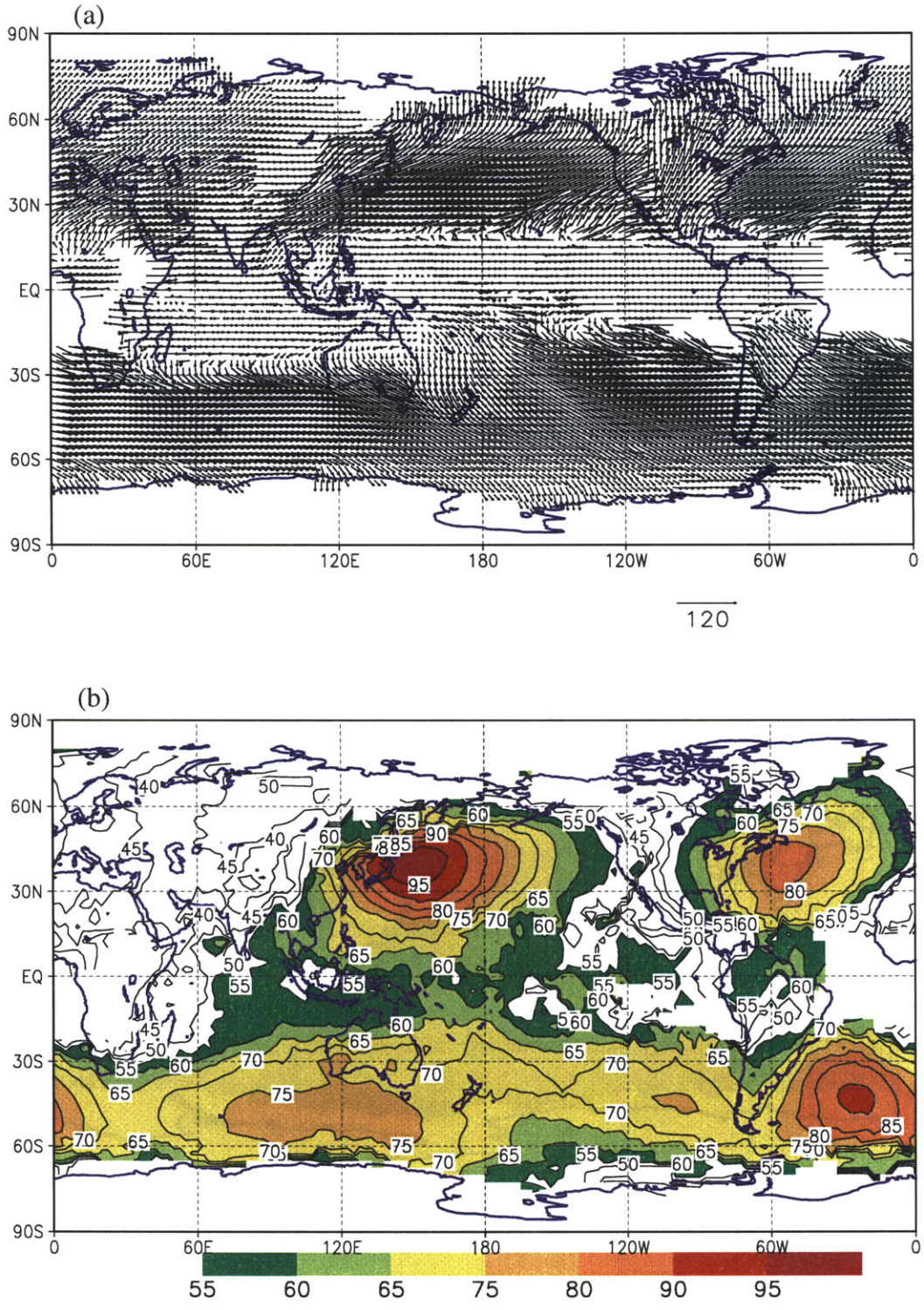

Figure 4.23: Same as Figure 4.22 except for NH spring (MAM).

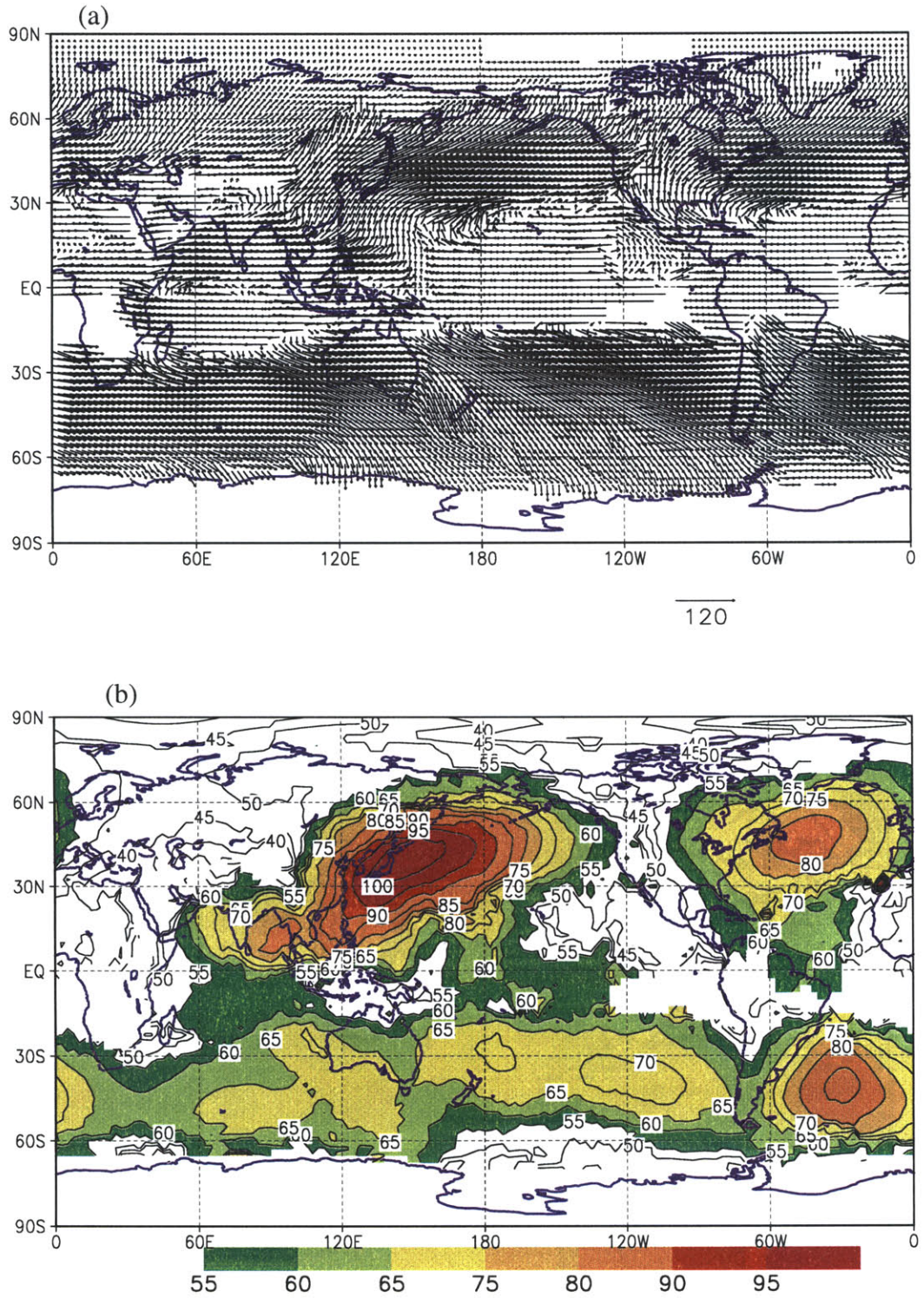

Figure 4.24: Same as Figure 4.22 except for NH summer (JJA).

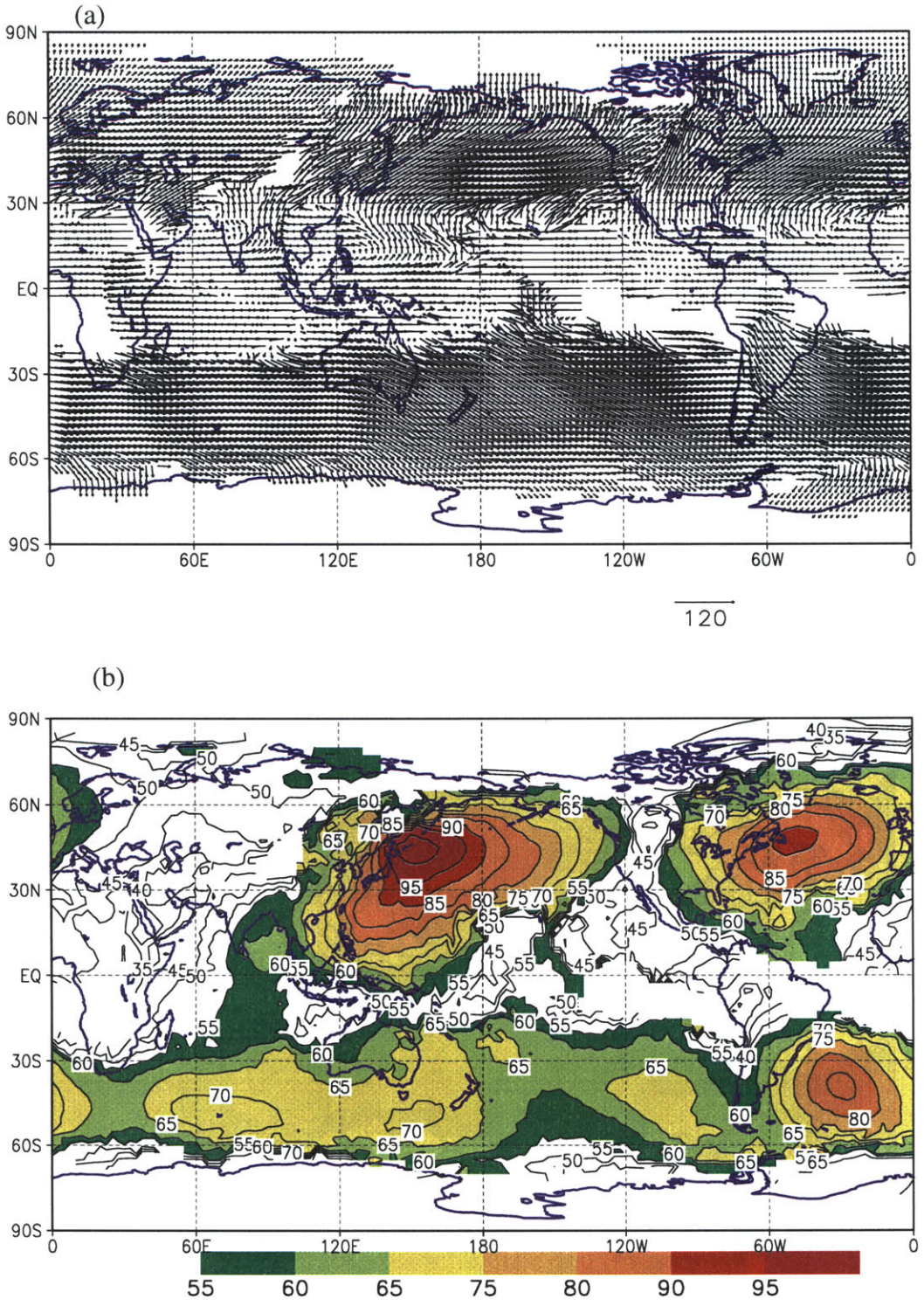

Figure 4.25: Same as Figure 4.22 except for NH autumn (SON).

circulations are supported by transient filamentary moisture fluxes and other disturbances on a scale less than that of the monsoon system. Broadly similar remarks on the collocation of the maxima for TR moisture transport and its density may be made over the western Atlantic (in both hemispheres) and Indian sectors, except that the intensity maxima in the South Pacific lie near 110°–150°W slightly to the north and upstream of high TR activities. In each hemisphere, the strongest TRs occur during the corresponding summertime over the northwest Pacific and off the east coast of South America, respectively. In general, water vapor transported by a TR in the NH is directed to the left of its track orientation (see the TR translational directions in Figures 4.7 through 4.10), while the reverse is true in the SH. Combined with the TR genesis and movement information, there is an evidence that during the summer, TRs born near the eastern seaboard of Asia tend to have a slower translational speed moving east-northeastward and stronger intensity. On the other hand, TRs developed over northwest Atlantic, though more frequent during the same season (JJA), have also a slower migrating velocity but weak intensity compared to other seasons. The strongest TR occurs during the wintertime over that sector (Figure 4.22). This is an interesting result that warrants further investigation. For instance, could these differences be related to the particular characteristics of tropical cyclones (i.e., the sizes, intensity, frequency, etc.) in the two oceanic basins?

As expected, the region that is host to the strongest TR in the SH is found off the east coast of South America. TR strength peaks during DJF and persists throughout the year there. Other TR strength maxima with large seasonality can be found over the southern Indian and to the east of dateline of the South Pacific sector.

Figure 4.26 illustrates the frequency distribution of individual TR moisture strength binned in every 50 kg m^{-1} s^{-1} for all seasons and in the NH and SH, respectively. A Gaus-

sian-like distribution for the TR strength is evident in both hemispheres with more skewness in the SH, suggesting a higher percentage of TRs has a similar strength in the SH. Over ~ 40% (~ 50%) of TRs have the strengths around 600 kg m^{-1} s^{-1} in the NH (SH). Again, larger seasonality of TR strength can be found in the NH.

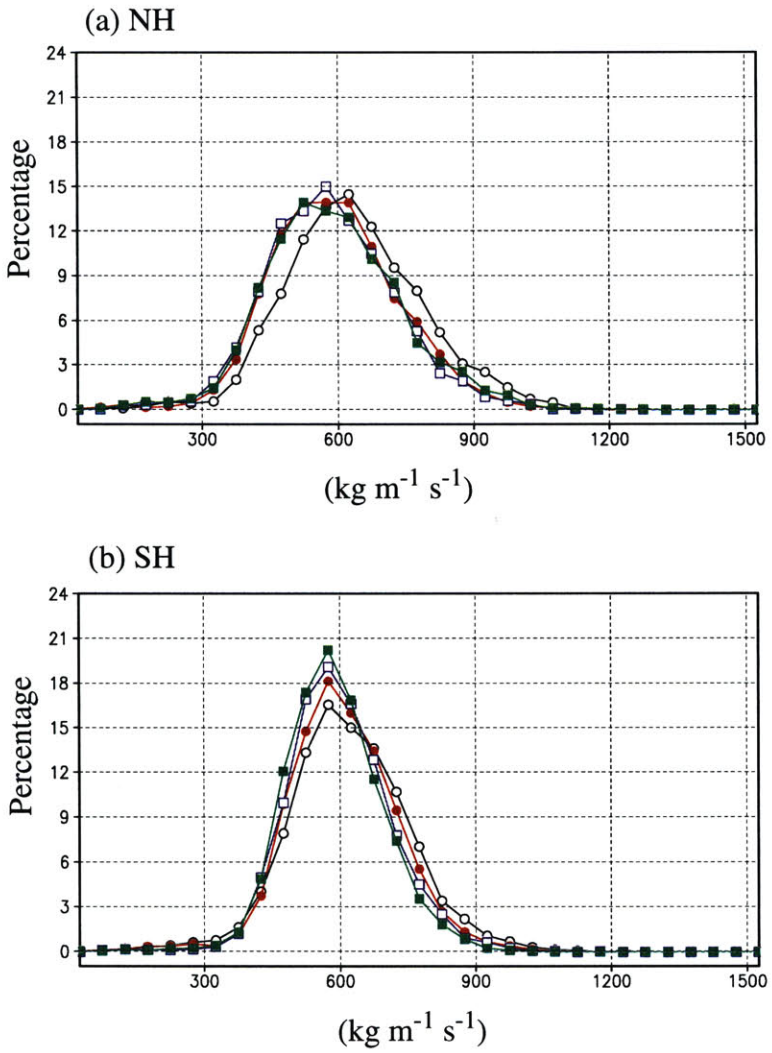

Figure 4.26: Frequency distribution of TR strength (binned in every 50 (kg m^{-1} s^{-1}) for (a) NH and (b) SH. Legends: DJF (black open circle), MAM (red solid circle), JJA (blue open square), and SON (green solid square).

Perhaps a more relevant piece of information that needs to be extracted from TR strength is its meridional component. This is owing to the fact that of the total energy typically carried by the atmosphere across midlatitudes toward the poles, nearly half is in the form of latent heat associated with the meridional flux of water vapor (Rosen 1999, his Figure 1.4). The meridional moisture flux contributed by TRs may, therefore, have important consequences for weather and climate. When examining the meridional component of TR intensity (Figure 4.27), a couple of interesting results stand out. The northward transport of water vapor by TRs peaks over the Bering Sea and the Gulf of Alaska in the North Pacific sector during northern winter (DJF). During summertime (JJA), moisture is carried by TRs to the north near the coastline of eastern China and up to near 60°N along about 120°E. It appears that the northward transport of vapor by TR is more efficient in higher latitudes and during a TR's decaying stage. The latter is especially true for the winter season (DJF), indicating that the TR axis aligns to a more north-south orientation when translating into its 'graveyard' (the river example shown in Figure 3.10 exhibits such a signature). That the maxima of northward moisture transport occur more broadly in higher latitudes in the North Atlantic is consistent with the distributions of other statistical quantities such as the system density and track flux (i.e., the axes of these maxima incline to a more N-S direction compared to those in the Pacific).

In the SH, the most significant southward transport occurs just east of the Andes and extends into the South Atlantic throughout the year. Contrary to that in the NH where the TR meridional fluxes peak mainly in the middle to high latitudes, the same components in the SH have their maxima mostly in the midlatitudes, some even locate in tropics (e.g., Figure 4.27d near 5°S, 140°W-170°W). This indicates that TR axes tend to be more N-S oriented due to the topographic effect over South America or to some mechanisms related to the South Pacific Convective Zone (SPCZ). Perhaps the most appealing result shown in

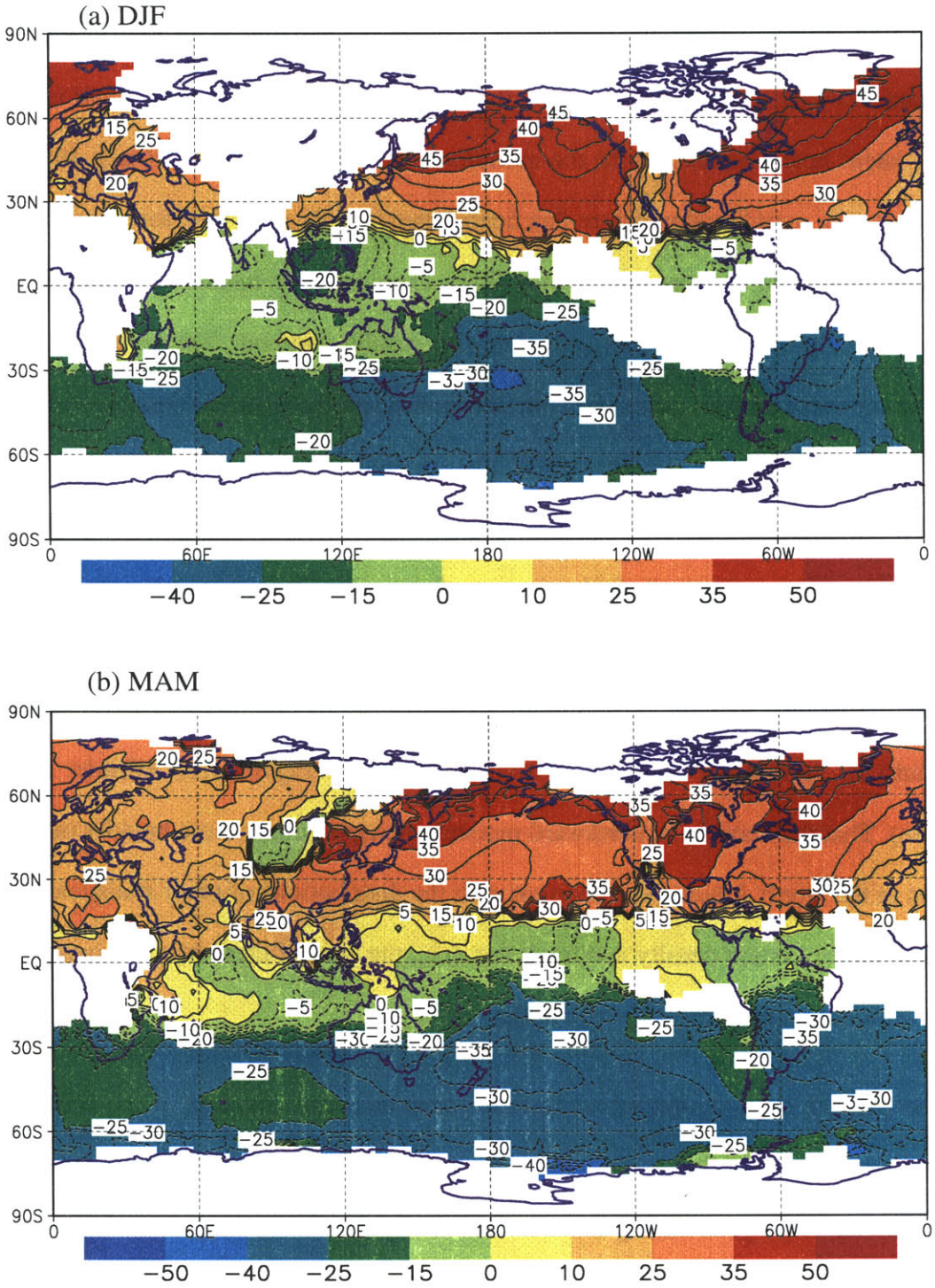

Figure 4.27: Mean magnitudes of meridional TR moisture fluxes in (a) DJF, (b) MAM, (c) JJA, and (d) SON. The unit is (kg m^{-1} s^{-1}). The contour interval is 5 (kg m^{-1} s^{-1}).

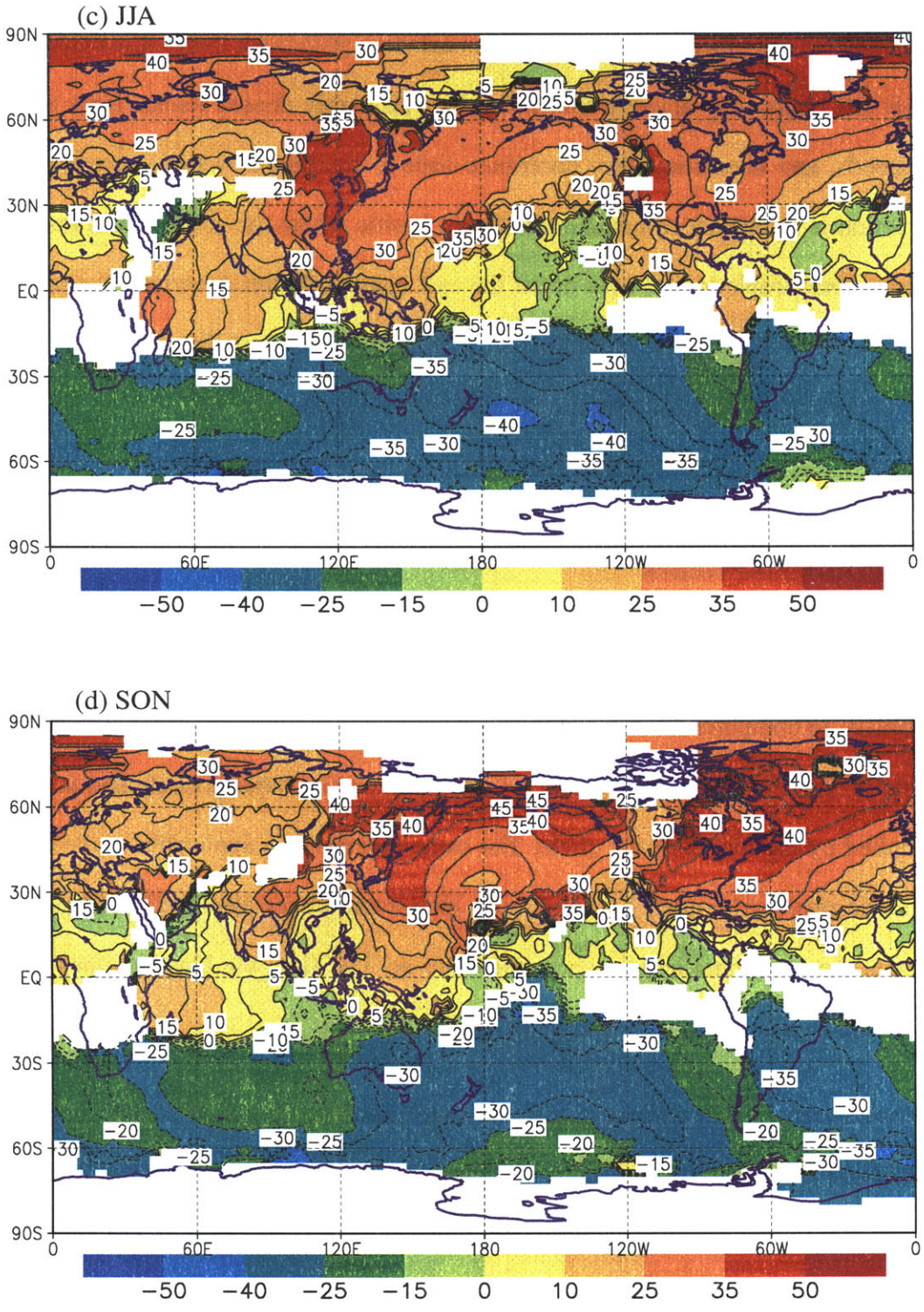

Figure 4.27: (*Continued*)

Figure 4.27 is the lack of large meridional transport over the southern Indian Ocean sector, where almost all the other statistical quantities exhibit significance there. It is evident that although TRs occur very actively over this area with highly densed tracks, large translational speeds, and intensities, they contribute little to meridional water vapor transport. The situation is somewhat reversed in the South Pacific where the southward transport is sometimes comparable to that over or off the east coast of South America. The seasonal signal shown by following the latitudinal shift of the zero transport line is in good agreement with the ITCZ migration over the western oceanic basins.

4.4.2 Meridional Profiles

Traditionally, to computer the mean meridional water vapor transport across each latitude, the vertical- and time-mean Q_φ is averaged around the entire latitude circle and the result is multiplied by the length of the circle. The same procedure is applicable in the case of tropospheric rivers using their seasonal mean meridional fluxes displayed in Figure 4.27 except that the latitudinal length where there are no TRs (i.e., the blank regions on the maps) should be subtracted from the whole circle.

The meridional profiles of the zonal and meridional vapor fluxes of TRs computed through above treatment are presented in Figure 4.28. A comparison with the latitudinal variations of the total zonal transport of water vapor plotted by Peixoto and Oort (their Figure 12.9, 1992) leads one to believe that just as TR is a major vehicle in transporting moisture meridionally, it is also a major contributor to the zonal moisture transport (especially in the mid to high latitudes), a point not appreciated much in the earlier river studies.

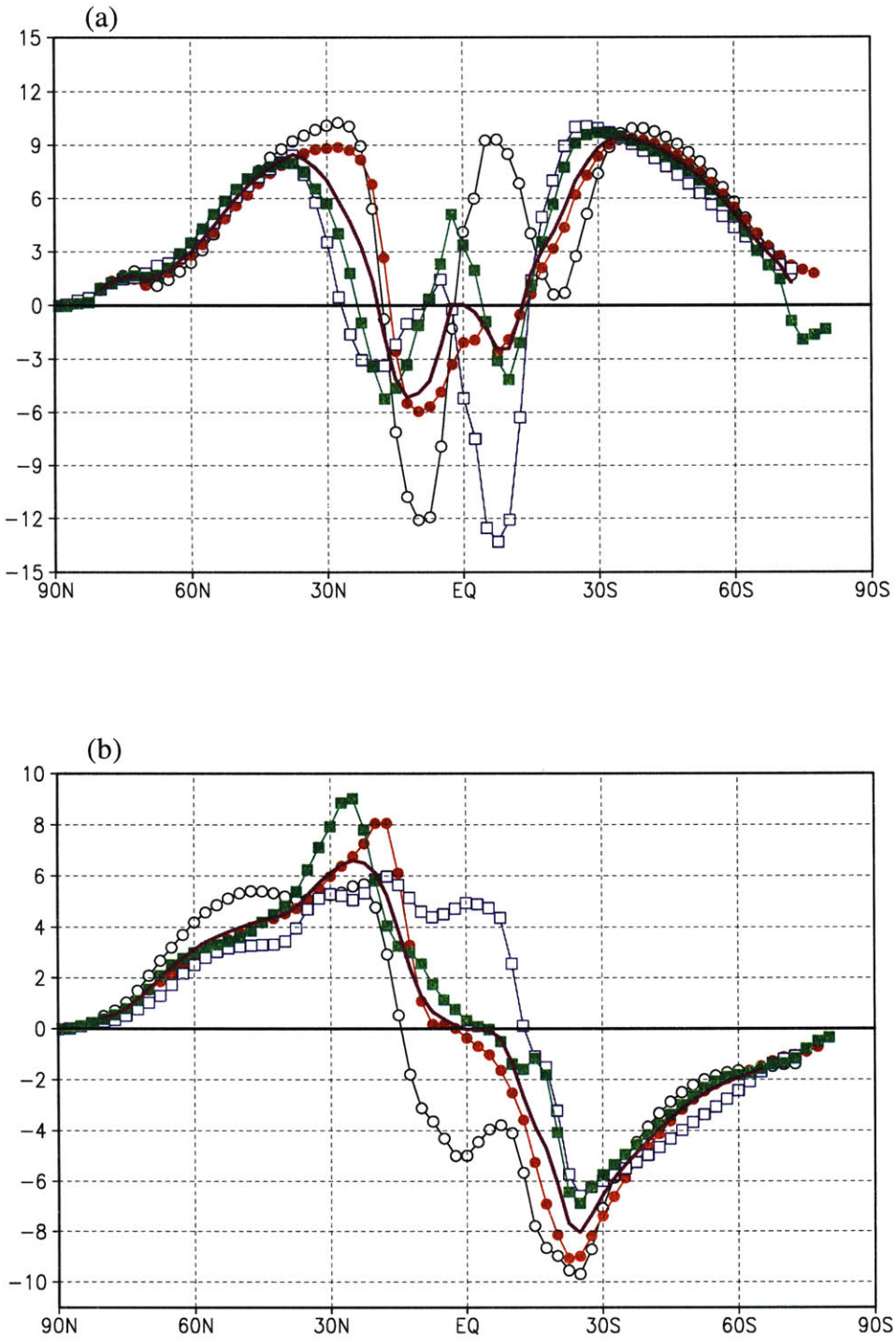

Figure 4.28: Zonally averaged (a) zonal and (b) meridional moisture fluxes of TRs. Units in 10^8 kg s^{-1}. Legends: DJF (black open circle), MAM (red solid circle), JJA (blue open square), SON (green solid square), and Annual (purple solid line).

The zonal transport of moisture by TRs shows a similar magnitude but a broader maximum in the mid to high latitudes in each hemisphere when compared to that of the total transport. The SH maxima exceed those of the NH. In the equatorial latitudes, significant seasonality can be found with a bimodal distribution being evident during all seasons except DJF, though a bimodal configuration in the total zonal transport calculated by Peixoto and Oort appeared in both DJF and JJA (the dominant maximum being in the winter hemisphere). The absence of a bimodal structure during DJF (i.e., the secondary westward maximum in the southern tropics replaced with a strong eastward maximum) suggests that the behavior of TRs there may not be correlated to the equatorial trough which is believed to be the cause of such a bimodal pattern (Peixoto and Oort 1992).

The zonally averaged meridional transport of moisture by TRs is shown in Figure 4.28b. In each hemisphere, one observes a sharp increase in TR meridional moisture transport from low to mid latitudes, with more broaden peak magnitudes in the NH. The result with which this can be compared is that of Zhu and Newell (1998) who utilized essentially a zonal averaging technique set by certain criteria to divide the total water vapor fluxes into river and broad components (see equation 4.1). The river component they derived (their Figure 6) displays a similar latitudinal variation pattern except in the tropical regions, where the transport derived by them appears to be quite similar to the pattern of the total meridional moisture flux (i.e., a northward transport peak near 10°S and a 'meteorological' equator near 5°N due to the transport convergence by the mean meridional circulation). Although this zonal mean pattern in the tropics is well known (see Figure 4.31 in the next subsection; similar curves can also be found in Peixoto et al., 1978; Peixoto and Oort, 1992; and Cohen et al., 2000), the large river fluxes which occurred there in their study may be questionable. The peak of this transport shown in their Figure 6 is even larger than its extratropical counterpart, notwithstanding they admitted that the rivers

therein were not so strong and narrow as the extratropical rivers owing to the relatively weaker humidity contrasts. The result is also contrary to the fact that there is much less TR activity near the equator (see Figures 4.2 and 4.18, or the high frequency map Figure 2.2 in Chapter 2 obtained by Newell and Zhu, 1994). This problem is probably due to the intrinsic deficiency of their algorithm which can not accurately extract the moisture fluxes associated with TRs in the tropical regions, although this is less severe in the middle and high latitudes. The interhemispheric water vapor exchange by TRs derived by our method seems more reasonable and the characteristics of seasonal variation (water vapor being transported from the winter hemisphere into the summer hemisphere, as pointed out by Peixoto and Oort, 1992) is still retained.

4.4.3 Comparison with the Transient Fluxes in Traditional Studies

It is instructive to compare our result with those derived from conventional method. According to Starr and Peixoto (1971), the total transport of water vapor can be expressed in terms of that by time mean motions and transient perturbations, i.e:

$$\overline{qu} = \bar{q}\,\bar{u} + \overline{q'u'} \tag{4.3a}$$

$$\overline{qv} = \bar{q}\,\bar{v} + \overline{q'v'} \tag{4.3b}$$

where the overbar denotes the time average and the prime represents the deviation from the time mean. A further convention that is often used is to express a variable with its zonal mean plus the departure from it. When apply the time average first and then the zonal average, one derives:

$$[\overline{qu}] = [\bar{q}][\bar{u}] + [\bar{q}^*][\bar{u}^*] + [\overline{q'u'}] \quad (4.4a)$$

$$[\overline{qv}] = [\bar{q}][\bar{v}] + [\bar{q}^*][\bar{v}^*] + [\overline{q'v'}] \quad (4.4b)$$

in which the brackets represent the zonal mean and the quantities with stars are the departures from their zonal means. Therefore, the time- and zonal-mean transport of water vapor in the atmosphere has been divided into the components represented by the terms on the right-hand-side of equation (4.4), corresponding to the time and zonal mean flows, stationary eddies, and transient perturbations. Integration of equations (4.3) and (4.4) in the vertical (similar to Equations 2.2 and 2.3) then leads to the expansion of the total meridional transport in terms of the various modes of transport. This vertical mean can be denoted by the angle brackets < >.

The maps of the vertically integrated mean moisture transport $<\bar{q}\,\overline{\mathbf{V}}>$ and the transient-eddy moisture transport $<\overline{q'\mathbf{V}'}>$ are shown in Figures 4.29 and Figure 4.30 for the winter and summer conditions, respectively. All are calculated from the 43 years of 6-hourly NCEP/NCAR reanalyses. The flow of mean water vapor transport in both seasons reflects the planetary behavior of the general circulation in the lower troposphere, since the specific humidity acts as a weighting factor for the wind field. Thus, the general pattern is consistent with the distribution of the mean flow, i.e., westerlies in the midlatitudes and easterlies in the tropical belt. Substantial meridional transport can be found in the middle and subtropical latitudes that is associated with the circulations along the polar fronts and the borders of the subtropical anticyclones. The largest variability of the mean flux during the year is observed over the region of the Asian summer monsoon. There is a strong concentrated interhemispheric flow into the Arabian Sea during the summer that is well connected to the monsoonal flow over the South and Southeast Asia.

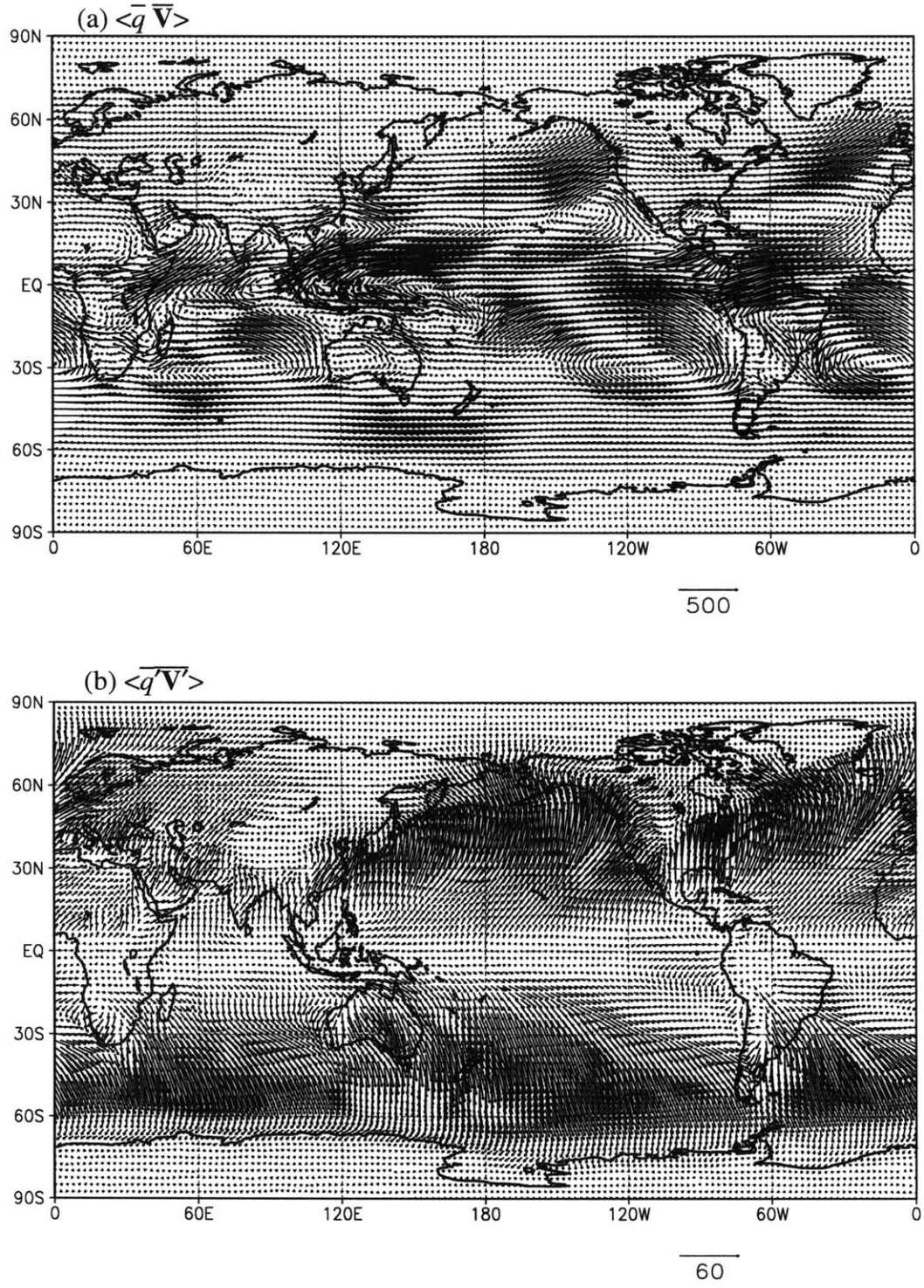

Figure 4.29: (a) Vertically integrated mean moisture transport <$\bar{q}$ $\bar{\mathbf{V}}$>, and (b) transient-eddy moisture transport <$\overline{q'\mathbf{V}'}$> for NH winter (DJF). The unit is (kg m^{-1} s^{-1}). Scale vector is shown at the bottom of the map.

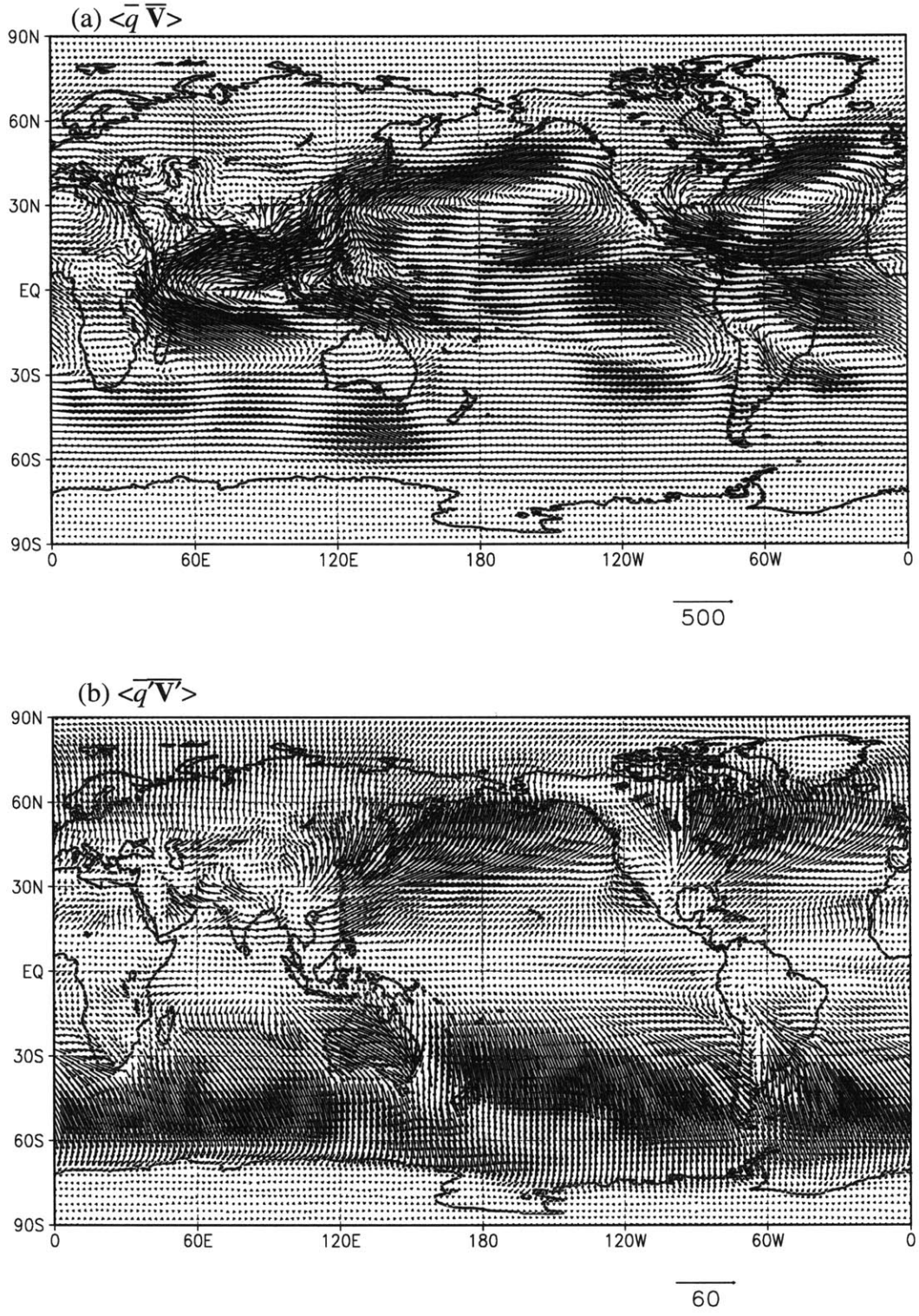

Figure 4.30: Same as Figure 4.29 except for NH summer (JJA).

On the vertically integrated transient-eddy flux maps (Figures 4.29b and 4.30b), the values of the fluxes are nearly one order smaller than those of mean fluxes, with predominately poleward flow in middle latitudes of both hemispheres throughout the year. In the polar regions and in the tropics, the meridional eddy transports are weak, almost vanishing over the equator. The influence of the land-sea contrast is evident in the location of the maxima just east of the continents and over the major oceanic basins, especially in the NH. There is no significant seasonality exhibited in most part of the globe for the two different seasons. Perhaps the most salient feature that contradicts the observations is the absence of significant transient-eddy fluxes associated with the Asia summer monsoon. That the persistent monsoon circulations are supported by the transient features is a well known fact (Krishnamurti and Surgi, 1987; Lau et al., 1998). However, Figure 4.30b shows that it is almost quiet over the South to Southeast Asia in summer. The water vapor flux by the mean flow in Figure 4.30a suggests that it is the mean easterly flux across the Arabian Sea and Bay of Bengal that supplies moisture to the monsoon region. Although mean motions contribute most of the water vapor flux at low latitudes (Starr and Peixoto, 1971; Peixoto and Oort, 1992), they do not seem to account for all the physical phenomena involved in the transport for this particular region. Therefore, both the mean flux and the transient-eddy flux maps appear to omit physical mechanisms thought to be important. Similar results were obtained by Zhu and Newell (1998) for a July sample containing the years 1991, 1994, and 1995.

The TR moisture flux maps (Figures 4.22 and 4.24), when compared with those of transient-eddy flux, show different geographical concentrations as well as their magnitudes. In the NH, the river fluxes show a general correspondence with the storm tracks, particularly over the oceans in winter; while the transient perturbations exhibit no such apparent links. During summer (JJA), large river fluxes cover the Indian Ocean and Southeast Asia mon-

soon region, reflecting the transient disturbances occurring there; while these were assigned to the mean fluxes in the conventional approach (Figure 4.30a). The river fluxes also contribute to the interhemispheric transport in the tropical regions (see Figure 4.28b) whereas little evidence can be observed for the transient-eddy fluxes. The seasonal river flux magnitudes are about a factor of 2 larger than those of the corresponding transient-eddy flux.

The meridional profiles of the vertical- and zonal-mean values of the moisture transport by all motions, transient eddies, and TRs for annual condition are displayed in Figure 4.31. We notice that the transient eddies are responsible for a great fraction of the total transport of water vapor in middle latitudes, while the rivers seem to account for a substantial fraction of the total moisture transport in both middle and subtropical regions. Inspection of the large oscillation of the total meridional flux in the tropical and subtropical regions confirms that it is due to the mean meridional circulations associated with the lower branches of the Hadley cells, according to the traditional flux partition. It appears that water vapor transported by the rivers may take on the partial load of this mean meridional transport (this can also be verified by the similar seasonal configurations of both transports, see Figure 12.12d in Peixoto and Oort, 1992) in low latitudes, whereas significant portion of the meridional transport contributed by the transient eddy in middle latitudes is still retained in the river flux profile. It may be noted that the zonally averaged annual mean meridional moisture flux poleward across 30°N and 30°S are about 6.23×10^8 kg s^{-1} and -6.67×10^8 kg s^{-1}, respectively, while the corresponding total TR meridional fluxes at these latitudes have nearly the same magnitudes, manifesting the importance of TR mechanism over there.

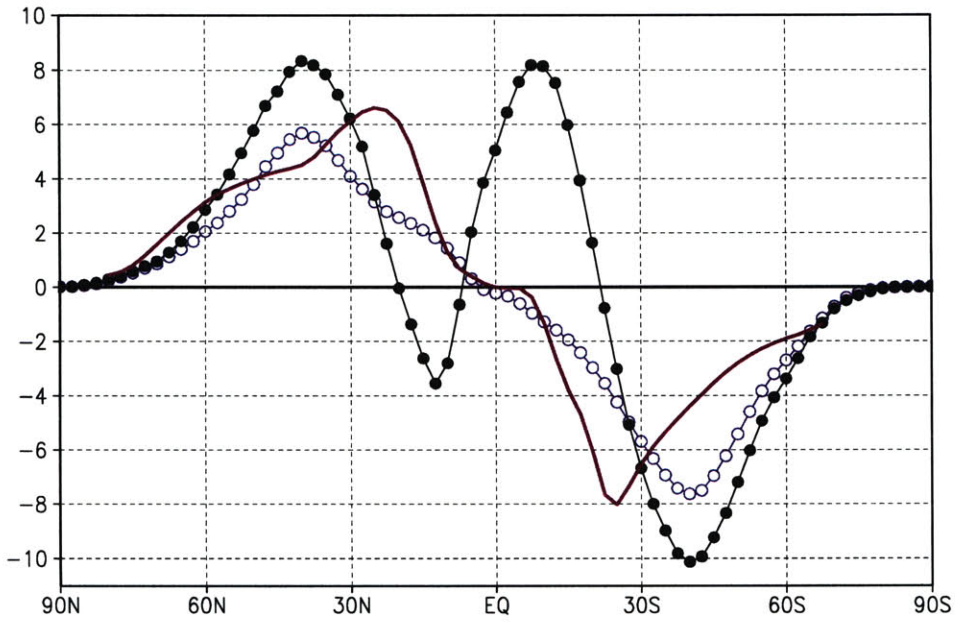

Figure 4.31: Annual mean meridional profiles of the vertical- and zonal-mean values of the moisture transport by (a) all motions (black solid circle), (b) transient eddies (blue open circle), and (c) TRs (purple line). Units in 10^8 kg s^{-1}.

4.5 Summary of the Chapter

We have presented in this chapter a climatology of Tropospheric Rivers derived from 43 years of NCEP/NCAR reanalyses regarded as one of the best representations of the global atmosphere. The application of a numerical scheme for finding and tracking TRs and the generation of unbiased data have made possible the development of a comprehensive set of statistics, many of which have never been presented previously. Through the use of an

objective scheme, we are able to ensure consistency in the techniques used to define and track systems throughout the period of study and produce data free from traditional manual constraints.

The results show that there are, on average, 4 - 5 rivers in the Northern Hemisphere and 5 rivers in the Southern Hemisphere at any given time. When stratified by 20° wide latitude bands the greatest number of TRs is found in the 30°-50° band of each hemisphere in all seasons. The axes of the greatest system densities are found principally over the two ocean basins in the NH and the three ocean basins in the SH in all seasons, and major localized maxima over the Bay of Bengal and Arabian Sea during JJA (related to the summer Asian monsoon) and over Northern Australia during DJF (related to the Australian monsoon). TR tracks are most concentrated near those principal oceanic regions of TR densities in all seasons, indicating that TRs are migratory in character but are nearly stationary over monsoon-related regions mentioned above. The movement of TRs is in a generally eastward direction with a weak poleward meridional component that increases in the mid to high latitudes in both hemispheres. Northern Hemisphere TRs form and intensify near the eastern seaboards of Asia and North America, with activity focused near the regions of strongest SST gradient. They move eastward and poleward during their lives before weakening in the two principal graveyards: over the Gulf of Alaska and to the southeast of Greenland. In comparison, SH TRs are more evenly distributed and tend to form in a band extending from the southeast coast of South America into the Atlantic, across the Indian Ocean (maximized near the tip of southern Africa), and throughout much of the Pacific middle latitudes. The corresponding genesis regions are also found to be adjacent to (or slightly equatorward of) the maximum SST gradients in these regions. Aside from regional features, for the most part genesis exceeds termination south (north) of about 45°N (45°S) in the NH (SH), while the converse is true north (south) of this lati-

tude. We have commented that based on limited published cyclogenesis and cyclolysis compilations, both TR genesis and termination maxima tend to be near the upstream equatorward flank of those of cyclogenesis and lysis except for cyclogenesis maxima occurring in the lee of major mountain ranges and over land due to the thermal effect. We suggest that TR formation and termination could be a leading predictor for the occurrence and decay of extratropical cyclones.

It has been shown that river axis lengths appear to be longer during the warmer seasons and longer in the SH. On average, the axis length of a TR is approximately 2284.0 km globally and annually. The mean lifetime of TRs that last at least 1 day is just a little over 2 days. Those that are located between 10° and 50° (at their half-lifetime) endure, on average, almost ~ 0.5 day longer than those in other latitudes. About 10% of all TRs travel less than 900 km and approximately 65% travel between 900 and 3000 km. It appears that the warmer seasons host a large number of TRs and TR tracks with shorter translation distance (not necessary shorter lives) but longer TR lengths. The possible biases of TR axis length, duration, and travel distance are also discussed. Features of various zonally averaged TR properties have also been examined and highlighted.

Among many important statistics that the objective scheme can produce are measures of TR strength and its influence. In attempting to understand the behavior and formation of TR systems and their role in weather and climate it is important to be able to quantify the 'strength' of these systems and their influence on climate maintenance. For example, a given region may be host to a large number of TRs but if they are relatively weak, their influence may be less than those over an area that is host to fewer but more intense systems. The same is also true for the meridional component of water vapor transport accomplished by TRs since this is the most relevant quantity for the global water cycle balance.

In quantifying the strength of a system, we consider the use of averaged TR water vapor fluxes over the associated TRCs within a TR as a measure of its strength. It is suggested that the TR strength defined in such a manner is a useful measure of a TR's status and effect on the circulation when compared to a 'point measure' which just picks the maximum value of a particular TRC. Our results indicate that the most intense TRs occur over the western portion of the oceanic basins (except for the South Pacific where the maxima are located near its southeast) with maxima somewhat to the poleward of the regions of maximum density in the NH, or approximately the same locations in the SH. In each hemisphere, the strongest TRs occur during the corresponding summertime over the northwest Pacific and off the east coast of South America, respectively. It is of interest to note that although TRs occur very actively over the Indian ocean sector with highly densed tracks, large translational speeds, and intensities, they contribute little to meridional water vapor transport, while a contrasting situation is found in the South Pacific where the southward transport is sometimes comparable to that over or off the east coast of South America. A comparison study on the TR moisture transport and the transient-eddy flow in conventional studies is conducted. Although both fluxes are responsible for a great fraction of the total transport of water vapor in middle latitudes, the rivers may also take on the partial load of mean meridional transport in low latitudes, which is typically assign to the Hadley cells in the conventional approach. Other significant differences include: (i) In the NH, the river fluxes show a general correspondence with the storm tracks, particularly over the oceans in winter; while the transient perturbations exhibit no such apparent links; (ii) During northern summer, large river fluxes cover the Indian Ocean and Southeast Asia monsoon region, reflecting the transient disturbances occurring there; while the region is mostly quiet shown on the transient-eddy flux maps and the monsoonal fluxes were assigned to the mean fluxes. (iii) The river fluxes contribute to the

interhemispheric transport in the tropical regions whereas little evidence can be observed for the transient-eddy fluxes. These results, which calculated from the long-term reanalysis data, support the previous finding derived from three July months by Zhu and Newell (1998): that the transient fluxes in traditional studies do not catch the filamentary structures completely and may therefore underestimate the fraction of transport assigned to moving systems, as well as lacking the geographical concentrations. The river moisture fluxes obtained from our objective scheme based on a Lagrangian approach are considered to be more representative for the moisture transport occurring in these translational systems.

The focus in this chapter has been the documentation of the mean behavior of various characteristics of TRs over a 43-year period. The data set derived, however, allows us to consider also many aspects of the variability of these features over the same period. The results of such an investigation are presented in the next chapter.

Chapter 5

Variability of Tropospheric River Behavior

5.1 Introduction

As fundamentally important as the time averaged aspects of the atmospheric system and its subcomponents, is its variability over the range of the study period. There is clear evidence for the existence of long term and systematic variations of the global atmosphere which, combined with possible anthropogenic factors, raises the question of the variation and/or trend of TR activity. An appreciation of the magnitude of this variability and the time-scales over which it is built up are important in constructing any climatology and in establishing secular trends. In reality, natural variability in the circulation patterns may be the result of changes in ocean heat storage, sea-ice extent and cloud cover, and of dynamic processes occurring within the atmosphere.

The investigation of temporal variations of the analyzed state is constructive. Although there is always doubt that trends or variabilities identified in the analyses may be fictitious in that at least some of the features identified may be associated with changes in opera-

tional analysis procedures, the relatively unchanged nature of the reanalysis scheme used in the development of the NCEP/NCAR data set (Kistler et al. 2001, see also data description in Chapter 2) simplifies the interpretation.

In this chapter, an analysis of the variability and trends exhibited by many aspects of TR behavior derived by applying a state-of-the-art TR identifying and tracking scheme to the moisture flux calculated from the 6-hourly NCEP/NCAR reanalyses for the period 1958-2000, is presented. The outcome is the first of its kind for TR variability.

Section 5.2 describes the time series of TR counts over the span of the reanalyses. Results of the geographical distributions of trends are presented in section 5.3. Section 5.4 provides a discussion on the relationship between TRs and the El Niño - Southern Oscillation (ENSO) phenomenon. A summary is given in Section 5.5.

5.2 Time Series

The numerical TR identifying and tracking scheme (TRICKS) allows us to summarize conveniently the time series of TR counts. Such series yield detailed temporal variations of annual and seasonal counts as well as the geographical distribution of trends. The time series of the annual average number of TRs per analysis for each hemisphere is presented in Figure 5.1. In the NH, the number of TRs shows a fairly steady decrease from the start of the period to a minimum around the late 1960s and early 1970s, and a detectable upward trend since then. In the SH, the TR count displays an overall increase.

The equations and accompanying statistics based on a least squares linear regression fit to the two time series are given below:

(a) NH:

$$Y_{N1} = -0.032X + 11.29, \quad R = -0.18, \quad C = 75.84\% \tag{5.1}$$

$$Y_{N2} = -0.31X + 65.30, \quad R = -0.67, \quad C = 99.91\% \tag{5.2}$$

$$Y_{N3} = 0.057X - 6.20, \quad R = 0.27, \quad C = 77.65\% \tag{5.3}$$

(b) SH:

$$Y_{S1} = 0.11X - 15.63, \quad R = 0.49, \quad C = 99.92\% \tag{5.4}$$

where Y is TR frequency (expressed as TRs per analysis), X is year divided by 10 (to yield the trend with units of TRs per decade), R is the correlation coefficient, and C is the confidence level. The meanings of the subscripts in the equations are: N denotes NH, S denotes SH, and subscripts *1*, *2*, and *3* represent the periods of 1958-2000, 1958-1978, and 1979-2000, respectively.

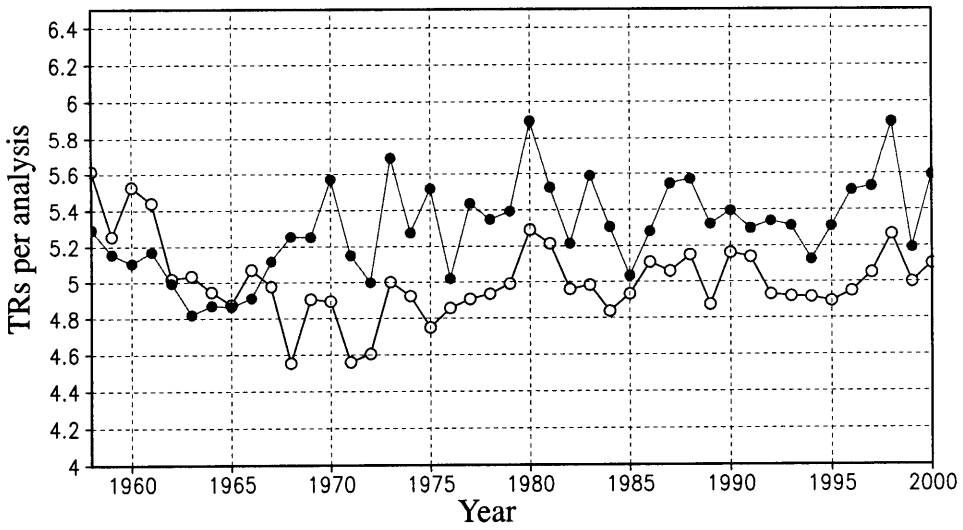

Figure 5.1: Time series of annual average number of TRs per analysis for NH (open circle) and SH (solid circle).

A slightly downward trend of -0.032 TRs decade^{-1} is found in the NH which failed to pass the 95% confidence level, while a slope of 0.11 TRs decade^{-1}, that is above the 95% confidence level, is exhibited in the SH. When the NH TR frequency data set is divided into two sub-periods, the least squares linear regression fit shows a decline of 0.31 TR events per decade (with 99.91% confidence level) for the period 1958-1978, and an increase of 0.057 TR events per decade (marginally above 77% level) for the period 1979-2000, respectively. It appears that the overall downward trend in the NH is largely due to the declination during the first two decades of the period.

Table 5.1 displays the trends and correlation coefficients when linear regression least squares fit is applied to the TR counts per analysis in the 20° latitude belts (from 70°S to 70°N), SH, NH, and Globe over the entire 43-year reanalysis period.

Table 5.1: Linear regression least squares fit to the TR counts per analysis in the 20° latitude belts, SH, NH, and Globe (GL). The equation and accompanying statistics are: $Y=bX+a$, where Y is the TR frequency; X is in units of year; b (the trend, with units in TRs decade^{-1}) and a is the best-fit parameter. The correlation coefficient r is also listed with values underlined when it is statistically significant at the 95% confidence level or higher.

	70°S - 50°S	50°S - 30°S	30°S - 10°S	10°S - 10°N	10°N - 30°N	30°N - 50°N	50°N - 70°N	SH	NH	GL
b	0.013	0.053	0.045	-0.06	-0.02	0.014	0.033	0.11	-0.032	0.074
a	-2.11	-7.11	-7.76	13.2	6.04	-0.25	-5.89	-15.6	11.29	-4.35
r	0.25	**0.45**	**0.39**	**-0.51**	**-0.33**	0.27	**0.66**	**0.49**	-0.18	0.24

It can been seen that for most latitudinal belts the correlation coefficients are statistically significant (above 95% confidence level), and that there has been a general reduction

in TR numbers within the tropical region between 10°S and 30°N, and an increase north and south of it. The greatest increases occur in the 50°–30°S belt in the SH and in the 50°–70°N in the NH, respectively.

Much effort has been made to document the relationship between the frequency trend of cyclones and the trend in surface air temperature (e.g., Jones et al. 1986; Hansen and Lebedeff 1987, 1988; Agee 1991, and Geng and Sugi 2001). Therefore, it is of consider able interest to examine the TR time series in relation to the climatic trend in surface air temperature. Figure 5.2 shows the time series of the mean annual surface temperature from NCEP/NCAR (actually the temperature is extracted from the lowest model level σ=0.995 which is very near to the surface) in the two hemispheres for the period of our analysis.

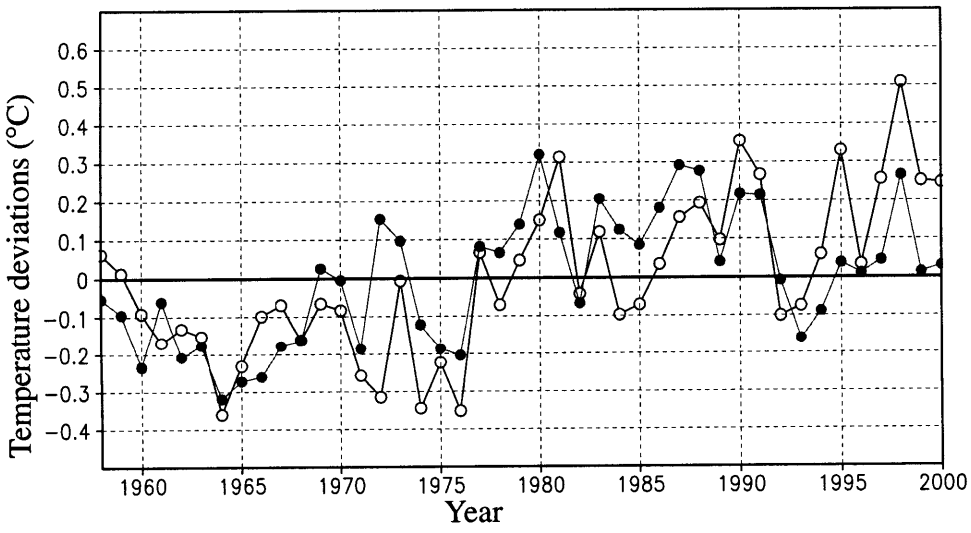

Figure 5.2: Time series of the annual mean surface air temperature deviations (°C) over 1958-2000 for the NH (open circle) and SH (solid circle).

All available temperature records for this century suggest a warming trend from 1900 to 1940, cooling from 1940 through 1978 (particularly so in the NH), and warming during the past two decades with an apparent overall trend of warming (Hansen and Lebedeff 1987, 1988; Agee 1991; and Casey and Cornillon 2001). Similar trends to those of TR counts during the corresponding time frames can also be detected in the surface air temperature (Figure 5.2). Least square linear regression fits were made to the plots and the following results obtained:

(a) NH:

$$T_{N1} = 0.11X - 20.95, \quad R = 0.64, \quad C = 99.99\% \tag{5.5}$$

$$T_{N2} = -0.049X + 9.40, \quad R = -0.23, \quad C = 70.31\% \tag{5.6}$$

$$T_{N3} = 0.097X - 19.05, \quad R = 0.37, \quad C = 91.58\% \tag{5.7}$$

(b) SH:

$$T_{S1} = 0.075X - 14.90, \quad R = 0.56, \quad C = 99.98\% \tag{5.8}$$

These statistical results document the warming and cooling periods of interest in the NH and SH, which now can be correlated with the TR frequency statistics. The linear correlation coefficients are 0.38 between Y_{N1} and T_{N1} for the whole period, 0.48 between Y_{N2} and T_{N2} for the cooling period, and 0.53 between Y_{N3} and T_{N3} for the warming period, respectively. Also, the correlation between Y_{S1} and T_{S1} is 0.65. Although these correlations are not high, they lend some support to the view that TR frequency decreases with decreasing surface temperature and increases with increasing temperature. In fact, all four correlations between the TR frequency and the surface air temperature are statistically significant at the 98% confidence level or higher. There are three out of the eleven correla-

tions are not statistically significant [i.e., equations (5.1), (5.3) and (5.6)], it warrants further investigation for particular regions and an update using longer time series.

Perhaps one way to ascertain the extent to which the TR frequency relates to the surface temperature is by breaking down the TR counts into four seasons (Figure 5.3). The time series in both hemispheres indicate that the behavior of the average TR counts is dominated by the warm seasons (JJA and SON in the NH, and DJF and MAM in the SH). On average, TRs occurring during the warm seasons appear to be ~ 40.9% more in the NH and ~ 28.0% more in the SH than those in the other half of the year (also see Table 4.1). The compensatory behaviors of the two hemispheres strongly suggest that TR frequency is proportional to the change in surface temperature.

All of the above results suggest that the dynamic climatology of the waves responsible for temperature trends is equally responsible for the frequency of TR events. How this happens is not simple or well understood, but it may be related to systematic climatological variations in the temperature gradients as we mentioned in Chapter 4.

It is useful to obtain an appreciation of the extent to which such a trend may be due to more TR tracks and/or longer TR lifespans. Figure 5.4 shows the annual total number of tracks and their mean duration in the two hemispheres. The overall patterns of the TR track numbers (Figure 5.4a) including the trends, larger counts in the SH than in the NH, and the percentage variation, are similar to those of the total counts (Figure 5.1), indicating that decrease (increase) in TR numbers is largely due to fewer (more) tracks rather than tracks tending to last a shorter (longer) time. This proposition is confirmed by the plots of annual mean TR lifespan in Figure 5.4b. It should be noted that the percentage variation in lifespan is much less than those exhibited by the TR counts and track numbers, and there are no significant lifespan differences between TRs in both hemispheres (in

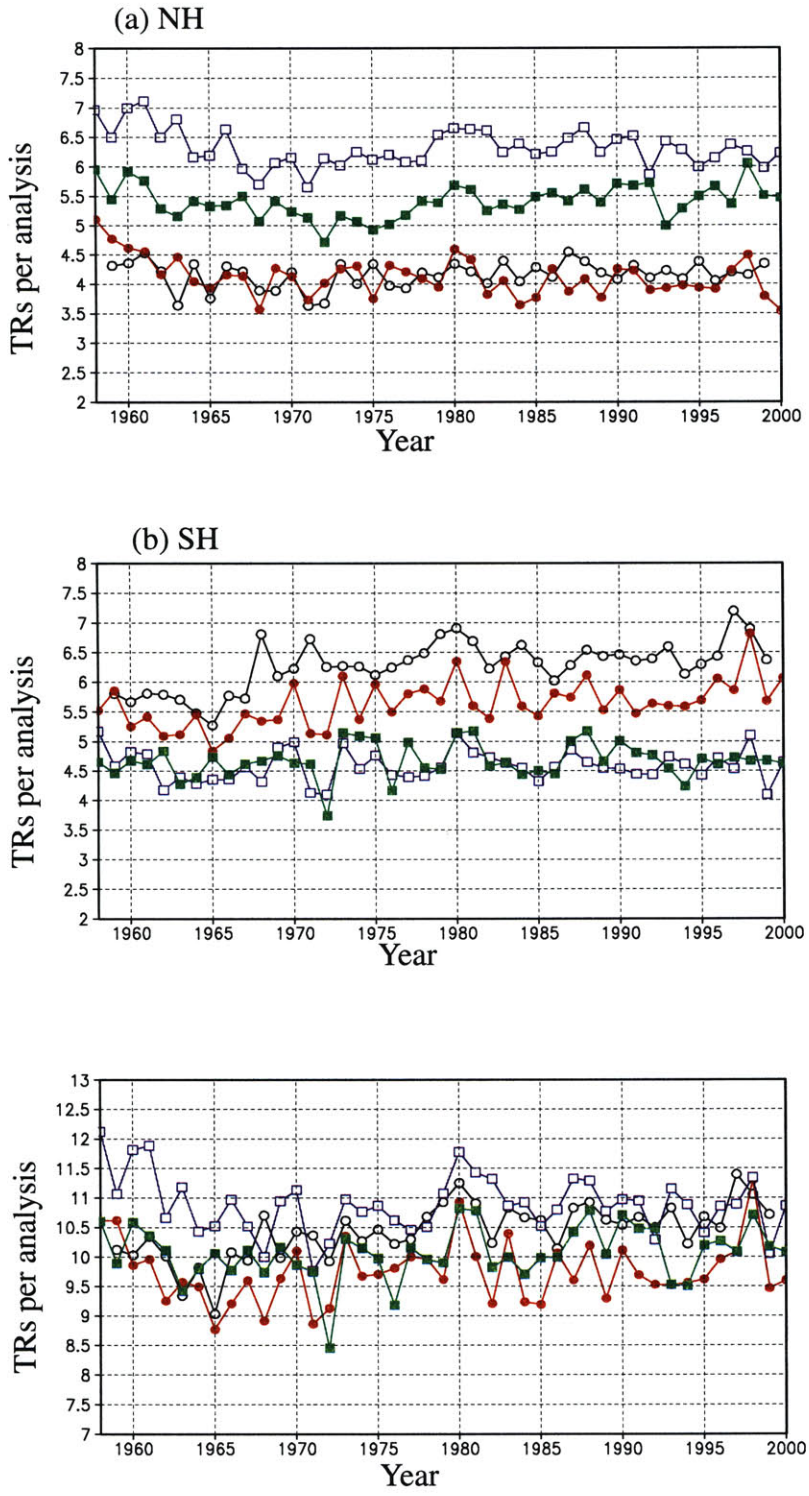

Figure 5.3: Time series for seasonal averages of number of TRs per analysis in the (a) NH, (b) SH, and (c) Globe. Legends: DJF (black open circle), MAM (red solid circle), JJA (blue open square), and SON (green solid square).

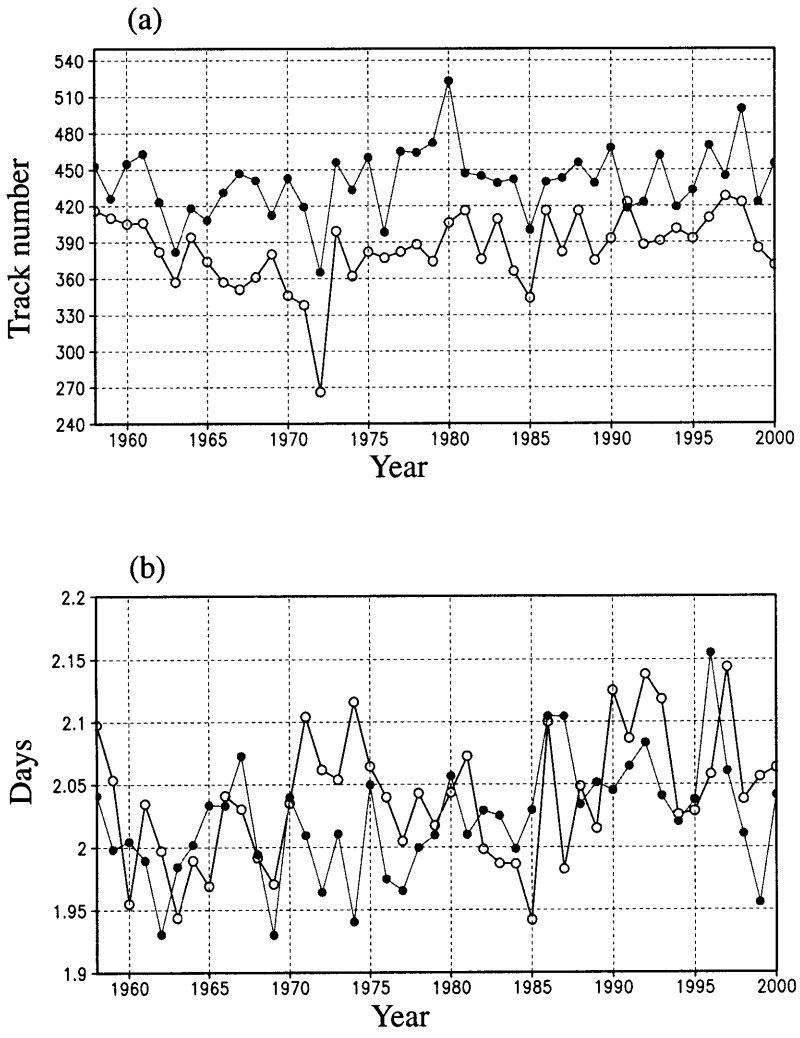

Figure 5.4: Time series of (a) annual total number of TR tracks, and (b) their mean duration for the NH (open circle) and SH (solid circle). (A TR must last at least 24 hours to be included in the compilations.)

fact, the average TR duration in the SH is shorter than that in the NH, see Figure 4.18 and Table 4.4).

Figure 5.5(a) shows the trends in annual mean TR strength in both hemispheres which displays a negative trend in the early part of the record (before 1965 in the NH and before 1963 in the SH) and a marked increase since then. Over the entire period a least squares fit

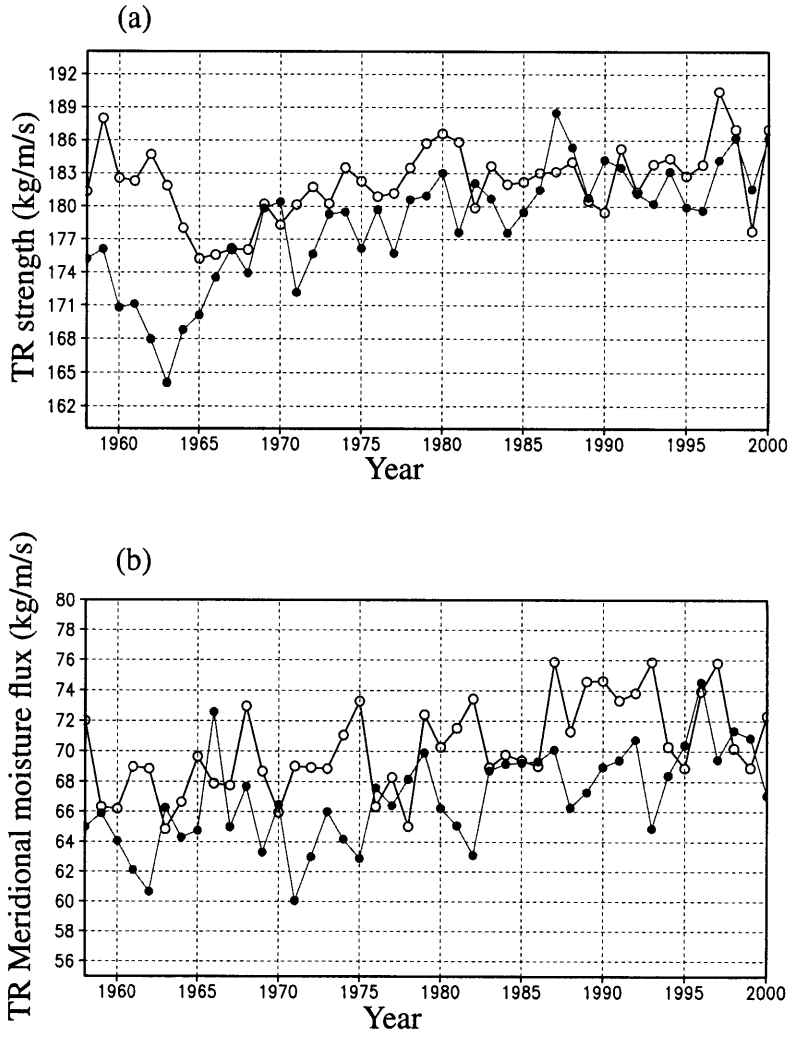

Figure 5.5: Time series of annual average (a) TR strength (kg m^{-1} s^{-1}) and (b) TR meridional moisture flux (kg m^{-1} s^{-1}) for the NH (open circle) and SH (solid circle). The meridional flux in the SH has been multiplied by a -1 factor for comparison purpose.

exhibits a trend of 1.04 (kg m^{-1} s^{-1}) $decade^{-1}$ (with 98.93% confidence level) in the NH and 3.36 (kg m^{-1} s^{-1}) $decade^{-1}$ (with 99.99% confidence level) in the SH. The time evolution of the mean TR meridional moisture flux (Figure 5.5b) shows a similar trend over the whole period (1.34 and -1.56 (kg m^{-1} s^{-1}) $decade^{-1}$ in the NH and the SH, respectively,

with confidence levels all above 99.99%), indicating a strengthened poleward water vapor transport in both hemispheres. When taken in conjunction with the changes in counts, it appears that the atmospheric moisture circulation has become more vigorous in the last couple of decades.

Agee (1991) studied the trends in cyclone and anticyclone frequency and compared those with periods of warming and cooling over the Northern Hemisphere. His results tend to indicate a decrease in events (both cyclones and anticyclones) during cooling and an increase during warming. He observed that colder than normal weather is characterized by large amplitude long waves entrenched in the flow (particularly so over the NH), while warmer than normal weather tends to occur with a flatter pattern of short waves that carries more numerous disturbances west to east across the oceans and continents. This certainly fits with the observational pictures presented here for TRs in the NH. Our results seem to disagree with some SH studies (e.g., Zhang and Wang 1997; Simmonds and Keay 2000b). Simmonds and Keay (2000b) found that the annual average number of cyclones per SH analysis rose from the start of year 1958 to a maximum in 1972, and showed an overall decline since then, suggesting that the downward trends in cyclone numbers are associated with a warming SH. Assuming that relative humidity remains constant (a reasonable assumption that is consistent with the observations, for example, Peixoto and Oort 1996), they noticed that the moisture content of the SH atmosphere would be enhanced by about 3.5% accompanying a temperature increase of 0.5°C since the mid-1960s. A greater percentage decrease in the number of extratropical cyclones found by Simmonds and Keay led them to a paradox for the moisture transport. Although they found that the mean radius and strength of cyclones have increased over the period and suggested that these increases have served to partially offset the effect of the remarkable decrease in cyclone numbers, which would otherwise tip the energy balance in the SH, they pointed out that

moisture transport is only one of the energy flux modes affected by the cyclones and the percentage changes in the moisture content and the number of cyclones may not be the same. We comment here that atmospheric water vapor transport may not always be associated with cyclones. For instance, the major corridor for poleward moisture transport in the SH running from South America to the South Atlantic for all seasons is mainly related to the regional topography as described by James and Anderson (1984). On the other hand, major moisture transports are always connected with TRs. Further, although the time series of TR numbers per SH analysis shows an out-of-phase relationship with that of cyclone numbers, it is in line with the trend of surface air temperature. Combined with other trends observed earlier, therefore, a more consistent picture can be obtained from a TR viewpoint on atmospheric water vapor transport.

5.3 Geographical Distributions of TR Density Trends

It is useful to gain knowledge of the geographical distributions of trends that the TR density has undergone over the 43-year reanalysis period. Figure 5.6 displays the linear trend (least squares linear regression fit) of the annual mean TR density and its zonal mean (the distributions of trends for each season are broadly similar to that displayed in the figure). The pattern exhibits notable differences in geographical distribution as well as zonal symmetry. Negative trends are found largely over tropical and subtropical regions and positive trends in middle to high latitudes (these results are consistent with the zonal means of TR counts when broken down into latitudinal belts given in Table 5.1). When the time series

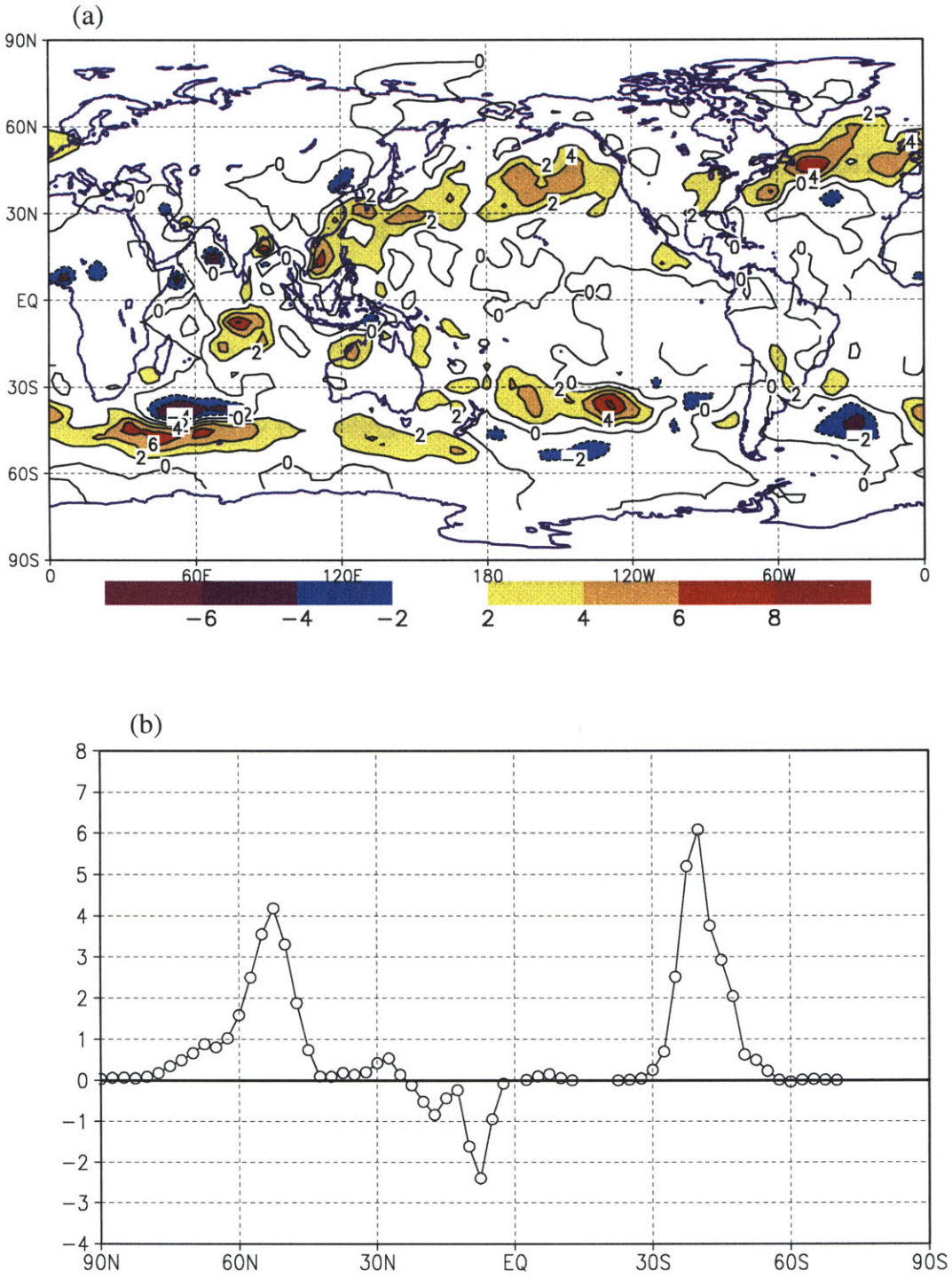

Figure 5.6: (a) Linear trend of the annual average TR density over the period 1958-2000 The unit is 10^{-5} TRs (°latitude)$^{-2}$ decade^{-1}. The contour interval is 2×10^{-5} TRs (°latitude)$^{-2}$ decade^{-1} and values greater than 2×10^{-5} or less than -2×10^{-5} TRs (°latitude)$^{-2}$ decade^{-1} are shaded; (b) Zonal mean of (a).

of TR counts discussed in the previous section are taken into account, one can see that the best-fit trends in the mid- and high- latitudes are to a large extent determined by the warming period since the late '70s. In the Northern Pacific, areas with positive trends in excess of 2×10^{-5} TRs (°latitude)$^{-2}$ decade^{-1} are located near the east coast of Southeast Asia and extend east-northeastward into the Gulf of Alaska. A generally upward trend can also be found in the Northern Atlantic extending even farther north. It should be pointed out that almost all of the trends greater (or less) than 2×10^{-5} TRs (°latitude)$^{-2}$ decade^{-1} (-2×10^{-5} TRs (°latitude)$^{-2}$ decade^{-1}) shown in Figure 5.6a are significantly different from zero at the 95% confidence level.

It appears that there are more structures in the SH mid latitudes: positive trends can be found in the southeastern Atlantic extending eastwards to the southern Indian Ocean and south of Australia, and in the South Pacific near 40°S. Areas of negative trends are also evident either to the north or to the south of their accompanying positive areas (none for the one to south of Australia). Whether this structure is related to the documented seesaw pattern identified in other quantities such as the mean sea-level pressure (MSLP) and 500 hPa geopotential in many studies of SH circulation features (e.g., Kidson 1975; Ghil and Mo 1991; and Sinclair 1997) remains as a question since the variability of TR densities shown here are restricted to the SH middle latitudes, although Simmonds and Keay (2000b) found that the pattern of cyclone density change resembled the so-called 'high-latitude mode' (negative trends in most locations south of about 40°S, and increasing to the north).

The distribution of trends in the annual means of TR genesis and termination resemble that of system density and are not reproduced here.

5.4 Relationship between TRs and ENSO Events

While the distribution and behavior of TRs in themselves are important components of the general atmospheric circulation, it is through relating the knowledge of these systems to the broader atmospheric system that we are able to gain an understanding of the mechanisms controlling the atmosphere. One of the most important and far reaching modes of variability of the atmospheric system is the El Niño -Southern Oscillation (ENSO) phenomenon. As first described by Walker (1923) and Walker and Bliss (1932), ENSO is now understood as an interannual, quasiperiodic, coupled mode of the tropical ocean-atmospheric system, with worldwide hydroclimatic teleconnections (Battisti and Sarachik, 1995). The strength, duration, and frequency of the El Niño and La Niña events, which comprise the two phases of ENSO, have varied significantly over the current century (Trenberth and Hoar 1996, 1997; Rajagopalan et al. 1997; Kestin et al. 1998). Many studies have investigated the relationships that exist between ENSO and regional and global patterns of such meteorological parameters as temperature, precipitation, and pressure (e.g., Trenberth 1976; Kiladis and Diaz 1986, 1989; Rocha 1992; Hoerling and Kumar 1997). The already cited associations of ENSO and precipitation, temperature, and pressure would be expected as the result of, and/or to be manifested in, changes in the distribution and intensity of synoptic systems. In this regard, TRs may be of similar importance. For example, it is of considerable interest to determine how water vapor transport might change if the planet were to warm from the rise in greenhouse gases. Presumably the moisture content of the atmosphere would increase in such a scenario (Sun and Oort 1995; Trenberth 1998), thus one might ask whether a moister atmosphere would generate larger, more intense TRs or smaller ones that carry vapor poleward more efficiently (similar to

the argument of Held 1993 on cyclone systems). In this section we will examine how variations of TRs are associated with those of ENSO.

To explore these possible associations we have calculated the time-synchronous correlation between a quantification of ENSO and various TR statistical quantities. The ENSO Index (ENSOI) defines ENSO years based on SST anomalies. The particular index chosen is from the Japan Meteorological Agency (JMA) because it selects well the known ENSO events (Meyers et al. 1999). The index is a 5-month running mean of spatially averaged SST anomalies over the tropical Pacific: 4°S-4°N, 150°W-90°W. Figure 5.7 displays this ENSOI with warming and cooling periods indicated. The monthly values were averaged over the four seasons to yield the seasonal values of the ENSOI.

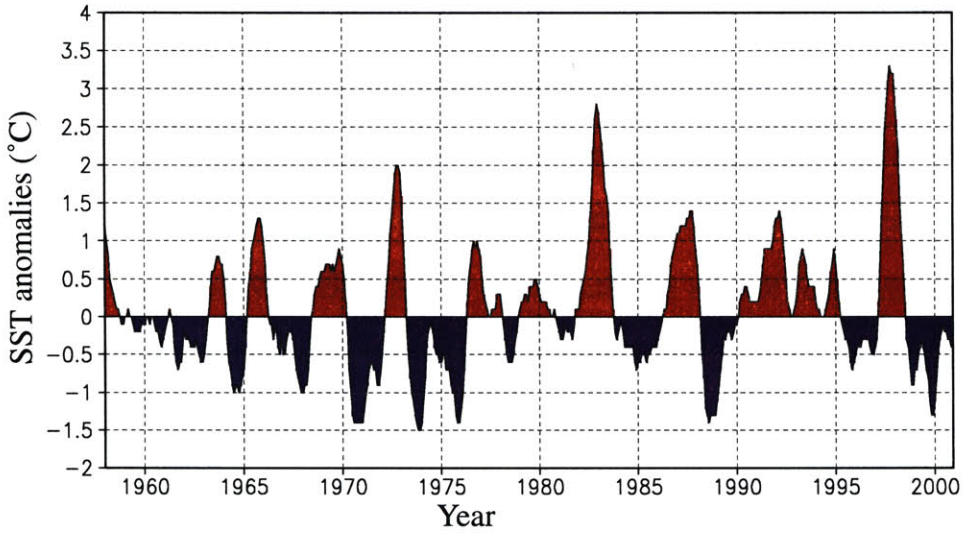

Figure 5.7: ENSO Index according to Japan Meteorological Agency (JMA) SST anomalies (°C).

As a background against which we consider the correlations between the TR properties and ENSO, we present the time-synchronous correlation of the ENSOI and the seasonally averaged precipitable water for the four seasons (Figure 5.8). Those regions for which the correlations are significant at, or above, the 90% significance level on a two-tailed test of the null hypothesis of zero correlation are stippled. In all seasons the correlations are dominated by the center of action in the tropical eastern Pacific (positive) in a triangle-shape with its base near the western coast of the Americas, and negative correlations can be found flanking its sides. The correlation is generally somewhat stronger during the winter season (DJF). The remainder of the global correlations are mixed and seasonally dependent. It is perhaps not surprising that the patterns shown here are quite similar to the ENSO modes revealed by other authors (e.g., Wu 1996) due to the high correlation between the precipitable water and the SST anomaly.

The correlation between the TR system density and the ENSOI is shown in Figure 5.9. Although the patterns show a relatively noisy structure, there are several features which need to be pointed out. During DJF (Figure 5.9a), the region of positive correlations is significant (stippled) over a substantial area in the central Pacific with a general orientation of WNW-ESE. The area of negative values in the southwestern Pacific with positive correlations to the east is consistent with the eastward extension of the South Pacific Convergence Zone (SPCZ) during the positive phase of ENSO with the region of increased cyclone activity associated with this feature shifting eastwards (see Trenberth and Shea 1987; Kiladis and van Loon 1988). In the oceanic regions of midlatitudes and higher latitudes of the NH, correlations are generally negative to the north of about 40°N and positive to the south indicating a tendency for the TRs to be placed more to the south during periods of positive ENSOI, especially over the western oceanic basins. Similar structure that suggests an equatorward (poleward) displacement of the region of highest TR density when

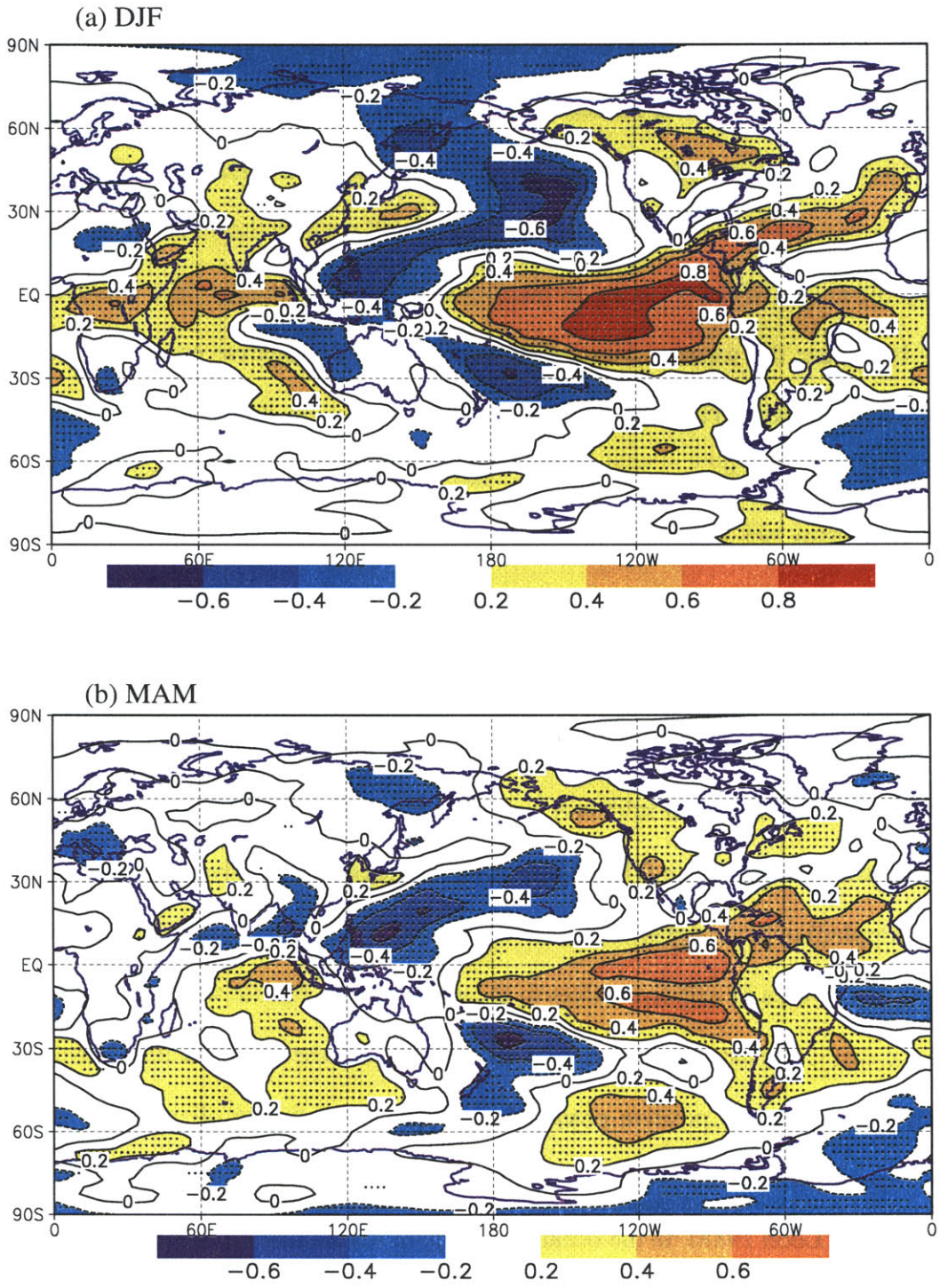

Figure 5.8: The time-synchronous correlation of the precipitable water with the ENSOI for (a) DJF, (b) MAM, (c) JJA, and (d) SON over the period 1958-2000. The contour interval is 0.2. Values greater (less) than 0.2 (-0.2) are shaded. Areas where correlations are significant at or above the 90% confidence level are stippled.

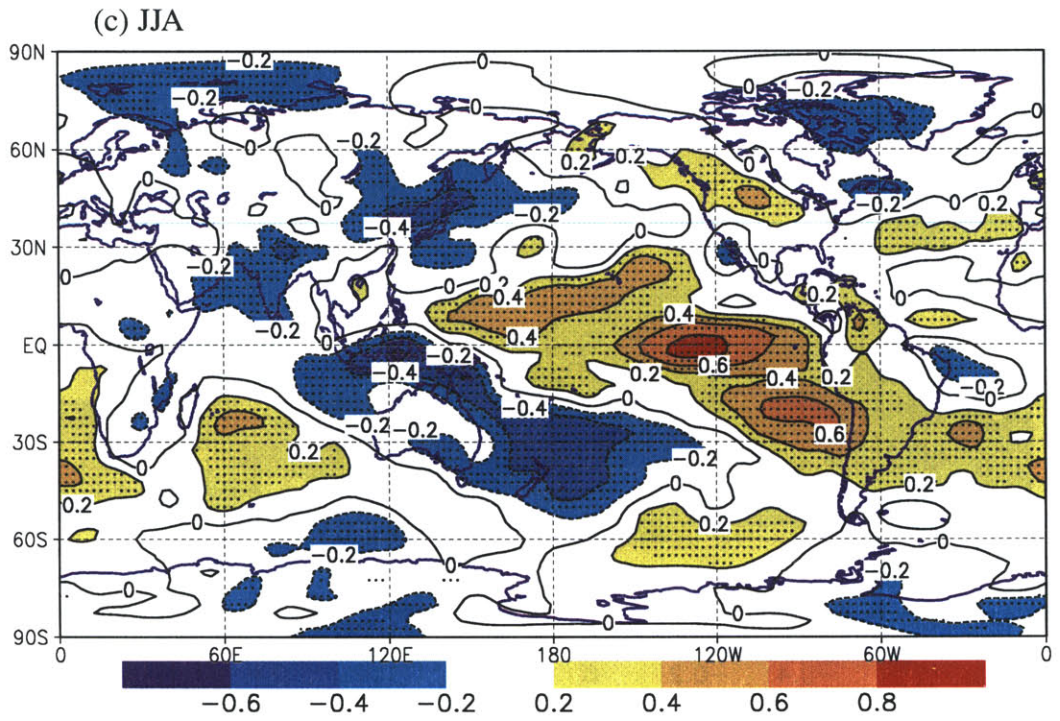

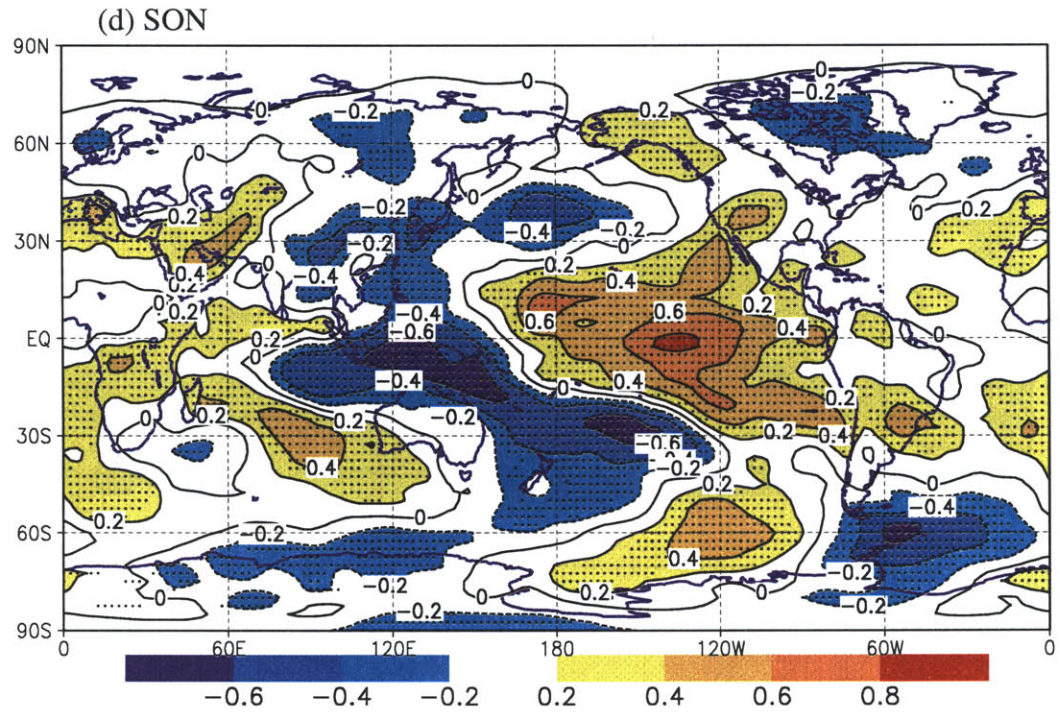

Figure 5.8: (*Continued*)

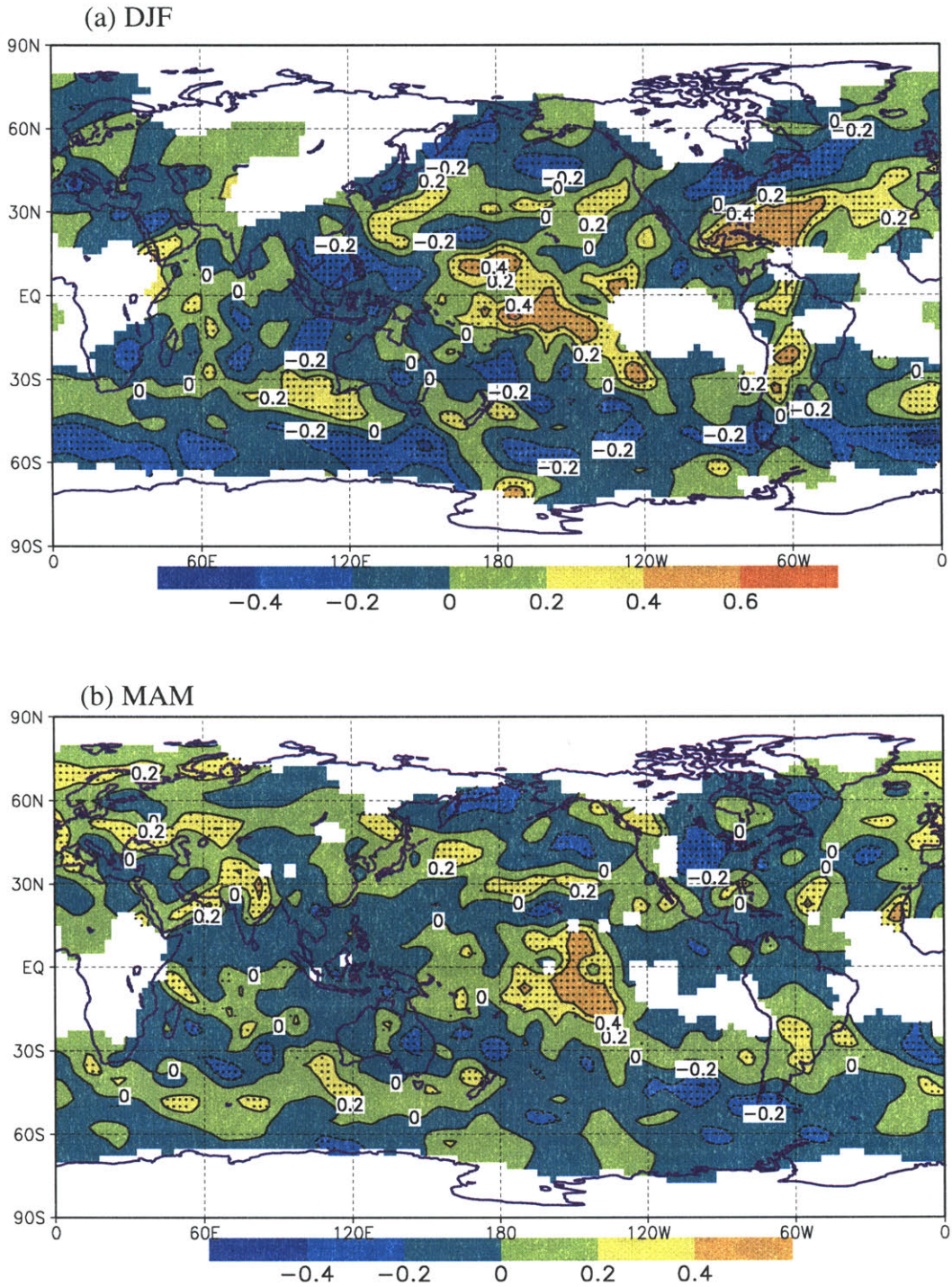

Figure 5.9: The time-synchronous correlation between the TR system density and the ENSOI for (a) DJF, (b) MAM, (c) JJA, and (d) SON over the period 1958-2000. The contour interval is 0.2. Areas where correlations are significant at or above the 90% confidence level are stippled.

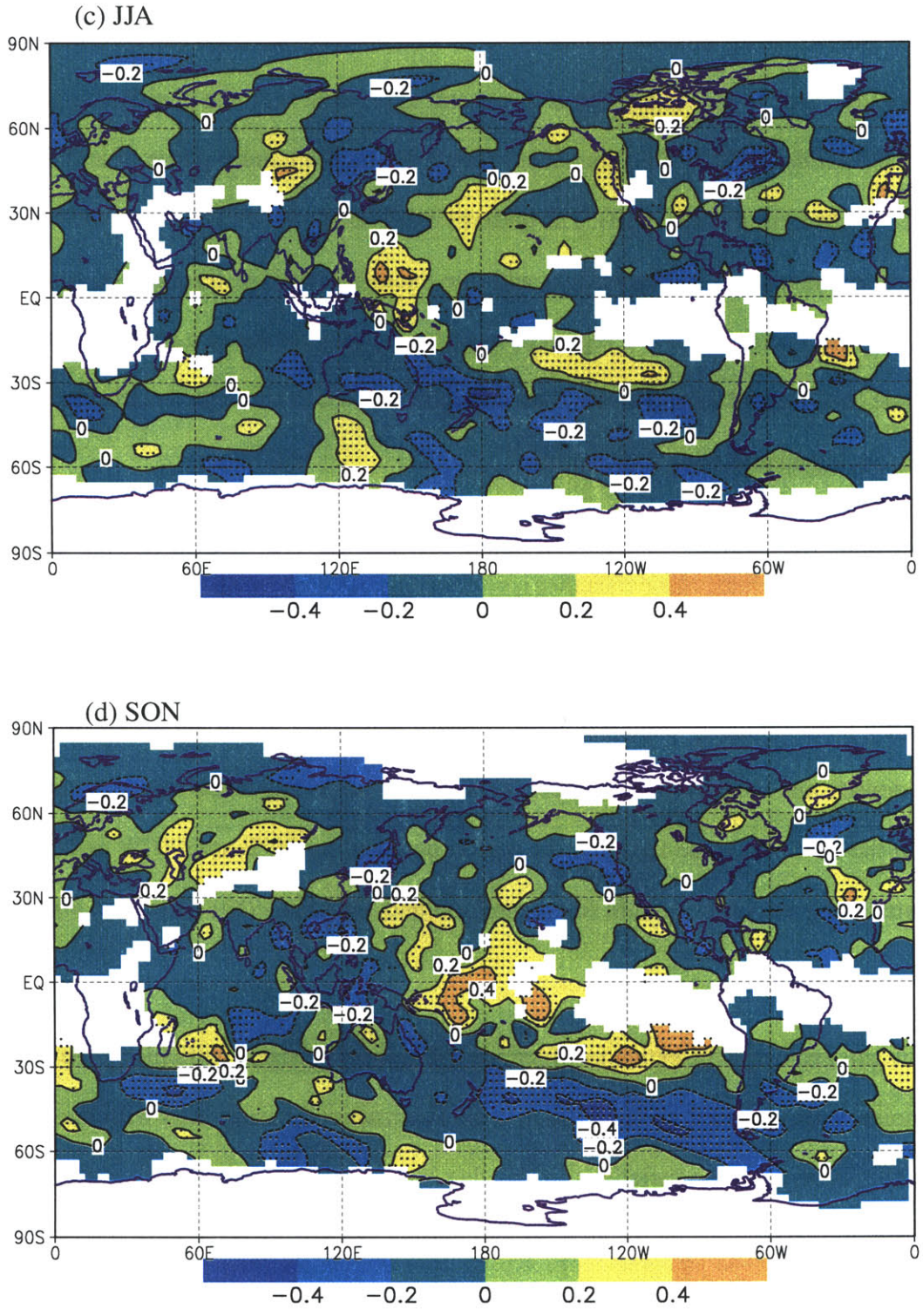

Figure 5.9: (*Continued*)

the ENSOI is positive (negative) can be found in the mid and high latitudes of the southern Atlantic, Indian Ocean, and over southern South America. A westward shift of TR density is also evident east of the Andes and is in general agreement with the positive correlation of rainfall with the ENSOI (i.e., abundant rainfall during the mature phase of an El Niño, see Marengo and Hastenrath 1993). The patterns exhibited in the other seasons are broadly similar to that displayed in Figure 5.9a with the exception of JJA: through the central to eastern tropical Pacific there is a region of negative correlation but of a generally reduced magnitude and limited significance; and no significant correlation is found over South America during austral winter and spring.

In general, the patterns of the correlation between the TR system density and the ENSOI and that between the precipitable water and the ENSOI, were found to be similar to which the centers of action located over the central Pacific and the regions nearby. Apparently such similarity does not imply a phase coherence in the variations of the TR system density and the precipitable water. This is not a surprising result since the strongest signal in the ENSO is to be found in the region bounded by 90°E and 90°W as has been demonstrated by previous authors (e.g., van loon and Madden 1981; Trenberth and Shea 1987).

It is worth exploring the extent to which the TR system strength, particularly the meridional moisture flux carried by the TRs, may be systematically associated with the ENSO signal. This is because the variations in this flux on interannual or longer timescales may have important consequences for weather and climate (Rosen 1999). Figure 5.10 exhibits the time-synchronous correlation of the TR meridional moisture flux with the ENSOI for DJF. Again, during ENSO warm phases, the action center is over the tropical Pacific with negative correlations being found across much of the North Pacific, eastern tropical

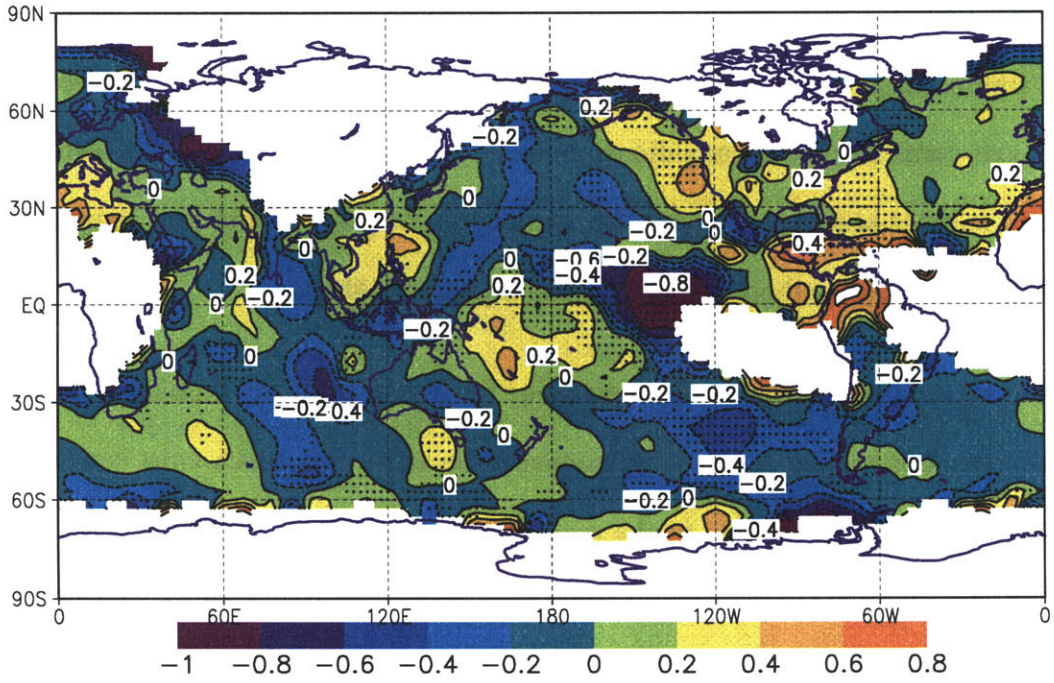

Figure 5.10: The time-synchronous correlation of the TR meridional water vapor fluxes during DJF with the ENSOI over the period 1958-2000. The contour interval is 0.2. Areas where correlations are significant at or above the 90% confidence level are stippled.

Pacific, and southeast Pacific, suggesting a decreased (enhanced) northwards (southwards) transport of water vapor; and positive correlations in the tropical South Pacific especially west of 160°W, yielding increased (decreased) northward (southward) moisture transport. This pattern indicates an enhanced meridional moisture convergence over the tropical North Pacific west of 160°W. In the northern extratropics, enhanced poleward fluxes during warm events also occur in the North Atlantic storm track and in the U.S. Pacific Northwest. The overall pattern strikingly resembles the map of meridional moisture-flux anomaly derived by Cohen et al. (2000) from the climatic mean of 14 warm-event DJFs (their Figure 4 bottom). Both figures are also similar to the meridional mass flux of

Waliser et al. (1999, Figure 13 of their paper) who investigated Hadley cell strength associated with ENSO signals, which suggests that enhanced lower-tropospheric winds contribute significantly in shaping the ENSO signal in the moisture flux. The time-synchronous correlation of the meridional moisture flux against the ENSOI are also calculated for the other seasons. Although the correlations are noisier and less significant, a general pattern similar to those in DJF remains (figures not shown).

While one needs to be cautious in interpreting the results obtained, even from relatively long data sets, this section serves to demonstrate the active ties which exist between the TRs which are synoptic aspects of the atmospheric circulation, and the broader atmospheric system.

5.5 Summary of the Chapter

This chapter was motivated by the unprecedented length of the NCEP/NCAR data which made possible a better sampling of the variability of moisture transport in the atmosphere. The application of a reliable numerical TR identifying and tracking scheme developed in Chapter 3 and the generation of unbiased TR data made it possible to produce TR variability result that is the first of its kind.

Our results have indicated that in the NH, the annual average number of TRs per analysis shows a fairly steady decrease at the start of the period to a minimum around the late 1960s and early 1970s, and a detectable upward trend since then. In the SH, the numbers

have shown an overall increase. Least squares best fit to the time series of TR counts shows that the slightly downward trend in the NH over the entire studied period is dominated by a significant (above 99% confidence level) reduction that occurred from 1958 to 1978, and a slope of 0.11 TRs decade^{-1} that is above the 95% confidence level is exhibited in the SH for the whole period. There has been a general reduction in TR numbers within the tropical region between 10°S and 30°N, and an increase north and south of it. The greatest increases occur in the 50°–30°S belt in the SH and in the 50°–70°N in the NH, respectively.

Corresponding trends in surface air temperature data have also been examined and attempts have been made to link the TR frequencies with them. The results suggest that warming and cooling trends are accompanied, respectively, by increases and decreases in TR frequencies (particularly so in the Southern Hemisphere).

When breaking down the TR counts into seasons, it is evident that TR counts are dominated by the warm seasons (JJA and SON in the NH, and DJF and MAM in the SH). On average, TRs occurring during the warm seasons appear to be ~ 40.9% more in the NH and ~ 28.0% more in the SH than those in the other half of the year.

The time series of the annual mean number of TR tracks resemble those of the TR counts, while no such relation can be found for the TR lifespan, indicating that the increase in TR numbers is largely due to more tracks rather than tracks tending to last longer. Both time series for the mean TR strength and mean TR meridional moisture flux exhibit an upward trend and strengthened poleward vapor transport, which suggest that the atmospheric moisture circulation has become more vigorous during the last couple of decades. In this context, our result of a trend toward larger moisture transport is in line

with other independent evidence which suggests that the global hydrological circulation may be accelerating (Chahine et al. 1997; Trenberth 1998; Cohen et al. 2000).

When compared to trends in cyclone and anticyclone frequencies obtained from previous studies, there appears to be an increase (decrease) in both surface cyclone and TR activities during long-term warming (cooling) in the NH. In the SH, however, while such a positive correlation between TR frequency and surface temperature is observed, mean cyclone counts have been seen to decrease since about 1970 indicating a negative correlation. We argue here that the geographical distribution of cyclones as well as their role in water vapor transport, is very different in the two hemispheres, hence the trends and variabilities of rivers.

The geographical distribution of long-term trends in TR system density show that negative trends are found largely over tropical and subtropical regions and positive trends in middle to high latitudes. The latter are mostly located over oceanic areas and account for most of the strong signals in the corresponding latitudinal belts.

Finally, our discussion of TR variability would not be complete without some reference to the changes that have been occurring in ENSO events over the studied period. We have presented synchronous correlations for the system density and meridional moisture flux of TRs against the ENSO index to demonstrate the active links which exist between the large-scale atmosphere-ocean system and the TRs. In general, the patterns of the correlation between the TR system density and the ENSOI and that between the precipitable water and the ENSOI showed similarity with the primary centers of action lying in the central Pacific regions. The correlation of TR system density against the ENSOI displayed a complex structure. There is a suggestion of an equatorward (poleward) displacement of the region of highest TR density during episodes of positive (negative) ENSOI. An east-

ward shift of the TR density corresponding to the eastward extension of the SPCZ and a westward displacement of system density east of the Andes that account for increased rainfall during positive ENSOI periods are also evident, particularly during DJF. The correlation between the TR meridional moisture flux and the ENSOI indicates that during ENSO warm events, there is an enhanced meridional moisture convergence in the tropical North Pacific west of 160°W. As pointed out by Cohen et al (2000), because of an increase in tropical SSTs and the frequency of warm events relative to cold events in the latter half of the data set, this interannual signal projects onto an overall trend toward enhanced meridional moisture transport in the global hydrological cycle.

Chapter 6

Conclusions and Future Work

6.1 General Remarks

In this thesis we investigated the atmospheric water vapor transport through a distinct synoptic phenomenon, namely, the Tropospheric River (TR), which is a local filamentary structure on a daily map of vertically integrated moisture flux. The rivers appear to account for a substantial fraction of the total moisture transport, especially for meridional transport at middle and subtropical latitudes. Owing to the inherent limitations of manual techniques, however, there has been no consensus on how to define a river objectively, which in turn has impeded attempts to compile statistics for this important synoptic occurrence. An objective numerical scheme, the Tropospheric River Identifying and TraCKing Scheme (TRICKS), has been developed to provide an efficient and much needed tool for the study of TR climatologies. The scheme was adapted from a cyclone finding and tracking program for the Southern Hemisphere from Melbourne University to expand its capability of identifying and tracking a one-dimensional maxima/minima atmospheric property at any given vertical level (or for integrated column quantities) on either global or

regional grid. When applying to the moisture-flux gridded data, the speed of a computer-based scheme has permitted a very satisfactory solution to the problem of applying differential methods for the TR Core (TRC) determination, TR identifying, and tracking. The resultant procedure enables both strong and weak, closed and open TRCs to be detected and accurately located. The relationships among the adjacent TRCs are evaluated to see whether they belong to the same river. A Tropospheric River Major Core (TRMC) is identified to represent the river movement and its path is tracked from birth to termination (which also signifies the birth and termination of a TR). Various statistics of TR distribution and movement are then analyzed. All these stages of the scheme are performed without intervention once a number of governing constants have been decided upon, thus allowing objective comparisons to be made between TR statistics obtained from different data sets.

The scheme has been tested and found to operate reliably at different stages. It has been shown to produce results consistent with those from manual analysis and can be applied with confidence not only to a range of operational analyses and model outputs, but also for a reworking of historical analyses.

The aim of compiling a synoptic climatology and variability for TRs objectively has been substantially achieved with application of this scheme to the vertically integrated moisture flux calculated from a 43-yr multidecade data set from the NCEP/NCAR reanalyses. The generation of unbiased data has made possible the development of a comprehensive set of statistics, many of which have never been presented previously.

In this chapter, the relationship between TR and regional climate and the possible mechanisms of TR formation are discussed in section 6.2. Main conclusions for mean TR

behavior and its variability are summarized in section 6.3. Future work will be addressed in the following section 6.4.

6.2 Discussion

Vertical integrals of moisture flux are dominated by events in the lower atmosphere because of the decrease of specific humidity with altitude. A TR defined by our automated objective method only depends on whether or not a filamental structure in these vertical integrals occurs, with no preference given to either components of wind or moisture content. Although such a scheme is very useful in identifying and tracking major water vapor transport events, it does not offer more detailed variations in the TR's vertical and horizontal structures. To appreciate the importance of TRs in both horizontal and vertical moisture transports, we present here a river case occurring over the North Atlantic at 00 UTC January 25, 1992. The same case was presented by Newell and Zhu (1994) using ECMWF data for only one along-stream vertical cross-section (see their Figure 2). A more detailed analysis was conducted using a different data set (the NCEP/NCAR reanalyses) with the important 925 hPa level data incorporated.

The vertically integrated moisture fluxes along with the mean sea-level pressure are displayed in Figures 6.1. A well-defined moisture filament carrying a substantial fraction of water vapor from the region off the southeast United States into Greenland is evident in the center of the domain. This river is apparently associated with the cyclonic system on its western and poleward edge with the minimum center pressure less than 975 hPa.

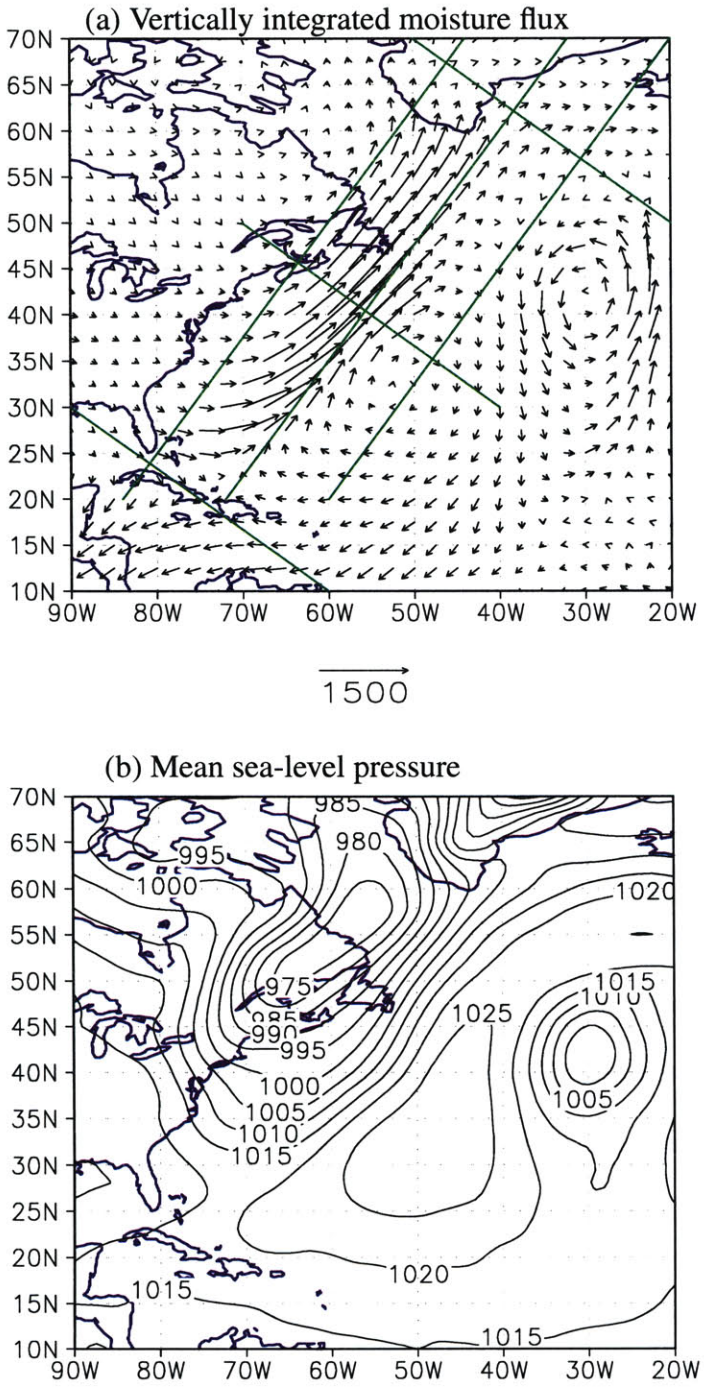

Figure 6.1: (a) Vertically integrated water vapor flux for 00 UTC January 25, 1992 showing a river terminating in Greenland from the western Atlantic. The longest arrow corresponds to about 1500 kg m^{-1} s^{-1}. The green lines indicate the cross-section lines for Figure 6.2; (b) Mean sea-level pressure (unit in hPa).

Significant moisture fluxes are found flowing parallel to and immediately ahead of the surface cold front. We define three along-stream and three cross-stream vertical cross-sections (indicated on Figure 6.1a) such that the differences in water vapor transport between the center of the filament (either along or normal to the stream, i.e., cross-sections from 20°N, 72°W to 70°N, 32°W; or from 50°N, 70°W to 30°N, 40°W) and the nearby cross-sections can be assessed. Figure 6.2 shows that along the river axis, the region is dominated by large southwesterly water vapor flux sloping upwards from low latitudes near the surface to higher altitudes at high latitudes (Figure 6.2b), with a maximum greater than 280 (kg kg^{-1} m s^{-1}) around 925 hPa above the ground. The fluxes are in general aligned to the equivalent potential temperature surface (dashed contours in the figures) indicating the flow is nearly saturated (note the vertical components of the flux vectors have been magnified by a factor of 5 but no magnification for the vertical components in flux magnitude contours). In conjunction with this poleward transport, upward moisture flux is also significant when examining the cross-stream cross-section in the middle of the filament in Figure 6.2e. The V-shaped θ_e contours with the dip line (corresponding to high θ_e values) co-located with the vertical line of maximum vertical moisture fluxes also suggests that the air within the filament is characterized by a highly concentrated horizontal warm moisture tongue, especially below 850 hPa. No such coherent structures can be found along the cross-sections some distance parallel to the river axis (Figures 6.2a and 6.2c), or near its head and tail (Figures 6.2d and 6.2f). These features are consistent with the finding by Zhu and Newell (1998) that the middle-latitude rivers were in or slightly ahead of the surface troughs. The equatorward and poleward flows on the west and east sides of the troughs, respectively, form filamentary wind shears or convergence lines over the surface. Sharp contrasts in temperature and humidity may occur along the convergence lines in the lower troposphere, and the poleward moisture fluxes are stronger than the equatorward fluxes

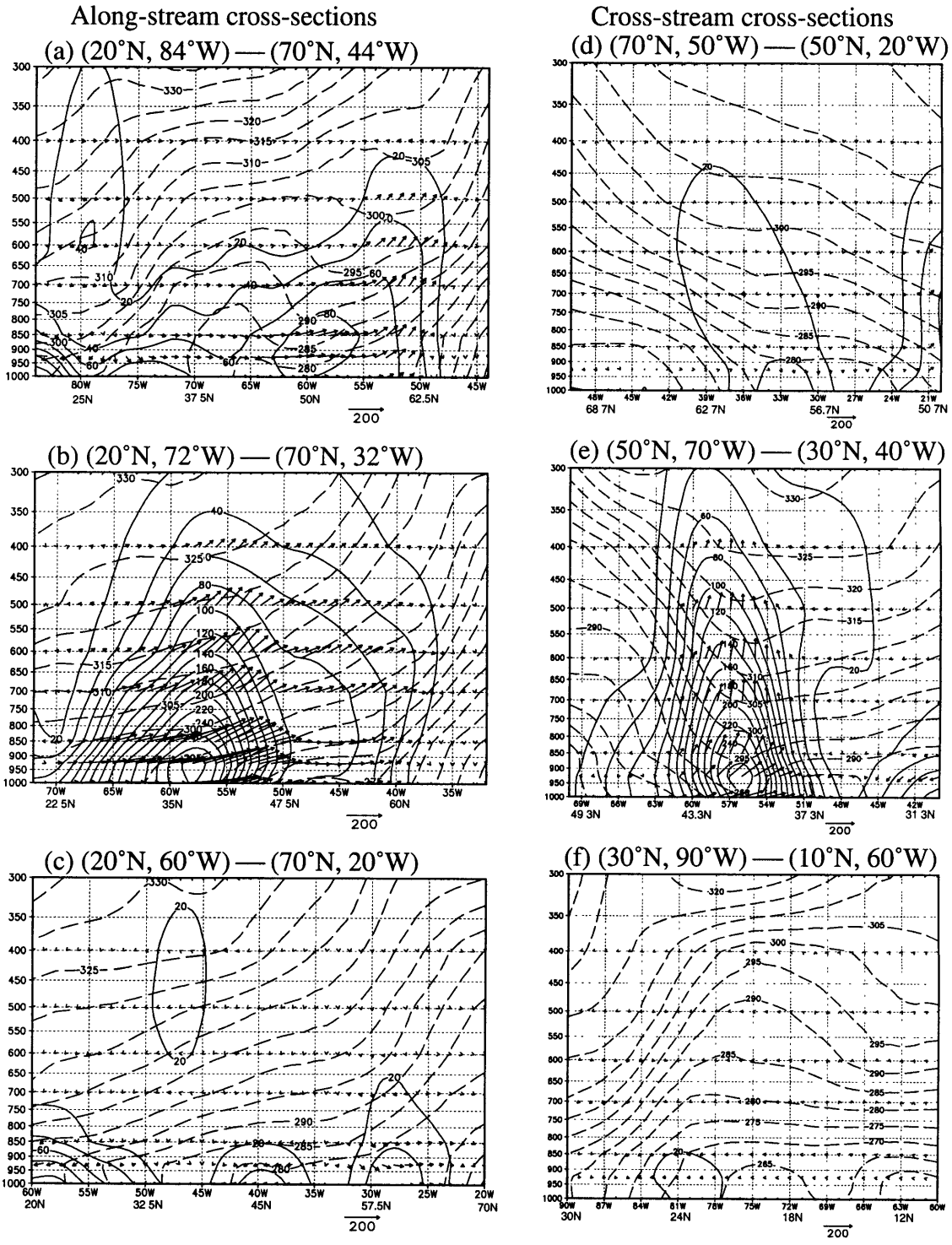

Figure 6.2: Along-stream (left) and cross-stream (right) vertical cross-sections showing water vapor flux vectors (the vertical component has been magnified by a factor of 5 to reveal its significance), flux magnitudes (solid lines, no magnification for the vertical component, contour interval 20×10^{-3} kg kg^{-1} m s^{-1}), and equivalent potential temperature (dashed lines, in K). The cross-section lines are indicated in Figure 6.1.

even if the opposite mass fluxes have the same intensity. The poleward fluxes formed by large-scale processes on the warm side of temperature fronts may be further intensified and narrowed by meso- and small-scale convective activities along the convergence lines. Formation of rivers may be independent of the genesis and development of baroclinic cyclones, though the cyclone activity may have an effect on the development of rivers. For example, when baroclinic waves are destabilized, the cold and dry air behind a polar front fills up the low levels of a new cyclone. As a result, the river is pushed to the eastern edge of the cyclone and may be intensified as the wind speed increases in the disturbance development.

As we mentioned in Chapter 1, the concept that moisture, horizontal and vertical motion, and clouds are found in a fairly narrow region associated with an extratropical cyclone is referred to as the warm conveyor belt (WCB) following Harrold (1973). There are many similarities which can be drawn between the river case presented here and the WCB. Ludlam (1966) described a model which shows how the baroclinic slantwise motions are organized on the large scale (Figure 6.3a). The dominant feature is the elongated band of clouds (hatched) that forms along the boundary of a major confluence zone at the leading edge of the trough. In the frame of reference moving with the trough-ridge system, warm air enters the cloud belt from the convective boundary layer at its southern end. As this air travels along the axis of the cloud belt it ascends into the middle and upper troposphere, producing low- and medium-level clouds and then a belt of upper-level cirrus that dissipates at the leading edge of the system.

Vertical sections derived from radiosonde ascents along the axis of WCBs confirm that the WCBs are mainly saturated flows of high wet-bulb potential temperature, rising from the lower troposphere at their southern end into the upper troposphere at their northern end

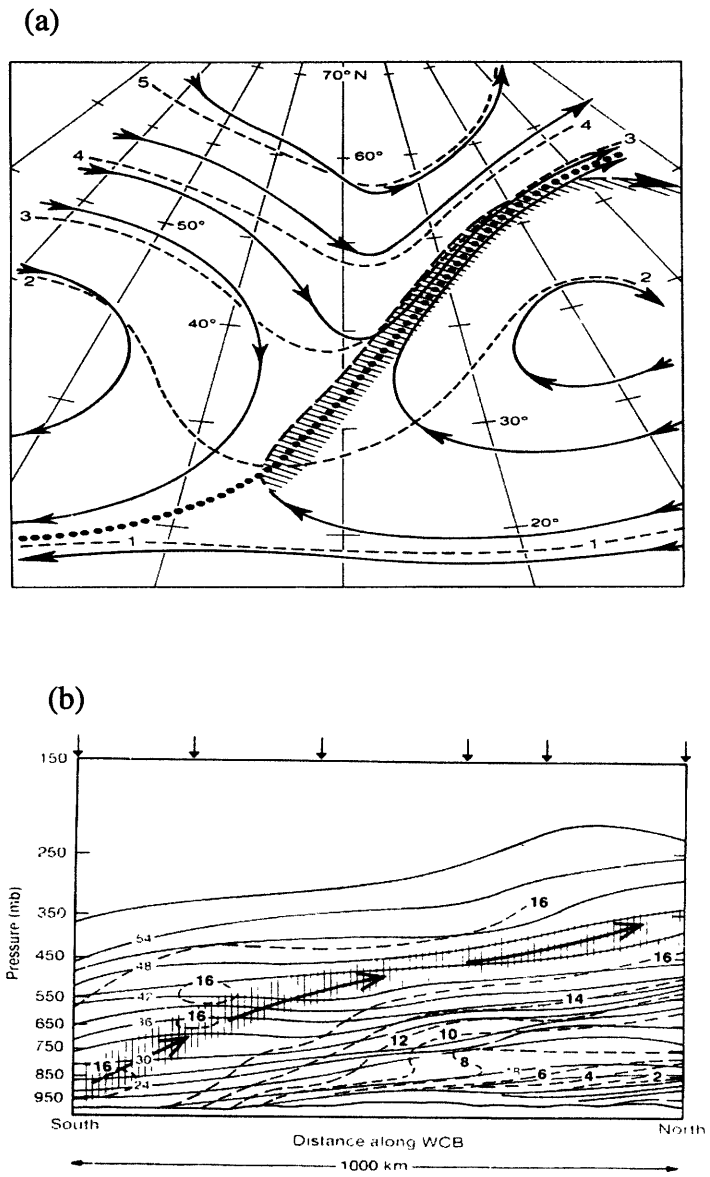

Figure 6.3: (a) Model of flow relative to a major middle-latitude trough within an isentropic surface sloping generally upward toward the north (heights indicated by dashed lines labeled in km). A sea-level cyclone is centered beneath this surface in the northern part of the diagram. A confluence line (dotted) in the flow aloft separates two distinct airstreams. The northward-moving stream ahead of the confluence line ascends above the dry isentropic surface and produces a cloud-belt (hatched) (Ludlam 1966); (b) Cross section along the axis of a WCB derived from a chain of six radiosondes over a distance of 1000 km in the eastern U.S., showing potential temperature θ (solid lines labeled in °C) and wet-bulb potential temperature θ_w (dashed lines labeled in °C) at 12 UTC 27 February 1984. Hatching represents the axis of maximum relative humidity (> 90 percent). Arrows parallel to the sloping layer of high-θ_w suggest motion of air within the WCB (Carlson 1987).

(Carlson 1987). This is clearly displayed in Figure 6.3b from an example of observed WBC. Considerable precipitation is generated in the WCB flow especially where it ascends rapidly in the low-to-middle troposphere.

As pointed out by Browning (1990), the WCB is not the only important well-defined flow within an extratropical disturbance; it is, however, the primary cloud-producing flow. Thus it has been found to be a particularly useful concept in practice to account for aspects of clouds and precipitation. Emanuel et al. (1987) showed that the warm southerly flow is substantially stronger than the cold northerly flow in a moist multilevel semigeostrophic model. They found that when the effective potential vorticity is small in regions of upward motion, growth rates are modestly increased and the region of ascent intensifies and collapses onto a thin ascending sheet. In the limit of zero moist potential vorticity the fastest growing wave has a finite growth rate which is several times larger than the dry model result while the horizontal scale is contracted significantly compared to the dry modes.

As we learned from mean tropospheric river behavior in Chapter 4, TRs occur frequently in many parts of the world. The river case above and several previous studies have shown these TRs to be associated with the development and evolution of synoptic events such as cyclogenesis, atmospheric bombs, deep convection, and heavy rainfall, etc. (e.g., Zhu and Newell 1994; Smirnov and Moore 1999). The relationship between TRs and these synoptic phenomena suggests that TRs are important contributors to regional climate. A strong TR is a recurrent feature of the precursor environment of mature systems. While it is likely that TRs by themselves do not cause the development of convective activity, since they produce broad regions of ascending motion, they help to produce a favorable environment in which convection can organize and persist. This hypothesis is

supported by noting that strong TRs are not present during the dissipation stages of a baroclinic system when divergence, cold advection, and descending motion are prevalent.

Apart from the relationship between TRs and the Asian summer monsoon as we discussed previously in Chapter 4, a close examination for relationships between TRs and various regional climate features such as low-level jets (LLJs) and mesoscale convective complexes (MCCs) is warranted. Although LLJs are important dynamically, they are not crucial contributors to transport if there is no water vapor associated with them. It is well known that MCCs account for a large portion of warm season rainfall over the United States (Fritsch et al. 1986; Heideman and Fritsch 1988) and produce significant amounts of high-level cloudiness as seen in monthly frequency counts of cloud-top temperatures (Maddox et al. 1992). Most of these regions of significant MCC activity also are regions of frequent TR activity as well. There is also evidence that some rivers appearing as orderly features may be several hundred or thousand kilometers away from cyclonic precipitation systems. In order to place TR in a clearer perspective relative to regional climate phenomena, further river case studies are needed to account for different types of TRs.

There are several possible physical mechanisms that may be related to the development and evolution of TRs in a wide variety of environments. For example, shallow baroclinicity caused by significant change in surface characteristics or gradients in sea surface temperature (recall in Chapter 4, TR genesis regions are found to be adjacent to the maximum SST gradients) may favor to produce or maintain TRs through geostrophic forcing. A TR also can occur/develop owing to the terrain effects (blocking or temperature gradient due to sloping terrain). These are important to understand since, once the mechanisms are known, the influence of numerical model grid spacing and physical parameterization schemes can be evaluated for the likelihood that a given model can simulate TRs.

6.3 Main Conclusions

6.3.1 Main Conclusions for the Mean TR Behavior

(1) Characteristics of TR distribution:

On average, there are 4 - 5 rivers per analysis in the Northern Hemisphere and 5 in the Southern Hemisphere. The axes of the greatest system densities are found principally in the middle latitudes over major oceanic basins in both hemispheres for all seasons, and major localized maxima are situated over the Bay of Bengal and Arabian Sea during JJA (related to the summer Asian monsoon) and over Northern Australia during DJF (related to the Australian monsoon). When stratified by 20° wide latitude bands the greatest number of TRs is found in the 30°-50° band of each hemisphere. TR tracks are most concentrated near those principal oceanic regions of TR densities in all seasons, indicating that TRs are migratory in character over these areas but are somewhat stationary over monsoon-related regions mentioned above.

(2) Characteristics of TR life cycle:

Northern Hemisphere TRs form and intensify near the eastern seaboards of Asia and North America, with activity focused near the regions of strongest SST gradient. They move eastward and poleward during their lives before weakening in the two principal graveyards: over the Gulf of Alaska and to the southeast of Greenland. In comparison, SH TRs are more evenly distributed and tend to form in a band extending from the southeast coast of South America into the Atlantic, across the Indian Ocean, and throughout much of the Pacific middle latitudes. The corresponding gen-

esis regions are also found to be adjacent to (or slightly equatorward of) the maximum SST gradients in these regions. Aside from regional features, for the most part genesis exceeds termination south (north) of about 45° N (45° S) in the NH (SH), while the converse is true north (south) of this latitude. Both TR genesis and termination maxima tend to be near the upstream equatorward flank of those of cyclogenesis and lysis except for cyclogenesis maxima occurring in the lee of major mountain ranges and over land due to the thermal effect. We suggest that TR formation and termination could be a leading predictor for the occurrence and decay of extratropical cyclones.

(3) TR properties

Our results indicate that the most intense TRs occur over the western portion of the oceanic basins (except for the South Pacific where the maxima are located near its southeast) with maxima somewhat to the poleward of the regions of maximum density in the NH, or approximately the same locations in the SH. In each hemisphere, the strongest TRs occur during the corresponding summertime over the northwest Pacific and off the east coast of South America, respectively. One unique feature is that although TRs occur very actively over the Indian ocean sector with highly densed tracks, large translational speeds, and intensities, they contribute little to meridional water vapor transport, while the reverse situation can be found in the South Pacific where southward transport is sometimes comparable to those over or off the east coast of South America. The rivers seem to account for a substantial fraction of the total meridional moisture transport in both middle and subtropical regions. TR axis length appears to be longer during the warmer seasons and in the SH. The mean axis length of a TR is approximately 2284.0 km. The mean lifetime of TRs that

last at least 1 day is just a little over 2 days. Those that are located between 10° and 50° (at their half-lifetime) endure, on average, almost ~ 0.5 day longer than those in other latitudes. About 10% of all TRs travel less than 900 km and approximately 25% travel in access of 3000 km.

6.3.2 Main Conclusions for the Variability of TR Behavior

(1) Characteristics of TR counts and property trends

The annual average number of TRs per analysis has undergone an overall increase during the last couple of decades, which is more significant in the Southern Hemisphere. Corresponding trends in surface air temperature data have also been examined and the results suggest that warming and cooling trends are accompanied, respectively, by increases and decreases in TR frequencies (particularly so in the Southern Hemisphere). When breaking down the TR counts into seasons, it is evident that TR counts are dominated by the warm seasons (JJA and SON in the NH, and DJF and MAM in the SH). On average, TRs occurring during the warm seasons appear to be ~ 40.9% more in the NH and ~ 28.0% more in the SH than those in the other half of the year. The time series of the annual mean number of TR tracks resemble those of the TR counts, while no such relation can be found for the TR lifespan, indicating that the increase in TR numbers is largely due to more tracks rather than tracks tending to last longer. Both time series for the mean TR strength and mean TR meridional moisture flux exhibit an upward trend and strengthened poleward vapor transport, which suggest that the atmospheric moisture circulation has become more vigorous

since the last two decades. When compared to trends in cyclone and anticyclone frequencies obtained from previous studies, there appears to be an increase in both surface cyclone and TR activities during long-term warming and vice versa in the NH. In the SH, while such a positive correlation between TR frequency and surface temperature is observed, mean cyclone counts have been seen to decrease since about 1970 indicating a negative correlation. We argue here that the geographical distribution of cyclones as well as their role in water vapor transport, is very different in the two hemispheres, hence the trends and variabilities of rivers.

(2) Geographical distributions of trends

During the studied period, there has been a general reduction in TR numbers within the tropical region between 10°S and 30°N, and an increase north and south of it. The greatest increases occur in the 50°–30°S belt in the SH and in the 50°–70°N in the NH. The distribution of long-term trends in TR system density show that negative trends are found largely over tropical and subtropical regions and positive trends in middle to high latitudes. The latter are mostly located over oceanic areas and account for most of the strong signals in the corresponding latitudinal belts.

(3) Relationships with ENSO events

The phenomenon with the largest known influence on interannual variability, ENSO, imparts a detectable signal on both TR system density and strength. There is a suggestion of an equatorward (poleward) displacement of the region of highest TR density during episodes of positive (negative) ENSO Index. An eastward shift of the TR density corresponding to the eastward extension of the SPCZ, and a westward displacement of system density east of the Andes that account for increased rainfall

during warm ENSO periods are also evident, particularly during DJF. The correlation between the TR meridional moisture flux and the ENSO Index indicates that during ENSO warm events, there is an enhanced meridional moisture convergence in the tropical North Pacific west of 160°W.

In summary, we comment that this work represents the first step in a Lagrangian analysis of TR behavior. Automated Lagrangian analysis has a history much shorter than Eulerian analysis. We see it as important that both perspectives of TRs be retained. It is crucial to bear in mind, however, that the two approaches are sometimes telling us different things and that direct comparison of results should be undertaken cautiously.

In what follows, we will discuss an outline of future directions for this research.

6.4 Future Work

6.4.1 Improvement of the Scheme

An immediate future effort should be directed to further improve TRICKS, especially the objective criteria for identifying a Tropospheric River. For example, a TR defined in the thesis only depends on whether or not a filamental structure with large moisture flux occurs, with no consideration of preference given to either components of wind or moisture content. A more refined criterion may require the magnitude of either the maximum

wind speed or the maximum moisture content (or some combinations of them) to decrease by a specified amount near the maximum in the cross-axial dimension in order to give a jetlike (filament like) profile.

Since the river width is estimated through an alternative way in the thesis which may compromise the accuracy for the mean river flux estimation, it is desirable to extend the scheme's ability for identifying rivers in two dimensions (i.e., both width and length) so that the influence of these systems can be more accurately estimated. Although such an endeavor can be validated meaningfully only when the gridded data have sufficient resolution to resolve the width of a river, a statistical criterion could be established for the coarse data set based on the examination from a high resolution data set. A potential data set that can be utilized for this purpose is that of current ECMWF operational analysis. The resolution of its global atmospheric model has been increased to T511 since November 2000. This is roughly equivalent to a resolution of 40 km.

6.4.2 TR Database

There is good reason to try to distinguish between the many types of TRs since the temporal and spatial scales associated with them can be vastly different, as can the forcing mechanisms. We hope to construct a TR database that contains various TR information at each track point obtained from an extended series of NCEP/NCAR reanalysis (1948 to present). This will establish a benchmark contemporary climatology that will advance our understanding of the behavior of these systems and how they respond to and influence climate variability. We will design an objective method for selecting cases from this TR database. This avoids laborious manual examination of thousands of synoptic charts to find suitable

TRs. Case selection will instead be done by a computer search of the database for TRs having specified properties. Selections can be on the basis of year, month, day, location, intensity (e.g., averaged $\nabla^2 q$, or averaged meridional TR moisture flux), stage of development, and from intensity change characteristics.

Water vapor flux divergence near the leading edge of a river is a possible predictor for the intensity change of the cyclone associated with the river. As pointed out by Zhu and Newell (1994), a moisture flux convergence of 10^{-4} kg m^{-2} s^{-1} is corresponding to a heating rate by the liberation of latent heat of about 2.7K day^{-1} if an atmospheric column 800 hPa is considered. The average of maximum convergence values for the 7 atmospheric bombs occurred in the North Pacific estimated by the authors is about 11.85×10^{-4} kg m^{-2} s^{-1}, corresponding to a heating rate of ~32K day^{-1} (this can be compared with the maximum rate of about 26K day^{-1} reported for an explosively deepening North Pacific cyclone for which a detailed heat budget was made by Liou and Elsberry, 1981). The role of latent heat is to make the ascent stronger than it would otherwise be and results in strong vortex stretching and a spin-up of the low-level vorticity. Though the maximum moisture flux divergence near the leading edge of a river can not be estimated directly from the current scheme, it is possible to include this quantity calculated from the original input moisture flux field after taking into consideration of the identified TR information.

Individual case studies based on intensive observational campaigns such as the Pacific Exploratory Mission (PEM) (including PEM-West phases A and B, and PEM-Tropics phases A and B) have revealed the rich palette of atmospheric layering structures and their life cycles. There is now a growing effort to bring much of this work together by attempting to classify precursor synoptic-scale flow patterns and different layers (e.g., Newell et

al. 1999; Gutowski et al. 2001). Automated case selection from objectively derived track data incorporating certain parameters as are germane to such classifications will increasingly be needed to assist with the huge task of assessing the relative importance of these structures.

TR climatologies in comparison may be sensitive to data sets used. It would be desirable to compare TR system climatologies from different data sets to identify systematic differences between the handling of TRs in different numerical models and assimilation systems. Work is about to commence on obtaining TR statistics from a GCM to assess its ability in replicating contemporary TR system behavior and to identify possible shifts in TR characteristics under climate change scenarios. In this task, it will be essential that small differences between different data sets are not artifacts of the TR finding and tracking methodology.

6.4.3 Numerical Simulation

Numerical models could be used to achieve the following objectives:

- to characterize the TR spatial structure and its evolution, *i.e.*, what are the large- and meso-scale mechanisms by which differences in surface characteristics, cumulus parameterization schemes, and regional circulation features associated with the initiation and subsequent persistence of the TRs?
- to establish the conditions under which a river appears to be torn off a tropical strip of westward-flowing moisture as often observed from daily maps.

- to study the effect of TRs on the development of moist disturbances, and the interactions between TRs and synoptic systems such as low-level jets, cyclogenesis, atmospheric bombs, deep convection, and heavy rainfall, etc.
- to investigate the role of TRs in association with some extreme weather events such as 1993 Upper Mississippi River basin flood and the extremely high rainfall event in 1994 summer over South China-Hong Kong region, etc.
- to investigate the cause and maintenance of annual and seasonal variations of global hydrological cycle using GCM, and study the role of TRs on climatological variabilities within the water balance considerations if the rivers can be simulated in a GCM model that has a sufficient grid resolution.

At present, simulation studies are being conducted using either a case study approach or simplified analytic initial conditions to examine TR sensitivities to various model parameters. In order to obtain a high-resolution picture of a TR's evolution, we used a limited area model (MM5V2) to simulate a TR occurring over eastern North America in the late September of 1996. The model description, experiment setup, and results are given in Appendix A. We showed that the geometry and dynamics of the filament determine the cloud and precipitation as well as the structure and evolution of the cyclonic system nearby. It also reveals that the river is a very effective mechanism for the poleward water vapor transport.

The advantage of using numerical models is the ability to separate the effects of various physical processes on the TR evolution. The model outputs make it possible to study quantitatively the mechanisms that produce TRs and the effects of various model parameterization schemes and model grid spacings on TR development.

By the same token, analytic solutions and numerical simulations using semigeostrophic Eady model with condensation heating such as those derived and conducted by Emanuel (1987) could be a useful tool for theoretical and numerical study on many processes which involved in various stages of a TR development.

Improved extended-range weather forecasts will result from more accurate numerical model predictions of the onset and duration of TR episodes. Automated techniques such as those described in the thesis are valuable tools for evaluating and comparing the performance of models in simulating such episodes. However, work is needed to develop more meaningful objective criteria for identifying persistent circulation features such as TRs that are responsible for extended periods of anomalous regional weather.

6.4.4 Upper Tropospheric Rivers

Many recent studies have stressed the importance of upper-tropospheric moisture in climate and radiation, emphasizing the need for an observational base to evaluate the upper-tropospheric hydrology in climate models. Satellite imagery in water vapor channels reveals extensive upper tropospheric "rivers of moisture" flowing from the tropics to the mid-latitudes. The extent to which the Earth's climate will warm as a result of increasing carbon dioxide in the atmosphere depends largely on the response of water vapor in the upper levels of the troposphere (roughly 5-10 km above the surface).

The overall cloud fields are produced by broad slantwise ascent within "conveyor belts" that redistribute heat, momentum and moisture over great distances (see for example Carlson, 1980; Saarikivi and Puhakka, 1990). The production of clouds at different

levels within the overall cloud system is also an indication of the role of these features in the transport of moisture throughout the troposphere. The warm conveyor belt in particular plays a critical role in lifting low level (and low latitude) moisture up to high levels of the troposphere. The extensive cirrus canopies linked with these systems are an excellent indication of the result of such a flow field. These cloud systems are associated with the subtropical jet stream and often connect the convective source of upper tropospheric water vapor in the tropics to extratropical weather systems. It is desirable to develop a similar objective scheme as in this thesis to identify and track these upper tropospheric rivers. Work is in progress in constructing a climatology (including its variability) by applying such a scheme to the partially vertically-integrated (from 700 hPa to 300 hPa) moisture fluxes calculated from the NCEP/NCAR reanalysis data.

Appendix A

A Numerical Case Study

A.1 Brief Description of the MM5V2 Model

The Fifth-Generation NCAR/Penn State Mesoscale Model (MM5) is the latest in a series that was developed from a mesoscale model used by Anthes at Penn State in the early '70s that was later documented by Anthes and Warner (1978). Since that time it has undergone many changes designed to broaden its usage. These include: (1) a multiple-nest capability, (2) nonhydrostatic dynamics, and (3) a four-dimensional data assimilation (4DDA) capability, as well as more physics options, and portability to a wider range of computing platforms.

The main advantages of MM5 Version 2 (MM5V2) are its non-hydrostatic option and more detailed model physics formulations incorporated in the cumulus convection, radiative transfer, and cloud schemes. It can be used for a broad spectrum of theoretical and real-time studies, including applications of both predictive simulation and 4DDA to monsoons, hurricanes, and cyclones. A schematic diagram (Figure A.1) is provided showing a

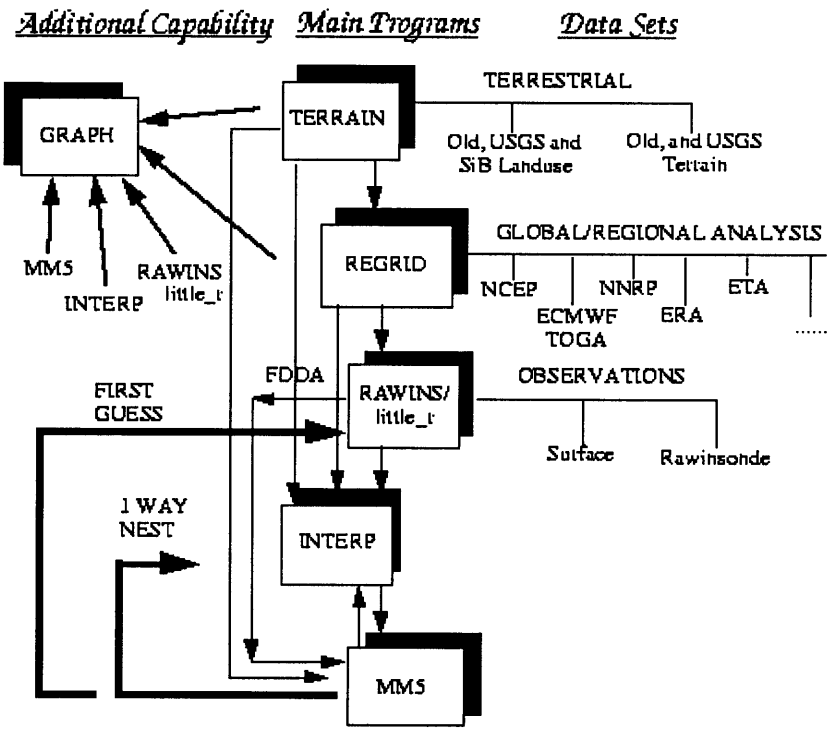

Figure A.1: The MM5V2 modeling system flow chart.

flow-chart of the complete modeling system. It is intended to show the order of the programs, flow of the data, and to briefly describe their primary functions.

The model uses a terrain following vertical coordinate and an Arakawa-Lamb B-staggered horizontal grid. Second-order centered spatial finite differences represent the gradients except for the rainfall term which uses a first-order upstream scheme for positive definiteness. A second-order leapfrog time-step scheme is used, but some terms are handled using a time-splitting scheme. More details on basic model dynamical structure can

be found in the latest MM5V2 Release Notes at http://www.mmm.ucar.edu/mm5/documents (1999).

A.2 Experiment Setup

In this section, we provide a brief description of the numerical experiment performed in the appendix. The experiment is designed to simulate the atmospheric and hydrological processes related to a river occurring over the eastern coast of North America. The simulation is initialized at 00 UTC September 27, 1996, and is integrated for three days. Figure A.2a depicts the domain and associated topography. Close attention has been paid to the selection of the model domain so that the boundary conditions do not fully constrain the model. The domain center is located at 45°N and 71°W. In the horizontal, the grid is 60 points in the east-west direction and 59 in the north-south with a resolution of 90 km. There are 23 vertical sigma levels with highest concentration of levels near the surface (0.995, 0.985, 0.97, 0.945, 0.91, 0.87, 0.825, 0.775, 0.725, 0.675, 0.625, 0.575, 0.525, 0.475, 0.425, 0.375, 0.325, 0.275, 0.225, 0.175, 0.125, 0.075, and 0.025). Default model physical options [nonhydrostatic, Grell convective parameterization (Grell, 1993), bulk Planetary Boundary Layer (PBL) scheme, and simple ice explicit moisture scheme (Dudhia 1993), etc.] are used.

Since MM5V2 is a regional model, it requires initial conditions as well as lateral boundary conditions to run. To produce lateral boundary conditions for a model run, one needs gridded data to cover the entire integration period. The input data of temperature, horizontal wind components, relative humidity, and sea-level pressure are obtained from

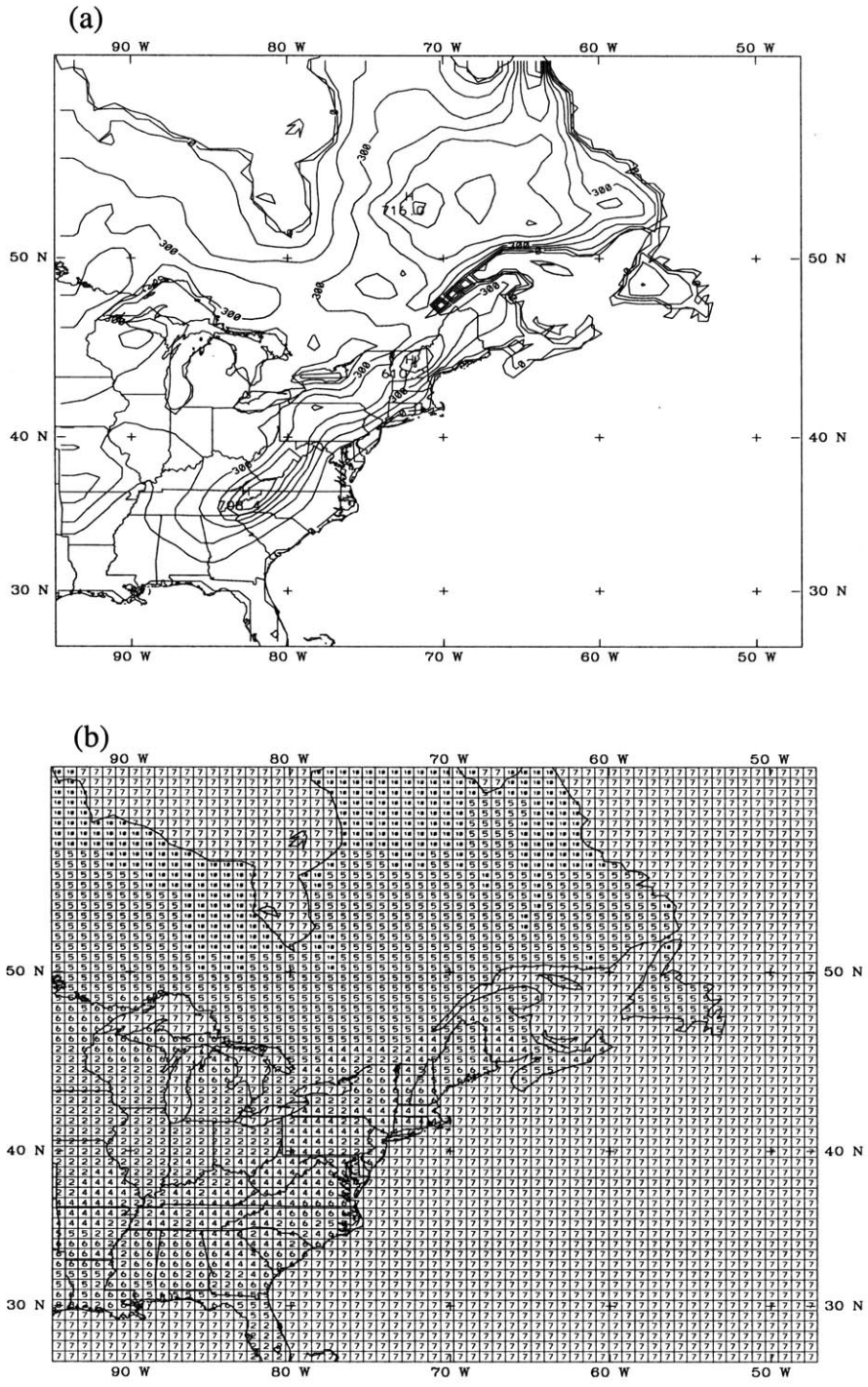

Figure A.2: (a) Model domain and terrain elevation (in meters). Contour interval is 100 m. (b) Land-use distribution (1: Urban land; 2: Agriculture; 3: Range-grassland; 4: Deciduous forest; 5: Coniferous forest; 6: Mixed forest and wet land; 7: Water; 8: Marsh or wet land; 9: Desert; 10: Tundra; 11: Permanent ice; 12: Tropical or subtropical forest; 13: Savannah).

2.5° × 2.5° ECMWF 12-hourly analysis stored in NCAR's Mass Storage System. Along with the other two dimensional information such as terrain elevation, land use (shown in Figure A.2b), and snow cover (all selected from suitable data sets to be compatible with our grid resolution), all variables have been interpolated to our model resolution through the MM5V2 pre-processing routine.

Major output data from MM5V2 are three-dimensional atmospheric forecast arrays including horizontal wind components, temperature, mixing ratios of water vapor, cloud water, and ice cloud, etc.; and two-dimensional surface properties including accumulated convective and nonconvective rainfall, surface latent heat flux, surface sensible heat flux, etc.

A.3 Results

The time series of a selected tropospheric river experiment is illustrated in this section. It consists of 13 snapshots of the vertically integrated (from surface to 300 hPa) moisture fluxes (Figure A.3), accumulated precipitation (Figure A.4), mean sea-level pressure (Figure A.5), and a vertical cross-section of meridional moisture flux (Figure A.6), taken at every 6-hour interval for three days.

A.3.1 Vertically Integrated Moisture Flux

The model seems to capture the whole process of a river progression with much more

detailed small-scale features. Initially, there was a weak and broad N- to NNE-ward moisture transport across much of the eastern United States. The head of this river was identifiable in the following snapshots during the first day where an arc line of strong moisture convergence occurred to the northeast of the Great Lakes area and moved consistently towards northeast. The river became more filamentary and elongated with moisture being transported more efficiently along a SW-NE line while the whole feature translated eastward out of the continent. A moisture-flux convergence line (i.e., a line within which the moisture fluxes seemed directionless with weak magnitudes) co-located next to the west of the river axis was also evident. River structure became less coherent after the 48 hour and the strength of the river showed an overall weakening since then.

A.3.2 Accumulated Precipitation

Figure A.4a shows the total predicted precipitation (both convective and nonconvective) during the whole simulation period, and A.4b through A.4m exhibit the accumulated rainfall for every 6 hours. Compared to the moisture flux (Figure A.3), the migration of the rainband followed coherently with that of the river with rainfall locations quite close to those of moisture-flux convergencies (i.e., near the head of the river and a line next to the west of the river axis). Peak precipitation was observed between 36h and 42h forecast interval with maximum precipitation rate of ~ 5 mm hour^{-1}. Large cross-axial gradients were also found in the precipitation band.

A.3.3 Mean Sea Level Pressure

As a background check against which this river developed, snapshots of the mean sea level pressure (MSLP) field are showed in Figure A.4. A depression initially found near 90°W, 42°N underwent a significant development into an extratropical cyclone (pressure fall averaged about 0.5 hPa $hour^{-1}$ during the first 48 hours). It is intriguing to note that the center of this cyclone moves to be close to the position occupied by the leading edge of the river a few hours ago, a feature that was also found in the previous river studies (e.g., Zhu and Newell 1994).

A.3.4 Vertical Cross-section of Meridional Moisture Flux

A vertical cross-section of the meridional moisture-flux magnitude (i.e., meridional velocity v times specific humidity q at the standard pressure levels) along 77.1428°W, where the major portion of the river passed through, displayed in Figure A.6. A substantial fraction of the water vapor originated near the surface of low latitudes were transported northward, with peak transport occurred between 900 and 800 hPa layer. The slantwise transport feature is one of the important aspects of Tropospheric River and warrants further investigation.

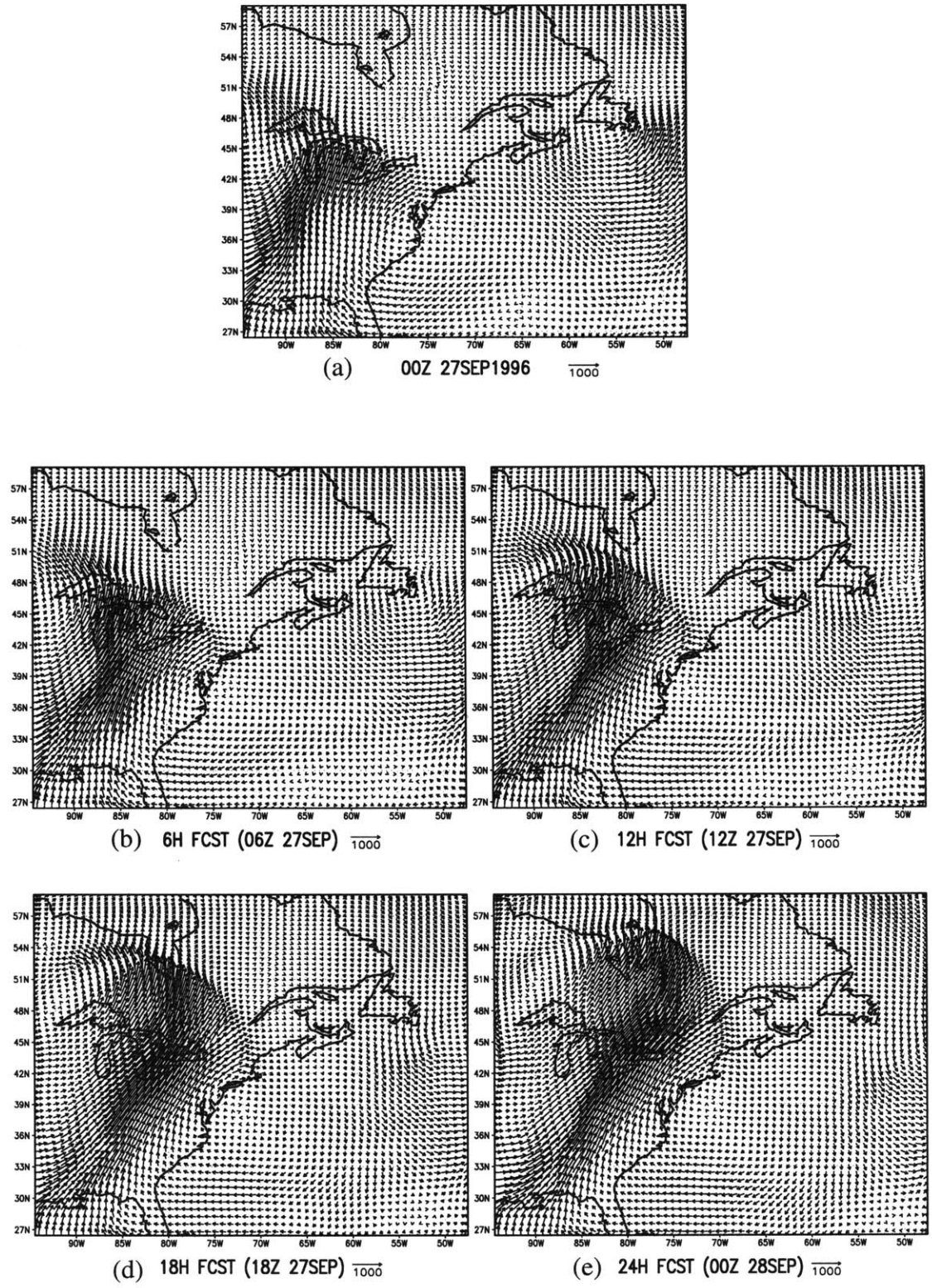

Figure A.3: Simulated vertically integrated moisture fluxes (unit: kg m^{-1} s^{-1}) at 6-hour intervals.

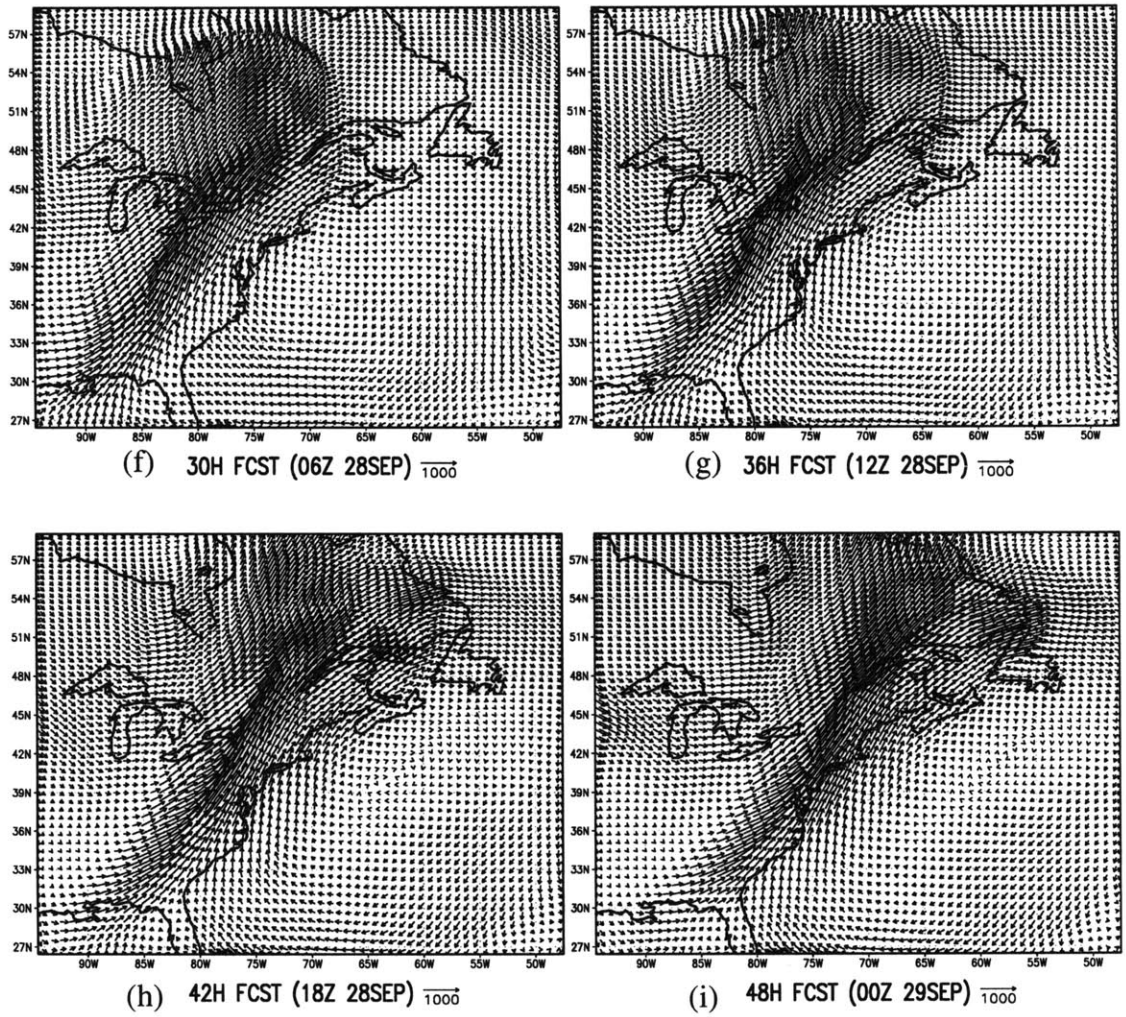

Figure A.3: (*Continued*)

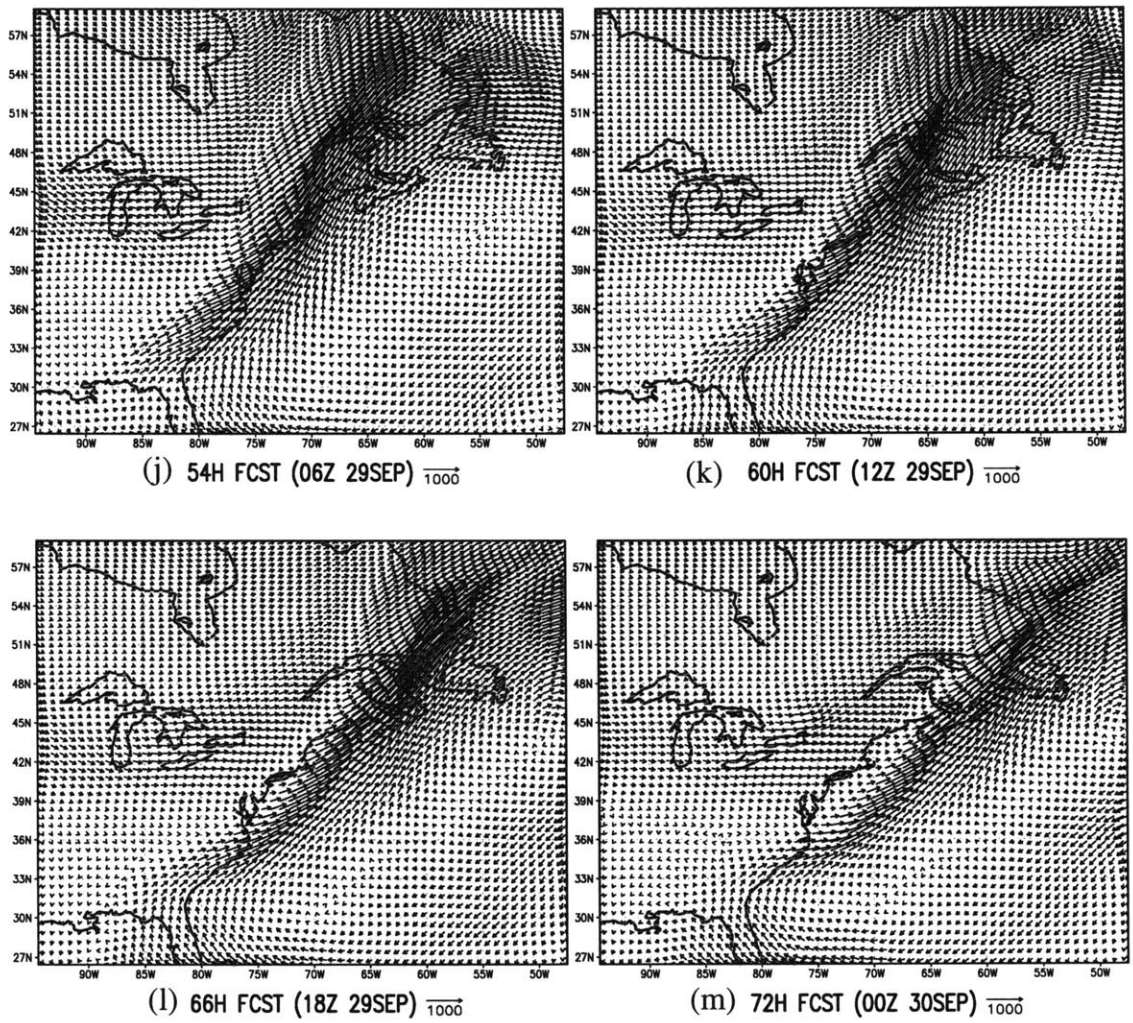

(j) 54H FCST (06Z 29SEP) $\overrightarrow{1000}$

(k) 60H FCST (12Z 29SEP) $\overrightarrow{1000}$

(l) 66H FCST (18Z 29SEP) $\overrightarrow{1000}$

(m) 72H FCST (00Z 30SEP) $\overrightarrow{1000}$

Figure A.3: (*Continued*)

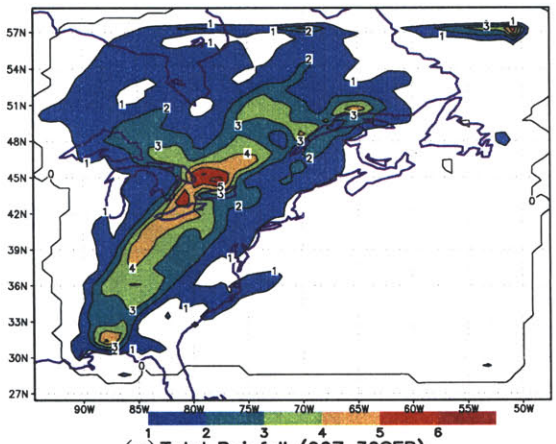

(a) Total Rainfall (00Z 30SEP)

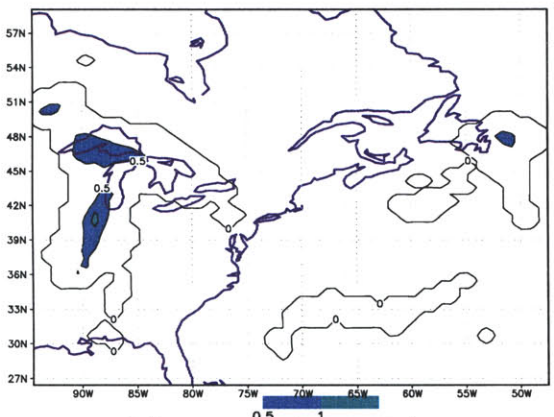

(b) 0–6H FCST (06Z 27SEP)

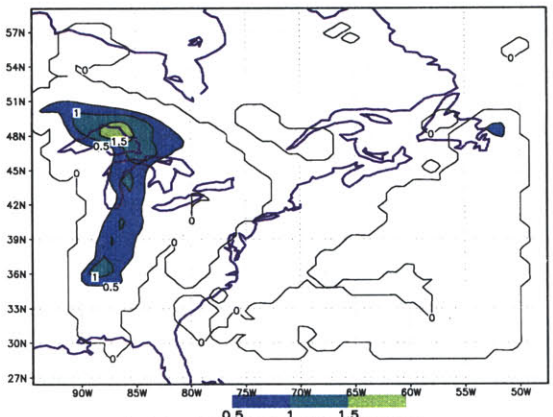

(c) 6–12H FCST (12Z 27SEP)

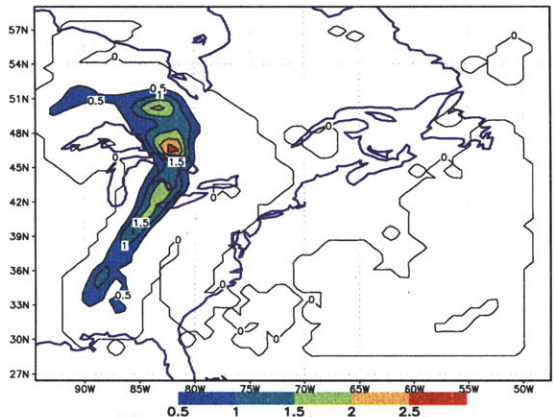

(d) 12–18H FCST (18Z 27SEP)

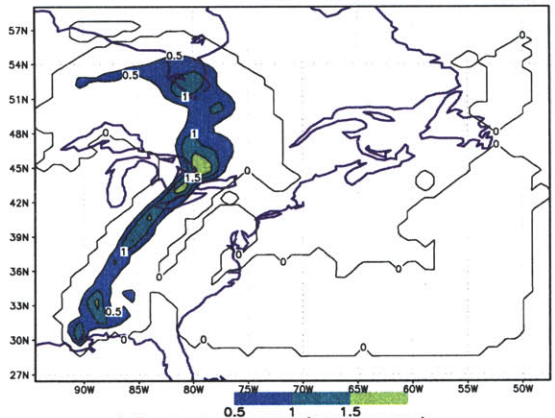

(e) 18–24H FCST (00Z 28SEP)

Figure A.4: (a) Accumulated total forecast rainfall (unit in cm) in 72 hours; (b)-(m): Accumulated rainfall for every 6 hours. Contour interval is 0.5 cm. Values greater than 0.5 cm are shaded.

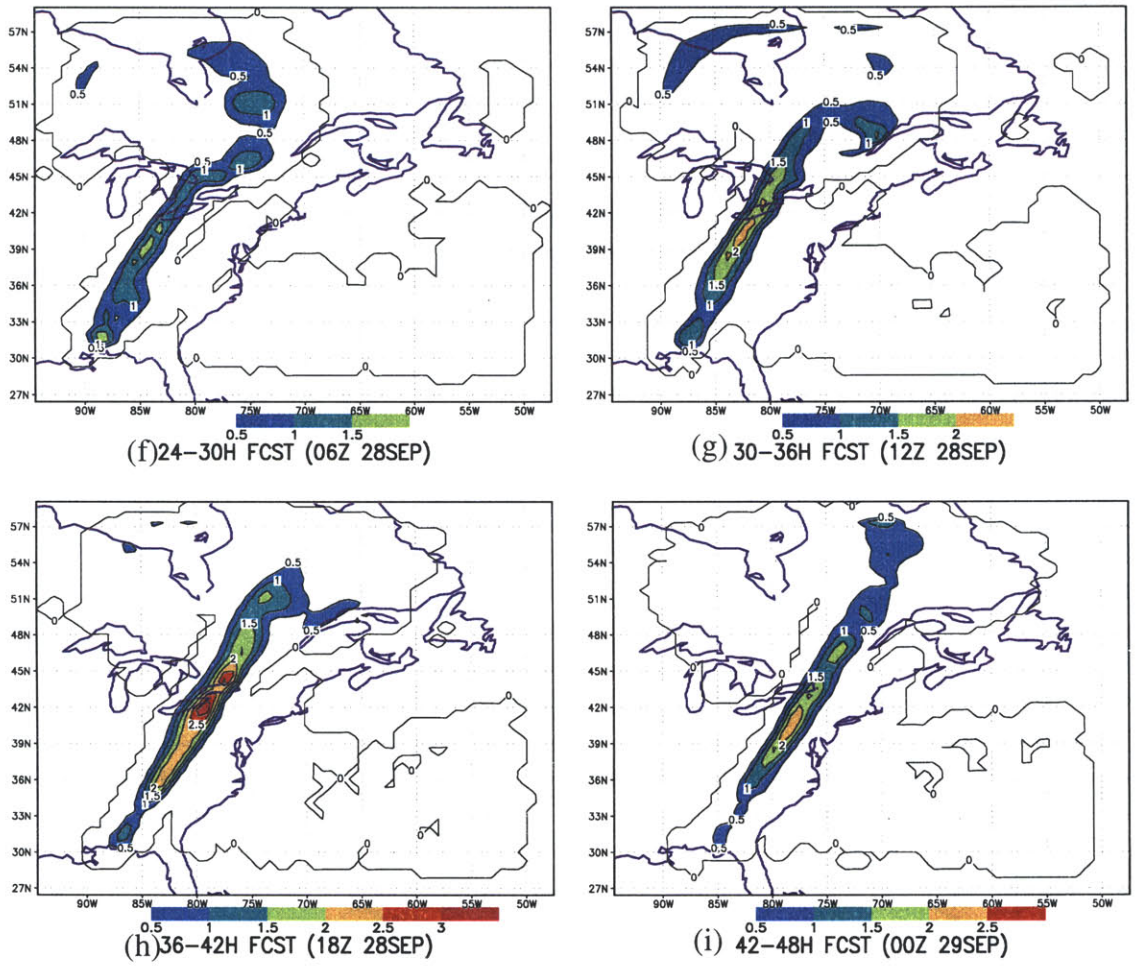

Figure A.4: (*Continued*)

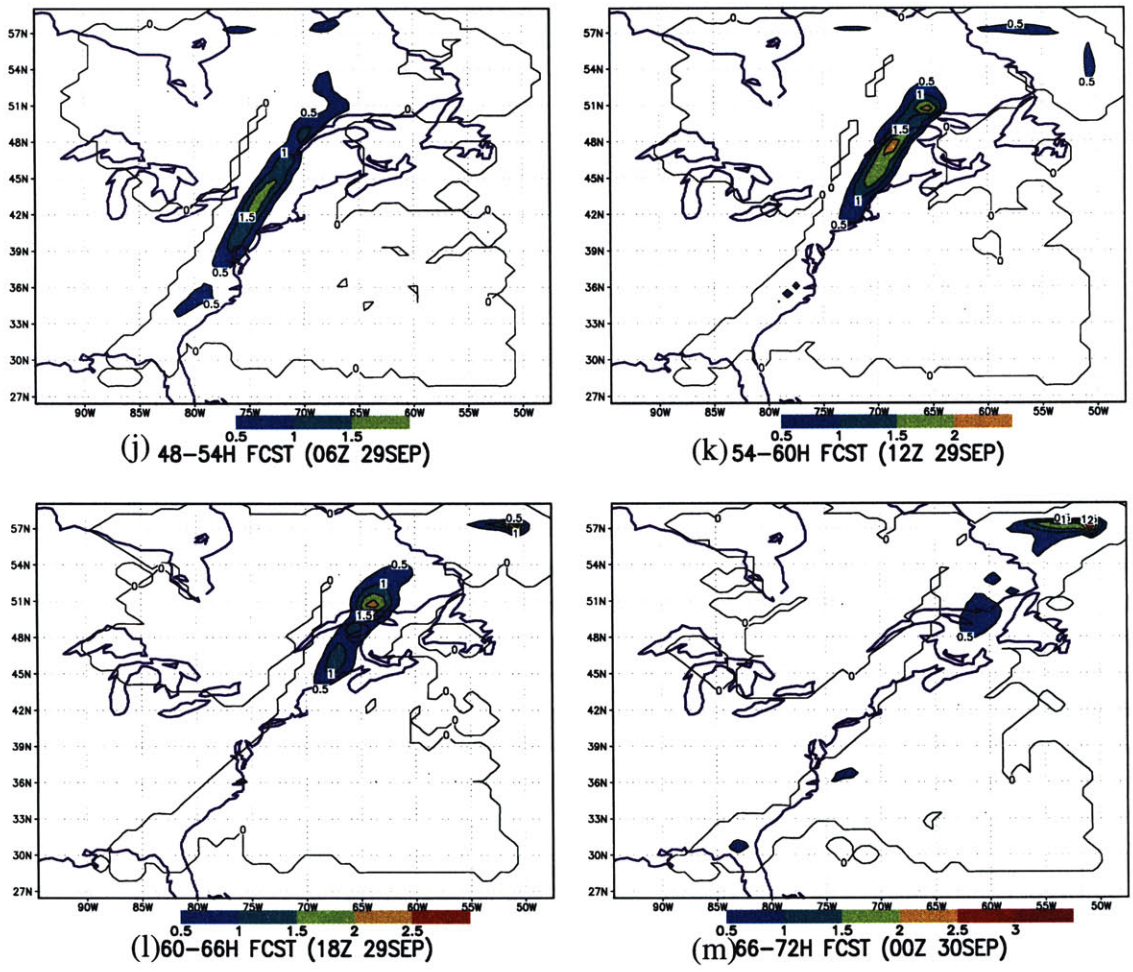

Figure A.4: (*Continued*)

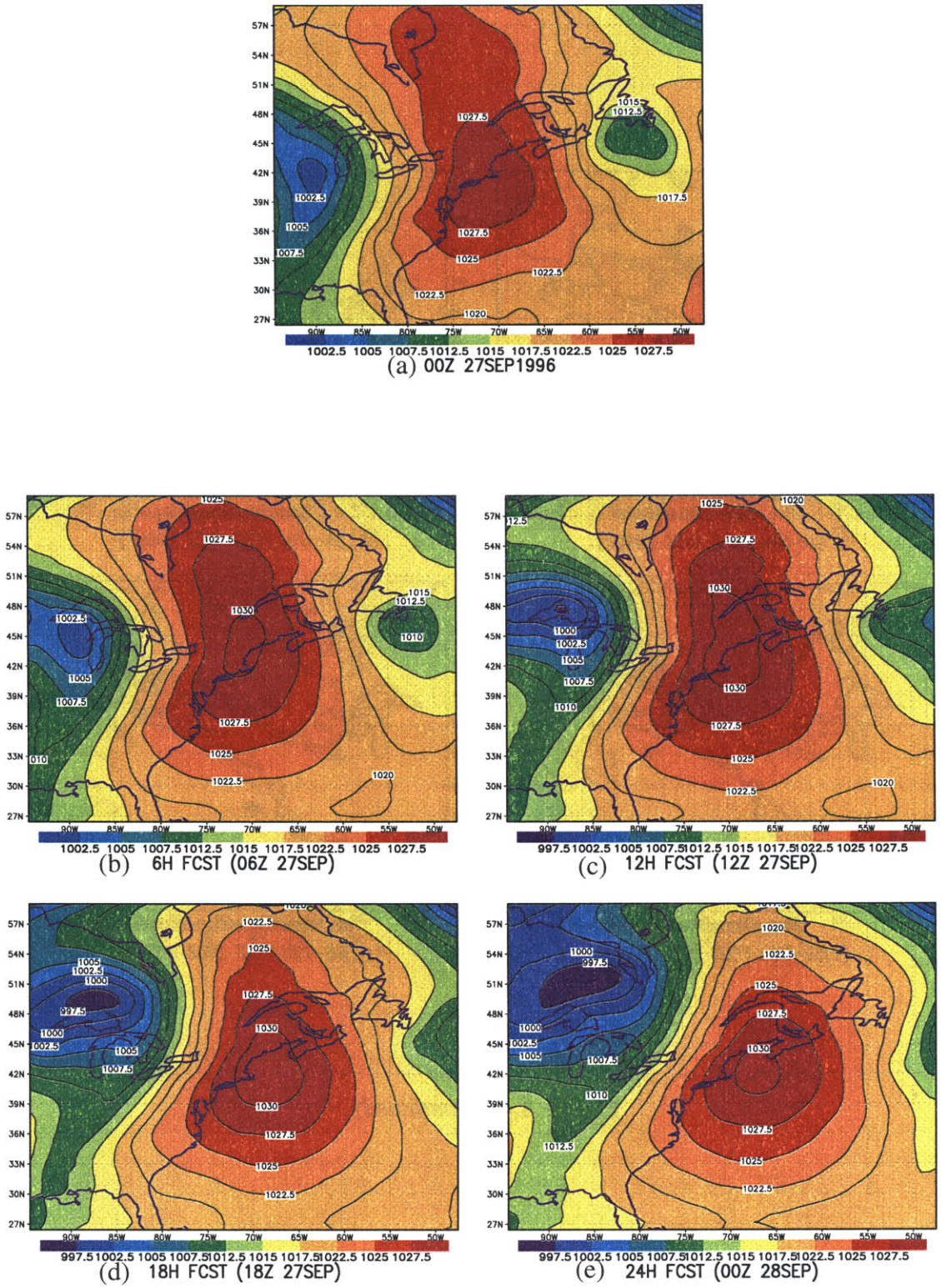

Figure A.5: Simulated sea-level pressure (unit in hPa) at 6-hour intervals.

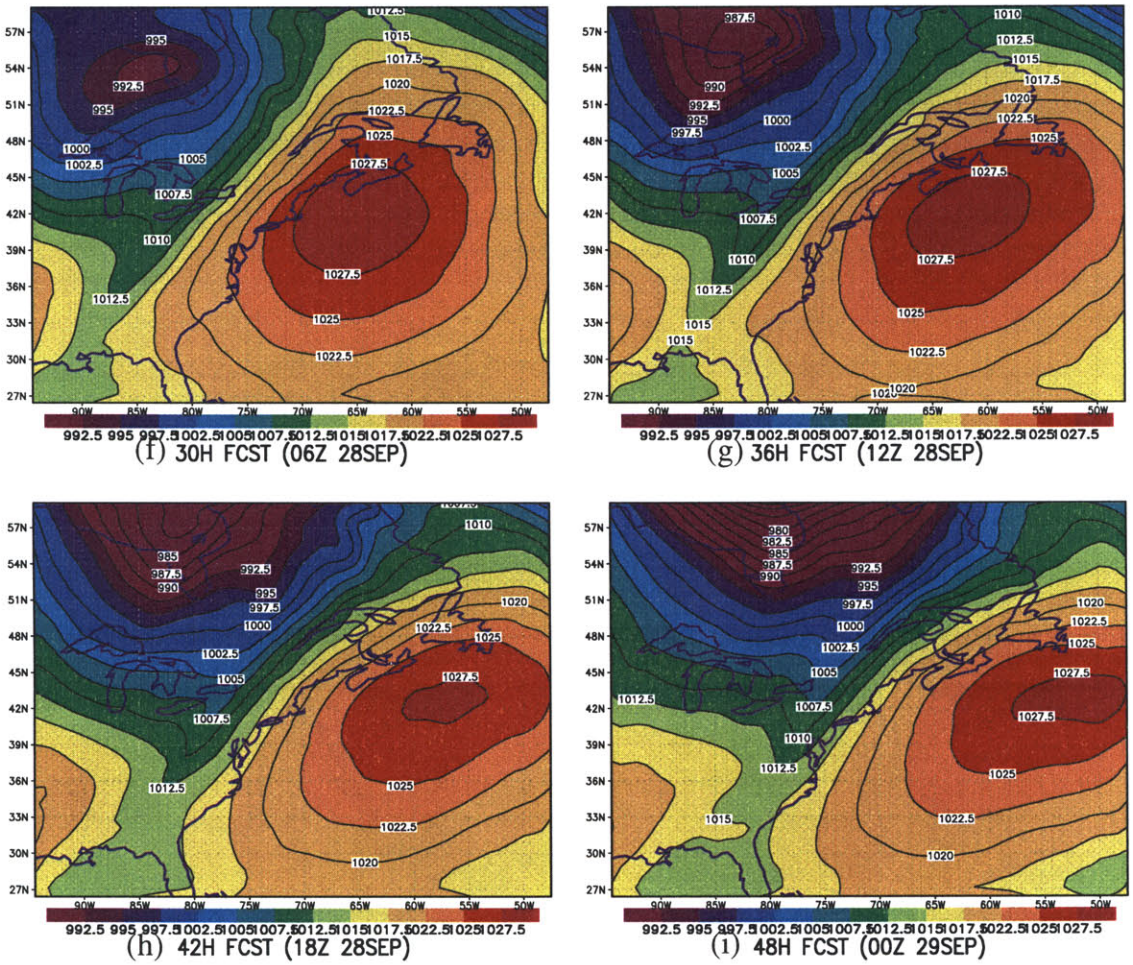

Figure A.5: (*Continued*)

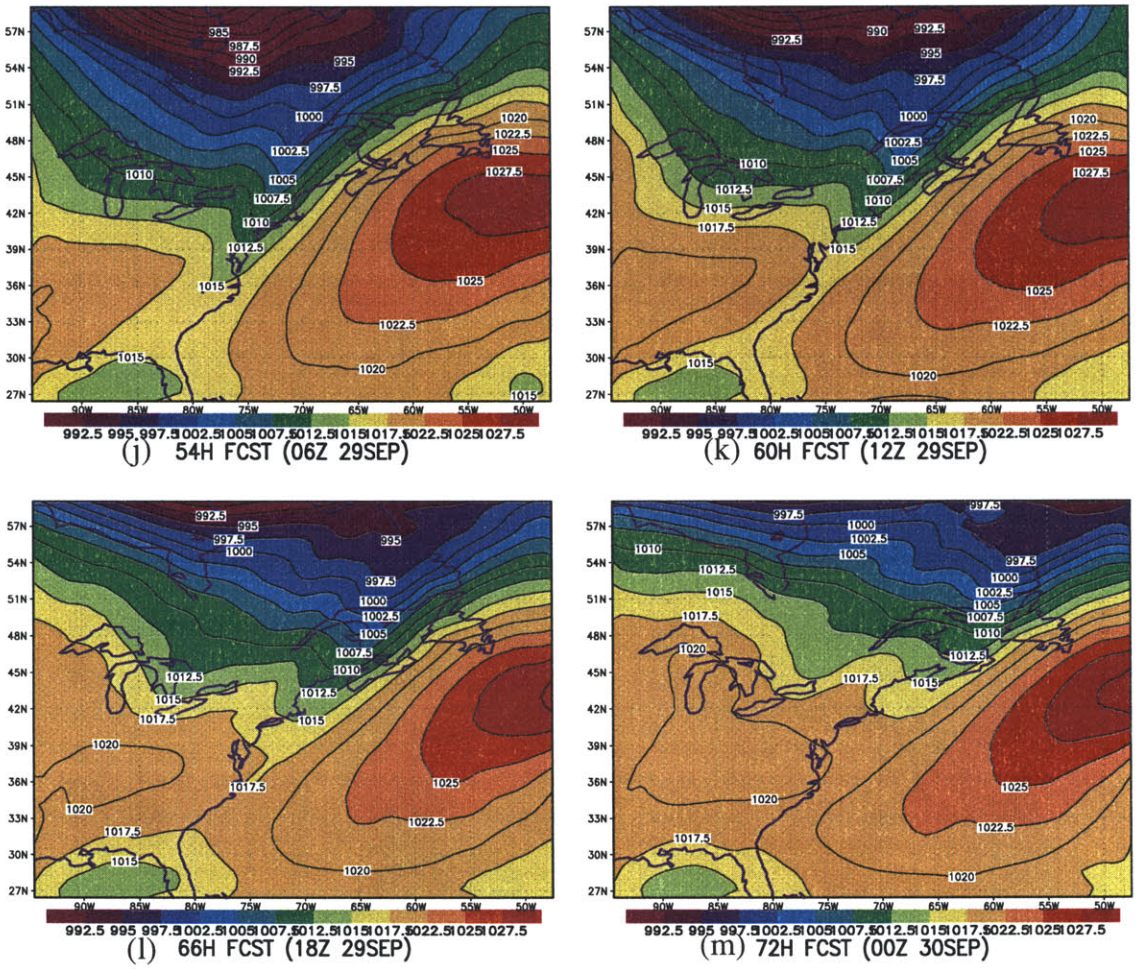

Figure A.5: (*Continued*)

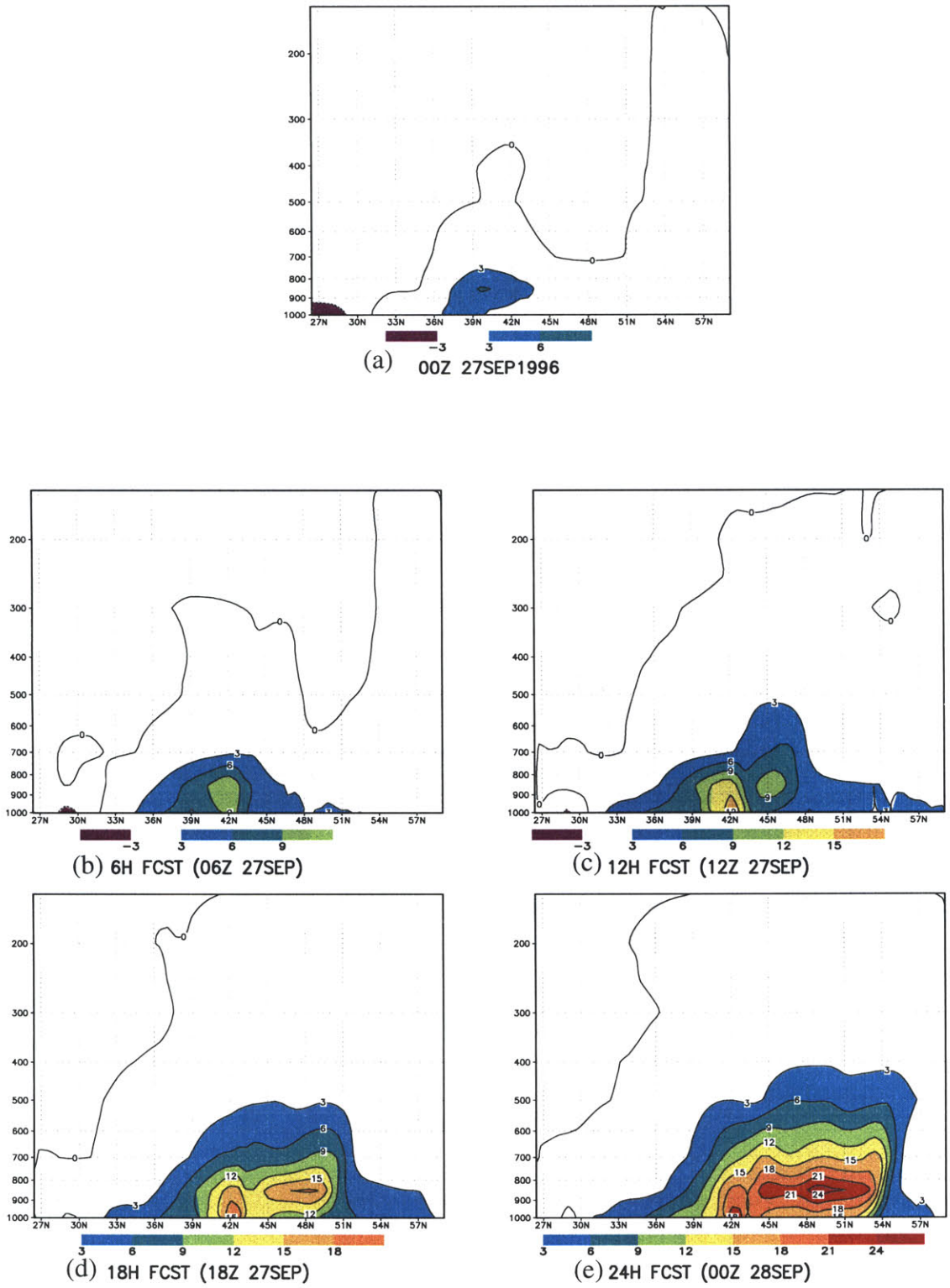

Figure A.6: Vertical cross-section of magnitude of the meridional moisture flux ($q \times v$) along 77.1428°W at 6-hour intervals (units in 10^{-2} kg kg^{-1} m s^{-1}).

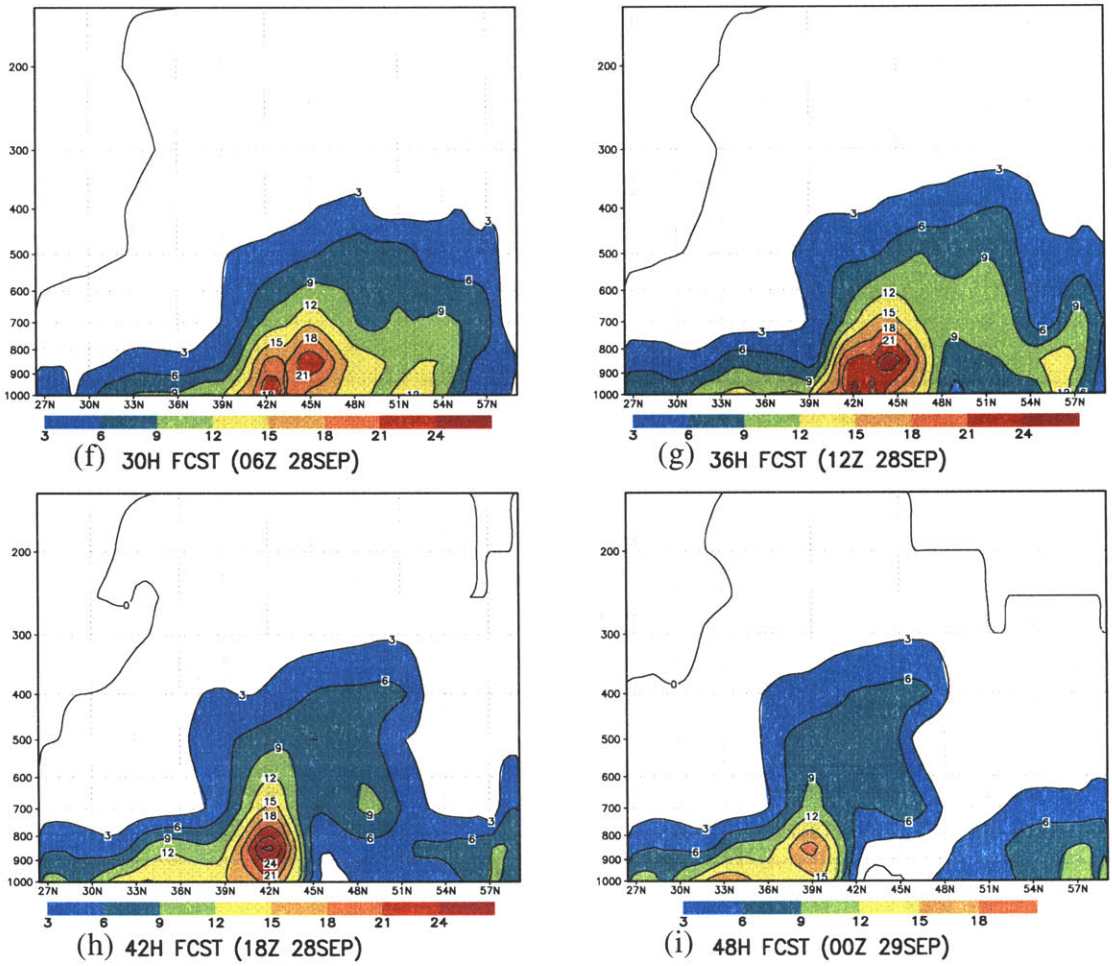

Figure A.6: (*Continued*)

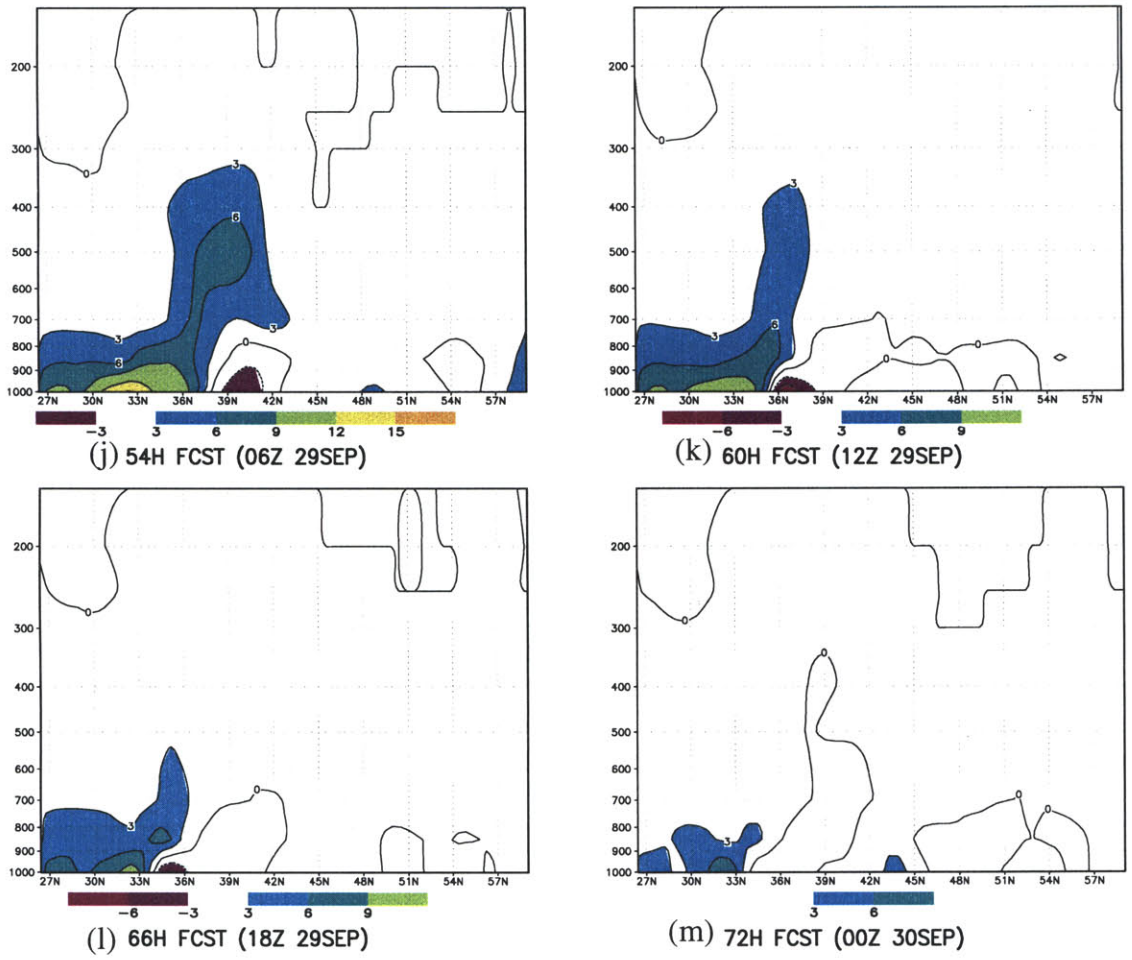

Figure A.6: (*Continued*)

References

Agee, E. M., 1991: Trends in cyclone and anticyclone frequency and comparison with periods of warming and cooling over the Northern Hemisphere, *J. Climate*, 4, 263-267.

Anderson, R. K., and V. J. Oliver, 1970: Some examples of the use of synchronous satellite pictures for studying changes in tropical cloudiness, *Proc. Symp. on Tropical Meteorology, Honolulu*, Amer. Meteor. Soc. EXII 1-6.

Anthes, R. A., and T. T. Warner, 1978: Development of hydrodynamic models suitable for air pollution and other mesometeorological studies, *Mon. Wea. Rev.*, 106, 1045-1078.

Arritt, R. W., and Coauthors, 2000: Project to Intercompare Regional Climate Simulations (PIRCS): Simulation of the 1993 flood over the central U. S., *Preprints of the 15th Conf. on Hydrology.* Amer. Meteor. Soc., Long Beach, CA 9-14 January.

Battisti, A. G., and E. S. Sarachik, 1995: Understanding and predicting ENSO, *Rev. Geophys.*, 33 (Suppl.), 1367-1376.

Bell, G. D., and L. F. Bosart, 1989: A 15-year climatology of Northern Hemisphere 500 mb closed cyclone and anticyclone centers, *Mon. Wea. Rev.*, 117, 2142-2163.

Benton, G. S., and M. A. Estoque, 1954: Water-vapor transfer over the North American continent, *J. Meteor.*, 11, 462-477.

Berbery, E. H., and E. M. Rasmusson, 1996: Studies of North American continental-scale hydrology using Eta model forecast products, *J. Geophys. Res.*, 101, 7305-7319.

Bluestein, H. B., 1993: *Synoptic-dynamic meteorology in midlatitudes. Volume II: Observations and theory of weather systems*, New York, 148-155.

Bony, S., J.-P. Duvel, and H. Le Treut, 1995: Observed dependence of the water vapor and clear-sky greenhouse effect on sea surface temperature: Comparison with climate warming experiments, *Climate Dyn.*, 11, 307-320.

Boyle, J., 1993: Sensitivity of dynamical quantities to horizontal resolution for a climate simulation using the ECMWF (cycle 33) model, *J. Climate*, 6, 796-815.

Brahmananda Rao, V. S. R. Chapa, and I. F. A. Cavalcanti, 1998: Moisture budget in the

tropics and the Walker circulation, *J. Geophys. Res.*, 103, No. D12, 13,713-13,728.

Browning, K. A., 1990: Organization of clouds and precipitation in extratropical cyclones, in *Extratropical Cyclones - The Erik Palmen Memorial Volume* (eds. Newton, C. and E. O. Holopainen), Amer. Meteor. Soc., Boston, 129-153.

Browning, K. A., and G. A. Monk, 1982: A simple model for the synoptic analysis of cold fronts, *Quart. J. Roy. Meteor. Soc.*, 108, 435-452.

Casey, K. S., and P. Cornillon, 2001: Global and regional sea surface temperature trends, *J. Climate*, 14, 3801-3818.

Carlson, T. N., 1980: Airflow through mid-latitude cyclones and the comma cloud pattern, *Mon. Wea. Rev.*, 108, 1498-1509.

Carlson, T. N., 1987: Cloud configuration in relation to relative isentropic motion. *Satellite and Radar Imagery Interpretation* (preprint vol., workshop at U.K. Meteorological Office), M. Bader and T. Waters, Eds, EUMETSAT, Darmstadt, FRG, 43-61.

Chahine, M. T., 1992: GEWEX: The global energy and water cycle experiment, *Eos. Trans.* Amer. Geophys. Union, 73, 9.

Chahine, M. T., R. Haskins, and E. Fetzer, 1997: Observation of the recycling rate of moisture in the atmosphere: 1988-1994, *GEWEX News*, 7, 1-4.

Chen, C.-T., M.-C. Yen, J. Pfaendtner, and Y. C. Sud, 1996: Annual variation of the global precipitable water and its maintenance: observation and climate-simulation, *Tellus*, 48A, 1-16.

Cohen, J. L., D. A. Salstein, and R. D. Rosen, 2000: Interannual variability in the meridional transport of water vapor, *J. Hydrometeor.*, 1, 547-553.

Davies, H. C., C. Shar, and H. Wernli, 1991: The palette of fronts and cyclones within a baroclinic wave development. *J. Atmos. Sci.*, 48, 1666-1688.

Donner, L. J., and P. J. Rasch, 1989: Cumulus initialization in a global model for numerical weather prediction, *Mon. Wea. Rev.*, 117, 2654-2671.

Dudhia, J. 1993: A nonhydrostatic version of the Penn State/NCAR mesoscale model: Validation tests and simulation of an Atlantic cyclone and cold front, *Mon. Wea. Rev.*, 121, 1493-1513.

Elliott, W. P., and D. J. Gaffen, 1991: On the utility of radiosonde humidity archives for climate studies, *Bull. Amer. Meteor. Soc.*, 72, 1507-1520.

Elliott, W. P., 1995: On detecting long-term changes in atmospheric moisture, *Climate Change*, 31, 349-367.

Emanuel, K. A., M. Fantini, and A. J. Thorpe, 1987: Baroclinic instability in an environment of small stability to slantwise moist convection. Part I: Two-dimensional models, *J. Atmos. Sci.*, 44, 1559-1573.

Fritsch, J. M., R. J. Kane, and C. R. Chelius, 1986: The contribution of mesoscale convective weather systems to the warm-season precipitation in the United States, *J. Climate Appl. Meteor.*, 25, 1333-1345.

Gaffen, D. J., and T. P. Barnett, 1992: A comparison of observations and model simulations of tropospheric water vapor, *J. Geophys. Res.*, 97, 2775-2780.

Gaffen, D. J., R. D. Rosen, D. A. Salstein, and J. S. Boyle, 1997: Evaluation of tropospheric water vapor simulations from the Atmospheric Model Intercomparison Project, *J. Climate*, 10, 1648-1661.

Geng, Q., and M. Sugi, 2001: Variability of the North Atlantic cyclone activity in winter analyzed from NCEP-NCAR reanalysis data, *J. Climate*, 14, 3863-3873.

Ghil, M., and K. Mo, 1991: Intraseasonal oscillations in the global atmosphere. Part II: Southern Hemisphere, *J. Atmos. Sci.*, 48, 780-790.

Giorgi, F., G. T. Bates, and S. J. Nieman, 1993: The multiyear surface climatology of a regional atmospheric model over the western United States, *J. Climate*, 6, 75-95.

Godfred-Spenning, C. R., and I. Simmonds, 1996: An analysis of Antarctic sea-ice and extratropical cyclone associations, *Intl. J. Climatol.*, 16, 1315-1332.

Grell, G. A., 1993: Prognostic evaluation of assumptions used by cumulus parameterizations, *Mon. Wea. Rev.*, 121, 764-787.

Grotjahn, R., 1990: Feature-based predictability of 500 hPa height in the Australia-New Zealand region, *Meteorol. Atmos. Phys.*, 42, 57-67.

Gutowski, W. J., Y. Chen, and Z. Otles, 1997: Atmospheric water vapor transport in NCEP-NCAR reanalyses: Comparison with river discharge in the central United States, *Bull. Amer. Meteor. Soc.*, 78, 1957-1969.

Gutowski, W. J., E. S. Takle, and R. W. Arritt, 1998: Project to Intercompare Regional Climate Simulations, Workshop II, 5-6 June 1997, *Bull. Amer. Meteor. Soc.*, 79, 657-659.

Gutowski, W. J., J. W. Seidel, A. B. Ervin, 2001: Water transport by thin moist layers in Project STORM soundings, *Mon. Wea. Rev.*, 129, 167-172.

Gyakum, J. R., R. H. Anderson, and E. L. Gruner, 1989: North Pacific cold season surface cyclone activity: 1975-1983, *Mon. Wea. Rev.*, 117, 1141-1155.

Hansen, J., and S. Lebedeff, 1987: Global trends of measured surface air temperature, *J. Geophys. Res.*, 92, 13,345-13, 372.

Hansen, J., and S. Lebedeff, 1988: Global surface air temperatures: Update through 1987, *Geophys. Res. Lett.*, 15, 323-326.

Harrold, T. W., 1973: Mechanisms influencing the distribution of precipitation within baroclinic disturbances, *Quart. J. Roy. Meteor. Soc.*, 99. 232-251.

Heideman, K. F., and J. M. Fritsch, 1988: Forcing mechanisms and other characteristics of significant summertime precipitation. *Wea. Forecasting*, 3, 115-130.

Held, I. M., 1993: Large-scale dynamics and global warming, *Bull. Amer. Meteor. Soc.*, 74, 228-241.

Higgins, R. W.,K. C. Mo, and S. D. Schubert, 1996: The moisture budget of the central United States in spring as evaluated from the NCEP/NCAR and the NASA/DAO

reanalyses, *Mon. Wea. Rev.*, 124, 939-963.

Hoerling, M. P., and A. Kumar, 1997: Origins of extreme climate states during the 1982-83 ENSO winter, *J. Climate*, 10, 2859-2870.

Houze, R. A., and P. V. Hobbs, 1982: Organization and structure of precipitating cloud systems, *Advances in Geophysics*, 41, Academic Press, 3405-3411.

Hu, Y, R. E. Newell, and Y. Zhu, 2001: Mean moisture circulation for PEM-Tropical missions, *J. Geophys. Res.,* 106, 32,445-32,467.

Huffman, G.J., R.F. Adler, P.A. Arkin, A. Chang, R. Ferraro, A. Gruber, J. Janowiak, R.J. Joyce, A. McNab, B. Rudolf, U. Schneider, and P. Xie, 1997: The Global Precipitation Climatology Project (GPCP) Combined Precipitation Data Set, *Bull. Amer. Meteor. Soc.*, 78, 5-20.

International GEWEX Project Office, 1994: *Implementation Plan for the GEWEX Continental-Scale International Project (GCIP)*, vol. II, *Research*, 100 pp., Int. GEWEX Proj. Off., Washington, D. C.

Iselin, J. P., and W. J. Gutowski Jr., 1997: Water vapor layers in STORM-FEST rawinsonde observations, *Mon. Wea. Rev.*, 125, 1954-1963.

Jackson, D. L., and G. L. Stephens, 1995: A study of SSM/I-derived columnar water vapor over the global oceans. *J. Climate*, 8, 2025-2038.

James, I. N., and D. L. T. Anderson, 1984: The seasonal mean flow and distribution of large-scale weather systems in the southern hemisphere: the effects of moisture transport, *Quart. J. Roy. Meteor. Soc.*, 110, 943-966.

Johnson, D. R., T. H. Zapotocny, F. M. Reams, B. J. Wolf, and R. B. Pierce, 1993: A comparison of simulated precipitation by hybrid isentropic-sigma and sigma models, *Mon. Wea. Rev.*, 121, 2088-2114.

Jones, P. D., S. C. B. Raper, R. S. Bradley, H. F. Diaz, P. M. Kelly, and T. M. L. Wigley, 1986: Northern Hemisphere surface air temperature variations: 1851-1984, *J. Climate Appl. Meteor.*, 25, 161-179.

Jones, D. A., and I. Simmonds, 1993: A climatology of Southern Hemisphere extratropical cyclones, *Climate Dyn.*, 9, 131-145.

Jones, D. A., and I. Simmonds, 1994: A climatology of Southern Hemisphere anticyclones. *Climate Dyn.*, 10, 333-348.

Joseph, B., and M. Moustaoui, 2000: Transport, moisture, and rain in a simple monsoonlike flow, *J. Atmos. Sci.*, 57, 1817-1838.

Kalnay, E., and Coauthors, 1996: The NCEP/NCAR 40-year Reanalysis Project. *Bull. Amer. Meteor. Soc.*, 77, 431-471.

Kestin, T. S., D. J. Karoly, J. Yano, and N. A. Rayner, 1998: Time-frequency variability of ENSO and stochastic simulations, *J. Climate*, 11, 2258-2272.

Kidson, J. W., 1975: Eigenvector analysis of monthly mean surface data, *Mon. Wea. Rev.*, 103, 177-186.

Kiladis, G. N., and H. F. Diaz, 1986: An analysis of the 1977-78 ENSO episode and comparison with 1982-83, *Mon. Wea. Rev.*, 114, 1035-1047.

Kiladis, G. N., and H. van Loon, 1988: The Southern Oscillation. Part VII: Meteorological anomalies over the Indian and Pacific sectors associated with the extremes of the oscillation, *Mon. Wea. Rev.*, 116, 120-136.

Kiladis, G. N., and H. F. Diaz, 1989: Global climate anomalies associated with extremes in the Southern Oscillation, *J. Climate,* 2, 1069-1090.

Kistler, R., and Coauthors, 2001: The NCEP-NCAR 50-year reanalysis: monthly means CD-ROM and documentation, *Bull. Amer. Meteor. Soc.*, 82, 247-267.

Koblenz, 1994: Report of the First Meeting of the GRDC Steering Committee, Germany, June 20 - 21, GRDC.

Krishnamurti, T. N., and N. Surgi, 1987: Observational aspects of summer monsoon, in *Monsoon Meteorology*, C.-P. Chang, T. N. Krishnamurti, Eds, Oxford University Press, pp 3-25.

Kuhnel, I., 1989: Tropical-extratropical cloudband climatology based on satellite data, *Intl. J. Climatol.*, 9, 441-463.

Lambert, S. J., 1988: A cyclone climatology of the Canadian Climate Center General Circulation Model, *J. Climate*, 1, 109-115.

Lau, K.-M., J. H. Kim, and Y. Sud, 1996, Intercomparison of hydrologic processes in AMIP GCMs, *Bull. Amer. Meteor. Soc.*, 77, 2209-2227.

Lau, K.-M., H.-T. Wu, and S. Yang, 1998: Hydrologic processes associated with the first transition of the Asian Summer Monsoon: A pilot satellite study, *Bull. Amer. Meteor. Soc.*, 79, 1871-1882.

Lefevre, R. J., and J. W. Nielsen-Gammon, 1995: An objective climatology of mobile troughs in the northern hemisphere, *Tellus*, 47A, 638-655.

Leighton, R. M., 1992: Monthly anticyclonicity and cyclonicity in the Southern Hemisphere: Averages for March and September, *Weather and Climate*, 12, 76-82.

Leighton, R. M., 1994: Monthly anticyclonicity and cyclonicity in the Australasian region: Averages for January, April, July and October, *Intl. J. Climatol.*, 14, 33-45.

Le Treut, H., and E. Kalnay, 1990: Comparison of observed and simulated cyclone frequency distribution as determined by an objective method, *Atmosfera*, 3, 57-71.

Liou, C.-S., and R. L. Elsberry, 1987: Heat budgets of analyses and forecasts of an explosively deepening maritime cyclone, *Mon. Wea. Rev.*, 115, 1809-1824.

Lorenz E. N., 1991: The general circulation of the atmosphere: an evolving problem, *Tellus*, 43AB, 8-15.

Ludlam, F. H., 1966: The cyclone problem: A history of models of the cyclonic storm. Inaugural lecture as professor of meteorology, 8 November 1966, published by Imperial College of Science and Technology, London, 49 pp.

Maddox, R. A., K. W. Howard, and A. J. Negri, 1992: Analyses of GOES infrared

convective cloud-top temperatures for extended periods: An overview of the 1990 warm season for a subtropical region. Preprints, *Sixth Conf. on Satellite Meteorology and Oceanography*, Atlanta, GA, Amer. Meteor. Soc., 205-208.

Marengo, J. A., and S. Hastenrath, 1993: Case studies of extreme climatic events in the Amazon Basin, *J. Climate*, 6, 617-627.

Matsuyama, H., 1992: The water budget in the Amazon River basin during the FGGE period, *J. Meteor. Soc. Japan*, 70(6), 1071-1083.

McGuirk, J. P., A. H. Thompson, and N. R. Smith, 1987: Moisture bursts over the tropical Pacific Ocean, *Mon. Wea. Rev.,* 115, 787-798.

Mesinger, F., 1984: A blocking technique for representation of mountains in atmospheric models, *Riv. Meteor. Aeronautica,* 44, 195-202.

Meyers, S. D., J. J., O'Brien, and E. Thelin, 1999: Reconstruction of monthly SST in the tropical Pacific Ocean during 1868-1993 using adaptive climate basis functions, *Mon. Wea. Rev.*, 127, 1599-1612.

Mo, K. C., and R. W. Higgins, 1996: Large-scale atmospheric moisture transport as evaluated in the NCEP/NCAR and the NASA/DAO reanalyses, *J. Climate*, 9, 1531-1545.

Murray, R. J., and I Simmonds, 1991: A numerical scheme for tracking cyclone centers from digital data. Part I: Development and operation of the scheme, *Aust. Meteor. Mag.*, 39, 155-166.

Murray, R. J., and I. Simmonds, 1995: Responses of climate and cyclones to reductions in Arctic winter sea ice, *J. Geophys. Res.*, 100, 4791-4806.

National Research Council, 1991: Opportunities in Hydrologic Sciences, National Academy Press, 348 pp.

National Research Council, 1999: *The GEWEX Global Water Vapor Project (GVaP) - U.S. Opportunities.* National Academy Press, 17 pp.

Newell, R. E., N. E. Newell, Y. Zhu, and C. Scott, 1992: Tropospheric rivers? - A pilot study, *Geophys. Res. Lett.*, 19, 2401-2404.

Newell, R. E., and Y. Zhu, 1994: Tropospheric rivers: A one-year record and a possible application to ice core data, *Geophys. Res. Lett.*, 21, 113-116.

Newell, R. E., and Coauthors, 1996: Vertical fine-scale atmospheric structure measured from NASA DC-8 during PEM-West A, *J. Geophys. Res.*, 101, 1943-1960.

Newell, R. E., V. Thouret, J. Y. N. Cho, P. Stoller, A. Marenco, and H. G. Smit, 1999: Ubiquity of quasi-horizontal layers in the troposphere, *Nature*, 398, 316-319.

Peixoto, J. P., 1973: *Atmospheric Vapor Flux Computations for Hydrological Purposes*, WMO Publ. No. 357, 83 pp.

Peixoto, J. P., R. D. Rosen, and D. A. Salstein, 1978: Seasonal variability in the pole-to-pole modes of water vapor transport during the IGY, *Arch. Meteor. Geophys. Bioklimatol.*, A27, 233-255.

Peixoto, J. P., D. A. Salstein, and R. D. Rosen, 1981: Interannual variation in large-scale moisture fields, *J. Geophys. Res.*, 86, 1255-1264.

Peixoto, J. P., and A. H. Oort, 1983: The atmospheric branch of the hydrological cycle and climate, *Variations of the global water budget*, A. Street-Perrott et al., Eds., D. Reidel, London, 5-65.

Peixoto, J. P., and A. H. Oort, 1992: *Physics of Climate*, American Institute of Physics, 520 pp.

Peixoto, J. P., and A. H. Oort, 1996: The climatology of relative humidity in the atmosphere, *J. Climate*, 9, 3443-3463.

Petterssen, S., 1956: *Weather Analysis and Forecasting*, Vol. 1. *Motion and Motion Systems.* McGraw-Hill, 428 pp.

Pratt, R. W., 1985: Review of radiosonde humidity and temperature errors, *J. Atmos. Oceanic Technol.*, 2, 404-407.

Rajagopalan, B., U. Lall, and M. A. Cane, 1997: Anomalous ENSO occurrences: An alternate view, *J. Climate*, 10, 2351-2357.

Randel, L. D., T. H. Vonder Haar, M. A. Ringerud, G. L. Stephens, T. J. Greenwald, and C. L. Combs, 1996: A new global water vapor dataset, *Bull. Amer. Meteor. Soc.*, 77, 1233-1246.

Rasmusson, E. M., 1967: Atmospheric water vapor transport and the water balance of North America. Part I: Characteristics of the water vapor flux field, *Mon. Wea. Rev.*, 95, 403-426.

Rasmusson, E. M., 1968: Atmospheric water vapor transport and the water balance of North America. Part II: Large-scale water balance investigation, *Mon. Wea. Rev.*, 96, 720-734.

Reichle, H. G., Jr., V. S. Connors, J. A. Holland, R. T. Sherrill, H. A. Walio, J. C. Casas, E. P. Condon, B. B. Gormsen, and W. Seiler, 1990: The distribution of middle tropospheric carbon monoxide during early October 1984, *J. Geophys. Res.*, 95, 9856-9865.

Reynolds, R. W., 1988: Real-time global sea surface temperature analysis, *J. Climate*, 1, 75-86.

Reynolds, R. W., and D. C. Marsico, 1993: An improved real-time global sea surface temperature analysis, *J. Climate*, 6, 114-119.

Reynolds, R. W., and T. M. Smith, 1994: Improved global sea surface temperature analyses using optimum interpolation, *J. Climate*, 7, 929-948.

Roads, J. O., S.-C. Chen, J. Kao, D. Langley, and G. Glatzmatier, 1992: Global aspects of the Los Alamos general circulation model hydrological cycle, *J. Geophys. Res.*, 97, 10051-10068.

Roads, J. O., S. Chen, A. Guetter, and K. Georgakakos, 1994: Large-scale aspects of the U. S. hydrological cycle, *Bull. Amer. Meteor. Soc.*, 75, 1589-1610.

Rocha, A., 1992: The influence of global sea surface temperatures on southern Africa summer climate. Ph. D. thesis, Department of Meteorology, University of Melbourne, Parkville, Australia.

Roebber, P. J., 1984: Statistical analysis and updated climatology of explosive cyclones, *Mon. Wea. Rev.*, 112, 1577-1589.

Rosen, R. D., D. A. Salstein and J. P. Peixoto, 1979: Variability in the annual fields of large-scale atmospheric water vapor transport, *Mon. Wea. Rev.*, 107, 26-37.

Rosen, R. D., and D. A. Salstein, 1980: A comparison between circulation statistics computed from conventional data and NMC Hough analyses, *Mon. Wea. Rev.*, 108, 1226-1247.

Rosen, R. D., 1999: The global energy cycle. *Global Energy and Water Cycle*, K. A. Browning and R. J. Gurney, Eds., Cambridge University Press, 1-9.

Rossow, W. B., L. C. Garder, P. J. Lu, and A. W. Walker, 1991: International Satellite Cloud Climatology Project (ISCCP) documentation of cloud data, *WMO/TD-No. 266, World Meteorological Organization*, 76 pp.

Salstein, D. A., R. D. Rosen and J. P. Peixoto, 1983: Modes of variability in annual hemispheric water vapor and transport fields, *J. Atmos. Sci.*, 40, 788-803.

Sanders, F., and J. R. Gyakum, 1980: Synoptic-dynamical climatology of the "bomb", *Mon. Wea. Rev.*, 108, 1589-1606.

Savijarvi, J. I., 1988: Global energy and moisture budgets from rawinsonde data, *Mon. Wea. Rev.*, 116, 417-430.

Saarikivi, P., and T. Puhakka, 1990: The structure and evolution of a wintertime occluded front, Tellus, 42A, 122-139.

Schmetz, J., W. P. Menzel, C. Celden, X. Wu, L. van de Berg, S. Nieman, C. Hayden, K. Holmlund, and C. Geijo, 1995: Monthly mean large-scale analyses of upper-troposphere humidity and wind field divergence derived from three geostationary satellite, *Bull. Amer. Meteor. Soc.*, 76, 1578-1584.

Schmitz, J. T., and S. L. Mullen, 1996: Water vapor transport associated with the summertime North American monsoon as depicted by ECMWF analyses, *J. Climate*, 1621-1634.

Simmonds, I., and X. Wu, 1993: Cyclone behaviour response to changes in winter Southern Hemisphere sea-ice concentration. *Quart. J. Roy. Meteor. Soc.*, 119, 1121-1148.

Simmonds, I., and R. Law, 1995: Associations between Antarctic katabatic flow and the upper level winter vortex, *Intl. J. Climatol.*, 15, 403-421.

Simmonds, I., and R. J. Murray, 1999: Southern extratropical cyclone behavior in ECMWF analyses during the FROST special observing periods, *Wea. Forecasting*, 14, 878-891.

Simmonds, I., R. J. Murray, and R.M. Leighton, 1999: A refinement of cyclone tracking methods with data from FROST, *Aust. Meteor. Mag.* 28, 617-622.

Simmonds, I., and K. Keay, 2000a: Mean southern hemisphere extratropical cyclone behavior in the 40-year NCEP-NCAR reanalysis, *J. Climate*, 13, 873-885.

Simmonds, I., and K. Keay, 2000b: Variability of southern hemisphere extratropical cyclone behavior, 1958-97, *J. Climate*, 13, 550-561.

Sinclair, M. R., 1997: Objective identification of cyclones and their circulation intensity, and climatology, *Wea. Forecasting*, 12, 596-612.

Slonaker, R. L., and M. L. van Woert, 1999: Atmospheric moisture transport across the Southern Ocean via satellite observations, *J. Geophys. Res.*, 104, 9229-9249.

Smirnov, V. V., and G. W. K. Moore, 1999: Spatial and temporal structure of atmospheric water vapor transport in the Mackenzie River Basin, *J. Climate*, 12, 681-696.

Soden, B. J., and F. P. Bretherton, 1994: Evaluation of water vapor distribution in general circulation models using satellite observations, *J. Geophys. Res.*, 99, 1187-1210.

Starr, V. P., and J. P. Peixoto, 1958: On the global balance of water vapor and the hydrology of deserts, *Tellus*, 10, 189-194.

Starr, V. P., and J. P. Peixoto, 1971: Pole-to-pole eddy transport of water vapor in the atmosphere during the IGY, *Arch. Meteor. Geophs. Biokl.*, 20A, 85-114.

Sun, D.-Z., and A. H. Oort, 1995: Humidity-temperature relationships in the tropical troposphere, *J. Climate*, 8, 1974-1987.

Takle, E. S., and Coauthors, 1999: Project to Intercompare Regional Climate Simulations (PIRCS): Description and initial results, *J. Geophys. Res.*, 104, 19,443-19,461.

Thorncroft, C. D., B. J. Hoskins, and M. E. McIntyre, 1993: Two paradigms of baroclinic wave life-cycle behavior. *Quart. J. Roy. Meteor. Soc.*, 119, 17-55.

Trenberth, K. E., 1976: Spatial and temporal variations of the Southern Oscillation, *Quart. J. Roy. Meteor. Soc.*, 102, 639-653.

Trenberth, K. E., and D. J. Shea, 1987: On the evolution of the Southern Oscillation, *Mon. Wea. Rev.*, 115, 3078-3096.

Trenberth, K. E., 1991: Storm tracks in the Southern Hemisphere, *J. Atmos. Sci.*, 48, 2159-2178.

Trenberth, K. E., and C. J. Guillemot, 1995: Evaluation of the global atmospheric moisture budget as seen from analysis, *J. Climate*, 8, 2255-2272.

Trenberth, K. E., and T. J. Hoar, 1996: The 1990-1995 El Niño - Southern Oscillation event: Longest on record, *Geophys. Res. lett.*, 23, 57-60.

Trenberth, K. E., and T. J. Hoar, 1997: El Niño and climate change. *Geophys. Res. lett.*, 24, 3057-3060.

Trenberth, K. E., 1998: Atmospheric moisture residence times and cycling: Implications for rainfall rates and climate change, *Climatic Change*, 39, 667-694.

Trenberth, K. E., and C. J. Guillemot, 1998: Evaluation of the atmospheric moisture and hydrological cycle in the NCEP/NCAR reanalyses, *Climate Dyn.*, 14, 213-231.

Trigo, I. E., T. D. Davies, and G. R. Bigg, 1999: Objective climatology of cyclones in the Mediterranean Region, *J. Climate*, 12, 1685-1696.

van Loon, H., 1979: The association between latitudinal temperature gradient and eddy transport. Part I: Transport of sensible heat in winter, *Mon. Wea. Rev.*, 107, 525-534.

Wade, C. G., 1994: An evaluation of problems affecting the measurement of low relative humidity on the United States radiosonde, *J. Atmos. Oceanic Technol.*, 11, 687-700.

Waliser, D. E., Z. Shi, J. R. Lanzante, and A. H. Oort, 1999: The Hadley circulation: Assessing NCEP/NCAR reanalyses and sparse in-situ estimation. *Climate Dyn.*, 15, 719-735.

Walker, G. T., 1923: Correlation in seasonal variations of weather, VIII. A preliminary study of world weather (World weather I), *Mem. Indian Meteorol. Dept.*, 23, 75-131.

Walker, G. T., and E. W. Bliss, 1932: World weather V, *Mem. R. Meteorol. Soc.*, 4, 53-84.

Wallace, J. M., G.-H. Lim, and M. L. Blackmon, 1988: Relationship between cyclone tracks, anticyclone tracks, and baroclinic waveguides, *J. Atmos. Sci.*, 45, 439-462.

Whittaker, L. M., and L. H. Horn, 1984: Northern Hemisphere extratropical cyclone activity for four mid-season months, *J. Climatol.*, 4, 297-310.

Wittmeyer, I. L., and T. H. Vonder Haar, 1994: Analysis of the global ISCCP TOVS water vapor climatology, *J. Climate*, 7, 325-333.

Wu, Z.-X., 1996: The influence of SST on air temperature in the tropics. Ph. D. thesis, Department of Earth, Atmospheric, and Planetary Sciences, Massachusetts Institute of Technology.

Zapotocny, T. H., D. R. Johnson, and F. M. Reams, 1993: A comparison of regional isentropic-sigma and sigma model simulations of the January 1979 Chicago Blizzard, *Mon. Wea. Rev.*, 121, 2115-2134.

Zhang, Y., and W.-C. Wang, 1997: Model-simulated northern winter cyclone and anticyclone activity under a greenhouse warming scenario, *J. Climate*, 10, 1616-1634.

Zhu, Y., and R. E. Newell, 1994: Atmospheric rivers and bombs, *Geophys. Res. Lett.*, 21, 1999-2002.

Zhu, Y., and R. E. Newell, 1998: A proposed algorithm for moisture fluxes from atmospheric rivers, *Mon. Wea. Rev.,* 126, 725-735.

Zhu, Z, 1997: Precipitation and water vapor transport simulated by a hybrid σ-θ coordinate GCM, *J. Climate,* 10, 988-1003.

Zishka, K. M. and P. J. Smith, 1980: The climatology of cyclones and anticyclones over North America and surrounding ocean environs for January and July, 1950-77, *Mon. Wea. Rev.*, 108, 387-401.